The Dissertation Committee for Chenglin Yang Certifies that this is the approved version of the following dissertation:

ON THE MULTIAXIAL CRUSHING OF LOW-DENSITY OPEN-CELL FOAMS

Committee:

Stelios Kyriakides, Supervisor

Rui Huang

Andrew M. Kraynik

Kenneth M. Liechti

Krishnaswamy Ravi-Chandar

ON THE MULTIAXIAL CRUSHING OF LOW-DENSITY OPEN-CELL FOAMS

by

Chenglin Yang

Dissertation

Presented to the Faculty of the Graduate School of

The University of Texas at Austin

in Partial Fulfillment

of the Requirements

for the Degree of

Doctor of Philosophy

The University of Texas at Austin

May 2020

Dedication

To my parents.

Acknowledgements

I would like to express my sincere gratitude to my advisor, Prof. Stelios Kyriakides, for all his teaching, guidance and support throughout my graduate studies. His knowledge, experience and deep understanding of the subject helped me through every step to accomplish this research. Also, his stringent attitude and tireless devotion to scientific excellence influence me deeply, not only during the past years that we worked together but also in the future.

I would like to thank Prof. Stavros Gaitanaros, from whom I learned a lot on past modeling frameworks of foams in the beginning of my graduate study. I am also grateful to Dr. Andrew Kraynik for sharing his deep insights on micromechanically accurate models of foams. I would like to express my gratitude to other members of my Ph.D. committee, Profs. Rui Huang, Kenneth M. Liechti and Krishnaswamy Ravi-Chandar for the time they have devoted to reviewing my dissertation and for their constructive comments.

Many thanks go also to all the members in this department who have helped me with technical or administrative problems. I feel fortunate to have interacted with a number of excellent fellow students during the invaluable stay in Austin, including Prof. Lin Yuan, Prof. Wei Gao, Prof. Dongjie Jiang, Prof. Nikolas Bouklas, Prof. Chenglin Wu, Dr. Nathan J. Bechle, Dr. Ziyi Cao, Dr. Seung Ryui Na, Dr. Shixuan Yang, Dr. Sundeep Palvadi, Dr. Yafei Liu, Dr. Kelin Chen, Dr. Martin F. Scales, Dr. Shutao Qiao, Dr. Liu Wang, John Mersch, Ben Harrison, Karlos Kazinakis, Yo-Sheng Lo, Zhaohe Dai, Jake Haley, Harvey Fulton, Solon Tsimpoukis, and Weihan Zhang.

Finally, I am grateful to my parents, who are always there no matter what.

On the Multiaxial Crushing of Low-Density Open-Cell Foams

Chenglin Yang, Ph.D.

The University of Texas at Austin, 2020

Supervisor: Stelios Kyriakides

Under uniaxial compression deformation in low-density foams localizes into narrow bands of crushed cells. Crushing spreads at nearly constant stress with crushed and relatively undeformed material coexisting. The material returns to homogeneous deformation with increasing stress when the crushing has spread over the whole specimen. The present study investigates how this partially unstable behavior of low-density foams transfers to the multiaxial setting as follows:

(i) The crushing behavior of random foams is investigated under "true" triaxial loadings. A micromechanically accurate cubical model of an Al-alloy open-cell foam with relative density of 0.08 is crushed by a numerical true triaxial apparatus in three directions for three families of radial displacement paths. For all paths studied, the foam traces the same three regime behavior observed under uniaxial compression. Local cell crushing developed in narrow bands of cells at boundaries and subsequently propagate to the rest of the domain until the whole domain is crushed.

(ii) A plasticity model is presented with a Drucker-Prager type yield function coupled with a non-associated flow rule. An essential component of the modeling effort is the introduction of a softening branch to the material stress-strain response. The constitutive model is incorporated in a cubical finite element model to simulate true triaxial crushing tests performed on the random foam in the continuum setting. Small geometric imperfections are used to trigger localized deformation in the form of planar bands of high strain. The bands broaden with the stresses tracing plateaus. For all loading paths, the calculated crushing responses reproduce those of the random foam very well. The study

clearly demonstrates that the homogenized model captures the partially inhomogeneous crushing behavior of foams.

(iii) The same random foam model is crushed under displacement controlled axial compression at different levels of external pressure. The study shows that such foams deform inhomogeneously under this triaxial loading also. The level of external pressure tends to lower the limit stress, the stress plateau, and the rest of the response. This behavior is subsequently simulated at the continuum level. It is demonstrated that the homogenized model again captures the three-regime response of the random foam.

Table of Contents

Chapter 1: Introduction

Cellular microstructure is widely used in nature and in synthetic materials and structures to conserve materials and reduce weight. Natural examples include many woods, stalks and roots of plants, cork, human bones, sponge, coral, shells etc. (Gibson and Ashby, 1997). Many fruits and vegetables have cellular microstructures also. Synthetic cellular materials that mimic nature have experienced an enormous increase in the past decades, so that today may be one of the most widely used man-made classes of materials. Synthetic cellular materials fall into two categories, two-dimensional honeycombs and space filling foams. Some space filling foams have open cell faces (open-cell foams) and others have faces that are covered by plates or membranes (closed-cell foams). These synthetic cellular materials can be made from all major material categories including metals, polymers, ceramics, paper and carbon. This dissertation investigates the mechanical behavior of open-cell foams.

1.1 APPLICATIONS OF FOAMS

The cellular microstructure of space filling foams bestows to them unique mechanical, thermal, acoustical and other properties that make them attractive in a broad range of applications (e.g., see Gibson and Ashby, 1997; Ashby et al., 2000). The breath in availability coupled with their high stiffness-to-weight and strength-to-weight ratios, have made them one of the most widely used classes of materials as cores in sandwich structures used in applications ranging from packaging to ship and aircraft panels. Polymeric foam sandwich cores include Polystyrene, Polyurethane, PVC (Polyvinyl Chloride), or PMI (Polymethacrylimide) foams, etc. (e.g., see *Enlighten* presented by Altair). Rigid closed-cell PMI foams are used, for example, in the aerospace industry in ailerons and helicopter rotor blades because of their excellent mechanical properties. In addition, PMI foams have a high fatigue life and can be easily thermoformed to complex geometries. One of the disadvantages of polymeric foams is that they tend to have lower tolerance to damage, compared to heavier solid laminate materials. Metal foams are also

used as sandwich cores to replace stamped-steel parts of a vehicle (e.g., Aluminum Foam Sandwich by German Automaker Karmann, reported in Banhart 2003).

Another advantage of foams is their relatively low crushing strength and extensive stress plateau. This gives them unique energy absorption and impact mitigation capacities that are exploited in applications ranging from car bumpers, to helmets and other blast protection structures. Flexible polymeric foams are used for personal protection applications such as cushions, sport shoe midsoles and helmets (Mills et al., 2003). Metal foams on the other hand are extensively used in the automotive industry. Aluminum foams are used, for example, as fillers of crashboxes placed between the bumper and the front rail of a car (Banhart 2003). Crashboxes are designed to absorb energy in relatively low speed crashes, protecting the passengers and the rest of the car. Adding Aluminum foam cores improves the energy absorption capacity of crashboxes compared to the non-filled extrusion alternatives (see also Hassen et al., 2000). It also leads to the advantage of weight saving and volume reduction of crashboxes (Fuganti et al., 2000).

Modern manufacturing techniques enable casting of foams in dies producing a parts with a dense aluminum skin and a foam interior. Such parts have high stiffness and excellent damping characteristics in addition to superior energy absorption. Banhart (2003) reported use of such composite components as engine mounts in vehicles (e.g., designed by LKR of Austria for the German automaker BMW).

Other applications of foams include titanium-based foams used as bone implants; polymeric foams used as thermal and acoustic insulation materials; air batteries, biomedical prostheses, catalyst supports, filters and fluid flow limiting devices, fuel cells, non-slip surfaces for trays, etc.

1.2 UNIAXIAL CRUSHING OF LOW-DENSITY FOAMS

An important goal of the research community has been to connect the microstructure and base material properties to the foam's unique properties. Connection of the microstructure to the initial elastic properties has, by and large, been accomplished, but relating it to the "strength," the stress plateau and the densification response remains a

2

challenge. For low-density foams used in many applications, this behavior is governed by inelastic action, localized crushing at the cell level, and ligament contact that is responsible for the spreading of the crushing.

A typical uniaxial crushing behavior of polyester urethane foams of relative density about 2.5% was described in Gong et al. (2005a) and Gong and Kyriakides (2005). The foams tested were crushed up to an average strain of about 0.5. The compressive stress-displacement response in the rise direction starts with a nearly linear elastic branch that terminates into a stress maximum. It then traces an extended plateau, followed by a second stiff branch. The foam deforms nearly uniformly during the initial stable regime of the response. Following the limit stress the specimen buckles in an overall manner, and concurrently deformation localizes in a banded manner. Subsequently, the bands grow with numbers and propagate to neighboring cells with the stress tracing the plateau. After the whole domain is crushed, the domain is densified and the stress picks up again. Similar surface deformation patterns were reported in Wang et al. (2000) using a digital image correlation technique. The foams are anisotropic, and the crushing response in the transverse direction monotonically increases. The deformation, on the other hand, is probably uniform when the foam is crushed in the transverse direction.

Jang and Kyriakides (2009a) reported that low-density open-cell Al-alloy foams under uniaxial crushing exhibit the same three-regime behavior (see axial stress-displacement response shown in Fig. 1.1). Here however deformation localizes into irregular bands that cover the whole cross section of the domain. With further compression such bands propagate until the whole domain is crushed. X-ray tomography was used to capture the propagation of crushing as illustrated by the set of images shown in Fig. 1.2 (see also Bart-Smith et al., 1998; Gioux et al., 2000). The images correspond to the numbered bullets on the response shown in Fig. 1.1. Cell crushing is limited by contact between cell ligaments, which stiffens the crushing zones and leads to a small recovery in the stress. The stress increase is sufficient to destabilize neighboring cells. This successive destabilization of neighboring cells is the mechanism through which the crushing front propagates until the whole domain is crushed as illustrated by images ②-④ in Fig. 1.2.

3

Beyond image ④, the material deforms essentially uniformly, requiring a significant increase in stress—*densification* regime.

In the case of this anisotropic aluminum foam the response and deformation in the transverse direction is similar to that in the rise direction but with somewhat lower stress maximum and plateau stress. Localized deformation in aluminum foams under uniaxial crushing was also reported in Bastawros et al. (2000), Schuler et al. (2013), Jung et al. (2015), and Aakash et al. (2019) using digital image correlation.

Motivated by capturing this inhomogeneous crushing behavior of foams, past studies has developed micromechanical models. The microstructures of low-density open-cell polymeric and Al-alloy foams were characterized in Gong et al. (2005a), Jang et al. (2008) and Jang and Kyriakides (2009a). With this as background, the foams were first idealized using the periodic space-filling 14-sided Kelvin cell assigned the major geometric characteristics established from the measurements on random monodisperse foams. Gong et al. (2005a) and Jang et al. (2008) reported that the Kelvin cell models capture the initial elastic properties of foams accurately. The calculated limit stresses were also found to be in a good agreement with the values measured in uniaxial compression experiments (Gong et al., 2005a; Jang et al., 2010). Similar calculations on elastic properties and compressive strength based on Kelvin cells can also be found in Warren and Kraynik (1997), Laroussi et al. (2002), Fischer et al. (2009), Fanelli et al. (2017) and Zhu et al. (2017).

Uniaxial crushing responses based on the Kelvin cell were found to trace the trends of experimental results up to large displacements very well (Gong and Kyriakides, 2005; Jang and Kyriakides, 2009b). Here periodicity conditions were released and spring elements were adopted to approximate ligament contact. A disadvantage of Kelvin cell models is that they are only applicable to monodisperse foams. Furthermore, the resultant crushing patterns are influenced by the periodicity of the microstructure and consequently differ from those of random foams. Studies on uniaxial crushing of foams beyond the onset of instability using similar spatial periodic structures are reported in Luxner et al. (2007) and Takahashi et al. (2010) among others.

The Kelvin cell studies were subsequently improved upon by the development of micromechanically accurate foam models (Jang et al., 2008, 2010; Gaitanaros et al., 2012, 2018). Such models are generated using the *Surface Evolver* software and able to mimic the random microstructure of real foams (Brakke, 1992). The ligaments are modeled straight with non-uniform cross sectional area distributions similar to those of the real foams, so that they end up with the same density as the foam analyzed. Jang et al. (2008, 2010) showed that such models reproduce the elastic properties and the strength of foams quite accurately.

Another significant improvement of random models is that a beam-to-beam contact algorithm is adopted, which plays a key role in the correct simulation of the stress plateau during the propagation phase of the crushing response. The performance of such random foams in the simulation of uniaxial crushing of an Aluminum foam was demonstrated in Gaitanaros et al. (2012). Figures 1.3 and 1.4 taken from this work show the compressive axial stress-displacement response from a foam model and a sequence of corresponding deformed configurations respectively. The compressive response is in very good agreement with measured ones. A band of collapsed cells is observed to initiate from the "weakest" site in image ①. Subsequently the crushed zone propagates through the rest of the domain until the whole model is crushed, as shown in image 2-⑤. The micromechanically accurate models were also used to successfully reproduce quasi-static and impact crushing of polydisperse foams as reported in Gaitanaros and Kyriakides (2014) and Gaitanaros et al. (2018).

1.3 MULTIAXIAL LOADINGS ON LOW-DENSITY FOAMS

Further progress in the understanding of the mechanical behavior of cellular materials and foams must also address their behavior under multiaxial loads. Multiaxial crushing experiments on low-density foams are challenging because of the associated large volume changes. Thus, experimental efforts to date have been mainly concerned with the onset of "yielding." They are divided in two main categories. In the first group the foam is surrounded by a membrane and tested in the traditional triaxial test setup involving external

5

pressure and axial compression. This family of triaxial tests is hitherto referred to "conventional" triaxial test. Triantafillou et al. (1989) used conventional triaxial tests to establish failure surfaces for polymeric and aluminum foams. Similar results for reticulated vitreous carbon foams (RVC) were reported in Triantafillou and Gibson (1990). Deshpande and Fleck (2000) reported a series of triaxial crushing results on Alporas (closed-cell) and Duocel (open-cell) Al-alloy foams of different relative densities. Ruan et al. (2007) reported that CYMAT (closed-cell) aluminum foams of relative density about 12% exhibit a limit load in the axial stress when under external pressure of 2 MPa. However for all the works listed, the microstructure and evolution of crushing events of foams tested were not examined. Gioux et al. (2000) showed images of deformed configurations of open-cell and closed-cell Al-alloy foams under hydrostatic compression. Local regions of higher deformation in the foam specimens were observed. The foams were loaded up to an axial strain of only about 7%.

In the second category, a specially shaped specimen is tested under displacement controlled loading in a type of three axis testing facility. Combaz et al. (2011) designed a triaxial test apparatus that surrounds cubical aluminum foam domains with three pairs of orthogonal loading platens. The displacements of the moving platens in the three directions were prescribed to produce proportional loading paths in stress space. Similarly, triaxial loadings were applied on anisotropic polymeric foams in Shafiq et al. (2015) by compressing three pairs of rigid blocks on cubical foam specimens. Each block was allowed to move in only one direction normal to the loading axis. They reported stress-strain responses with load maxima followed by softening branches. In both works the crushing was terminated at relatively low strains and no information about the deformation of the microstructure is provided. Alternative biaxial experimental results can be found in (Gdoutos et al., 2002; Mohr and Doyoyo, 2003; Blazy et al., 2004; Jung and Diebels, 2017).

Analytical efforts aimed at modeling the mechanical behavior of foams under multiaxial loads are rather limited. Gong et al. (2005b) and Ayyagari and Vural (2016) reported the onset of instability (or "yielding") of low-density foams under multiaxial loads using elastic Kelvin cell foams. Zhu et al. (2019) crushed model foams with relative density

of 10% with a Voronoi closed-cell microstructure under various radial displacement paths. They reported several triaxial responses with extended stress plateaus and microstructures with localized deformations.

However, micromechanically accurate models of random foams, although insightful and accurate, are numerically intensive and not ideal as constitutive models, prompting the pursuit of "homogenized" alternatives. To date, despite strong evidence in the literature that under compression low-density foams crush inhomogeneously, present continuum constitutive models of foams, assume the material to harden monotonically and consequently do not capture the inhomogeneous behavior. Zhang et al. (1997) proposed a volumetric hardening compressible constitutive model for polymeric foams, with a quadratic yield function and non-associated flow rule. Miller (2000) introduced a quadratic dependence on the pressure in the Drucker-Prager (1952) yield criterion customized for aluminum foams. To date the most widely used constitutive model is due to Deshpande and Fleck (2000). They used results from different multiaxial stress paths to generate an isotropic quadratic yield surface in the (I_1, J_2) space. An associated plastic flow rule was adopted and the hardening law used in the work was assumed to depend on stress paths. The constitutive model was used to reproduce a number of crushing responses for aluminum foams. However, the deformation of such models is homogeneous. The model was later implemented in ABAQUS and other FEA software.

Deshpande and Fleck (2001) extended the application of the model to polymeric foams. Xue and Hutchinson (2004), Tagarielli et al. (2005) and Ayyagari and Vural (2015) proposed extended versions of the model for transversely isotropic foams. Linear pressure dependence resulting in asymmetry in compression and tension was also examined in Ayyagari and Vural (2015). Zhu et al. (2019) reported that the parameter α^2 which determines the shape of the yield surface follows a nonlinear softening-stiffening trend against equivalent plastic strain. Similar results can be found also in Chen et al. (2000).

In summary, experimental studies on multiaxial crushing of foams to large volume changes remain a challenge, and existing data lack both foam microstructure information

and its evolution during crushing. Most of the present constitutive models adopt a quadratic Drucker-Prager type yield function and a hardening material model, which lead to homogeneous deformation under uniaxial and multiaxial stress states. Both of these deficiencies in the current state of the art will be addressed in this dissertation.

1.4 OUTLINE OF THE WORK

In the present study we aim to establish the response of low-density open-cell Al-alloy foams under triaxial loadings crushed to large volume changes. Having developed confidence in the veracity of the micromechanically accurate modeling framework developed for random foams, the "testing" is performed numerically. Chapter 2 describes the random foam models used in this study. They are based on the framework developed in Jang et al. (2008) and Gaitanaros et al. (2012). Chapter 3 presents a true triaxial apparatus that is used to crush cubical random foam models under three sets of radial displacement paths. A Drucker-Prager type compressible constitutive model for continuum modeling of multiaxial crushing of foams is presented and calibrated in Chapter 4. In Chapter 5, crushing simulation of the true triaxial numerical tests from Chapter 3 are performed in the continuum setting. The predictions are evaluated by direct comparison to those of the random foam results. Chapter 6 describes conventional triaxial tests of foams first on random foams and the responses are subsequently simulated using homogenized models.
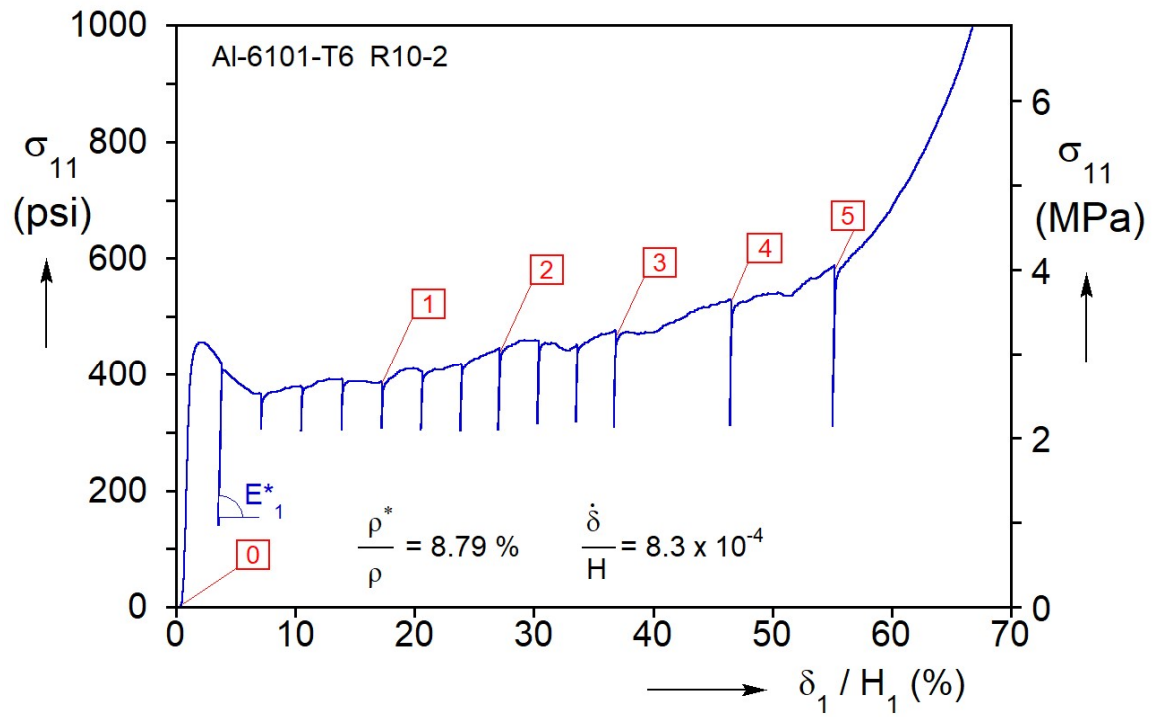
Fig. 1.1:   Compressive uniaxial nominal stress-displacement response of a Duocel®
Al-alloy foam (from Jang and Kyriakides, 2009a).
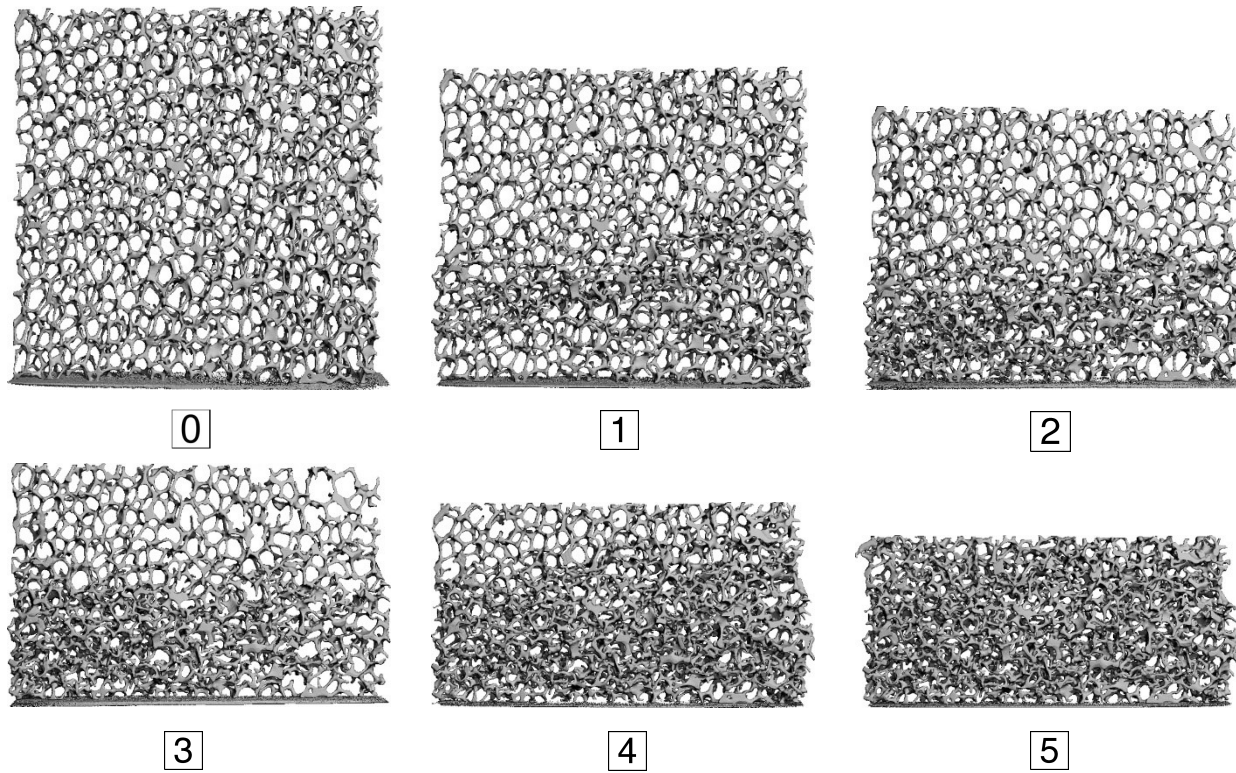
Fig. 1.2:   Sequence of cross-sectional deformed configurations corresponding to the numbered points on the response in Fig. 1.1 taken with X-ray tomography (from Jang and Kyriakides, 2009a).
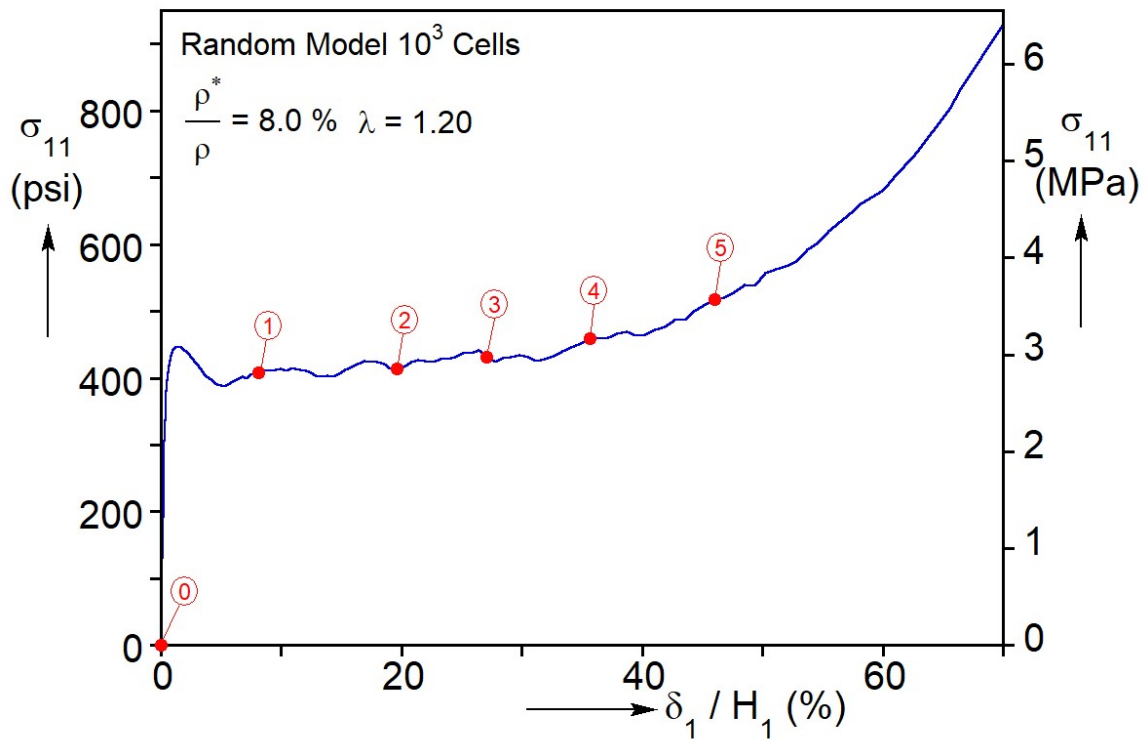
Fig. 1.3: Calculated compressive uniaxial stress-displacement response in the rise direction of a micromechanically accurate model with 10^3 cells (from Gaitanaros et al., 2012).
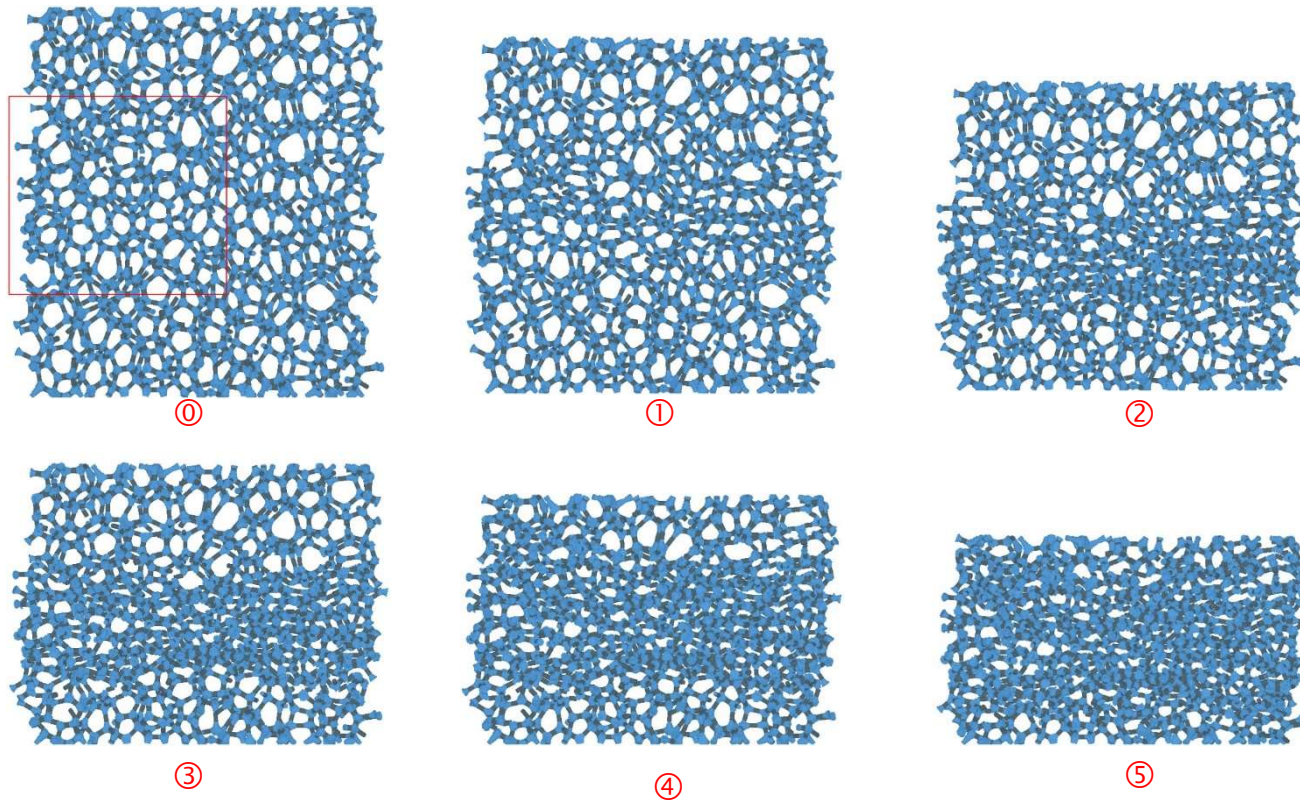
Fig. 1.4:   Sequence of deformed configurations corresponding to the numbered bullets on the response shown in Fig. 1.3 (from Gaitanaros et al., 2012).

Chapter 2: Random Foam Model[12]

Open-cell solid foams consist of randomly packed polyhedral cells that result from the foaming process. The low-density open-cell Aluminum foams used in this study are cast into templates made from polymeric foams (Ashby et al., 2000): the polymer in the cast is evaporated and liquid Al is poured in its place. The mold is then removed leaving behind the aluminum foam with the same microstructure as the original polymeric one. This includes the distribution of polyhedral cells that have anywhere from 9 to 17 faces when the foam is nearly monodisperse (Matzke, 1946), their anisotropies, etc. The material is concentrated in the nearly straight edges of the polyhedral cells and in the nodes usually formed by four intersecting ligaments. A long-term goal of the research community has been to connect the microstructure and base material properties to the foams' unique properties such as their high stiffness-to-weight ratios, strength-to-weight ratios, and unique energy absorption capacities.

Our research group has developed a family of micromechanically accurate models that have been shown to reproduce most of the mechanical properties of open-cell foams (Jang et al., 2008; Gaitanaros et al., 2012; Gaitanaros and Kyriakides 2015; Gaitanaros et al., 2018). The models start as a skeletal isotropic random soap froth generated using the Surface Evolver software (Kraynik et al. 2003b, 2004). Such soap froths reproduce all major geometric characteristics of liquid foams such as the polyhedral cell geometry, the length distribution of ligaments, etc. They skeletal microstructure is dressed with solid with the ligament cross sectional area distribution that corresponds to that of actual Al-alloy foams. The correct distribution of material is maintained in the discretization of the ligaments when developing finite element models of the foam blocks.

This Chapter describes how the large-scale micromechanically accurate foam models used in this study are generated. The procedure is based on the framework

---

[1] Yang, C., Kyriakides, S., 2019. Multiaxial crushing of open-cell foams. *Int'l J. Solids Structures* **159**, 239-256. Chenglin Yang contributed as first author.

[2] Yang, C., Kyriakides, S., 2019. Crushing of low density foams under triaxial loadings. *Extreme Mechanics Letters* (accepted). Chenglin Yang contributed as first author.

developed in Jang et al. (2008) and Gaitanaros et al. (2012). Section 2.1 describes the numerical generation of a skeletal version of a N^3 cell model that is based on a random spatially periodic soap froth generated by the Surface Evolver. Section 2.2 describes the discretization of the ligaments with circular cross-sections but variable diameters along the length. The contact algorithm required in the foam crushing simulations for arresting local cell crushing is also outlined. Finally the mechanical properties of the Al-alloy base material are briefly discussed.

2.1 GEOMETRY

The random foam models that are analyzed in this study originate from random spatially periodic soap froths generated by the Surface Evolver (Brakke, 1992) as described in Kraynik et al. (2003b, 2004). The generation procedure has the following steps. A primitive Voronoi froth with foam-like characteristics is generated first from randomly packed hard spheres of equal radius in molecular dynamics. Each Voronoi cell consists of all points that lie closest to a random seed, i.e., the center of each sphere. Next, the Voronoi structure is used as an initial condition in the Surface Evolver to generate the limiting case of a "dry" foam in which the liquid volume fraction is zero and the films can be modeled as two-dimensional surfaces. The software minimizes energy and balances mechanical forces by satisfying Plateau's laws (Plateau, 1873; Weaire and Hutzler, 1999): *I. the faces of cells are surfaces of constant mean curvature; II. three faces meet at equal dihedral angels of* 120°; *and III. four edges meet at the tetrahedral angle* $\cos^{-1}(-1/3) \approx 109.47^{\circ}$. In this study, monodisperse foam models are used, thus the additional constraint that all cells have the same volume is also applied.

The next step includes a *relaxation* process that requires a large number of topological transitions that involve cell-neighbor switching. Since the solution is a local energy minimum, the surface area can be further reduced by subjecting the foam to large-deformation tension-compression cycles that provoke additional neighbor switching. This process is referred to as *annealing*. The resulting structures are in excellent agreement with

14

Matzke's (1946) experimental study, indicating that the foam structures being produced are realistic. The simulation generates a skeletal version of monodisperse, periodic and isotropic foams. Accurate data on geometric properties such as the volume, surface area, and edge length of the entire foam, individual cells, and cell-level features are provided in Kraynik et al. (2003a, 2003b, 2004, 2005, 2006).

The skeletal version of the random foam model used in this study is generated by joining the vertices of the random cellular microstructure with straight lines. In the analyses performed the foam is required to be an exact cube. For this tailoring the periodicity of the domain is removed followed by removal of a thin layer of material from each surface. For a 10^3 cell model, removal of a layer reduces the width of each side by approximately 2%. Typically about 200 end nodes are left on each surface. A 3-D rendering of a 10^3 cell skeletal model that has been cropped is shown in Fig. 2.1.

2.2 FINITE ELEMENT MODELING

2.2.1 Discretization and Material Distribution

The straight ligaments in the random foam model are dressed with shear deformable beams with circular cross-sections but variable diameters along the length. The area distribution follows that developed from measurements on ERG Duocel® Al-6101-T6 foams reported in Jang et al. (2008):

$$A(\xi) = A_o f(\xi) = A_o (36\xi^4 + \xi^2 + 1), \qquad \xi = x/l, \qquad (2.1)$$

where A_o depends on the ligament length l, through

$$A_o = \bar{A}_o g(\eta) = \bar{A}_o (0.6633 + 0.2648\eta^{-2.5963}), \qquad \eta = l/\bar{l}, \qquad (2.2)$$

here, $\bar{A}_o$ and $\bar{l}$ are the average of the measured values of mid-span cross sectional area and length respectively.

Since the ligaments are modeled as beams, there is an overlap of material at the nodes, which is corrected for the purposes of calculating the relative density through the following expression (Jang et al. 2008):

15

$$\frac{\rho^*}{\rho} = k\left(\frac{R_o}{\bar{l}}\right)^n \tag{2.3}$$

where R_o is the average radius of all ligaments at mid-span. It is noted that k and n depend on the anisotropy. Table 4 of Jang et al. (2008) report k and n values for foams of different anisotropy values. For isotropic foams, $k = 2.0263$ and $n = 1.7072$. The foam model used in the study has a relative density $\rho^* / \rho = 0.08$. Assigning this to Eq. (2.3), together with the average length of all ligaments in the skeletal random foams, enables the calculation of R_o.

The ligaments are then discretized in LS-DYNA (2019) with the Hughes-Liu linear beam element (1981) that is derived from the isoparametric 8-node solid element. The element allows for finite deformations of the beam axis, finite rotations of its normal as well as transverse shear deformations. A constant moment is generated along the length of the element, which implies each ligament must be assigned with a sufficient number of elements. In addition, a reference surface located at an offset location facilitates contact on the outer surface of the beam, a key characteristic for the present problem.

The discretization is chosen for accurate representation of the area variation along the ligament, the order of the element, and for optimal performance in ligament contact. The discretization method is very similar to that in Gaitanaros et al. (2012) with minor adjustments to the current model, and will be outlined here for completeness. First, the ligaments are categorized in two groups: ones with $l < \bar{l}$ and the rest with $l \geq \bar{l}$. The average length of each group is designated as l_1 and l_2, respectively. Based on the measured average lengths of the foam, the mean mid-span cross sectional area in each group, $A_o|_{\bar{l}_\alpha}$, $\alpha = 1,2$, is calculated by assigning l_α, $\alpha = 1,2$, $\bar{A}_o$ and $\bar{l}$ to Eq. (2.2).

The area variation along the ligament is applied as following: the first group is further discretized with 7 elements and the second with 9 elements. All elements are assigned a uniform circular cross sectional area, using the discretized version of Eq. (2.1):

$$A(\xi) = A_o\big|_{\bar{l}_\alpha} \, f(\xi)\big|_{\bar{l}_\alpha} \,, \quad \alpha = 1, 2 \tag{2.4}$$

The values of $f(\xi)\big|_{\bar{l}_\alpha}$ for the two groups of ligaments are given in (Gaitanaros et al., 2012, Gaitanaros and Kyriakides, 2014) and for clarity in Table 2.1. Figure 2.2 shows an expanded view of a few cells that demonstrate the area variation of ligaments.

In the present model, there are a few very short and thick ligaments in the first group (~2% of the total number of ligaments). LS-DYNA is an explicit code, where a stable time increment depends on the smallest element length. Thus, a higher computational efficiency is achieved by assigning 3 elements and the two largest cross sectional areas from the first group to these ligaments.

Table 2.1:   Cross sectional area of beam elements for the two ligament groups

ξ	$f(\xi)\big|_{\bar{l}_1}$	$f(\xi)\big|_{\bar{l}_2}$
$\lvert\xi\rvert \leq 0.18$	1.0	1.0
$0.18 \leq \lvert\xi\rvert \leq 0.34$	1.2425	-
$0.18 \leq \lvert\xi\rvert \leq 0.26$	-	1.0
$0.26 \leq \lvert\xi\rvert \leq 0.34$	-	1.3925
$0.34 \leq \lvert\xi\rvert \leq 0.42$	1.9122	1.9122
$0.42 \leq \lvert\xi\rvert \leq 0.5$	2.8484	2.8484

Figure 2.3 shows a slice of the random foam model from the $y - x$ plane that consists of ligaments dressed with beam elements. The model has 10^3 cells and for clarity the image is limited to $0.12H$ thick (a little thicker than one cell).

2.2.2 Contact Algorithm

Contact between ligaments of collapsing cells is responsible for arresting local crushing, in the process enabling the spreading of crushing to neighboring and other cells. Consequently, the modeling of contact plays a crucial role in the ability of the model to

17

reproduce the stress plateau and the following second stiffening regime. In this study, the general automatic contact algorithm of LS-DYNA is adopted in the model as beam-to-beam contact, together with the penalty formulation of Gaitanaros et al. (2012). The algorithm generates a circular cylindrical contact surface for every element, which corresponds to our circular cross sections.

The penalty formulation uses an interface stiffness of the same order of magnitude as the stiffness of the contacting elements. At every step of the analysis penetrations are investigated along the length of each element by finding the intersection point between nearby beam elements and checking to see if their outer surfaces overlap. If they do, the contact force is computed and is applied to the nodal points of the interacting elements.

In addition, contacts between excess materials are excluded in the model. As noted above, the use of beam elements leads to excess material at the nodes. This excess material was corrected for the calculation of the density of the model but the overlaps remain in the numerical model. The overlaps at the nodes cause initial interpenetrations between beam elements and non-physical contacts that lead to numerical instabilities. This difficulty is bypassed by excluding the two elements adjacent to the nodes from developing contact. The group of very short ligaments is also excluded from developing contact because of initial interpenetrations.

Coulomb friction with a coefficient of 0.4 is used for beam-to-beam contact. It is shown that friction between contacting ligaments was found to play an important role in stabilizing the numerical solution. Moreover, friction prevents "dynamic" sliding between ligaments especially when the compressive force increases during the densification regime. It is noted that contacts between the foam model and the surrounding plates in the next chapters are frictionless.

2.2.3 Base Material Properties

The foam Al alloy is treated as an elastic-plastic solid assigned the true stress-logarithm strain version of the properties measured in an independent tensile test in Jang

and Kyriakides (2009b). Figure 2.4 shows that a Ramberg-Osgood fit of the measured nominal stress-engineering strain response

$$\varepsilon = \frac{\sigma}{E}\left[1 + \frac{3}{7}\left(\frac{\sigma}{\sigma_y}\right)^{n-1}\right] \tag{2.5}$$

with parameters: $E = 10^4$ ksi (69 GPa), $\sigma_y = 28$ ksi (193 MPa), $n = 48$. In LS-DYNA the material response is represented by piecewise linear segments and used to calibrate isotropic plasticity.
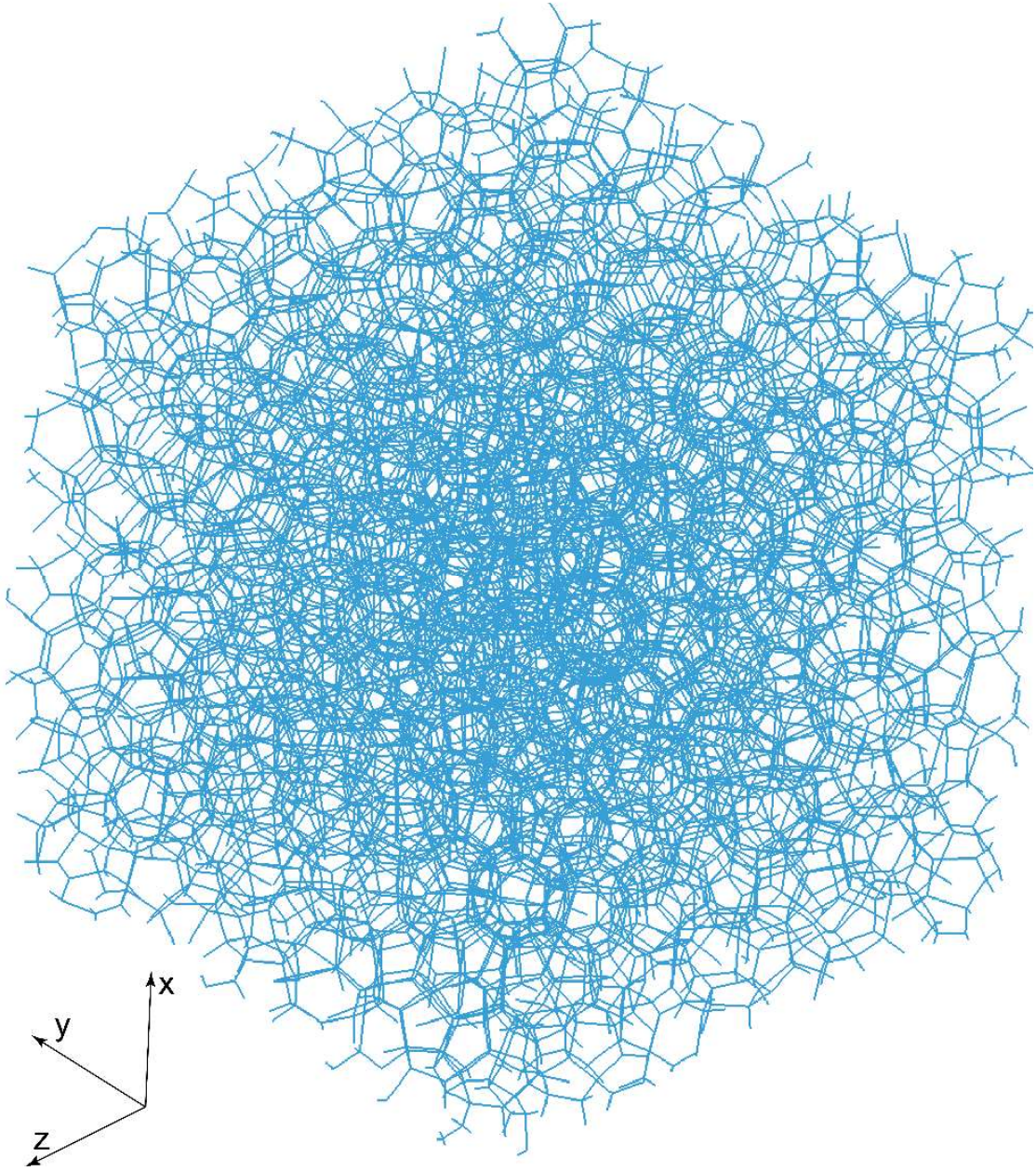
Fig. 2.1: Skeletal 3-D rendering of the 10^3 cell model foam.
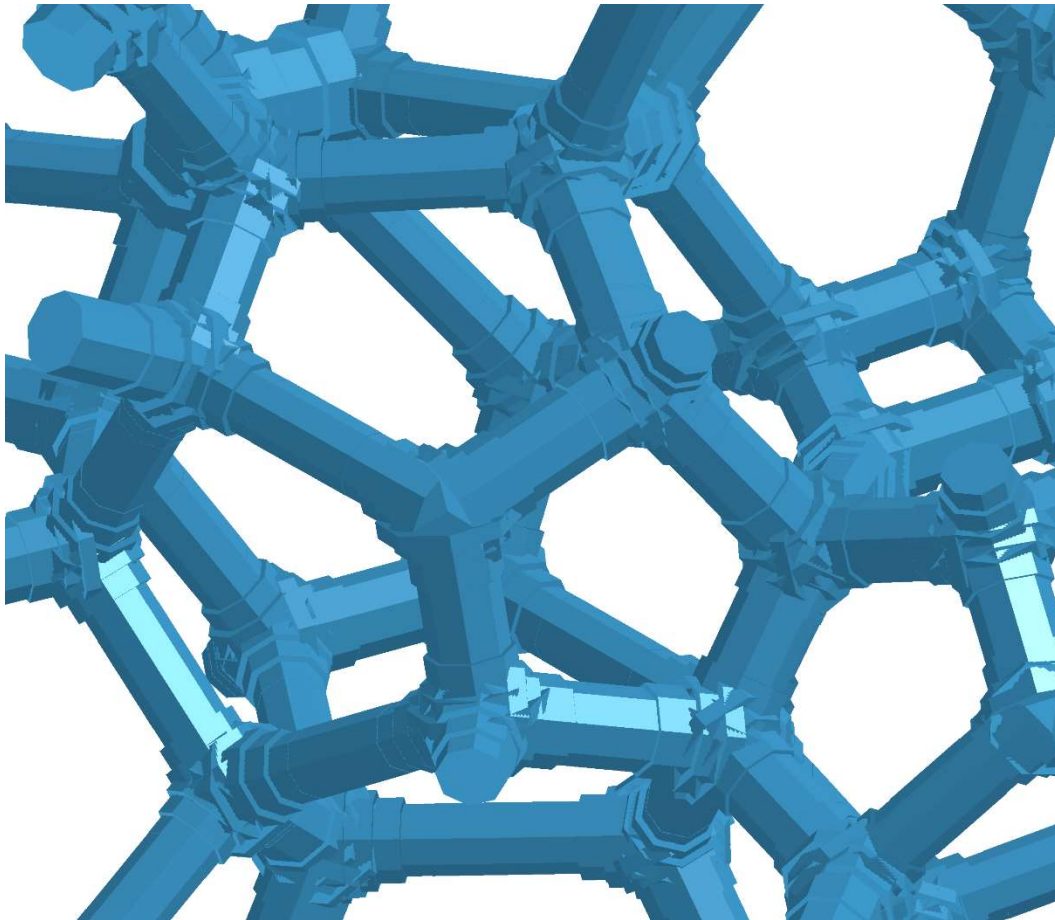
Fig. 2.2:   A typical cell that consists of ligaments from the two length groups discretized with 7 and 9 elements. (Note: the ligaments have circular cross sections. The polygonal cross section in the image is a LS-DYNA display effect).
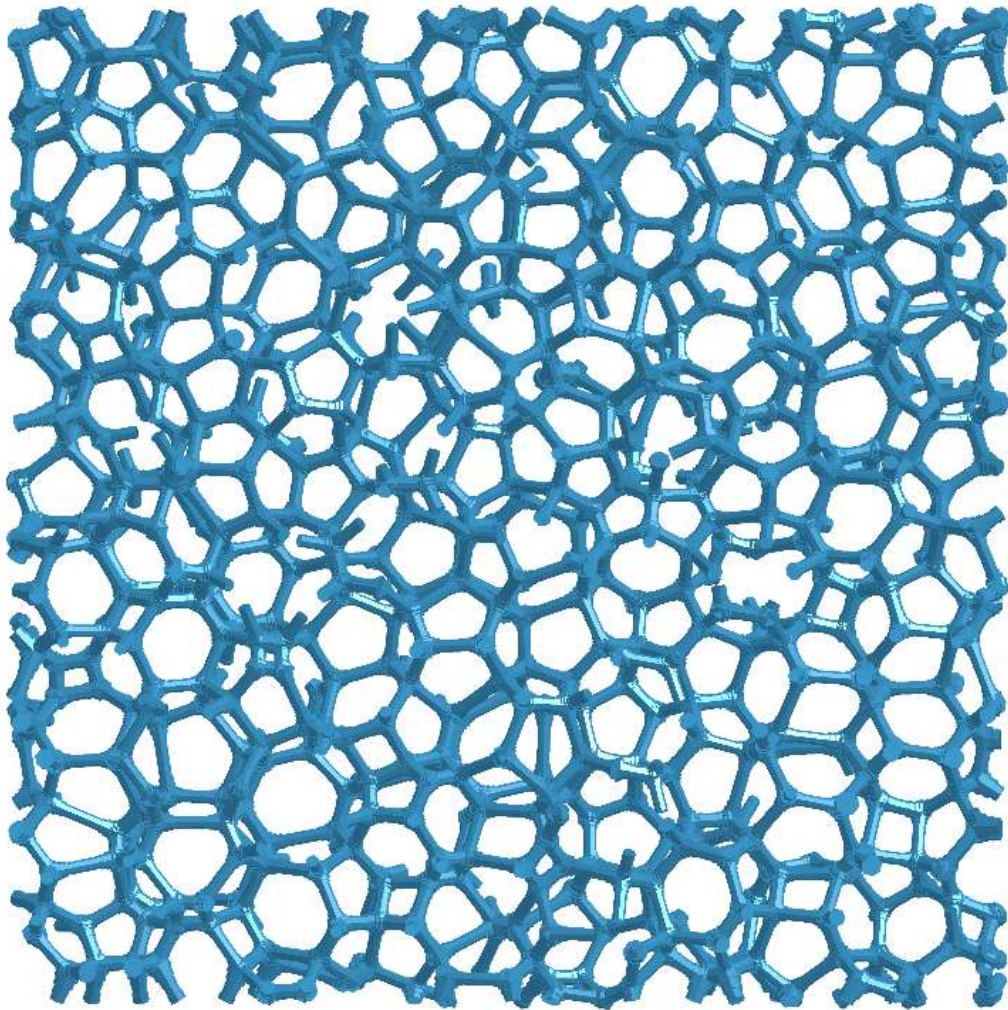
Fig. 2.3:   A 10^3 cell model foam slice from the $y - x$ central plane; ligaments are now dressed with beam elements.
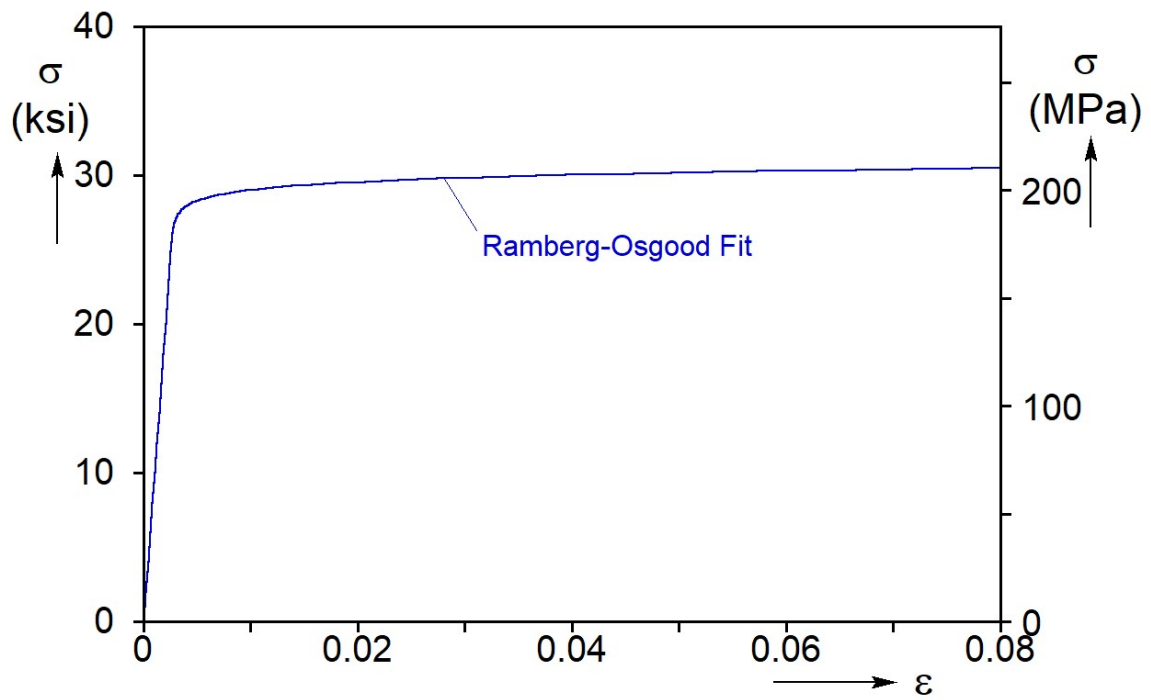
Fig. 2.4:   A Ramberg-Osgood fit of Al-6106-T6 foam base material.

Chapter 3: True Triaxial Crushing of Random Foam Models[3]

Multiaxial crushing experiments on low-density foams are challenging because of the associated large volume changes. The literature on the subject is rather sparse and has been mainly concerned with the onset of "yielding." To date results with complete crushing responses and evolution of the microstructure of foams under triaxial loads have not been reported. This challenge is addressed in this Chapter by investigating the crushing behavior of foams under triaxial loads numerically using the isotropic random foam model developed from Chapter 2.

Papka and Kyriakides (1999a) designed and built a biaxial crushing testing facility. They used this facility to conduct a set of biaxial crushing experiments on a polycarbonate honeycomb with circular cells by prescribing a set of radial displacement paths. In this Chapter the mechanism of this biaxial testing machine is adopted and extended to generate numerically a true triaxial apparatus. The objective of this apparatus is to perform crushing of random foam models in three orthogonal directions to large volume changes. The apparatus is used to generate crushing responses and concurrently monitor the evolution of the microstructure of the foam. Section 3.1 describes the true triaxial test setup developed. Sections 3.2 to 3.4 describe simulations of triaxial crushing of the random foam model. Section 3.5 describes unique properties measured from the random foam models. A significant part of the results in this Chapter appears in Yang and Kyriakides (2019a), hitherto referred to as YK19a.

3.1 CRUSHING TEST SETUP

3.1.1 True Triaxial Numerical Apparatus

Papka and Kyriakides (1999a) developed a biaxial testing machine that enabled crushing of low-density honeycomb specimens to volume reduction of up to 95%. The specimen is compressed between two pairs of parallel orthogonal plates each connected to

---

[3] Yang, C., Kyriakides, S., 2019. Multiaxial crushing of open-cell foams. *Int'l J. Solids Structures* **159**, 239-256. Chenglin Yang contributed as first author.

a rigid block. The blocks are moved by two orthogonal actuators and their relative motions are accommodated by a set of linear slides (see Fig. 3 of Papka and Kyriakides, 1999a). They used the machine to crush a polymeric honeycomb with circular cells under various biaxial displacement ratios. The biaxial crushing was simulated numerically using a micromechanically accurate model of the honeycomb. The model was crushed between four rigid planes that moved in the same way as the plates in the physical machine (see Fig. 4 in Papka and Kyriakides, 1999b). This setup was used to successfully reproduce the biaxial crushing responses recorded in the experiments.

The present numerical apparatus is based on the same principle as the biaxial crushing machine extended to a three-dimensional orthogonal setting. It consists of three pairs of parallel rigid planar surfaces arranged as shown in Fig. 3.1a. A cubical specimen of dimensions $H \times H \times H$ is placed in a cavity of the same size formed by the six planes. The blue member of each pair of parallel plates is restrained from motion along the direction of its normal. Crushing in this direction is achieved by prescribing the normal displacement, $\delta_i, i = x, y, z$, of the yellow plate of this pair. As is the case in the biaxial crushing machine, as crushing progresses the area in contact with the specimen in each direction is reduced. This is accommodated by allowing the planes to slide relative to each other as shown schematically in Fig. 3.1b. The kinematics of the planes are as shown in Table 3.1, where the symbol ✓ stands for free to move in this direction, and ✓✓ represents prescribed displacement. Number 0 implies no motion is allowed in this direction .

Table 3.1:   Degrees of freedom of six planes of crushing apparatus

Motion	Plane					
	$x = 0$	$x = H$	$y = 0$	$y = H$	$z = 0$	$z = H$
x	0	✓✓	✓	0	✓	0
y	0	✓	0	✓✓	✓	0
z	0	✓	0	✓	0	✓✓

The numerical apparatus operates very much like the so-called "true triaxial" testing facility for soils, the first version of which was developed at Cambridge University

in the early 1970s (Hambly, 1969; Pearce, 1971; Wood 1975). The word "true" was added to triaxial in order to distinguish this test setup from the conventional axisymmetric triaxial test used in geotechnical materials testing. Crushing of foams under the more conventional triaxial loading will be discussed in Chapter 6. Thus, to distinguish between the two test setups we use the name "true triaxial test" for the present apparatus.

3.1.2 Boundary and Loading Conditions

A cubical random foam model with 10^3 cells described in Chapter 2 is placed in the cavity of the apparatus (Fig. 3.1a). End nodes on each surface will come into contact with the rigid plates. This contact is frictionless, but in the way of reducing the edge effects, the rotational degrees of freedom of the contacting nodes are constrained.

The random foam model is crushed in the three directions by prescribing the motion of the surrounding rigid plates. The prescribed displacements, δ_i, can be arbitrary but for the crushing simulations presented in this study they will follow radial paths in the $\{x, y, z\}$ space. In particular, three families of radial displacements will be considered:

$$\delta(n,1,1)^T, \ \ 0 \leq n \leq 5, \ \ \delta(n,0.5,1)^T, \ \ 0 \leq n \leq 5, \ \ \delta(n,0,1)^T, \ \ 0 \leq n \leq 5 \tag{3.1}$$

where δ is the amplitude in the z-direction as shown in Fig. 3.2.

LS-DYNA is an explicit code, so quasi-static loading is achieved by selecting the loading time history, $\delta(t)$, slow enough to keep the kinetic energy much smaller than the internal energy throughout the loading history. In this work, the loading history in the z-direction, $\delta_z(t)$ is carefully chosen following the smooth step function originally from ABAQUS:

$$\delta_z(\xi) = \delta_o + (\delta_1 - \delta_o)\xi^3(10 - 15\xi + 6\xi^2) \tag{3.2}$$

where $\xi = (t - t_i)/(t_{i+1} - t_i)$, δ_o and δ_1 are the start and end displacement of the function, respectively. The scheme ensures that the loading increments are extremely small at the initial stage, and gradually enlarge when the deformation reaches the densification stage. This has to be balanced by the fact that a complete crushing response of a model with more

26

than 81,000 elements and about 500,000 degrees of freedom, which includes contact is very computationally intensive.

3.2 ANALYSIS OF THE SET $\delta(n,1,1)^T$

3.2.1 Equi-triaxial Crushing: $\delta(1,1,1)^T$

The analysis of the set $\delta(n,1,1)^T$ starts with the random foam model crushed in the triaxial apparatus in an equi-triaxial manner. This is achieved by prescribing the same displacement histories, $\delta_i(t)$, to the three active planes, and is designated as $\delta(t)(1,1,1)^T$. The model foam is crushed down to $0.6H$ in each of the three directions, which implies that the volume is reduced to $0.216H^3$. The crushing involved 138 displacement output increments, enough to capture the key information of the responses in the three directions, including limit stresses, stress minima, stress levels of extended plateaus, etc. In view of the large changes in cross-sectional area of the specimen, the true stresses will be reported as $\{s_x, s_y, s_z\}$ in this chapter and YK19a, where each component represents the reaction force on the respective plane divided by the current area of the side.

The calculated results are presented in Figs. 3.3 – 3.5. Figure 3.3a shows the resultant true stress-normalized displacement response measured in each direction. Figure 3.3b shows the mean stress plotted against the change in volume up to $\delta v / v_o = 0.75$, where

$$\bar{s} = (s_x + s_y + s_z)/3 = I_1/3 \tag{3.3}$$

and

$$\delta v / v_o = [1-(1-\bar{\delta}_x)(1-\bar{\delta}_y)(1-\bar{\delta}_z)], \qquad \bar{\delta}_i = \delta_i / H. \tag{3.4}$$

The foam is isotropic so the three responses in Fig. 3.3a follow very similar trajectories. Figures 3.4 and 3.5 show a select number of deformed sections of the model in the $y-x$ and $y-z$ planes respectively, which correspond to the numbered bullets on

27

the $s_x - \overline{\delta}_x$ response (same time steps for the other two responses). To reduce the expected edge effects on the observed cell deformation, the sections are taken from the middle of the cubical domain, as shown schematically in Fig. 3.6. For clarity, the images are limited to slices $0.12H$ thick (a little thicker than one cell).

The foam initially deforms elastically and the three $s_i - \overline{\delta}_i$ responses rise sharply, and so does the $\overline{s} - \delta\overline{\upsilon}$, here $\delta\overline{\upsilon} = \upsilon / \upsilon_o$. The measured bulk modulus is $\kappa^* / \kappa = 0.00961$, which compares with 0.0112 yielded by the periodic Kelvin cell formula in Gong et al. (2005a). At higher stresses, ligaments start to yield and the overall stiffness of the foam gradually degrades. The three $s_i - \overline{\delta}_i$ responses develop stress maxima at about 450 psi (3.10 MPa) at average strains of about 0.004 (the actual stresses and the corresponding strains are slightly different in the three directions because of the randomness of the microstructure). It is worth pointing out that the limit stresses are influenced to some degree by the specific interface conditions between the foam and the plates. The mean stress maximum is 450.6 psi (3.11 MPa) at the corresponding volume change $\delta\overline{\upsilon} = 0.012$. Both the mean stress maximum and the corresponding volume change follow Eqs. (3.3) and (3.4). Up to this point, the deformation of the foam model is distributed throughout the domain and can be considered as uniform.

Beyond the stress maxima, the stresses decay down to about 350 psi (2.41 MPa) and, simultaneously, deformation starts to localize at the "weakest" parts of the domain, which in this study are the cells in contact with the rigid plates. Images ① in Figs. 3.4 and 3.5, at normalized displacements of about 0.032, correspond approximately to the lowest stresses recorded. The ligaments in contact with the moving planes, originally at $y = H$ and $z = H$, have undergone significant local bending, and the adjacent cells have started collapsing. Interesting, in the third direction similar localized deformation takes place at the plane $x = 0$. Examination of the complete specimen confirms that the ligament bending and cell crushing observed in these three edges are representative of what takes place across the complete planes. As the local cell deformation increases, ligament contact develops

which stiffens the crushing zones, leading to a small recovery in the stress. The stress increase is sufficient to destabilize neighboring cells, so in images ② and ③, at normalized displacements of about 0.051 and 0.093, the cell crushing has spread inward at all three planes, while the stresses are staying between 370 and 380 psi (2.55- 2.62 MPa). This takes place while the rest of the foam domain remains essentially intact. In summary, three nearly planar crushing fronts are propagating from the outer boundaries inward with most of the domain remaining essentially undeformed.

Crushing continues, but due to the progressive reduction in surface areas, the true stresses start to gradually increase reaching levels of about 420 psi (2.90 MPa) by point ④ at $\bar{\delta} \approx 0.15$. The corresponding images show the crushing fronts have moved inward from the three planes significantly. Moreover, crushing appears to be more intense at the corners formed by two active planes. Additionally, although crushing has now also commenced at zones adjacent to the other three planes, which thus far have been relatively unaffected, a significant part of the center of the foam remains intact.

At point ⑤ at $\bar{\delta} = 0.195$, the stresses have risen to an average level of about 465 psi (3.21 MPa). Crushing now is taking place next to all six bounding planes propagating inward. The volume is down to about $0.52H^3$, most of it occupied by nearly intact foam at the center of the cube. In images ⑥ at $\bar{\delta} = 0.272$, the inward propagation of crushing emanating from the six bounding planes has continued and the stresses have risen to an average of about 595 psi (4.10 MPa). A central nearly spherical zone appears intact with complete cells, which remain unaffected. Beyond this point, the stresses trace an even steeper upward trend, reaching a level of 820 psi (5.66 MPa) at point ⑦ at $\bar{\delta} \approx 0.34$. The volume is now reduced to about $0.29H^3$ but a small spherical volume of relatively intact cells remain in the center. $\bar{s}$ is the average of the stresses in the three directions, so the $\bar{s} - \delta\bar{\upsilon}$ follows a very similar trajectory.

In summary, in this section, the model foam crushed in the triaxial apparatus in a displacement-controlled equi-triaxial manner, exhibits an initial elastic response. This terminates into local stress maximum beyond which deformation localizes. Because of the

finiteness of the domain, crushing initiates at the boundaries that are in contact with the rigid plates and progresses inwards. Even though following the initial local stress minimum the true stresses recorded increase with displacement, crushed and intact material coexists until the whole domain densifies at a relatively high stress level.

3.2.2 Effect of the geometry variation of $\delta(1,1,1)^T$

When using finite size domains to represent the behavior of the infinite medium, it is necessary to test the sensitivity of the solution to the domain size. To this end, we analyze the response of random foam models of different sizes to equi-triaxial loading $\delta(1,1,1)^T$. Calculations are preformed for models with 6^3, 8^3, 10^3 and 12^3 cells. The models are generated in the same manner, are isotropic and are assigned a relative density of 0.08. Discretization and other numerical parameters are the same. Figures 3.7a-c show the four stress-displacement responses in the x-, y- and z-directions. Comparing the four responses, it is clear that increasing the domain from 6^3 to 8^3 cells shifts the stress levels to higher levels in all three directions. A smaller increase occurs when the domain is increased to 10^3 cells. The responses of the 10^3 to 12^3 cell models have the same limit stresses and very similar stress levels in the three directions. However in the y-direction, the two responses separate somewhat in the re-stiffening branch. Overall, the solution of the 10^3 domain is considered converged. The 10^3 cell domain will thus be used in all subsequent crushing calculations.

The foam models considered have random microstructures and as a result no two models generated in the Surface Evolver are the same. It is thus worth examining the effect of the small differences in the microstructure of the same size models on the calculated response. To this end we consider two such microstructures, designated as Models I and II, that are dressed in the same manner, and assigned the same density. Figure 3.8 compares the $\delta(1,1,1)^T$ responses in the three directions (not specified) from the two 10^3 cell models. Model II is the model used in this study. The two sets of responses have the same general trends. More specifically, the elastic moduli are very similar, and so are the stress maxima

and minima. The overall responses trace very similar trajectories. As pointed out in Gaitanaros et al. (2012) the small differences in the responses can be expected to get reduced as the size of the domain increases.

3.2.3 Triaxial Crushing: $\delta(3,1,1)^T$

The second loading history analyzed is $\delta(t)(3,1,1)^T$. Here the foam is crushed equally along the y- and z-directions, but at a rate three times faster along the x-direction. Figure 3.9a shows the true stress-normalized displacement responses recorded in the three directions, and Fig 3.9b the corresponding mean stress-change in volume response. Figures 3.10 and 3.11 show a select number of deformed sections of the model in the $y-x$ and $y-z$ planes respectively that correspond to the numbered bullets on the response. The configurations are taken from the same time steps in the loading history $\delta(t)$, and as a result the corresponding displacements in the y- and z-directions are one third of those in the x-direction, and are marked with different bullets. The responses again rise elastically to stress maxima, followed by drops associated with localized deformation that spreads at lower stress levels. The $s_y - \bar{\delta}_y$ and $s_z - \bar{\delta}_z$ responses are similar and limited to normalized displacement of about 0.2, whereas the $s_x - \bar{\delta}_x$ response extends to $\bar{\delta}_x = 0.6$. The $\bar{s} - \delta\bar{\upsilon}$ response follows a similar three branch trajectory extending to $\delta\bar{\upsilon} \approx 0.74$ (or the volume is down to 0.26 of the original volume). The slopes of the initial linear elastic branches of the responses are the same in the y- and z-direction and larger than the slope in the x-direction, in accordance with the isotropic material behavior. A more detailed discussion of the elastic behavior will appear in Section 3.2.4 together with other cases in the same family of loading paths $\delta(n,1,1)^T$. The initial stress maxima in the y- and z-direction are at about 430 psi (2.97 MPa), whereas in the x-direction the stress rises to about 463 psi (3.19 MPa). The loads are caused by bending and plastic deformation of the ligaments at the boundaries, so they occur at slightly different times, with the x-direction occurring first, the z-direction second, and the one in the y-direction last.

Beyond the stress maxima, deformation localizes once again at one of the contact surfaces in each direction, while the three stresses drop down to local minima (in the y- and z-directions about 320 psi and 350 psi in the x-direction – 2.21 and 2.41 MPa— with corresponding displacements $\bar{\delta}_y = 0.034$, $\bar{\delta}_z = 0.029$ and $\bar{\delta}_x = 0.026$). They then rise to a nearly common stress plateau of about 390 psi (2.69 MPa). In images ① in Figs. 3.10 and 3.11 at $\bar{\delta}_x = 0.0576$ and one-third this value in the other two directions, edge ligaments and the adjacent row of cells along the plane originally at $x = H$ have started collapsing and some ligament contact has developed. Because of this local stabilization, the stress has risen to about 400 psi (2.76 MPa). Since the foam has experienced only one-third the displacement along the y- and z-directions, the zones adjacent to these contact planes are much less deformed, and the stresses are still on their downward trajectory.

In images ② at $\bar{\delta}_x = 0.200$, local crushing has commenced along the $y = 0$ plane and the plane originally at $z = H$. By this time, the stresses in the two directions have gone past their local minima and are approaching the level of s_x. Concurrently, a nearly planar crushing front has propagated from the top along the x-direction, and a small amount of crushing has appeared along the $x = 0$ plane. Figure 3.9b shows the volume to have been already reduced by about 30%.

In image ③ in Fig 3.10 at $\bar{\delta}_x = 0.278$ and $\delta\bar{\upsilon} \approx 0.40$, the propagation of the crushing front on the side of the moving plane along the x-direction has continued, and the one at $x = 0$ has also progressed while the stress has not changed significantly. The crushing front at $y = 0$ has spread inwards and some mild crushing has commenced on the opposite side. The corresponding image in Fig. 3.11 shows that crushing in the z-direction is limited to the cells adjacent to the moving plane.

In images ④ at $\bar{\delta}_x = 0.344$ and $\delta\bar{\upsilon} \approx 0.49$, s_x has risen to 485 psi (3.34 MPa). Crushing has propagated inwards along the x-direction from both sides. The same is the case for the y-direction, while in the z-direction the crushing along $z = 0$ remains limited.

In images ⑤ at $\bar{\delta}_x = 0.389$ and $\delta\bar{\upsilon} \approx 0.54$, $s_x = 500$ psi (3.45 MPa) and the same trend continues in the x- and y-directions, but deformation along the $z = 0$ plane remains limited. The crushing along the x-direction is very significant but a substantial number of cells in the center are seen in Fig. 3.10 to remain relatively undeformed (the events are similar in the $x-z$ plane). This is clearly illustrated in the corresponding image in the $y-z$ central plane image in Fig. 3.11. It is worth pointing out that the central planar views in Figs 3.10 and 3.11 are representative of the complete planes that cells in the center remain intact. Since in the x-direction crushing propagates from the endplates inwards, $y-z$ plane cuts closer to the endplates show cell deformation occurring earlier and being more pronounced than at the central plane in Fig. 3.11. This difference between the central region and regions close to the endplates applies to the other two planes as well. This variation in the extent of crushing is illustrated Fig. 3.12 where deformed configurations at $\bar{\delta}_x = 0.39$ from the central $y-x$ plane cut and a cut about $0.08H$ from $z = H$ are compared. Both cuts have the same thickness.

In images ⑥ and ⑦ at $\bar{\delta}_x = 0.467$ and 0.519, s_x rises respectively to 576 and 668 psi (3.97 and 4.61 MPa). The x-direction crushing has reduced the volume down to $0.38H^3$ in ⑥ but a significant number of cells in the center remain intact. In ⑦ with the volume down to about $0.33H^3$, most of the foam is crushed but a number of cells in the center of the deformed domain remain essentially intact. Beyond images ⑦, Fig. 3.9a records s_x up to 900 psi at $\bar{\delta}_x = 0.586$. Dashed lines in s_y and s_z show the responses in the y- and z-directions at the same time step beyond $\bar{\delta}_x = 0.586$.

3.2.4 Set of Triaxial Crushing Results for: $\delta(n,1,1)^T$

In this section we examine the triaxial crushing results for the set of loading paths $\delta(n,1,1)^T$. Similar calculations for additional cases in the $\delta(t)(n,1,1)^T$ loading history family were performed in which n was assigned the following values:

$n \in (0.33, 0.67, 1.0, 1.5, 3.0, 5.0)$. The complete $s_x - \bar{\delta}_x$ and $s_y - \bar{\delta}_y$ responses recorded are plotted in Figs. 3.13a and b; for better visualization the early parts of the stress-displacement responses are also shown expanded in Figs. 3.14a and b, where the abscissa is limited to average strains of 0.07. Figure 3.15 shows the corresponding mean stress-change in volume responses.

Overall, the stress-displacement responses follow the trends observed for $n = 1.0$ and 3.0. All responses start with a linear elastic branch that terminates into a stress maximum. Deformation starts to localize and the stress subsequently drops down to a local minimum, which results from local stabilization in collapsing cells due to ligament contact. The responses recover and start to trace plateaus, which at higher compressive displacements evolve into rising trajectories due to the reduction of area.

The slopes of the initial elastic parts of the responses, σ_x / ε_x and σ_y / ε_y, are plotted in Fig. 3.16 against n with solid bullets. Included in the figure with dashed lines are corresponding plots produced by the following isotropic linearly elastic constitutive relations

$$\frac{\sigma_x}{\varepsilon_x} = \frac{E^*}{(1+v^*)(1-2v^*)} \frac{n(1-v^*)+2v^*}{n},$$

$$\frac{\sigma_y}{\varepsilon_y} = \frac{E^*}{(1+v^*)(1-2v^*)}(1+nv^*). \tag{3.5}$$

Here $\{E^*, v^*\} = \{63.2 \text{ ksi}, 0.365\}$ were evaluated for optimal fitting of the measured slopes using an unconstrained optimization algorithm. The details of derivation of the constitutive relations and the optimal fitting are discussed in Appendix. A. By comparison, the corresponding values yielded by the Kelvin cell formulas in Gong et al. (2005a) are $\{63.3 \text{ ksi}, 0.404\}$. The elastic modulus is also in quite good agreement with values in Jang et al. (2008) established from uniaxial compression of periodic isotropic random foams. It is worth noting, however, that as was the case for its predecessor developed in Gaitanaros et al. (2012) for uniaxial compression, the present meshing of the

34

model is aimed for crushing calculations, which may reduce its accuracy in the prediction of elastic properties.

The early parts of the inelastic responses trace quite similar trajectories (Fig. 3.14). Five of the stress maxima in the *x*-direction are at about 450 psi (3.10 MPa) while the value for $n = 0.33$ is at 428 psi (2.95 MPa). The stress maxima in the *y*-direction are at similar levels and have likewise modest variation. However, now the lowest value occurs for $n = 5.0$. The stress minima in the *x*-direction occur at about $\bar{\delta}_x \approx 0.025$ and the stress is around 345 psi (2.38 MPa) for five cases and 307 psi (2.12 MPa) for $n = 0.33$. They all recover around $\bar{\delta}_x \approx 0.05$, tracing short stress plateaus that range between 380 and 400 psi (2.62-2.76 MPa). In the *y*-direction the stress minima occur also at $\bar{\delta}_y \approx 0.025$, which clearly means they occur at different times than the minima in the *x*-direction. Subsequently, the stresses rise and trace either a small undulation or a plateau around 378 psi (2.61 MPa).

At higher displacements, the stresses start increasing (Fig. 3.13). The increase in stress depends on *n*; in the *x*-direction, for the lower values of *n* the stress picks up at smaller displacements, and the increase is becoming more gradual as *n* increases. The responses in the *y*-direction exhibit the opposite trend. For the larger values of *n* the stress picks up at smaller values of $\bar{\delta}_y$, and the upswing is increasingly delayed for smaller values of *n*.

It is important to point out that beyond the initial stress maximum the deformation is inhomogeneous for all values of *n* up to points ⑦ on the response. This is illustrated in Fig. 3.17 that shows a pair of deformed configurations for each *n* corresponding to $\delta\bar{v} \approx 0.5$. The configurations on the left column come from the $y - x$ central plane, and the ones on the right from $y - z$ central plane (see Fig. 3.6). All images show coexistence of crushed and essentially intact cells. The events at smaller and larger volume changes are similar to those reported for $n = 1.0$ and 3.0.

The mean stress-change in volume $(\bar{s} - \delta\bar{v})$ responses in Fig. 3.15 exhibit similar trajectories to those of the stress-displacement ones. The elastic bulk modulus is nearly the

35

same for the six cases, ranging between κ^*/κ of 0.00955 for $n = 0.33$ and 0.00965 for $n = 5.0$ with the average of 0.00961 ($\kappa = 8.17 \times 10^3$ ksi). The corresponding value based on $\{E^*, \nu^*\}$ from Fig. 3.16 is 0.00959. The local mean stress maxima are again close, ranging between 415 to 451 psi (2.86-3.11 MPa) for $n = 5.0$ and 1.0 respectively. Beyond the maxima, the responses stay banded together, exhibiting a similar small level of variation in stress. The stresses drop down to about 360 psi (2.28 MPa) tracing an extended plateau up to $\delta\overline{\upsilon} \approx 0.4$ beyond which they gradually rise with volume change. With the exception of the response for $n = 5.0$ which strays slightly, the other five responses stay banded up to the end of crushing when the volume is reduced by 70%.

One key characteristic for the low density foam is its unique energy absorption capacity resulting from relatively low crushing strength and extended stress plateaus. The energy absorbed per unit undeformed volume, $\mathcal{E}$, is calculated as the sum from the three directions:

$$\mathcal{E} = \sum_i \int \sigma_i d\overline{\delta}_i , \qquad\qquad i = x, y, z. \qquad\qquad (3.6)$$

Here σ_i is designated as the nominal stress in each direction. Figure 3.18 shows $\mathcal{E}$ at different values of change in volume, $\delta\overline{\upsilon}$, against n. $\mathcal{E}$ remains essentially invariant to n for all values of volume change. It will be interesting to examine if this insensitivity to this loading parameter holds for other triaxial loading histories.

3.3 ANALYSIS OF THE SET $\delta(n, 0.5, 1)^T$

3.3.1 Triaxial Crushing: $\delta(3, 0.5, 1)^T$

The second family of loading paths considered is $\delta(n, 0.5, 1)^T$ (see Fig. 3.2). The loading path $\delta(3, 0.5, 1)^T$ is examined is some detail in order to establish the general characteristics of this loading family. Figure 3.19 shows the three sets of stress-normalized displacement responses plotted together. Figures 3.20 and 3.21 show a select number of

deformed sections in the $z-x$ and $y-z$ planes taken once more from the central planes, as shown in Fig. 3.6. Crushing in the y-direction is limited, so configurations in the plane $y-x$ are less interesting and are not shown. The configurations again were taken at the same time steps and, as a result, they correspond to different stages of the crushing history in each plane. The general characteristics of the three responses are similar to those discussed for the loading history $\delta(3,1,1)^T$ in Fig. 3.9a, except that here the responses are different in the three directions. The elastic moduli follow the isotopic relationships, with values similar to those reported in the previous section. The stress maxima are at different levels and they occur at different displacements as shown in Table 3.2.

Table 3.2:   Stress maxima in the three directions for the loading path $\delta(3,0.5,1)^T$

	x	y	z
s_i psi (MPa)	463 (3.19)	410 (2.83)	435 (3.00)
$\bar{\delta}_i$ (%)	0.60	0.46	0.44

    Crushing again starts at the edges in contact with the rigid plates. In the x- and z-directions crushing initiates at the moving plates, and in the y-direction at the stationary plate at $y=0$. The responses develop local stress minima, which are ordered as the stress maxima, but correspond again to different time steps in the loading history (compare the positions of the solids bullets on each response). At stations ① in Figs. 3.19, σ_x has gone through a local stress minimum and has started tracing a stress plateau at about 380 psi (2.62 MPa). In the corresponding image in Fig. 3.20, a row of cells in contact with the moving x-plane, have crushed. In the z-direction at this station the displacement is one third of $\bar{\delta}_x$ and σ_z is still on the descending branch. Thus only minor ligament bending is observed in Fig. 3.21. In the y-direction the response is even further behind with even less localized deformation registering. At station ② the localized crushing in the x-direction has increased significantly while σ_x remains essentially unchanged. The z-side in contact with

the moving plane shows more local ligament bending and the corresponding stress has gone through its local minimum and is on an increasing trajectory. The deformation in the y-direction remains limited with σ_y reaching its lowest level.

Subsequently, as was the case for the previous loading paths, crushing progresses from the boundaries inwards. The x-direction response traces an extended stress plateau. Image ③ in the $z-x$ plane shows that crushing has commenced from the stationary plane at $x=0$ also, and subsequently propagates inwards from both sides. In image ④, a significant number of cells in the center of the plane remain intact. At higher values of $\bar{\delta}_x$, the number of uncrushed cells gets progressively reduced and simultaneously the stress rises at a steeper rate.

Crushing in the z-direction is more limited and even more so in the y-direction. Consequently, Fig. 3.21 shows that in the early stages of the loading history most of the cells in the $y-z$ plane remain intact. The extent of crushing increases in images ⑤-⑦, but in ⑦ a significant number of cells remain relatively uncrushed, even though they have undergone some distortion. It is again pointed out that since in the x-direction crushing is progressing inwards from the endplates, $y-z$ planar cuts made closer to the end-plates show earlier and more pronounced cell deformation than in the central plane depicted in Fig. 3.21. s_z is always somewhat lower than the corresponding s_x, and s_y lags behind the other two values throughout the loading history. To highlight this difference, the s_y and s_z responses are drawn with solid line up to the increment that corresponds to s_x = 1000 psi (6.90 MPa), and subsequently with dashed lines.

3.3.2 Set of Triaxial Crushing Results for: $\delta(n,0.5,1)^T$

Six cases are analyzed from the family of crushing calculations under radial loading paths in which the displacements are different in the three direction, $\delta(t)(n,0.5,1)^T$, with the variable n taking values $n \in (0.33, 0.67, 1.0, 1.5, 3.0, 5.0)$. The responses for all loading

38

histories in this set are plotted in Fig. 3.22. Figure 3.22a-3.22c shows the six $s_x - \bar{\delta}_x$, $s_y - \bar{\delta}_y$, and $s_z - \bar{\delta}_z$ responses. The initial linear parts of the responses follow the isotropic material trend observed for the previous loading history set. They were used to estimate the elastic moduli using the optimization algorithm outlined in Section 3.2.4 and the results are: $\{E^*, \nu^*\} = \{67.3 \text{ ksi}, 0.357\}$; in other words, slightly different values than those yielded by the six $\delta(n,1,1)^T$ responses. Figure 3.23 shows the slopes of the initial elastic parts of the responses, σ_x / ε_x, σ_y / ε_y, and σ_z / ε_z against n with solid bullets, fitted with the following isotropic linearly elastic constitutive relations

$$\frac{\sigma_x}{\varepsilon_x} = \frac{E^*}{(1+\nu^*)(1-2\nu^*)} \frac{n(1-\nu^*)+3\nu^*/2}{n},$$

$$\frac{\sigma_y}{\varepsilon_y} = \frac{E^*}{(1+\nu^*)(1-2\nu^*)} (1+\nu^*+2n\nu^*),$$

$$\frac{\sigma_z}{\varepsilon_z} = \frac{E^*}{(1+\nu^*)(1-2\nu^*)} (1-\frac{\nu^*}{2}+n\nu^*). \tag{3.7}$$

All the responses exhibit stress maxima and minima, the values of which are generally quite closely packed and occur at similar displacements for each path. However, the differences between directions outlined for the case above transfer to the whole set. The x-direction responses fall in accordance with the value of n, so $n = 0.33$ undergoes the minimum axial crushing and $n = 5.0$ the maximum. For this reason, the y- and z-direction responses are ordered in the opposite manner in Figs. 3.22b and 3.22c. It is important to point out that for this family of radial paths as well, beyond the stress maxima, the deformation is inhomogeneous for all values of n. This is illustrated in Fig. 3.24 that shows a pair of deformed configurations for each n corresponding to $\delta\bar{\upsilon} \approx 0.5$. The configurations on the left column come from the $z-x$, and the ones on the right from the $y-z$ central plane. All images show coexistence of crushed and uncrushed cells. The behavior at smaller and larger volume changes are along the lines of those in Figs. 3.20 and 3.21.

39

The mean stress-change in volume responses for this set are plotted in Fig. 3.25. The linear elastic branches exhibit an average bulk modulus of about $\kappa^*/\kappa \approx 0.00962$, in a range of 0.00956 ($n = 0.33$) to 0.00967 ($n = 5.0$). The corresponding predicted value from $\{E^*, \nu^*\}$ of the set is 0.00959. Both the averaged measured and predicted values are close to the values reported in Section 3.2.4. All responses exhibit maxima that are closely grouped together. They then drop down to local minima followed by plateaus that extend to about $\delta \bar{\upsilon} \approx 0.4$. For larger volume changes, the foam densifies and the mean stress follows an increasing trend. With the exception of $n = 5.0$, which strays somewhat, the other five responses are banded together up to a volume change of 70%.

The energy absorbed per unit undeformed volume, $\mathcal{E}$, at different values of change in volume, is plotted in Fig. 3.26 against n. $\mathcal{E}$ remains essentially invariant to n for all values of volume change.

3.4 ANALYSIS OF THE SET $\delta(n,0,1)^T$

3.4.1 Triaxial Crushing: $\delta(3,0,1)^T$

The third family of loading paths considered is $\delta(n,0,1)^T$ in which the displacement in the y-direction is zero (see Fig. 3.2). We again consider first the case with $n = 3.0$, $\delta(3,0,1)^T$ in order to establish the general characteristics of this loading family. Figure 3.27 shows the measured stress-normalized displacement responses in the x- and z-directions, which show similar trends to the responses reported for the $\delta(3,1,1)^T$ and $\delta(3,0.5,1)^T$ radial paths. The main difference is that, since $\delta_y = 0$, no response is traced for the y-direction, although the stationary plates at $y = 0$ and $y = H$ develop reaction forces. Figures 3.28 and 3.29 show a select number of deformed sections taken from the $z-x$ and $y-z$ central planes. The two responses start with linear branches with slopes that reflect the initial linear elastic and isotropic behavior of the material. They terminate

into stress maxima beyond which the foam starts to crush. The responses develop stress minima that occur at different time increments. Image ① in Fig. 3.28 shows crushing to have commenced at the x-direction moving plate. At the same time the deformation in the zone adjacent to $z = H$ is limited, and s_z is still on the descending slope. Images ② in Figs. 3.28 and 3.29 show crushing to be also taking place at the z-direction moving plate. Concurrently, very limited deformation is observed at the y-direction edges.

In images ③ and ④, at $\bar{\delta}_x = 0.204$ and 0.319, crushing has continued to propagate inwards from both moving plates, while s_x remains relatively unchanged, presumably because the $y - z$ cross-sectional area of the foam does not change significantly (see images ①-④ in Fig. 3.29). Throughout this loading history, crushed and essentially intact cells are observed to coexist. By image ⑤ in Fig. 3.28, crushing has commenced from the stationary x-direction plate also, and the relatively intact cells are now concentrated in the center of the plane; s_x starts to increase and so does s_z. By contrast, deformation in the central $y - z$ plane in Fig. 3.29 is limited to the side of the moving z-plate. We point out, however, that a $y - z$ planar cut made closer to the upper x-direction plate shows more pronounced cell deformation than in the central plane in Fig. 3.29. Subsequently, the now densified foam continues to crush but with increasing stresses. Relatively undeformed cells continue to be observed in image ⑥, but by image ⑦ the foam appears densified in the x-direction.

3.4.2 Set of Triaxial Crushing Results for: $\delta(n,0,1)^T$

Similar calculations for additional cases in the $\delta(t)(n,0,1)^T$ loading history family were performed in which n was again assigned the values: $n \in (0.33, 0.67, 1.0, 1.5, 3.0, 5.0)$. The $s_x - \bar{\delta}_x$ and $s_z - \bar{\delta}_z$ responses corresponding to all radial loading paths in this set are plotted in Figs. 3.30a and b, respectively. They follow similar trends to those reported for the other two families of radial paths, and will be discussed in less detail. The elastic

constants yielded by this set are: $\{E^*, v^*\} = \{66.8 \text{ ksi}, 0.358\}$, values comparable but slightly different from those of the other two sets. The slopes of the initial elastic parts of the responses, σ_x / ε_x, and σ_z / ε_z are plotted against n with solid bullets, Fig. 3.31. Included are the isotropic linearly elastic constitutive relations in Eq. (3.8) fitted with dashed lines.

$$\frac{\sigma_x}{\varepsilon_x} = \frac{E^*}{(1+v^*)(1-2v^*)} \frac{n(1-v^*)+v^*}{n},$$

$$\frac{\sigma_z}{\varepsilon_z} = \frac{E^*}{(1+v^*)(1-2v^*)}(1-v^*+nv^*). \tag{3.8}$$

All responses in Fig. 3.30 exhibit stress maxima beyond which localized crushing of cells takes place. The responses trace stress minima followed by stress plateaus, the extents of which in the x-direction go with n and in the z-direction go with n^{-1}. For all values of n, the deformation beyond the stress maximum is inhomogeneous with crushed and relatively undeformed zones of cells coexisting. Figure 3.32 shows deformed configurations in the $z-x$ and $y-z$ central planes for each n corresponding to $\delta\overline{\upsilon} \approx 0.5$. The events at smaller and larger volume changes follow the trends in Fig. 3.32 and observed in the calculation of the path $\delta(3,0,1)^T$ in Figs. 3.28 and 3.29. The stresses pick up when the material becomes densified in the dominant loading direction.

Figure 3.33 shows plots of the mean stress-change in volume responses for this set. The linear elastic branches yield a bulk modulus $\kappa^*/\kappa \approx 0.00965$, which is very comparable to that produced by the other two loading histories. The responses exhibit local maxima and drop down to stress plateaus that remain at nearly the same level up to $\delta\overline{\upsilon} \approx 0.4$. They stay banded together but exhibit more difference between them than the other two sets of results. At higher volume change, the stresses pick up with the $n = 5.0$ response being somewhat lower than the others.

The energy absorbed per unit undeformed volume, $\mathcal{E}$, at different values of $\delta\overline{\upsilon}$, is plotted in Fig. 3.34 for different values of n. $\mathcal{E}$ again remains essentially invariant to n for all values of volume change.

3.5 ANALYSIS ACROSS THE THREE FAMILIES OF LOADING PATHS

The stress-displacement responses from the three families of loading paths reported in Chapter 3 exhibit similar trends. This section analyzes unique properties of Al-alloy foams measured from the triaxial crushing calculations of the isotropic random foam model across the three families of loading paths. The model foam exhibits an initial linear elastic and isotropic behavior. Fitting of the slopes of the initial linear parts of the three responses for the six radial paths of each family produced the following estimates for the foam elastic modulus and Poisson's ratio as shown in Table 3.3.

Table 3.3:   Elastic modulus and Poisson's ratio of the three families of loading paths

	E *ksi (MPa)	v *
$(n,1,1)$	63.2 (436)	0.365
$(n,0.5,1)$	67.3 (464)	0.357
$(n,0,1)$	66.8 (460)	0.358

The observed differences in Table 3.3 are caused by the finite size of the random microstructure and by small differences introduced at the edges by the "cropping" performed for cleaner interphasing with the endplates. For comparison, the corresponding values yielded by the Kelvin cell foam formulas in Gong et al. (2005a) are {63.27 ksi, 0.404}.

The stresses measured at plastic work of 0.09 psi (0.62 kPa) from the three families are used to develop a Druckler-Prager type of initial yield surface for this compressible material. The yield function is calibrated using the stress-displacement responses from the 18 triaxial tests reported here (see a more detailed description of the constitutive model in

43

Chapter 4). The data shows a quadratic relationship between the two stress invariants given by

$$[3J_2 + \alpha^2 (I_1/3)^2]^{1/2} = \sigma_o[1 + (\alpha/3)^2]^{1/2} \qquad (3.9)$$

(similar to Deshpande and Fleck, 2000). For the chosen value of plastic work, $\alpha = 0.78$.

The limit stresses, $s_{iL}, i = x, y, z$, recorded in the 18 crushing simulations are plotted in Fig. 3.35 against the parameter n. The x-direction values corresponding to the same n fall together and so do the ones in the z-direction. The y-direction values become lower when the ratio δ_y / δ_z decreases. $s_{xL}(n)$ exhibit somewhat lower values for $n < 1$, they increase with n, and remain nearly constant for $n \geq 1.5$. s_{yL} and s_{zL} follow the opposite trend with n. They start at relatively higher values and decrease as n increases.

The mean stress-change in volume responses for the $(n,1,1)^T$ and $(n,0.5,1)^T$ responses were at approximately the same stress levels, whereas those for the $(n,0,1)^T$ traced somewhat lower stress levels.

The energy absorbed at a given volume change was the same for each value of n in each set. Figure 3.36 plots $\mathcal{E}$ against $\delta \overline{\upsilon}$ for three cases from each of the three radial path families. Clearly, $\mathcal{E}$ is linearly related to $\delta \overline{\upsilon}$ and no significant difference is observed between the values corresponding to the nine data points at each value of $\delta \overline{\upsilon}$.

3.6 SUMMARY

Crushing experiments under triaxial loads are difficult, primarily because of the large volume changes involved. To address this challenge a true triaxial numerical apparatus has been used to crush a micromechanically accurate cubical model of an isotropic Al-alloy open-cell foam with relative density of 0.08 down to volume changes of about 70%. The model foam has been crushed under three families of radial displacement paths in the (x, y, z) space designated in Eq. (3.1). The first set $\delta(t)(n,1,1)^T$ involves the displacement in the y-direction the same as in the z-direction. It includes the calculation of

equi-triaxial crushing: $\delta(1,1,1)^T$. The second set $\delta(t)(n,0.5,1)^T$ allows the displacement to be different in the three directions. In the third set, $\delta(t)(n,0,1)^T$, the displacement in the y-direction is zero. Thus, this set is regarded as loading paths for "confined" biaxial crushing. In each family, crushing calculations are carried out for six radial loading paths, with the variable n taking values $n \in (0.33, 0.67, 1.0, 1.5, 3.0, 5.0)$. Reported are the true stress-displacement responses in the three directions and corresponding foam deformed configurations; the mean stress-volume change responses; and the energy absorbed as a function of the volume change.

For all loading paths, the true stress-deformation responses in the three directions exhibit an initial linearly isotropic elastic branch that terminates into a stress maximum. Deformation localizes usually at the boundaries in contact with the rigid plates of the apparatus leading to a drop in stress. Contact of ligaments arrests local deformation, the stress traces a minimum, and local crushing starts to spread to the rest of the domain. The direction undergoing the maximum displacement traces an extended stress plateau with the crushing fronts moving inwards from the boundaries of the domain. The other directions undergo less crushing and develop shorter stress plateaus. As the crushing increases the true stresses start to rise, partly due to the reduction of cross sectional areas. Throughout the loading history crushed and relatively undeformed cells coexist. Clearly, homogenized inelastic constitutive models that assume the material to deform homogenously are inappropriate for this class of foams.

The mean stress-change in volume responses of each set coalesced reasonably well and exhibit banded trajectories following the trends observed in the true stress-displacement responses. The energy absorbed per unit undeformed volume, $\mathcal{E}$, is found to be linear with $\delta\overline{\upsilon}$ and invariant to n. Furthermore, no significant difference is observed across the three sets at the same $\delta\overline{\upsilon}$.

The observations of multiaxial crushing of the random foam model will guide the development of the compressible constitutive model in the following chapters.
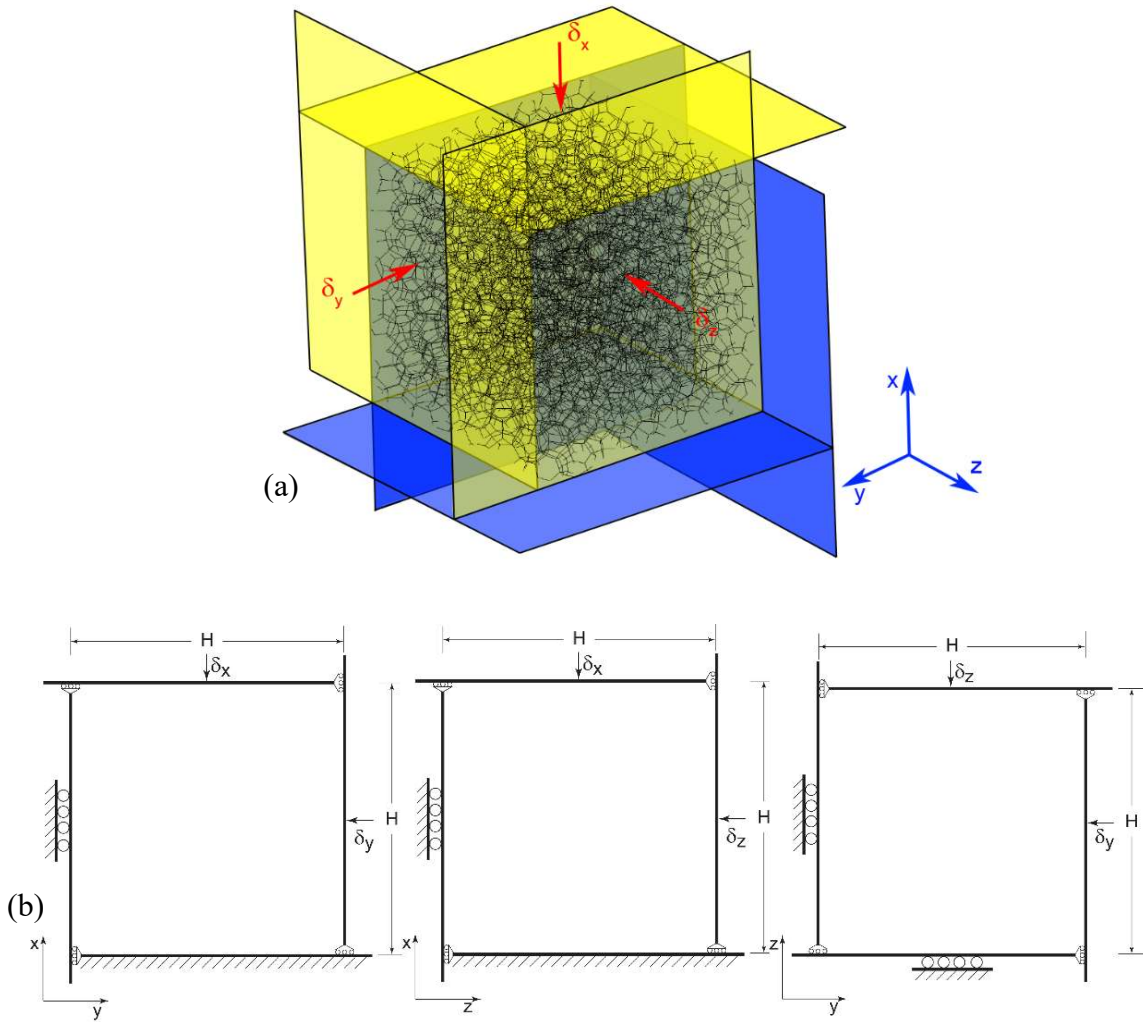
Fig. 3.1: (a) True triaxial numerical apparatus used in the present study consisting of three pairs of orthogonal planes. (b) Planar views of the apparatus showing the degrees of freedom of the six plates.

46
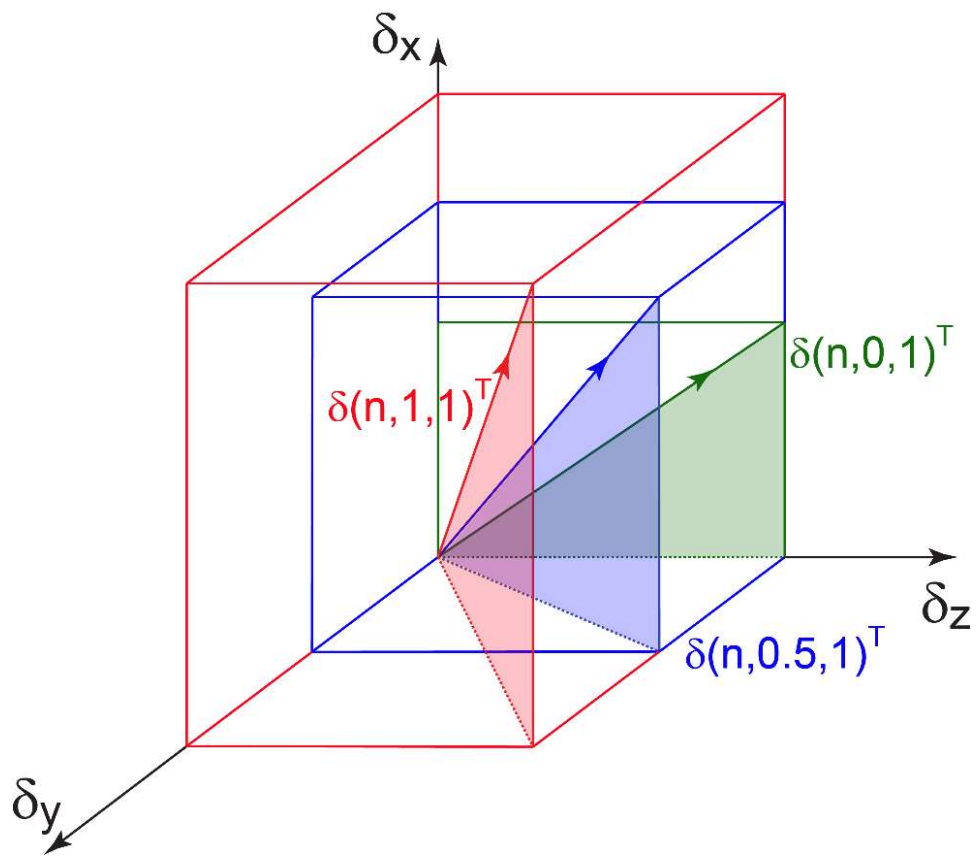
Fig. 3.2: Three families of radial paths adopted in the crushing of the model foam.
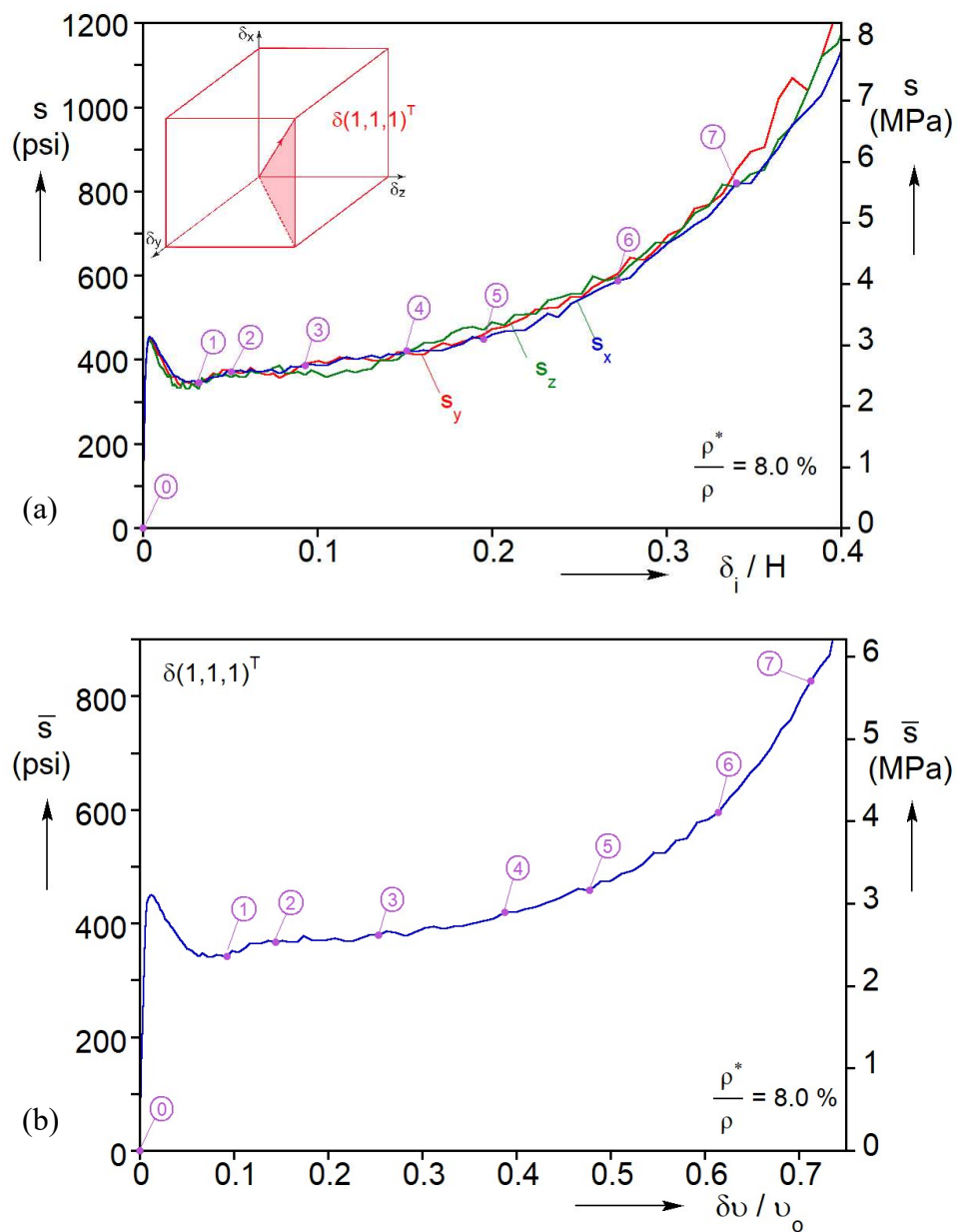
Fig. 3.3: (a) Calculated true stress-displacement responses in the *x*-, *y*- and *z*-directions for the $\delta(1,1,1)^T$ loading path, and (b) corresponding mean stress-change in volume response.
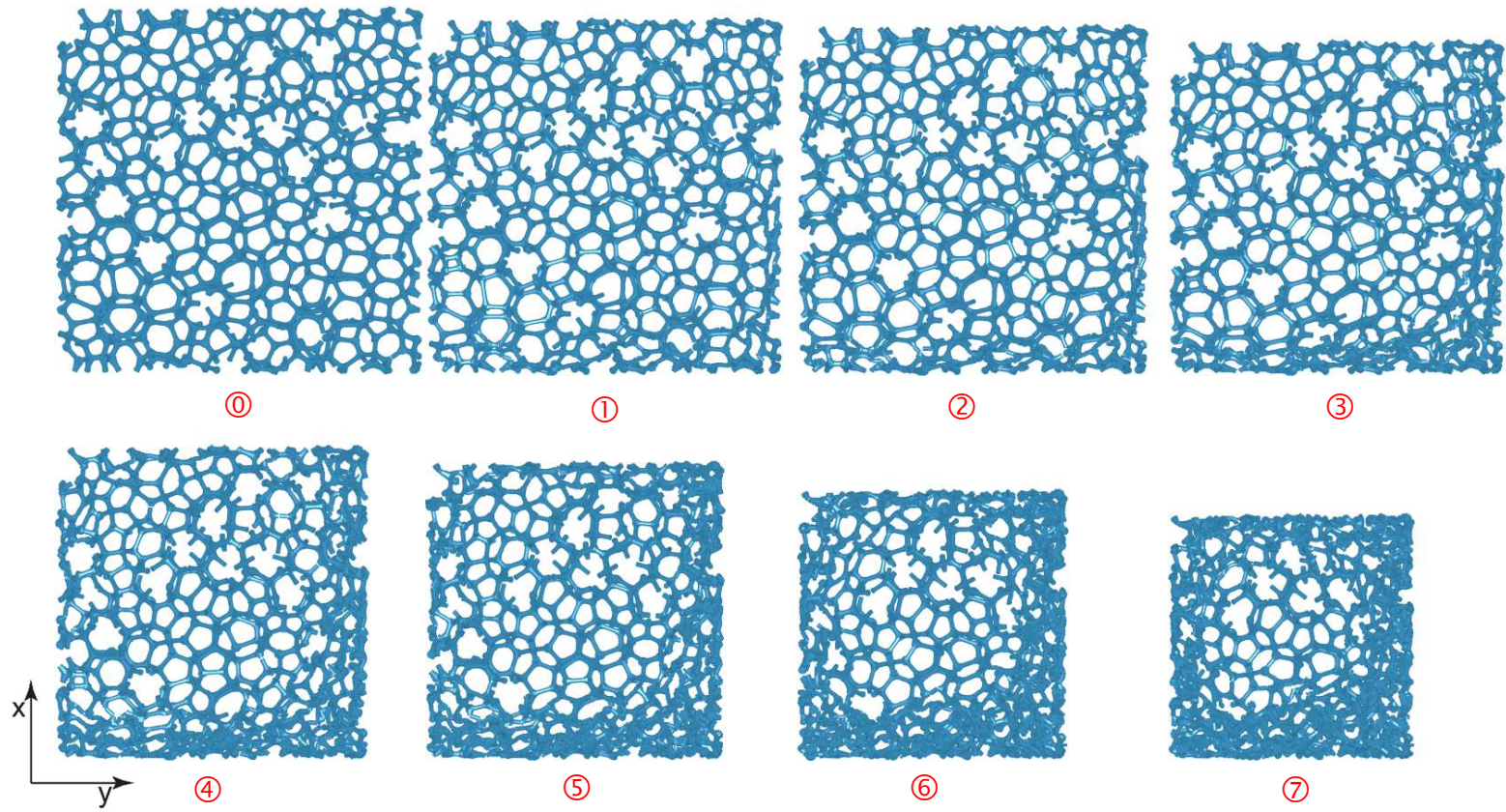
Fig. 3.4: Sequence of deformed foam images from the $y-x$ central plane corresponding to the numbered points on the responses in Fig. 3.3a and 3.3b.
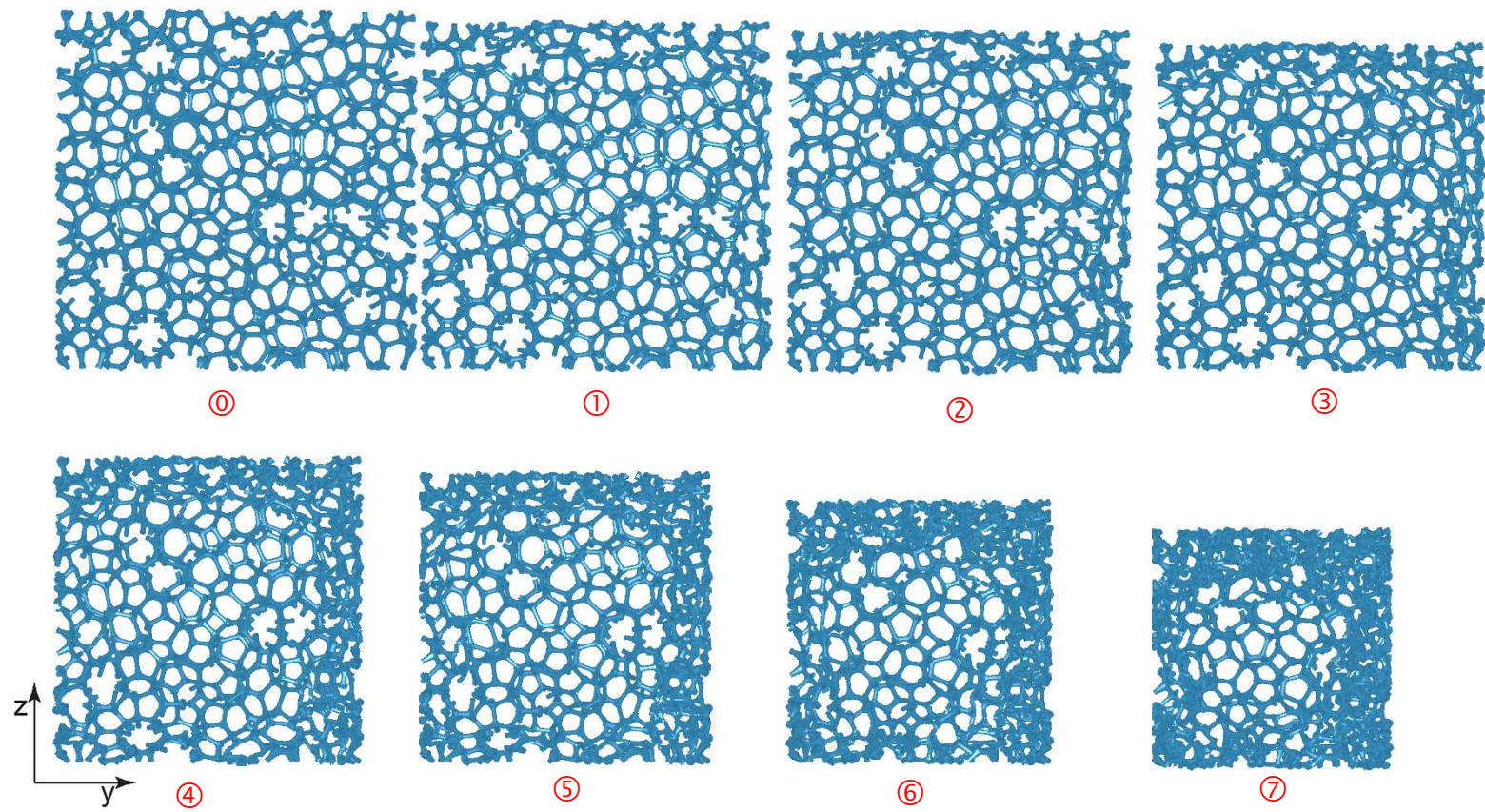
Fig. 3.5:   Sequence of deformed foam images from the $y-z$ central plane corresponding to the numbered points on the responses in Fig. 3.3a and 3.3b.
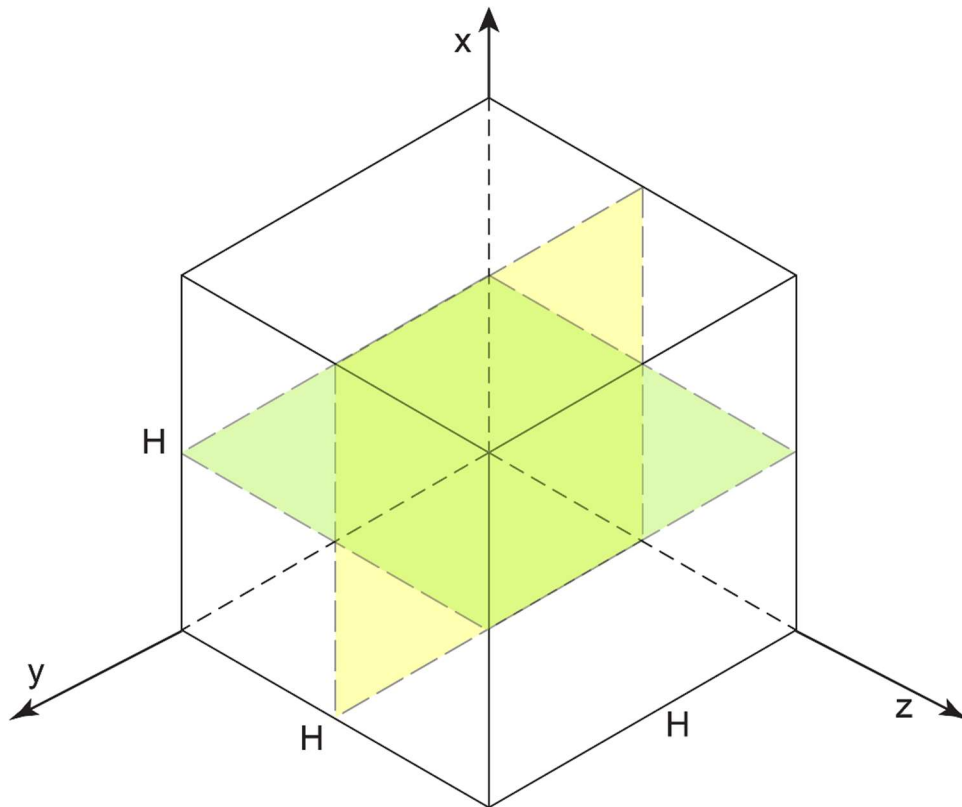
Fig. 3.6:   Depiction of the $y - x$ and $y - z$ central planes.
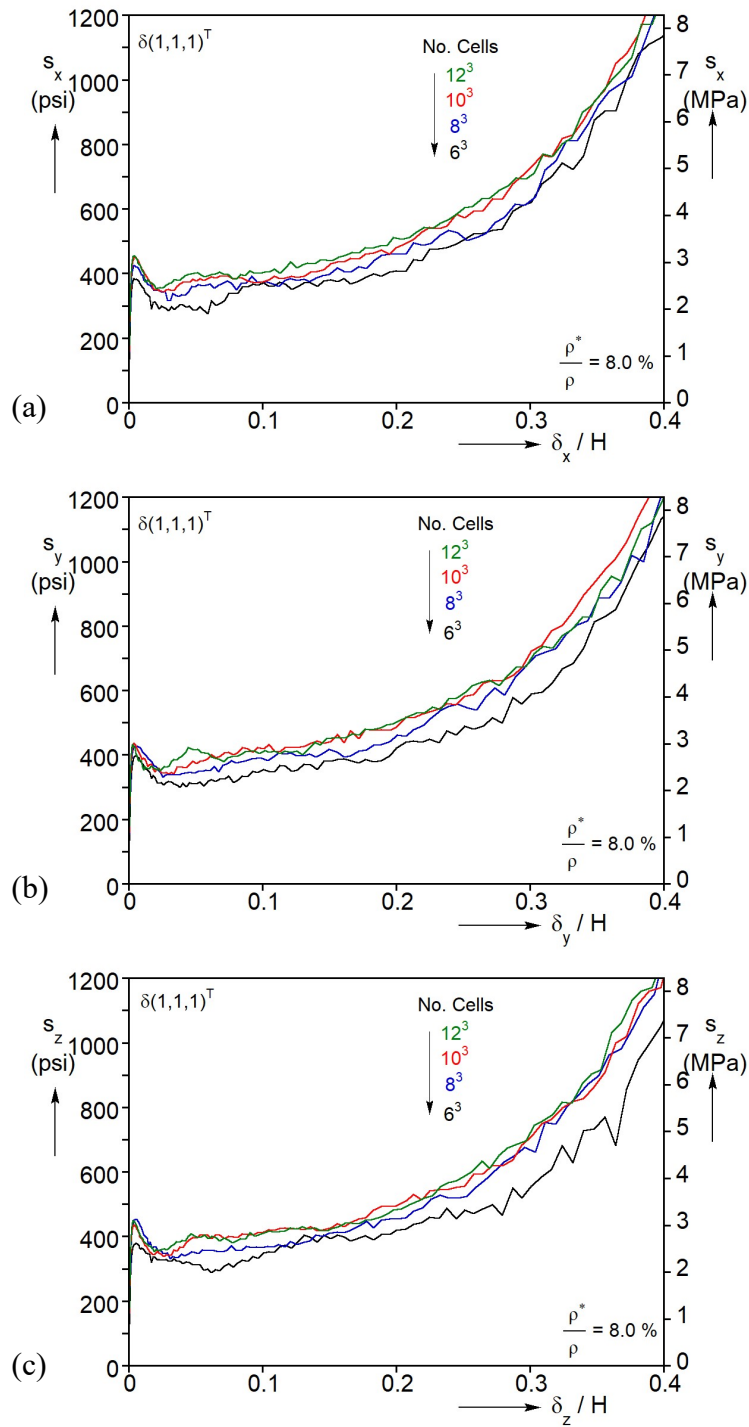
Fig. 3.7: The $\delta(1,1,1)^T$ responses from random foam models of different domain sizes: (a) in the *x*-direction, (b) *y*-direction, and (c) *z*-direction.
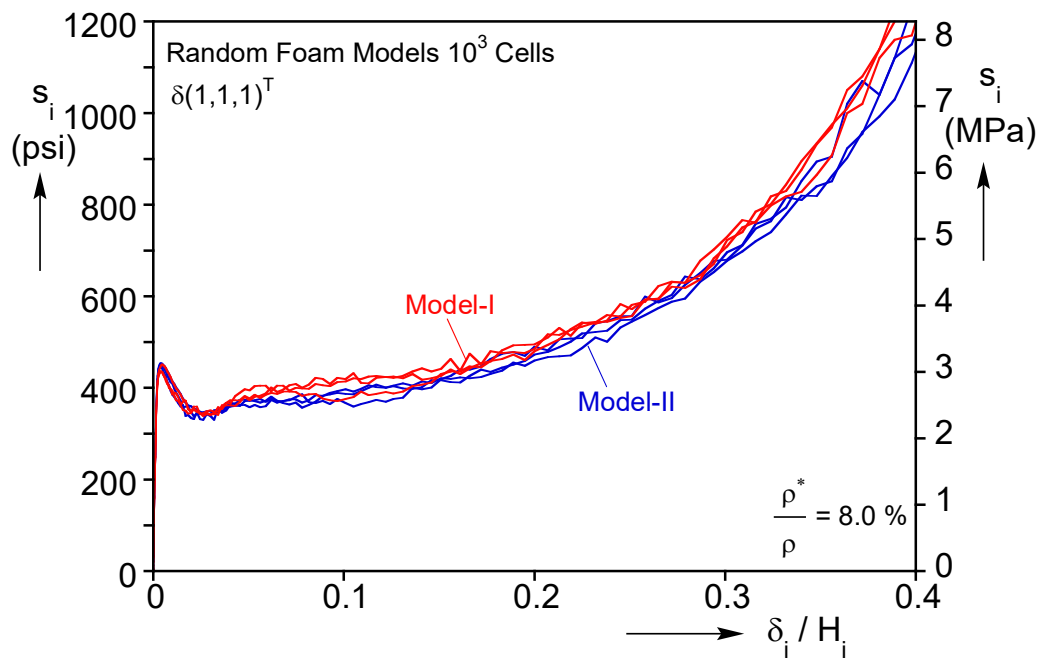
Fig. 3.8: Comparison of the $\delta(1,1,1)^T$ responses in the three directions from two 10^3 cell models.
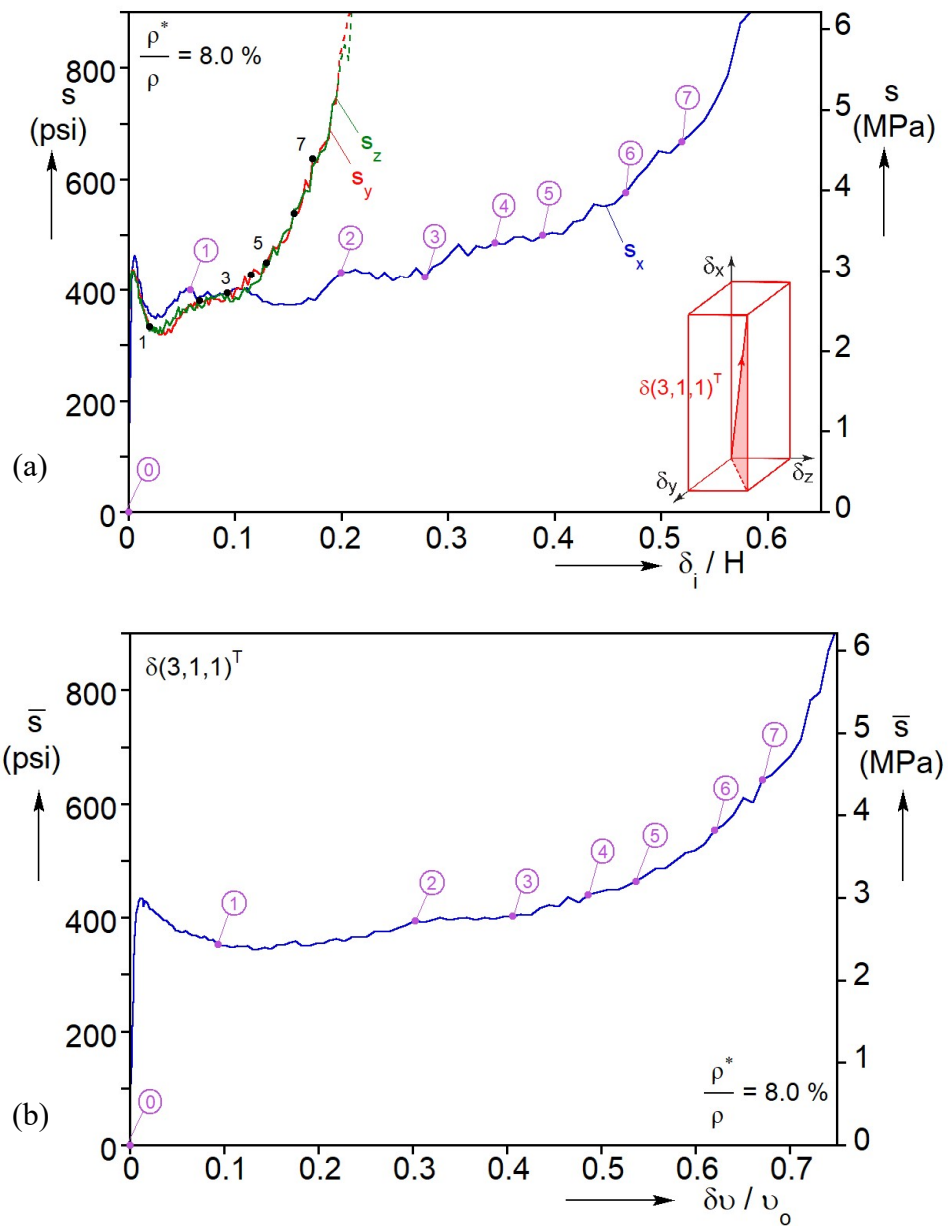
Fig. 3.9: (a) Calculated true stress-displacement responses in the *x*-, *y*- and *z*-directions for the $\delta(3,1,1)^T$ loading path, and (b) corresponding mean stress-change in volume response.
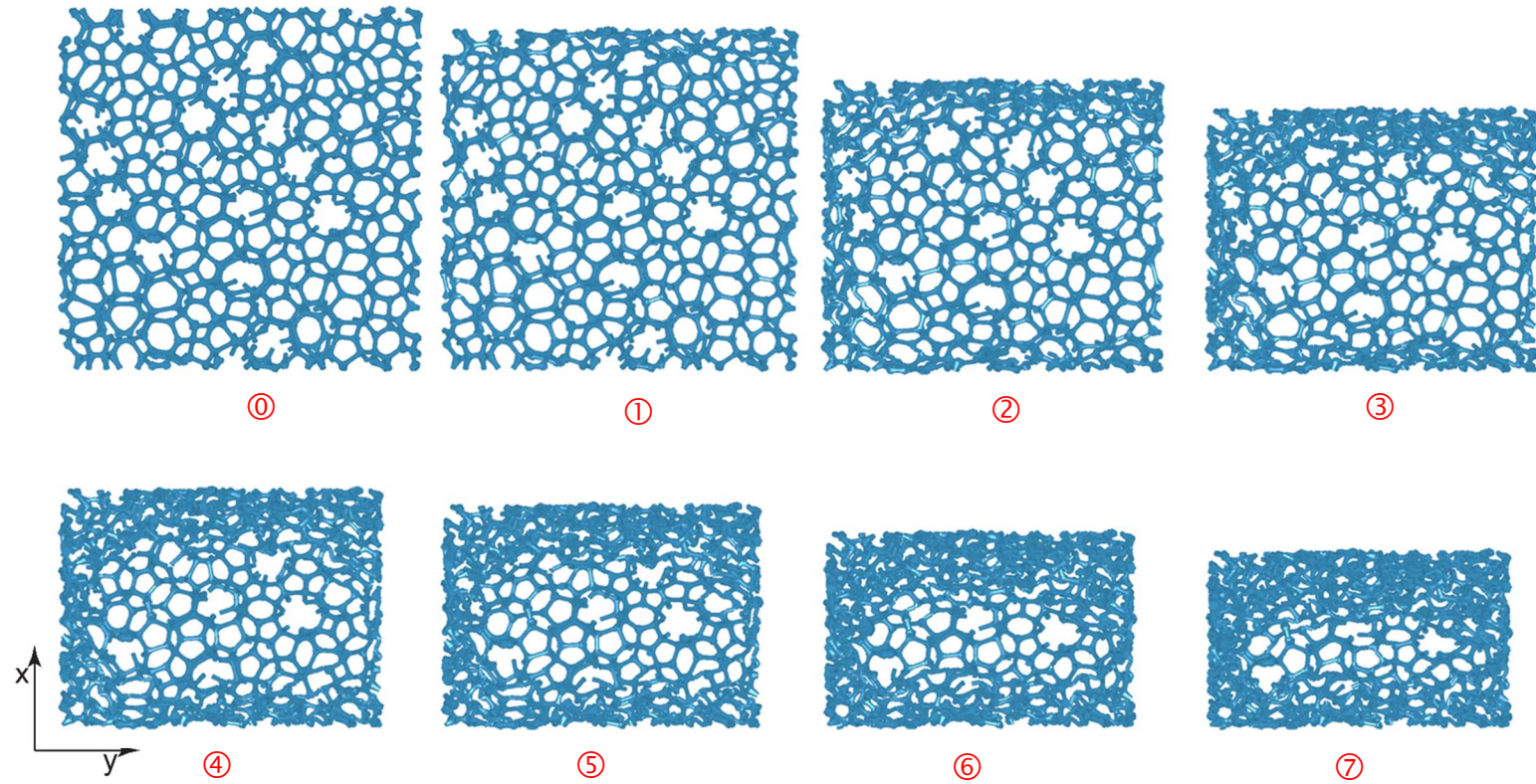
Fig. 3.10: Sequence of deformed foam images from the $y-x$ central plane corresponding to the numbered points on the responses in Fig. 3.9a and b.
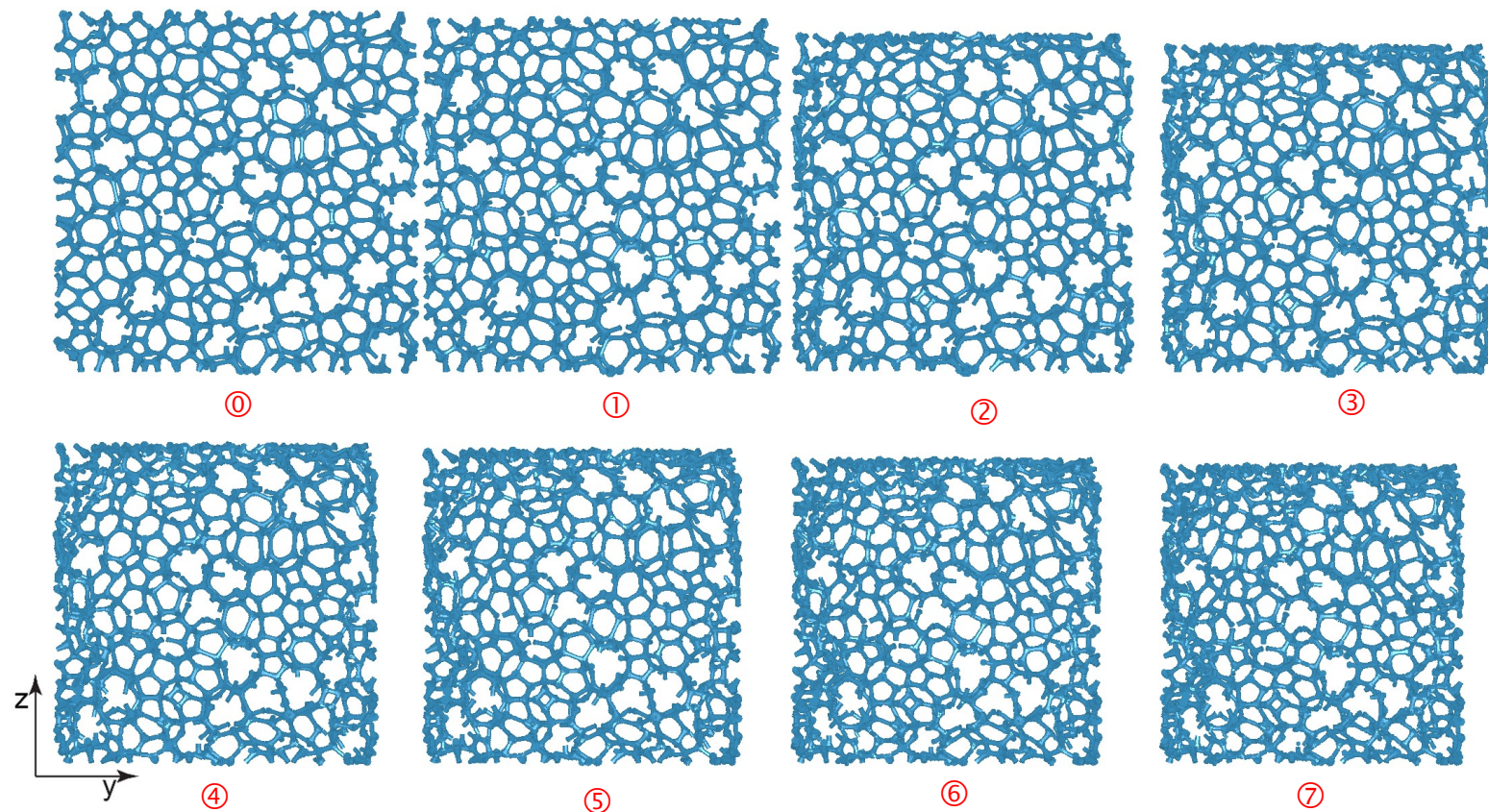
Fig. 3.11: Sequence of deformed foam images from the $y - z$ central plane corresponding to the numbered points on the responses in Fig. 3.9a and b.
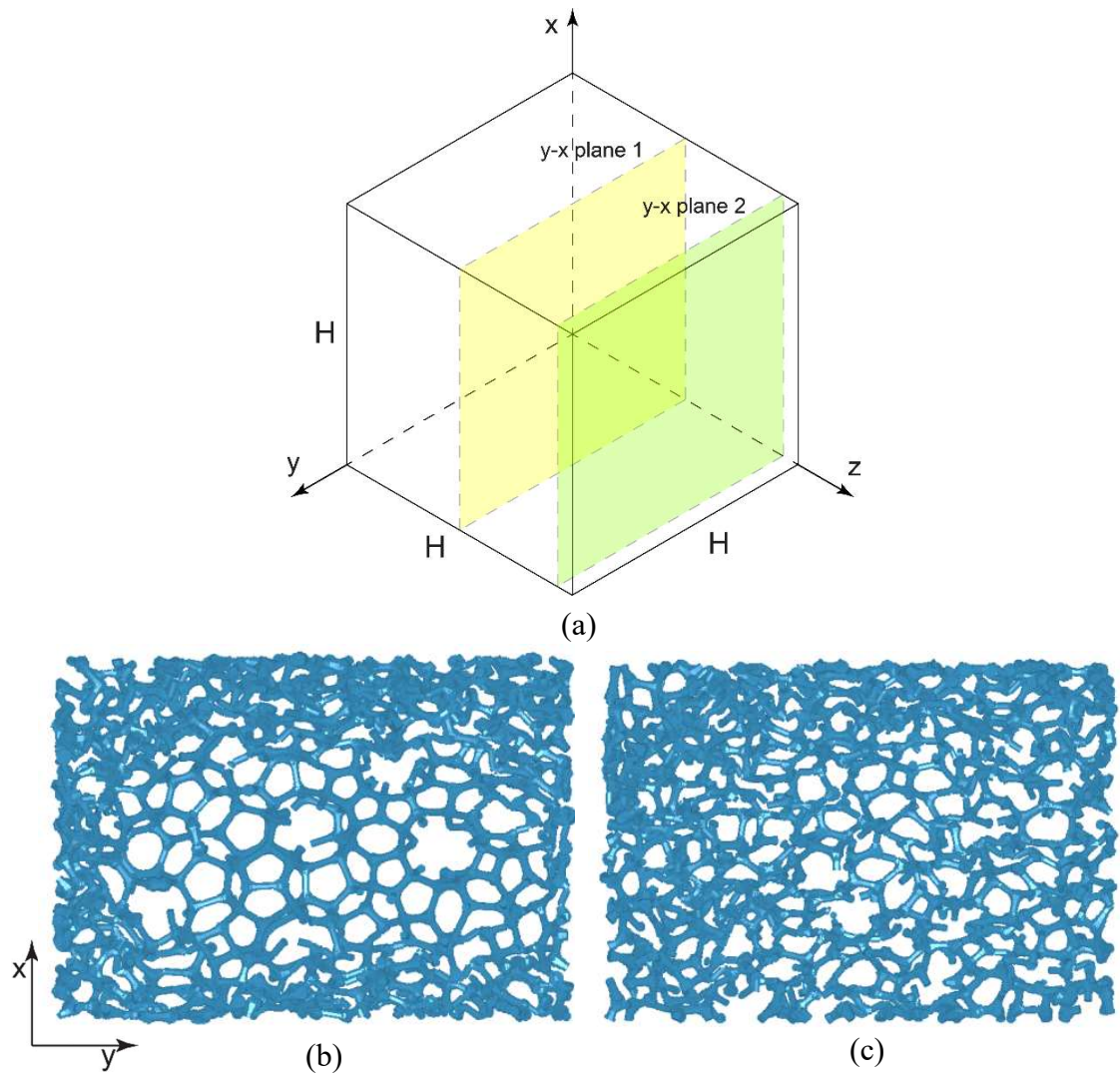
Fig. 3.12: (a) Location of the central plane cut and the cut adjacent to $z = H$. (b) Deformed configurations of model slices at $\bar{\delta}_x = 0.39$ for the $(3,1,1)^T$ loading path from the central $y - x$ plane, and (c) the $y - x$ plane closer to $z = H$.
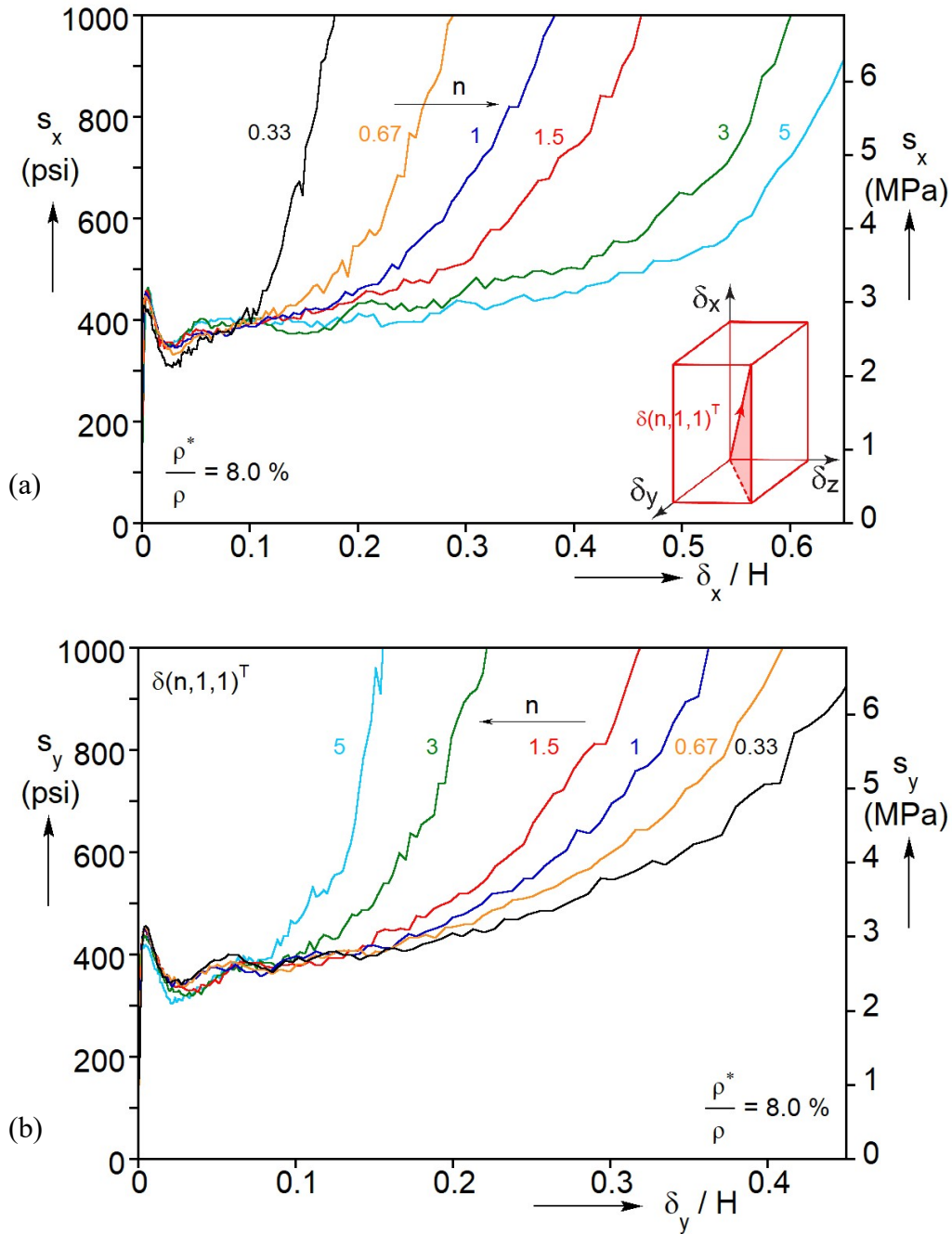
Fig. 3.13:   Calculated true stress-displacement responses for the $(n,1,1)^T$ family of loading paths: (a) in the x-direction and (b) in the y-direction.
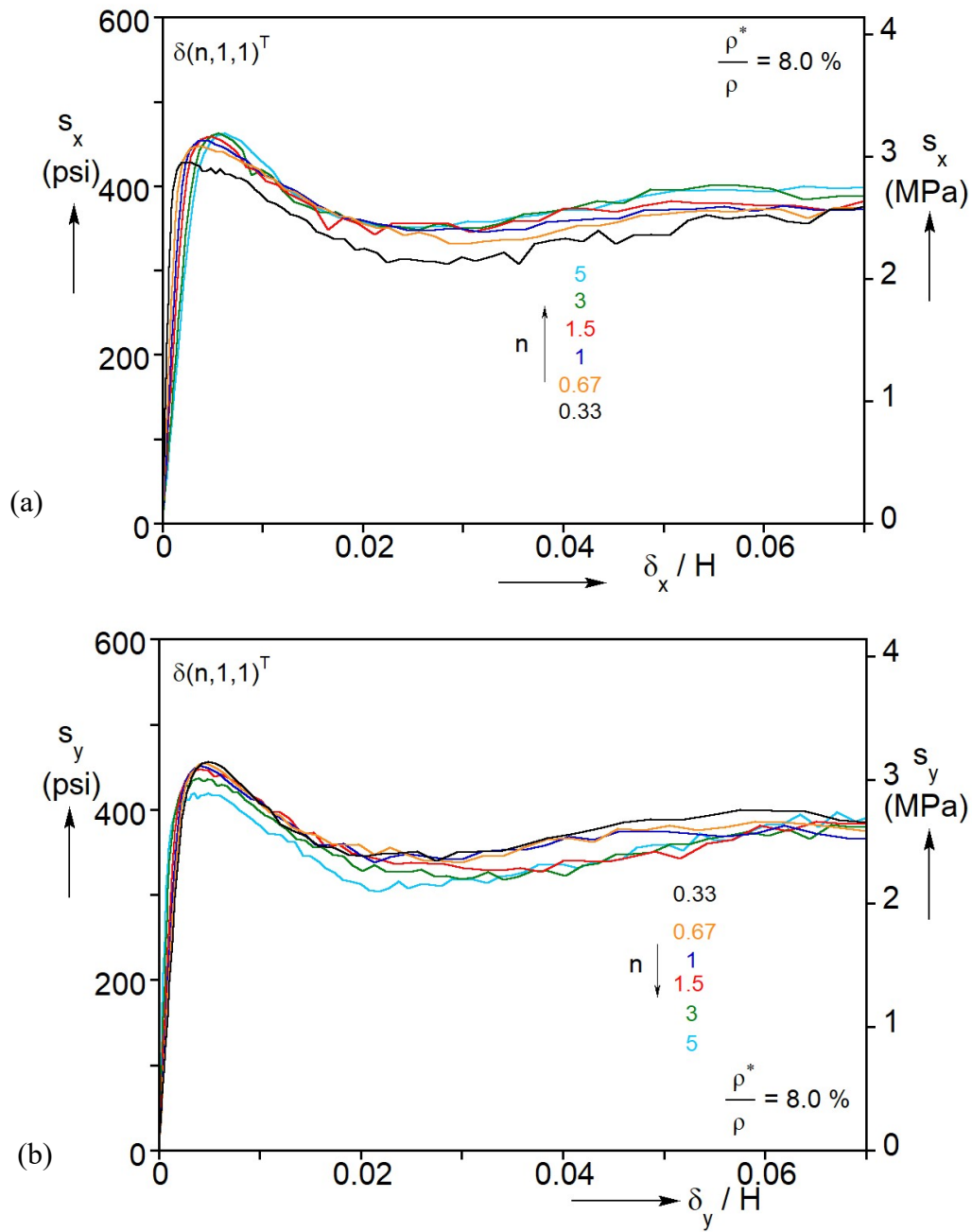
Fig. 3.14:   Expanded views showing the initial parts of the calculated true stress-
displacement responses for the $(n,1,1)^T$ family of loading paths: (a) in the *x*-
direction and (b) in the *y*-direction.
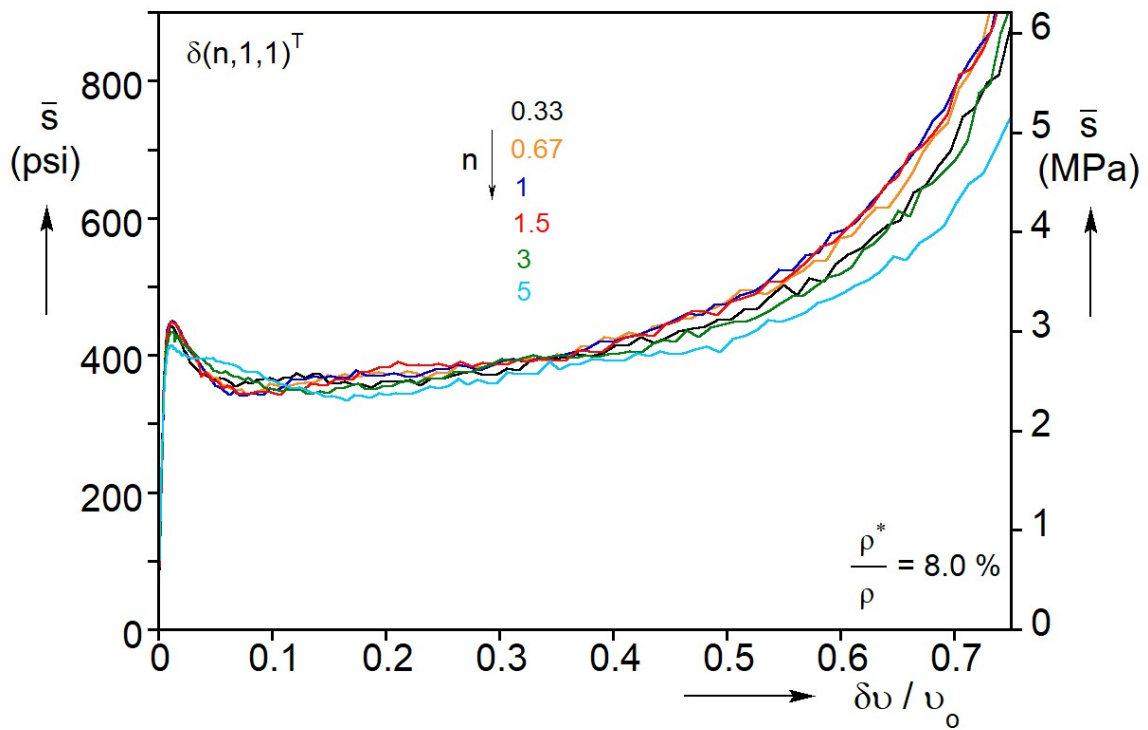
Fig. 3.15: Calculated mean stress-change in volume responses for the $(n,1,1)^T$ family of loading paths.
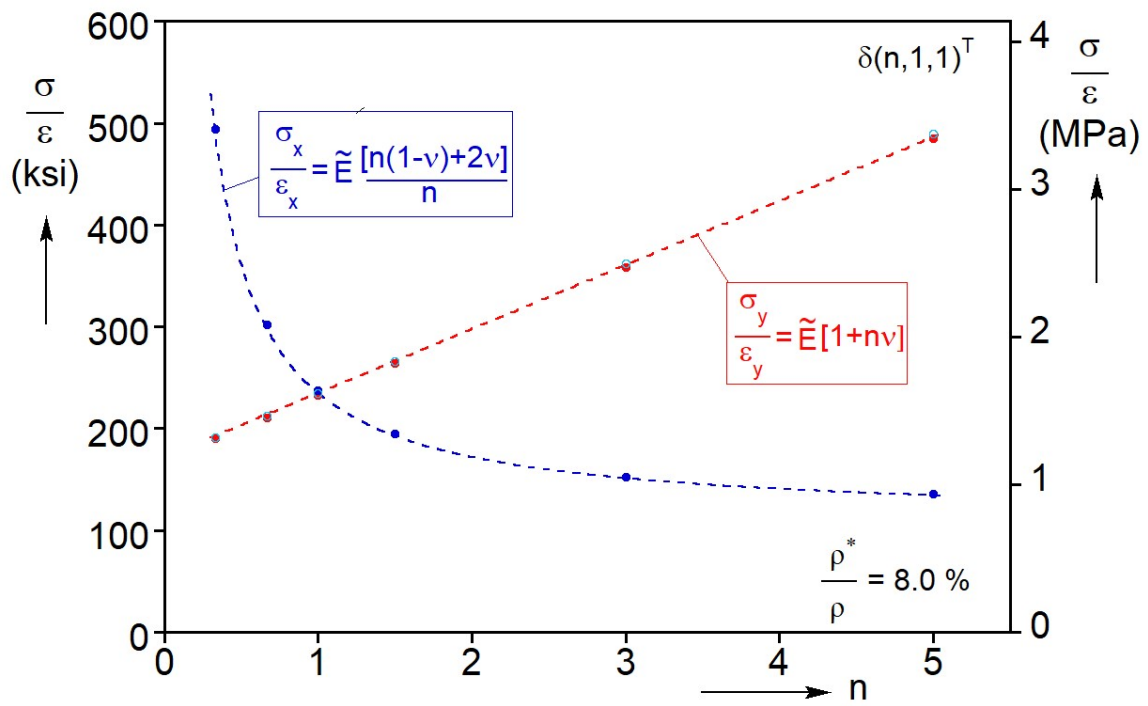
Fig. 3.16: Measured slopes of initial elastic responses for the $(n,1,1)^T$ family plotted against n, and linear elastic isotropic fits $\{\tilde{E} = E / [(1+v)(1-2v)]\}$.
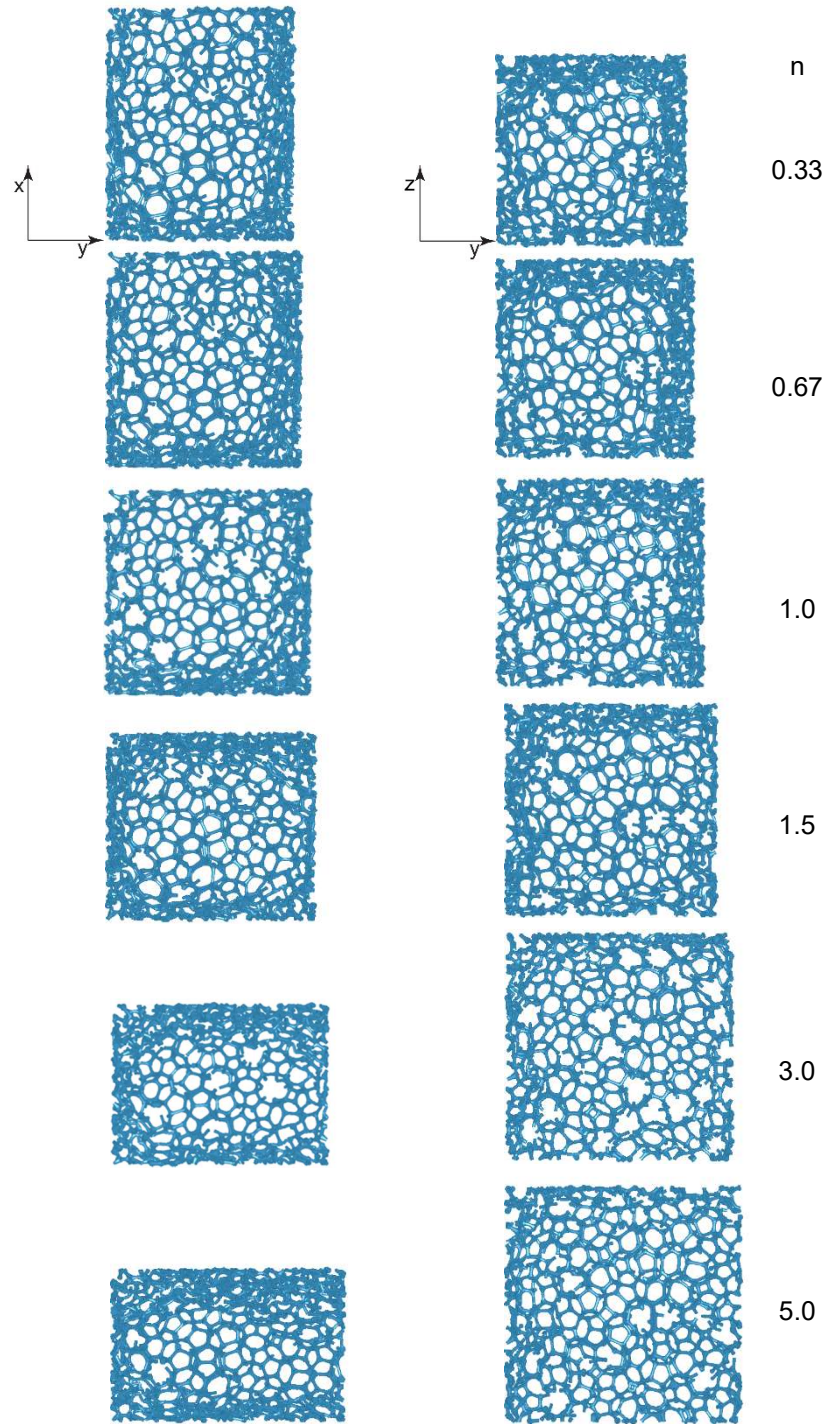
Fig. 3.17: Images from the $y-x$ and $y-z$ central planes at $\delta\overline{\upsilon} \approx 0.5$ for different values of n for the $(n,1,1)^T$ family of loading paths.
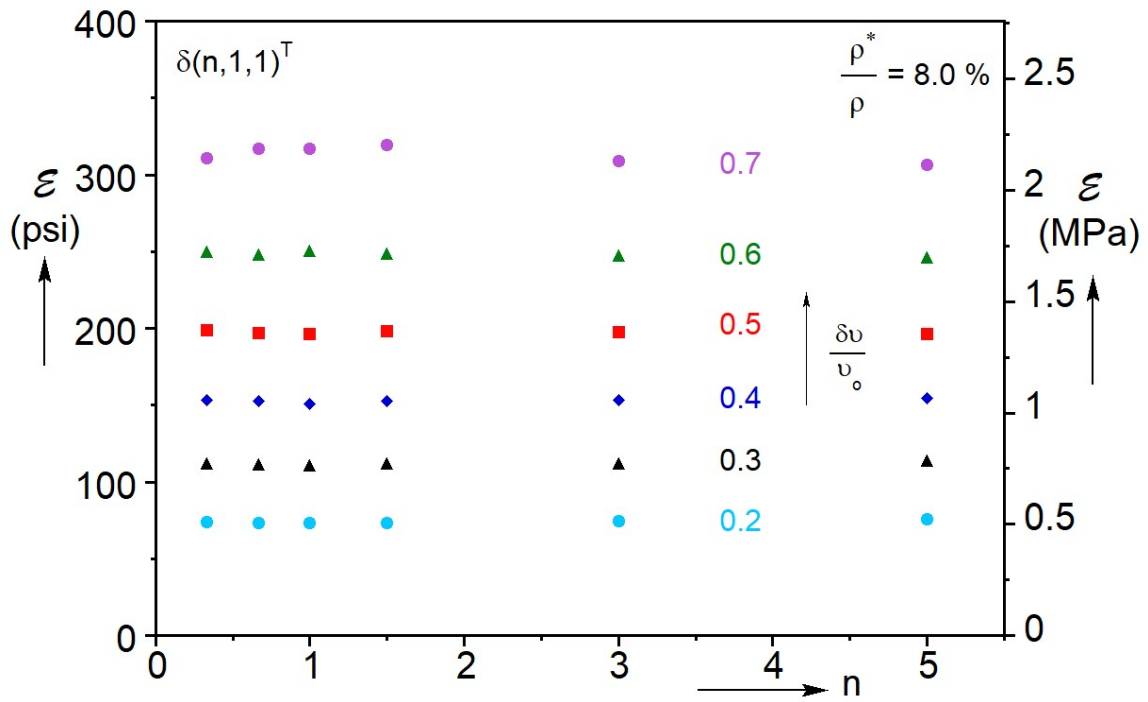
Fig. 3.18:   Deformation energies as a function of n for various values of $\delta\bar{\upsilon}$ for the $(n,1,1)^T$ loading paths.
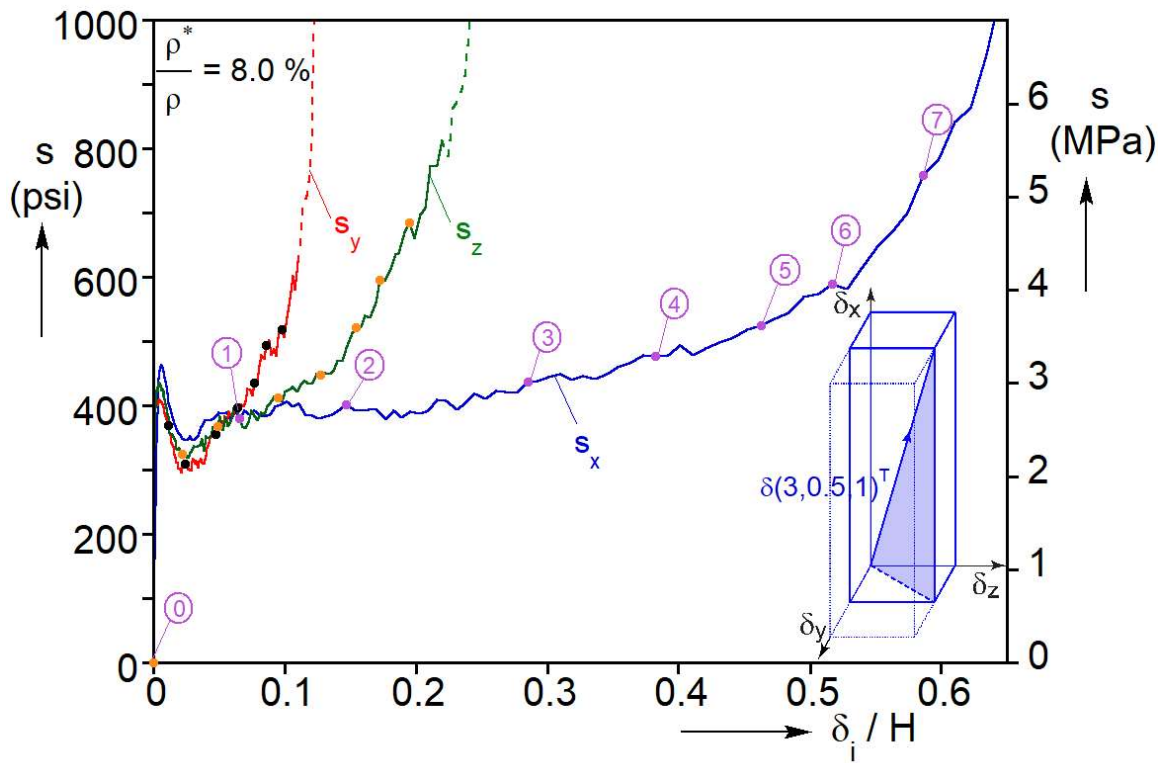
Fig. 3.19: Calculated true stress-displacement responses in the *x*-, *y*-, and *z*-directions for the $(3, 0.5, 1)^T$ loading path.
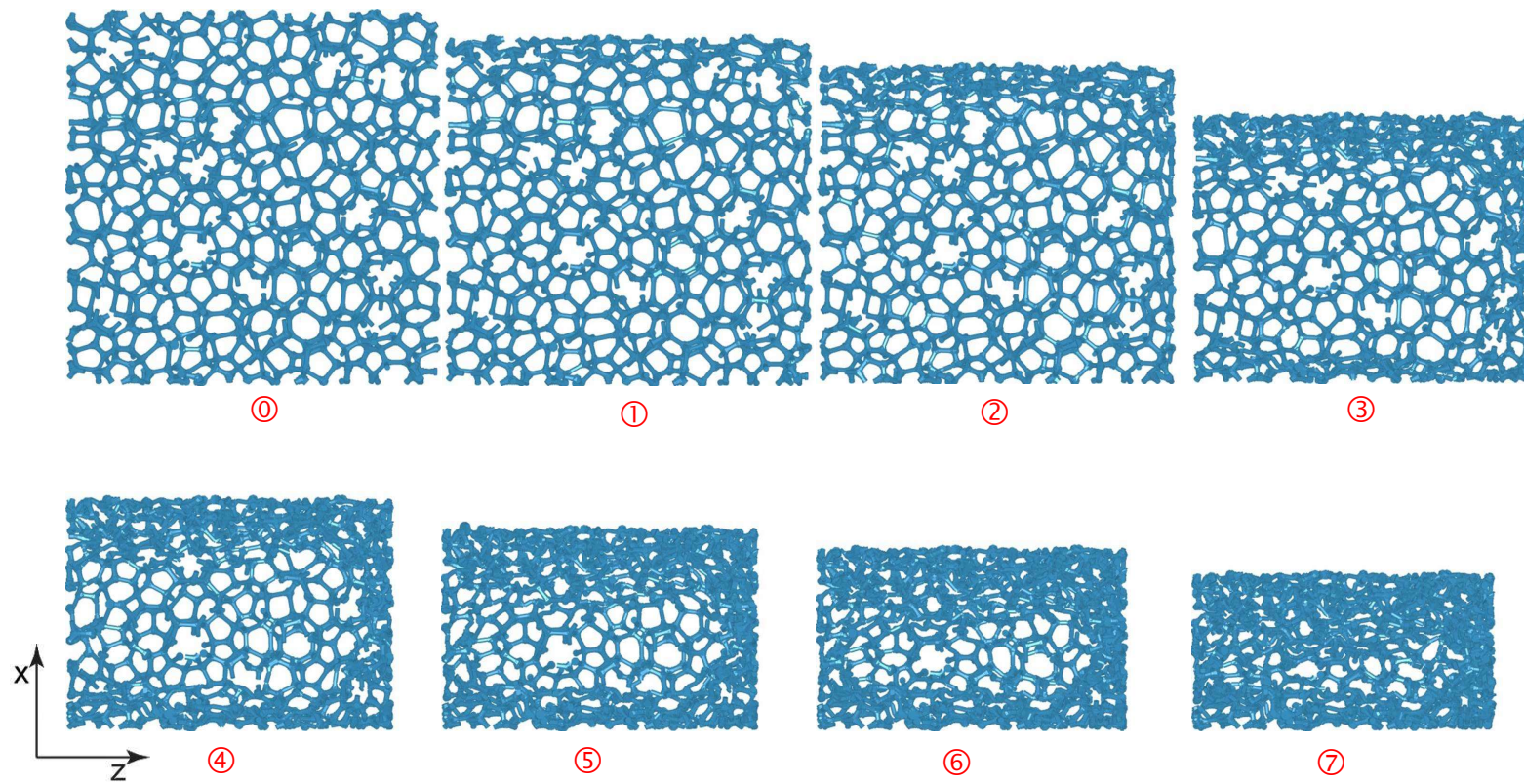
Fig. 3.20: Sequence of deformed foam images from the $z-x$ central plane corresponding to the numbered points on the responses in Fig. 3.19.
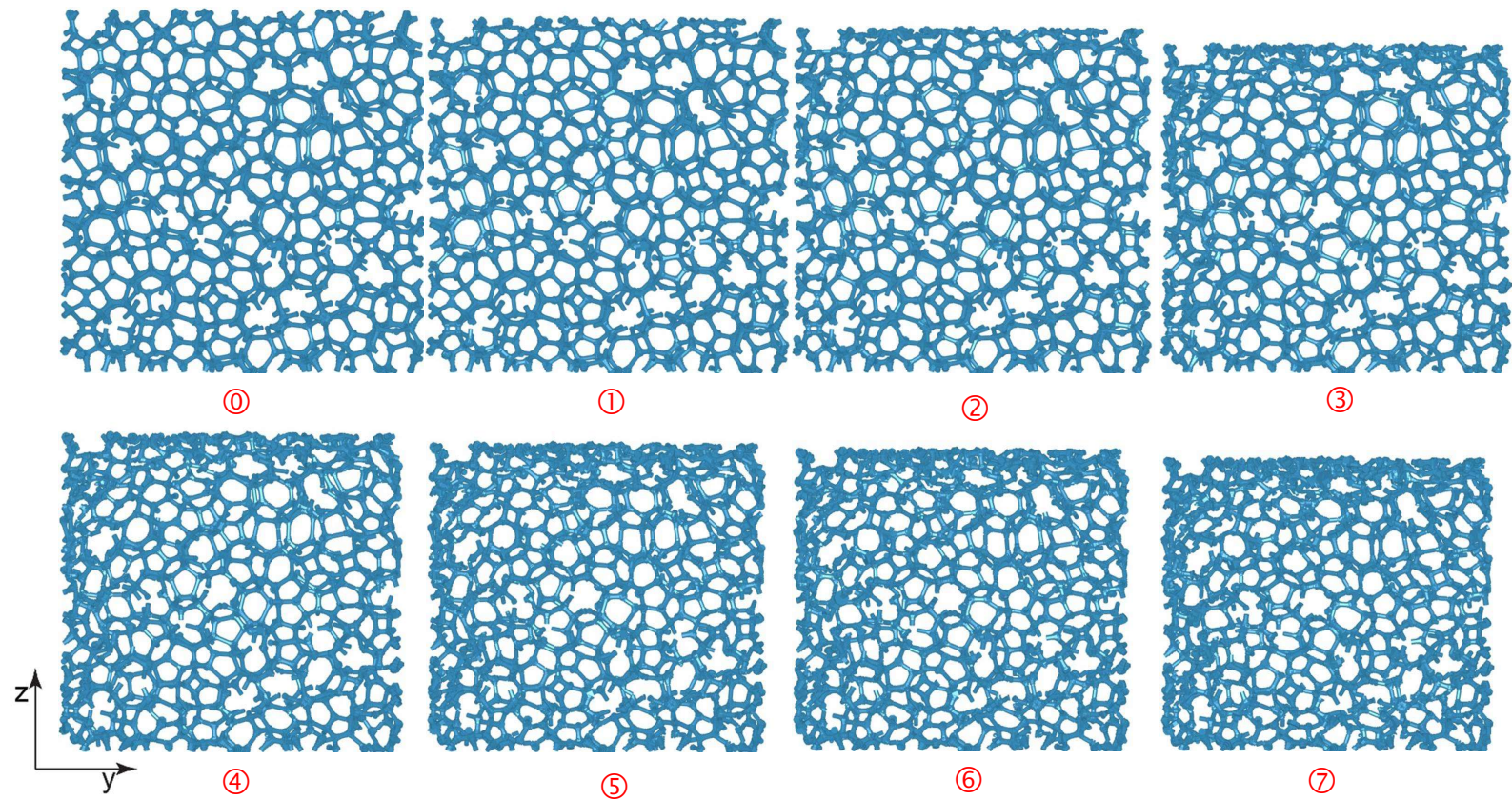
Fig. 3.21: Sequence of deformed foam images from the $y-z$ central plane corresponding to the numbered points on the responses in Fig. 3.19.
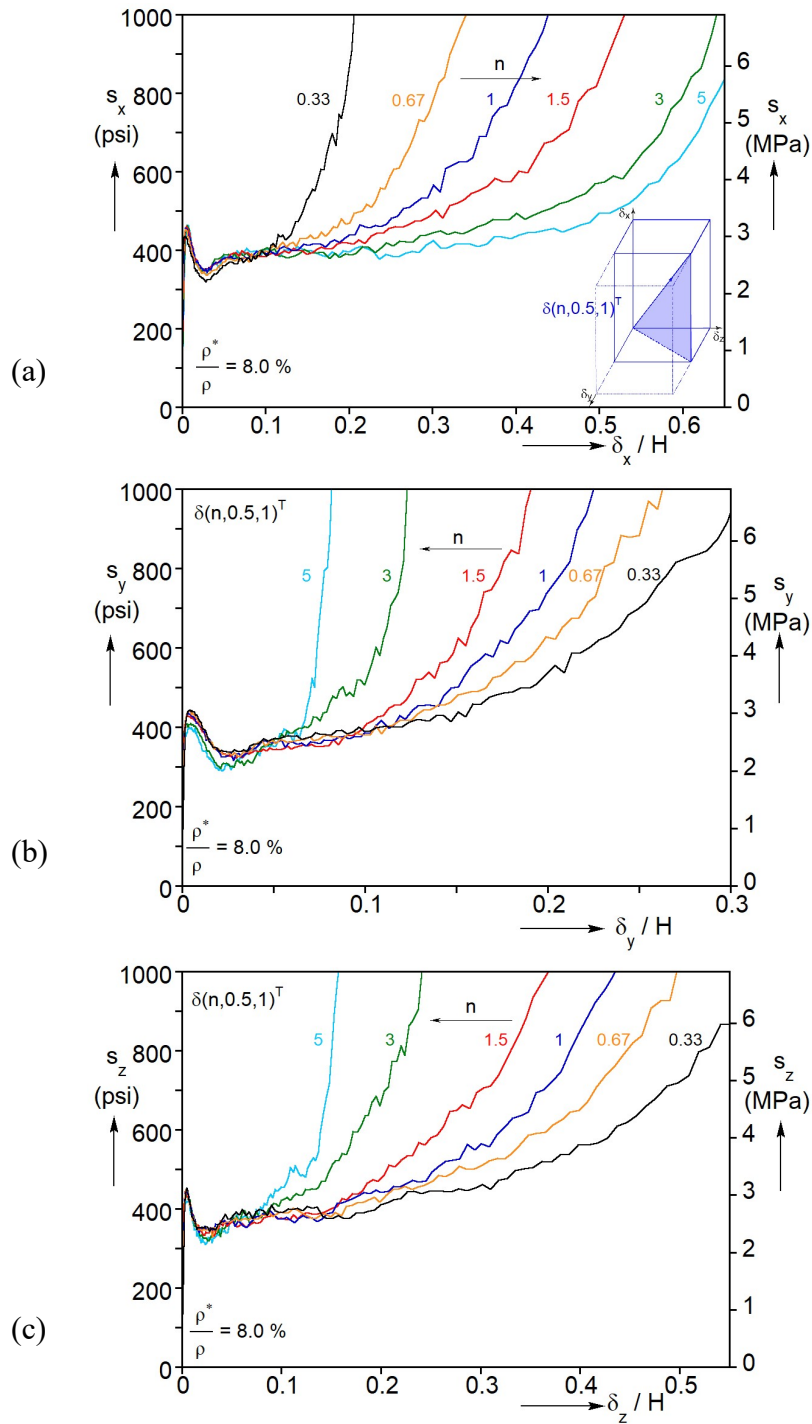
Fig. 3.22: Calculated true stress-displacement responses for the $(n, 0.5, 1)^T$ family of loading paths: (a) in the x-direction, (b) y-direction, and (c) z-direction.
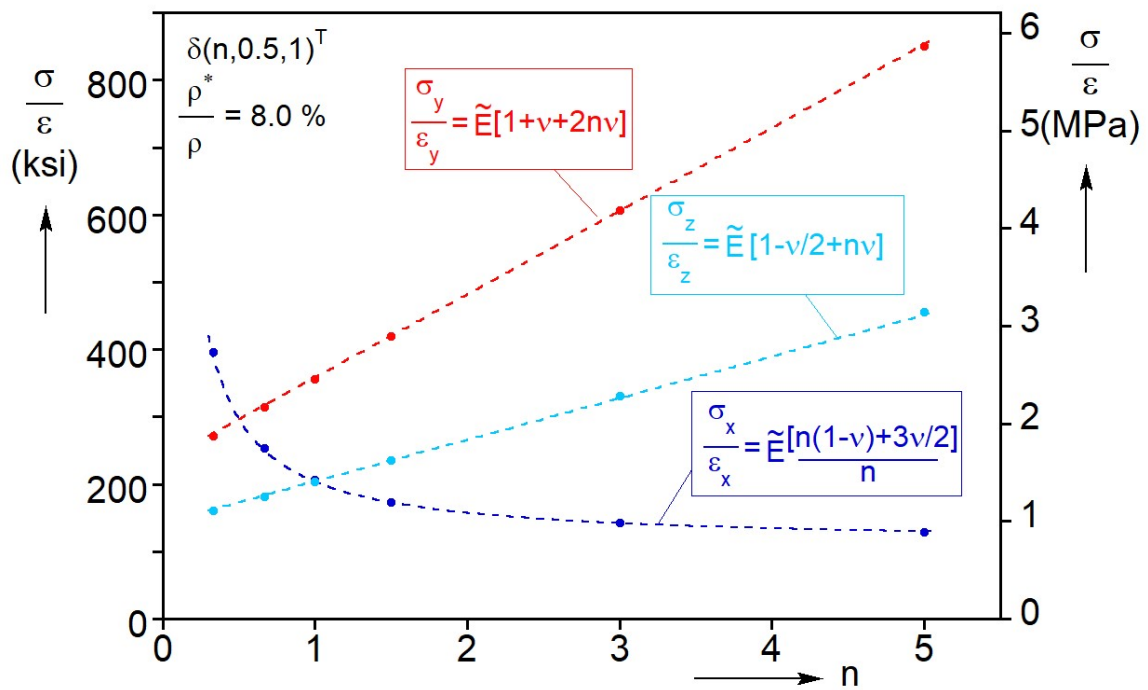
Fig. 3.23:   Measured slopes of initial elastic responses for the $(n, 0.5, 1)^T$ family plotted against n and linear elastic isotropic fits $\{\tilde{E} = E / [(1+\nu)(1-2\nu)]\}$.
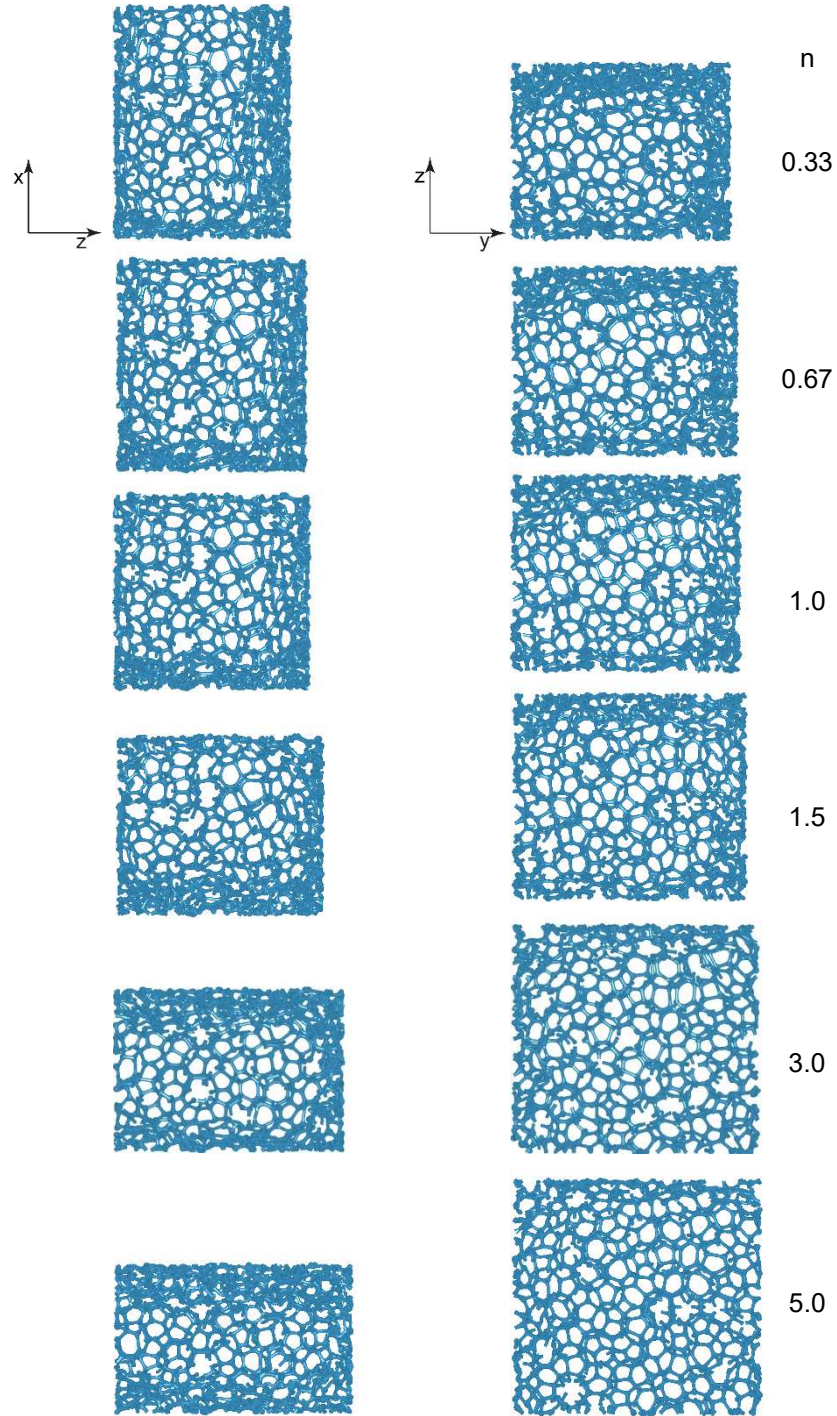
Fig. 3.24: Images from the $z-x$ and $y-z$ central planes at $\delta\bar{\upsilon} \approx 0.5$ for different values of n for the $(n, 0.5, 1)^T$ family of loading paths.
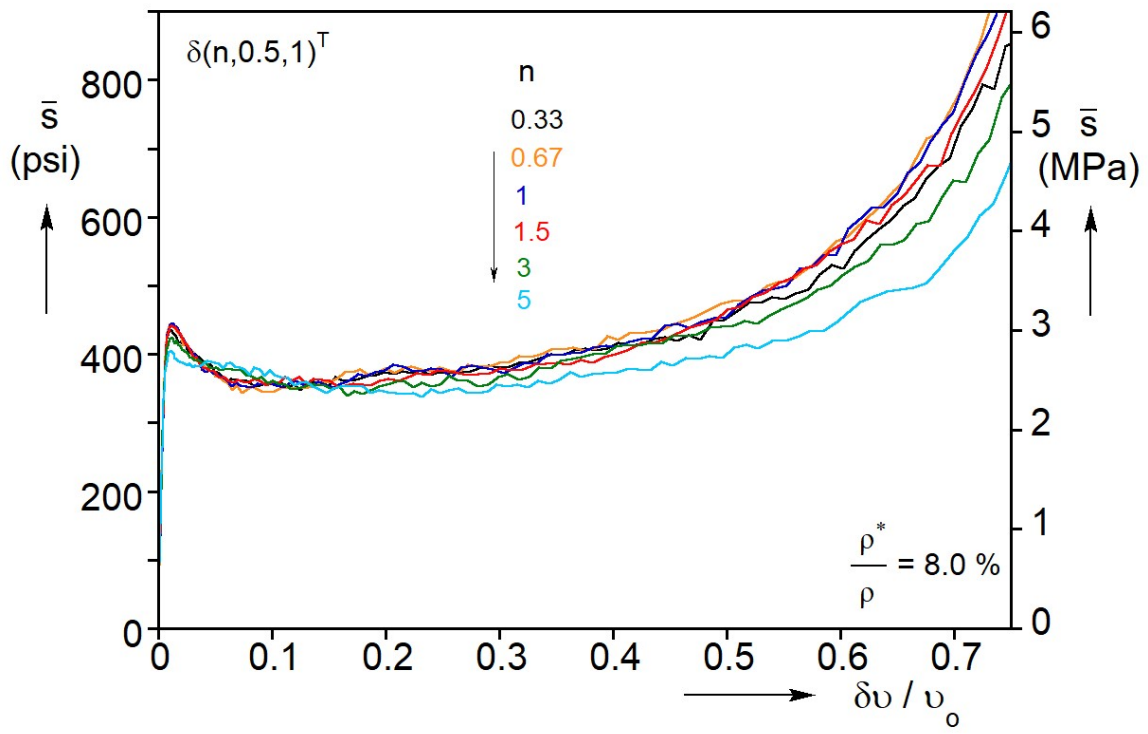
Fig. 3.25:   Calculated mean stress-change in volume responses for the $(n, 0.5, 1)^T$ family of loading paths.
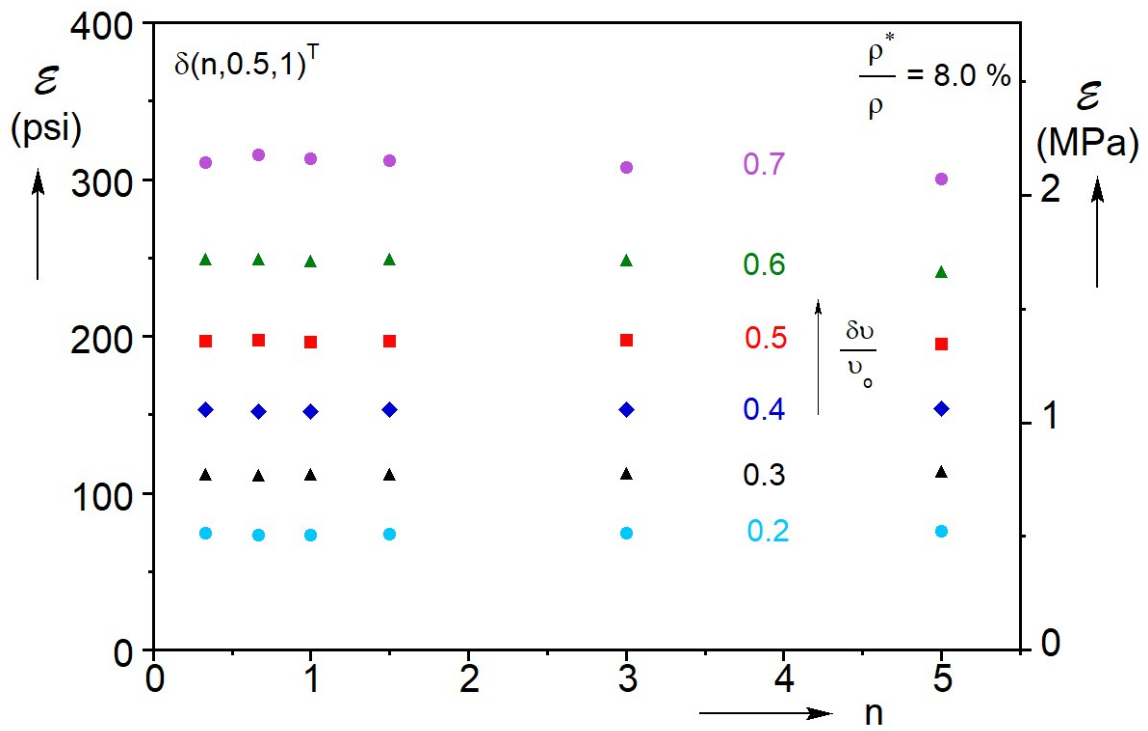
Fig. 3.26: Deformation energies as a function of n for various values of $\delta\overline{\upsilon}$ for the $(n,0.5,1)^T$ loading paths.
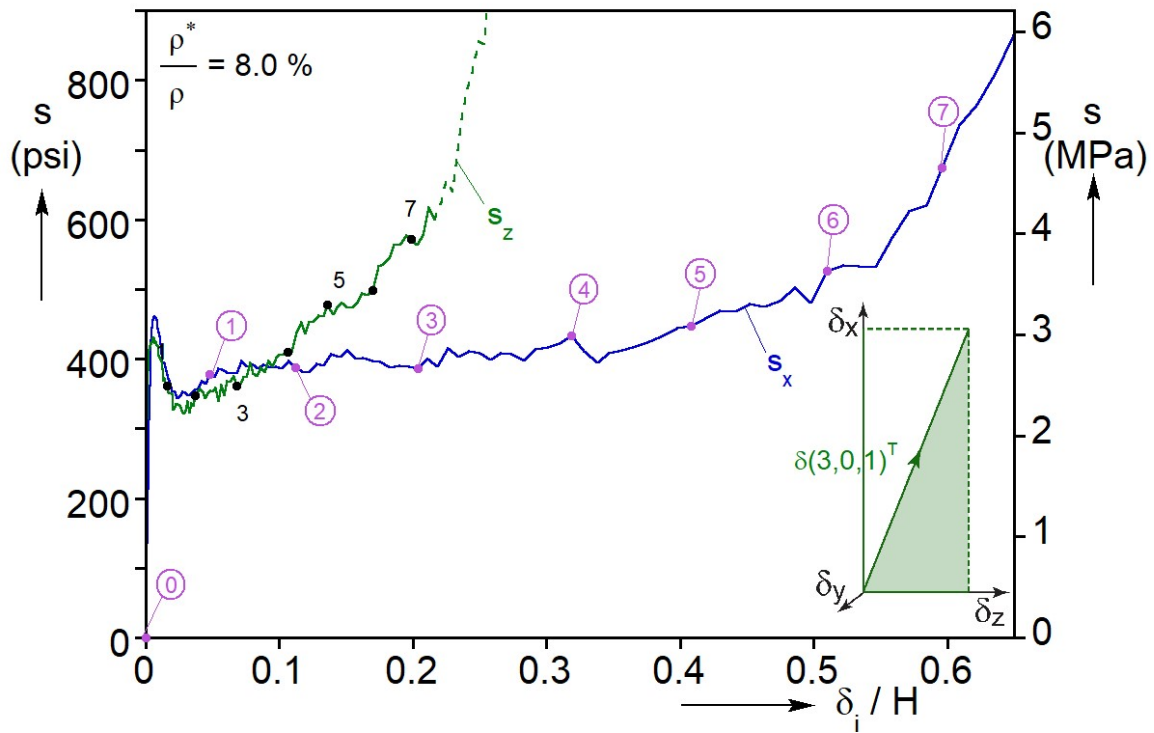
Fig. 3.27:   Calculated true stress-displacement responses in the *x*- and *z*-directions for the $\delta(3,0,1)^T$ loading path.
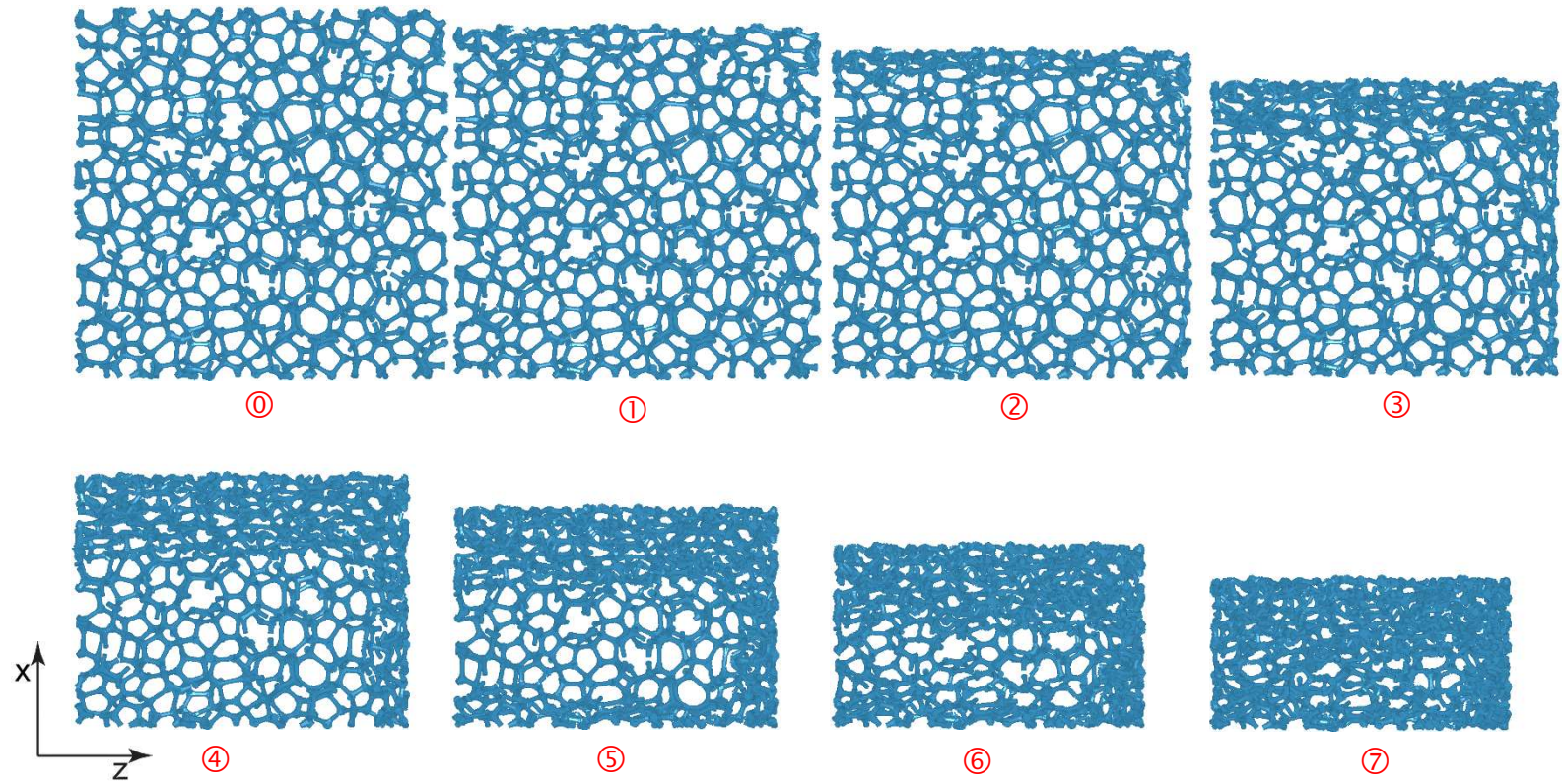
Fig. 3.28: Sequence of deformed foam images from the $z-x$ central plane corresponding to the numbered points on the responses in Fig. 3.27.
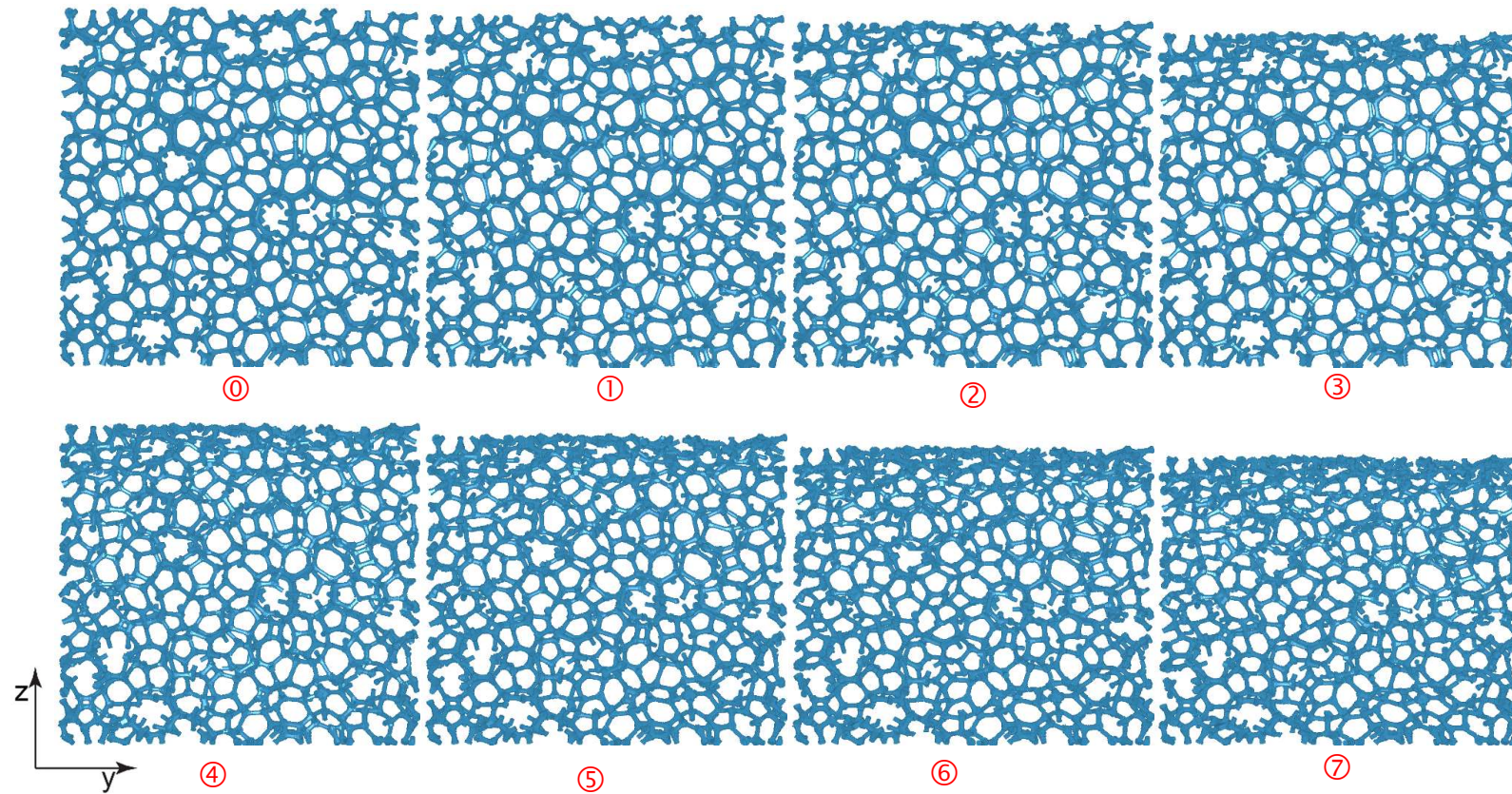
Fig. 3.29: Sequence of deformed foam images from the $y-z$ central plane corresponding to the numbered points on the responses in Fig. 3.27.
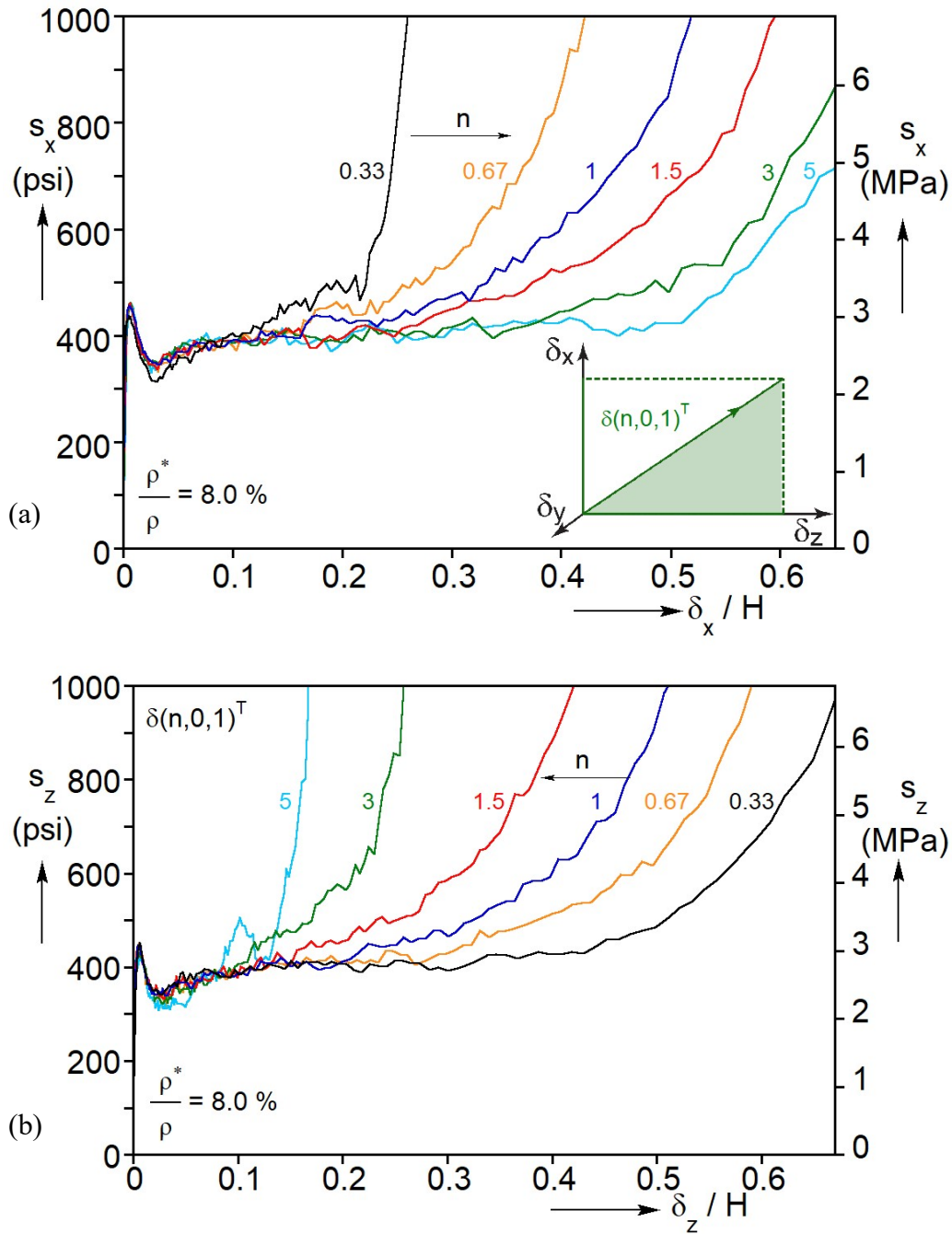
Fig. 3.30: Calculated true stress-displacement responses for the $(n,0,1)^T$ family of loading paths: (a) in the *x*-direction and (b) in the *z*-direction.
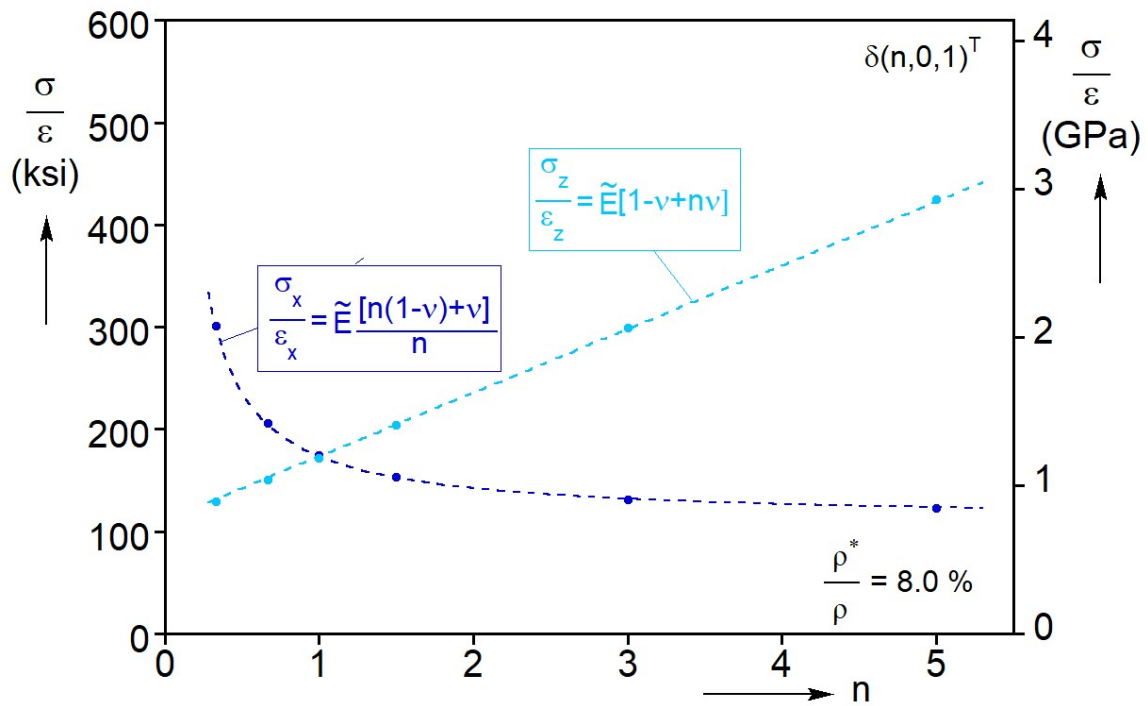
Fig. 3.31:   Measured slopes of initial elastic responses for the $(n,0,1)^T$ family plotted against n and linear elastic isotropic fits $\{\tilde{E} = E /[(1+\nu)(1-2\nu)]\}$.
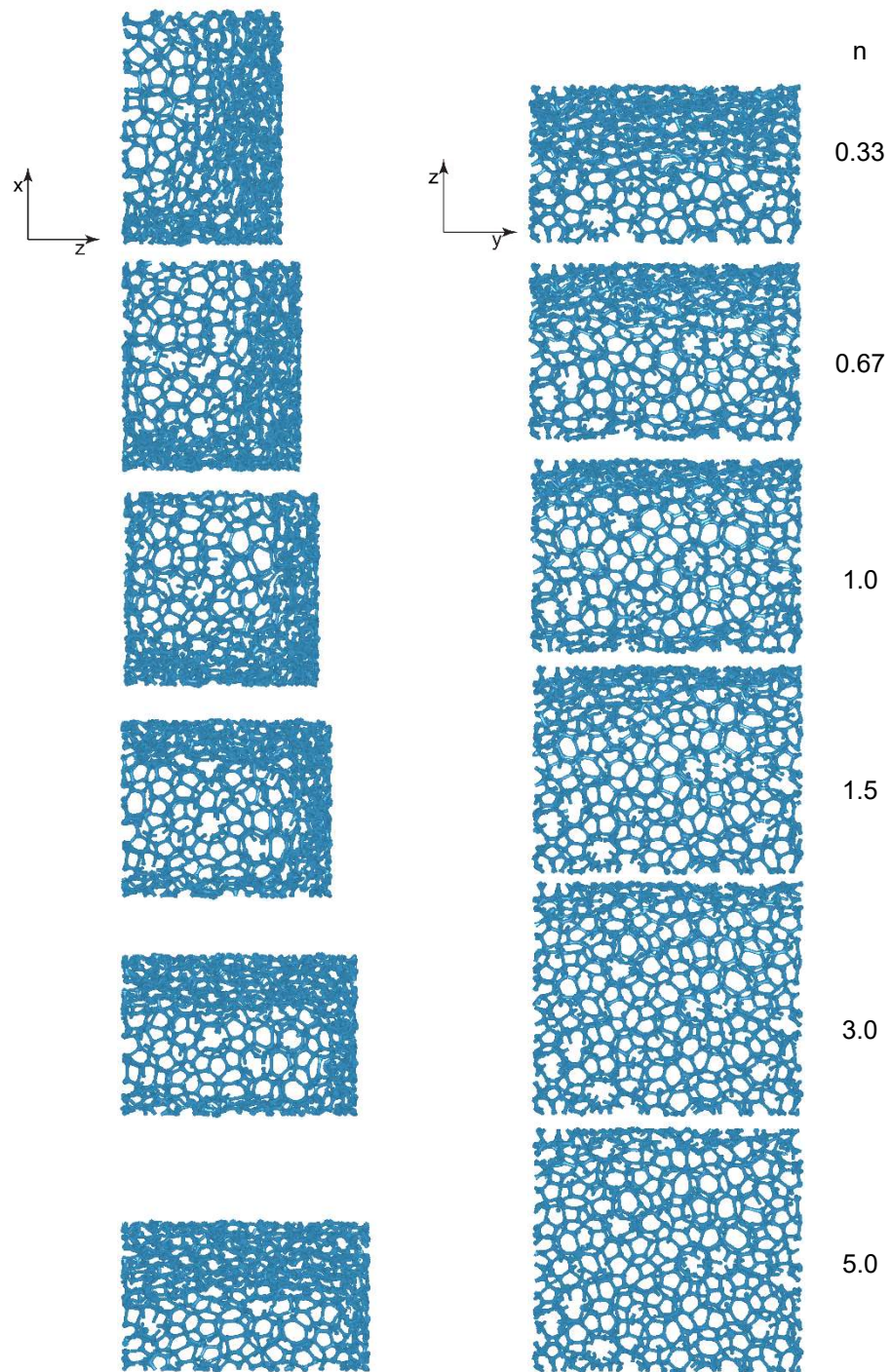
Fig. 3.32: Images from the $z-x$ and $y-z$ central planes at $\delta\overline{\upsilon} \approx 0.5$ for different values of n for the $(n,0,1)^T$ family of loading paths.
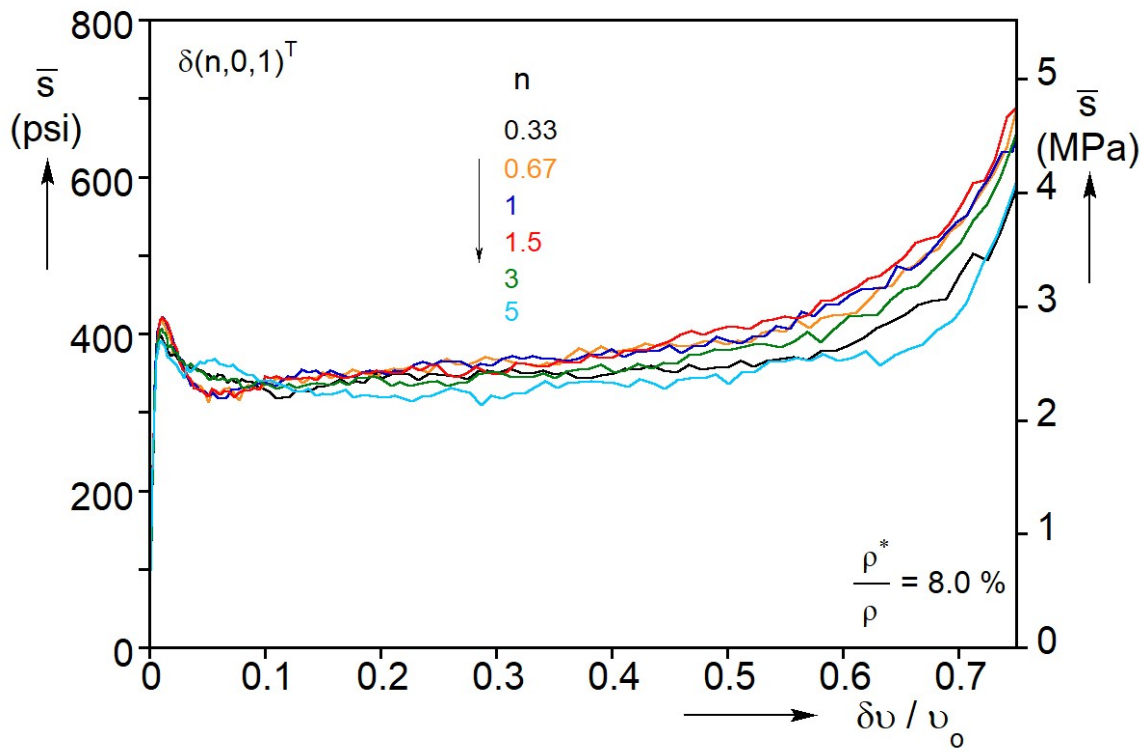
Fig. 3.33: Calculated mean stress-change in volume responses for the $(n,0,1)^T$ family of loading paths.
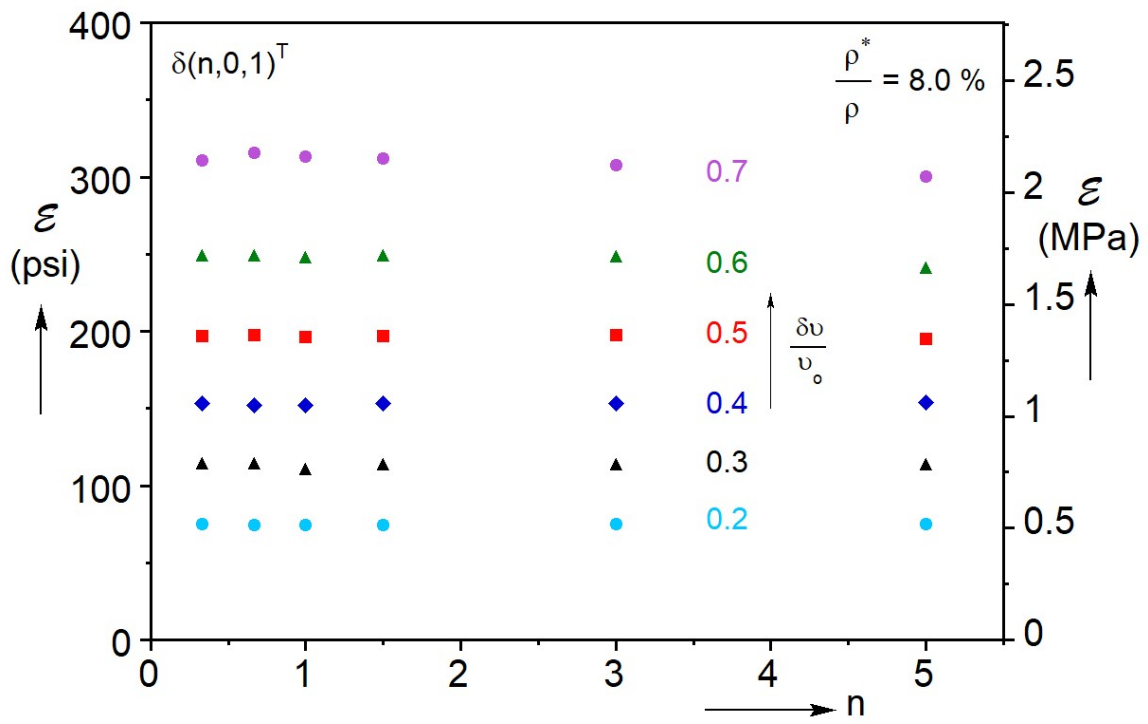
Fig. 3.34:   Deformation energies as a function of *n* for various values of $\delta\overline{\upsilon}$ for the $(n,0,1)^T$ loading paths.
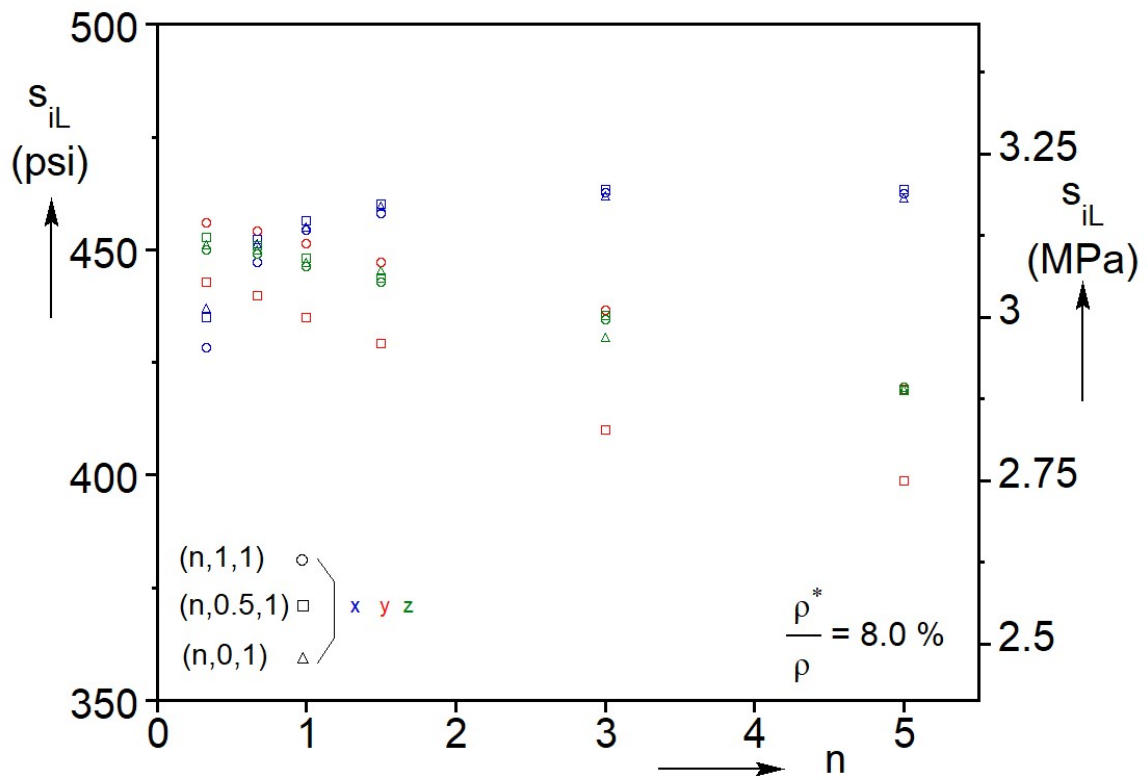
Fig. 3.35: Limit stresses in the three directions plotted against *n* for the three radial paths analyzed.
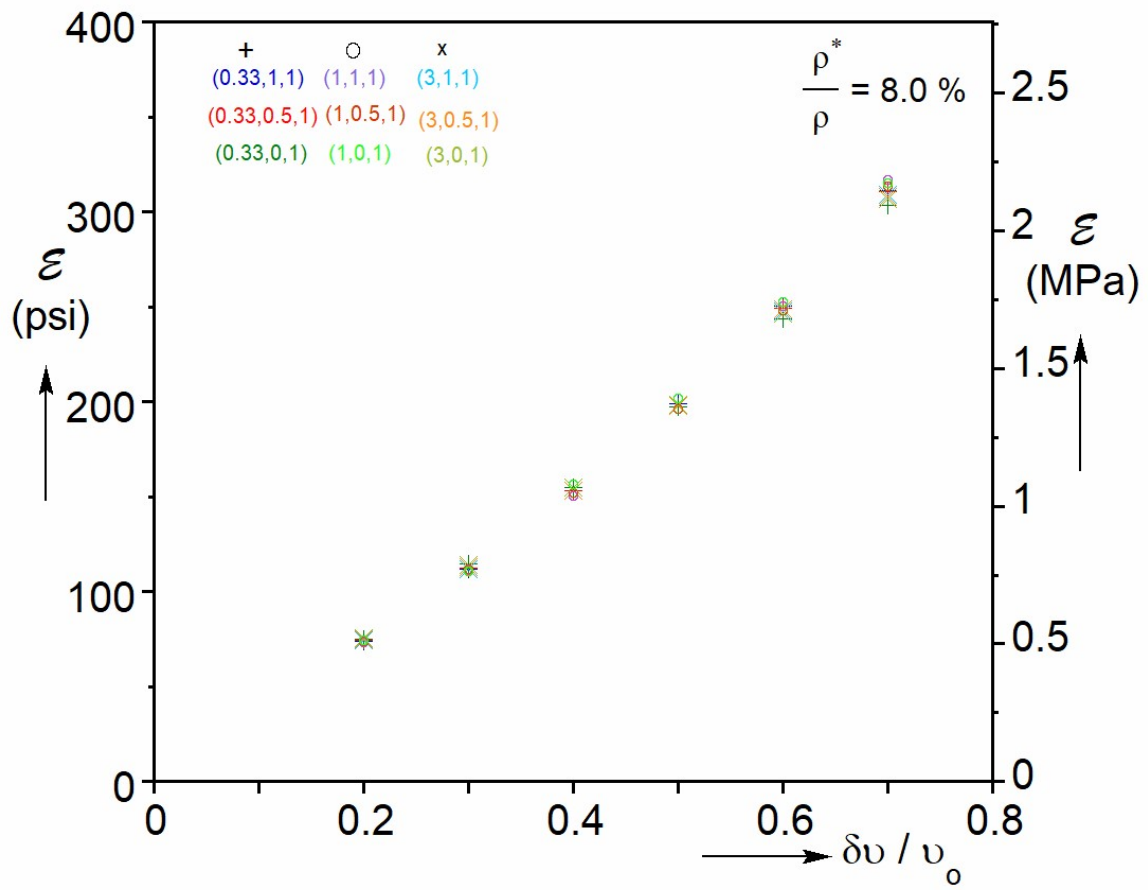
Fig. 3.36: Deformation energies at discrete values of change in volume from nine loading paths.

Chapter 4: Continuum Constitutive Model for Low-Density Foams[45]

As reported in Chapter 1, it is well established that under compression low-density metallic and polymeric foams deform inhomogeneously, developing zones of locally buckled and crushed cells. Persistent compression causes the crushing to spread with the stress remaining relatively unchanged. For the Al-alloy foam used in this study, uniaxial crushing experiments as well as micromechanically accurate foam models have confirmed the co-existence of zones of crushed and intact material as the stress plateau is traced (e.g., see Jang and Kyriakides, 2009a; Gaitanaros et al., 2012). Chapter 3 demonstrated that this behavior carries over to the multiaxial crushing setting (see also Yang and Kyriakides, 2019a). Despite the plethora of evidence of inhomogeneous crushing behavior, present continuum constitutive models of foams assume the material to harden monotonically and consequently do not capture this partially inhomogeneous behavior (e.g., Deshpande and Fleck, 2000, 2001; Zhu et al., 2019).

In an effort to address this deficiency, this chapter presents an extension of the Deshpande and Fleck (2000) compressible constitutive family of models for foams with the aim of capturing the partially inhomogeneous crushing behavior. The model is calibrated using the stress-"average strain" responses of the 18 sets of triaxial crushing simulations reported in Chapter 3. Section 4.1 describes the framework of the constitutive model. Section 4.2 describes essential parameters for the isotropic elastic and the compressible plasticity part of the model chosen based on true triaxial crushing results in Chapter 3.

4.1 CONSTITUTIVE MODEL FRAMEWORK

The aluminum alloy foam is modeled as a compressible isotropic elastoplastic rate-independent solid. The strain increments are decomposed into an elastic part and a plastic

---

[4] Yang, C., Kyriakides, S., 2019. Continuum modeling of crushing of low-density foams. *J. Mech. Phys. Solids*, https://doi.org/10.1016/j.jmps.2019.103688. Chenglin Yang contributed as first author.

[5] Yang, C., Kyriakides, S., 2019. Crushing of low density foams under triaxial loadings. *Extreme Mechanics Letters* (accepted). Chenglin Yang contributed as first author.

part, $d\varepsilon_{ij} = d\varepsilon_{ij}^e + d\varepsilon_{ij}^p$. Elastic deformations are linear and isotropic and thus elastic stress-strain increment relations are given by

$$d\varepsilon_{ij}^e = \frac{1+\nu}{E}d\sigma_{ij} - \frac{\nu}{E}d\sigma_{kk}\delta_{ij}, \qquad \text{or} \qquad d\sigma_{ij} = C(E,\nu)_{ijkl}d\varepsilon_{kl}^e \qquad (4.1)$$

where $\{E,\nu\}$ are the elastic modulus and Poisson's ratio of the material. It is noted that the true stresses in the three directions in Chapter 3 are reported as $\{s_x, s_y, s_z\}$. However, to distinguish from the deviatoric stress components s_{ij} in the constitutive model here, σ_{ij} are designated as the components of the Cauchy stress tensor.

The yield function is assumed to be a compressible Drucker-Prager type, similar to the one adopted in Deshpande and Fleck (2000), in the form of

$$f = \left[3J_2 + \alpha^2(I_1/3)^2\right]^{1/2} = \sigma_e \qquad (4.2)$$

where $I_1 = \sigma_{kk}$, $J_2 = s_{ij}s_{ij}/2$, and $s_{ij} = \sigma_{ij} - \sigma_{kk}\delta_{ij}/3$. The constant α determines the shape of the yield surface and will be evaluated using data from Chapter 3. As is common in such models, a non-associated flow rule is adopted for added flexibility represented by

$$g = \left[3J_2 + \beta^2(I_1/3)^2\right]^{1/2}. \qquad (4.3)$$

The constant β decides the shape of the flow potential and is determined in Section 4.2. The flow rule is then given by

$$d\varepsilon_{ij}^p = \Lambda\frac{\partial g}{\partial \sigma_{ij}}. \qquad (4.4)$$

The equivalent stress, σ_e, represents the current size of the yield surface and is given by

$$\sigma_e = \left[3J_2 + \alpha^2(I_1/3)^2\right]^{1/2}. \qquad (4.5)$$

83

The work compatible equivalent strain increment is developed as follows: The plastic strain decomposes into a hydrostatic and deviatoric part, $d\varepsilon_{ij}^p = de_{ij}^p + \frac{1}{3}d\varepsilon_{kk}^p\delta_{ij}$. Using the flow rule, the deviatoric and hydrostatic components can be expressed as

$$de_{ij}^p = \frac{\Lambda}{g}\frac{3}{2}s_{ij}, \qquad\qquad d\varepsilon_{kk}^p = \frac{\Lambda}{g}\frac{\beta^2}{3}\sigma_{kk}. \qquad\qquad (4.6)$$

Next, Eq. (4.5) squared becomes

$$\sigma_e^2 = 3J_2 + \alpha^2(I_1/3)^2 = \frac{3}{2}s_{ij}s_{ij} + \frac{\alpha^2}{9}\sigma_{kk}^2. \qquad\qquad (4.7)$$

Using Eq. (4.6) in Eq. (4.7) it becomes

$$\sigma_e^2 = \left(\frac{g}{\Lambda}\right)^2\frac{2}{3}de_{ij}^p de_{ij}^p + \left(\frac{g}{\Lambda}\right)^2\frac{\alpha^2}{\beta^4}d\varepsilon_{kk}^{p\,2}. \qquad\qquad (4.8)$$

From Eq. (4.8) Λ can be expressed as

$$\Lambda = \frac{g}{\sigma_e}\left[\frac{2}{3}d\varepsilon_{ij}^p d\varepsilon_{ij}^p + \left(\frac{\alpha^2}{\beta^4} - \frac{2}{9}\right)(d\varepsilon_{kk}^p)^2\right]^{1/2}. \qquad\qquad (4.9)$$

The work compatible equivalent strain increment is evaluated from

$$\sigma_e d\varepsilon_e^p = \sigma_{ij}d\varepsilon_{ij}^p = \Lambda\sigma_{ij}\frac{\partial g}{\partial\sigma_{ij}} = \Lambda g, \qquad\qquad (4.10)$$

which yields:

$$d\varepsilon_e^p = \left(\frac{g}{\sigma_e}\right)^2\left[\frac{2}{3}d\varepsilon_{ij}^p d\varepsilon_{ij}^p + \left(\frac{\alpha^2}{\beta^4} - \frac{2}{9}\right)(d\varepsilon_{kk}^p)^2\right]^{1/2}. \qquad\qquad (4.11)$$

Eq. (4.11) can be used to convert the true stress-displacement responses from the calculations of various loading paths reported in Chapter 3 to equivalent stress-plastic strain relations for material calibration. Furthermore, $d\varepsilon_{ij}^p$ developed from Eq. (4.9) and (4.10) can be implemented in an implicit algorithm.

Back to the flow rule, Eq. (4.4) can then be expressed as

$$d\varepsilon_{ij}^{p} = d\varepsilon_{e}^{p} \frac{\sigma_e}{2g^2}[3s_{ij} + 2\beta^2\sigma_{kk}\delta_{ij}/9]. \tag{4.12}$$

Next, consider that the incremental stress-strain relationship starts with the form

$$d\sigma_{ij} = C_{ijkl}\left(d\varepsilon_{kl} - d\varepsilon_{kl}^{p}\right) = C_{ijkl}\left(d\varepsilon_{kl} - \Lambda\frac{\partial g}{\partial\sigma_{kl}}\right). \tag{4.13}$$

Eq. (4.13) is further developed using the consistency condition of the constitutive equations

$$\dot{f} = 0. \tag{4.14}$$

Combine Eq. (4.14) and (4.2), the consistency equation can be expanded as

$$\frac{\partial f}{\partial\sigma_{ij}}\dot{\sigma}_{ij} - \frac{\partial\sigma_e}{\partial\varepsilon_e^{p}}\dot{\varepsilon}_e^{p} = 0. \tag{4.15}$$

where f is in the form of $\left[3J_2 + \alpha^2(I_1/3)^2\right]^{1/2}$ from Eq. (4.2) and $\partial\sigma_e/\partial\varepsilon_e^{p}$ is obtained from the equivalent stress-plastic strain relation of the material. From Eq. (4.11) $\dot{\varepsilon}_e^{p}$ can be replaced by $g\Lambda/\sigma_e$, and thus the equation can be rewritten as

$$\frac{\partial f}{\partial\sigma_{ij}}\dot{\sigma}_{ij} - \frac{\partial\sigma_e}{\partial\varepsilon_e^{p}}\frac{g}{\sigma_e}\Lambda = 0. \tag{4.16}$$

Λ is obtained by putting Eq. (4.13) in (4.16)

$$\Lambda = \frac{\partial f}{\partial\sigma_{mn}}C_{mnkl}\dot{\varepsilon}_{kl} \Bigg/ \left[\frac{\partial f}{\partial\sigma_{rs}}C_{rsuv}\frac{\partial g}{\partial\sigma_{uv}} + \frac{\partial\sigma_e}{\partial\varepsilon_e^{p}}\frac{g}{\sigma_e}\right]. \tag{4.17}$$

From Eq. (4.13) to (4.17), finally the incremental stress-strain relationship can be written as

$$d\sigma_{ij} = \left\{C_{ijkl} - C_{ijpq}\frac{\partial g}{\partial\sigma_{pq}}\frac{\partial f}{\partial\sigma_{mn}}C_{mnkl} \Bigg/ \left[\frac{\partial f}{\partial\sigma_{rs}}C_{rsuv}\frac{\partial g}{\partial\sigma_{uv}} + \frac{\partial\sigma_e}{\partial\varepsilon_e^{p}}\frac{g}{\sigma_e}\right]\right\}d\varepsilon_{kl} \tag{4.18}$$

4.2 MODEL CALIBRATION

4.2.1 Parameters for the Constitutive Model

The constitutive model is implemented in the "crushable foam isotropic hardening model" in ABAQUS (see Users Manual 2014), which is calibrated using directly the stress-"average strain" responses of the 18 sets of triaxial crushing simulations reported in Chapter 3. The elastic modulus and Poisson's ratio of the material is assigned approximately the average values measured in the family of crushing responses: $\{E, \nu\} = \{63.27\,\text{ksi-}436\,\text{MPa}, 0.36\}$. More specifically, ν is assigned the average of the fitted values of the three families shown in Table 3.3, and E is assigned a value close to the fitted value of the set $\delta(n, 1, 1)^T$.

The yield surface is established using the stress and strain values at plastic work of $W^p = 0.09$ psi (0.62 kPa) of all the 18 sets of crushing calculations. The plastic work is calculated in the same way as the energy absorbed $\mathcal{E}$ in Section 3.2.4, but with the elastic part subtracted. A least squares fit algorithm was then used to determine an optimal value of 0.78 for the parameter α. Figure 4.1 shows the resultant yield surface in the normalized distortional-mean stress plane (σ_o is the yield stress in the uniaxial compression test). Included with different symbols for each set are the data from the simulations. It is noted that the upper left data point in the family of uniaxial compression is from the simulation using the setup described in Gaitanaros et al. (2012), while the lower right uniaxial value is from the simulation in which the displacement in the *y*- and *z*-directions are restrained.

In the way of motivating the non-associative flow rule adopted, the local normal $\left(\dfrac{3\partial f}{\partial I_1}, \dfrac{1}{\sqrt{3}} \dfrac{\partial f}{\partial J_2^{1/2}} \right)$ at three locations on the yield surface as well as the flow direction established from the responses, $\left(\dfrac{3\partial g}{\partial I_1}, \dfrac{1}{\sqrt{3}} \dfrac{\partial g}{\partial J_2^{1/2}} \right)$, are displayed by red and green color arrows respectively. The calculation of the two directions using the stress and strain values

86

from the simulations is presented in Appendix B. Clearly, the two sets of directions are different.

In ABAQUS' version of this model, the plastic potential parameter β is tied to a "plastic" Poisson's ratio. This connection is not possible for the present material because of the inhomogeneous nature of the deformations. Instead, β is set at 1.5 chosen as it produces the best overall predictions of stress plateau levels in the simulations of the crushing responses using the continuum model.

4.2.2 Material Stress-Strain Relation for True Triaxial Crushing

The "crushable foam isotropic hardening model" in ABAQUS is calibrated to a hardening uniaxial compressive foam response. All foam crushing responses in Chapter 3 developed stress maxima followed by localized deformation, which gradually spread through the domain tracing stress plateaus of different extents. Aiming to reproduce this inhomogeneous deformation at the continuum level, a softening branch is introduced to the material response. Figure 4.2 plots the equivalent stress-strain, $\sigma_e - \varepsilon_e^p$, response evaluated for $\delta(1,1,1)^T$ loading and $\beta = 1.5$. Here $\varepsilon_e^p = \int_t \dot{\varepsilon}_e^p \, dt$ where $\dot{\varepsilon}_e^p \equiv d\varepsilon_e^p$ is based on the average logarithmic plastic strain increments of the crushing simulations using Eq. (4.6). Included with a dashed line is the material response adopted. It consists of three branches: (i) a linear softening branch for $\varepsilon_e^p \leq 0.75$ with $E_t^p = -200 \, \text{psi}$ (1.38 MPa); (ii) a branch that follows the "measured" hardening part of the response for $\varepsilon_e^p \geq 0.82$; and (iii) a branch that connects (i) and (ii). This equivalent stress-strain relation will be implemented in the homogenized foam model for true triaxial crushing tests in Chapter 5. More details on the choices made follow.

a.   The whole set of $\sigma_e - \varepsilon_e^p$ responses evaluated in the same fashion from the crushing responses of the $\delta(n,1,1)^T$ family is plotted in Fig. 4.3. The six responses coalesce nicely over the stress plateaus up to a strain of about 0.8. However, they

exhibit different hardening for higher strains. The behavior repeats in the other two families $\delta(n,0.5,1)^T$ and $\delta(n,0,1)^T$ as shown in Fig 4.4a and b, respectively. This of course is a significant weakness caused by the simplicity of the assumed constitutive model. Dependence of hardening on equivalent strain has also been reported in Deshpande and Fleck (2000) and Shafiq et al. (2015), who adopted associated plasticity models based on yield functions similar to Eq. (4.2). Chen et al. (2000) and Zhu et al. (2019) reported a dependence of the yield surface shape on strain.

b.   The stress level of the softening branch is chosen such that the equal area Maxwell construction, $\sigma^* = 295.14$ psi (2.04 MPa), drawn with a fine dashed line in Fig. 4.2, coincides with the stress plateau. The softening slope and its extent are selected for optimal performance. The effect of the choice of E_t^p on the results will be examined in the parametric study in Chapter 5.

Interestingly, the equivalent stresses-change in volume responses, $\sigma_e - \delta v / v_o$, exhibit a uniform hardening trend at larger volume changes. Figure 4.5 shows one example of the six responses from the $\delta(n,1,1)^T$ family. The six responses are banded together all the way up to $\delta v / v_o = 0.75$. This behavior may prove to be useful in any future extensions of the present constitutive model.

4.2.3 Material Stress-Strain Relation for Conventional Triaxial Crushing

Chapter 6 uses this constitutive model to simulate a set of conventional triaxial tests performed on the random foam in the continuum setting. In these tests the foam is loaded under external pressure and then compressed in one direction under displacement control. The equivalent stress-strain relationship used is similar to the one in Section 4.2.2 except that the softening branch has been lowered as described below.

Figure 4.6 shows the equivalent stress-strain $(\sigma_e - \varepsilon_e^p)$ response derived from the results of the equi-triaxial crushing numerical test in Chapter 3. Included is the equivalent stress-strain relation of a representative response from the triaxial set of tests in which the pressure is 100 psi (0.69 MPa). Shown with a dashed line is the material response adopted in the calculations of Chapter 6. The initial yield stress is 288.4 psi (1.99 MPa). The response has a short ascending branch to 339.2 psi (2.34 MPa) at $\varepsilon_e^p = 0.01$. Here it connects to a linear softening branch with plastic modulus of $E_t^p = -200$ psi (-1.38 MPa) that extends to $\varepsilon_e^p = 0.64$. For strains larger than 0.77 the assumed response follows the hardening part of the equi-triaxial test. The response is completed by adding a hardening section between $0.64 \leq \varepsilon_e^p \leq 0.77$ to connect the softening and hardening branches as shown in Fig. 4.6. With these parameters the assumed response is similar to that in Fig. 4.2 but the negative branch has been lowered somewhat for the Maxwell level to be in better agreement with the stress plateau of the conventional triaxial response.
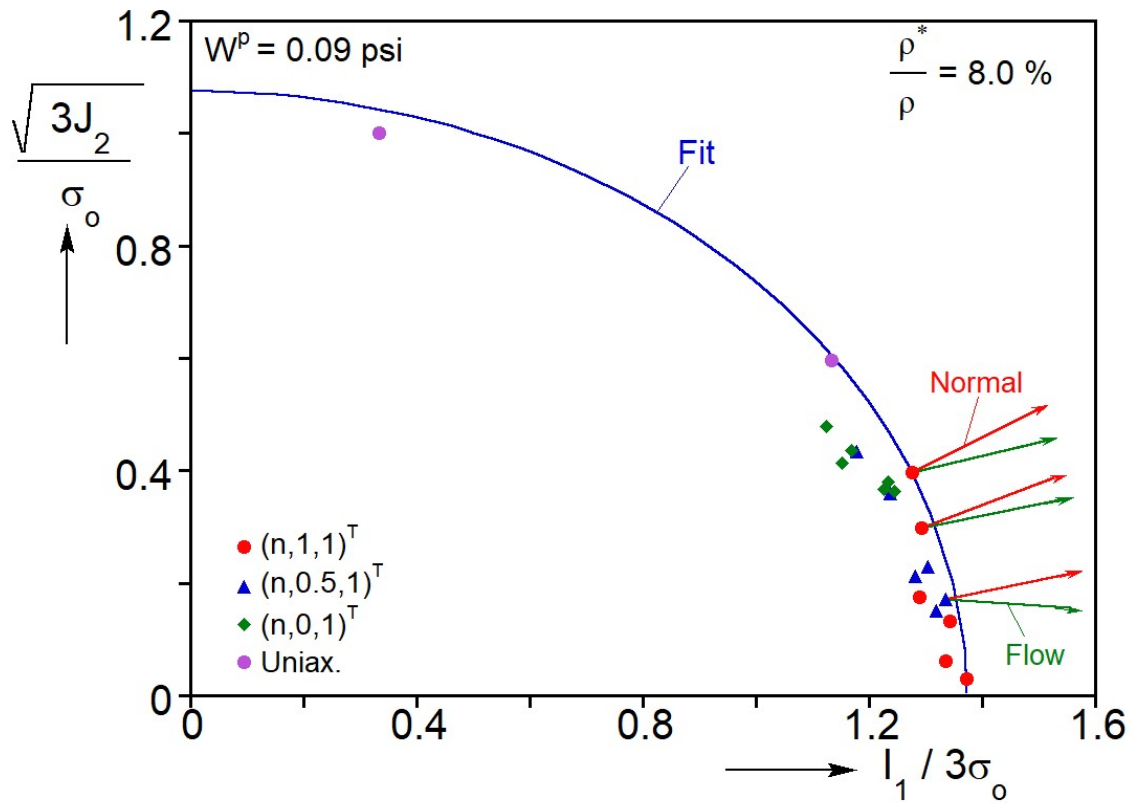
Fig. 4.1: Initial yield surface in the $\sqrt{3J_2}/\sigma_o - I_1/3\sigma_o$ plane calibrated using the results from the three loading families analyzed in Chapter 3. Included are the local normals and the flow directions for three responses; their difference supports the adoption of a non-associative flow rule.
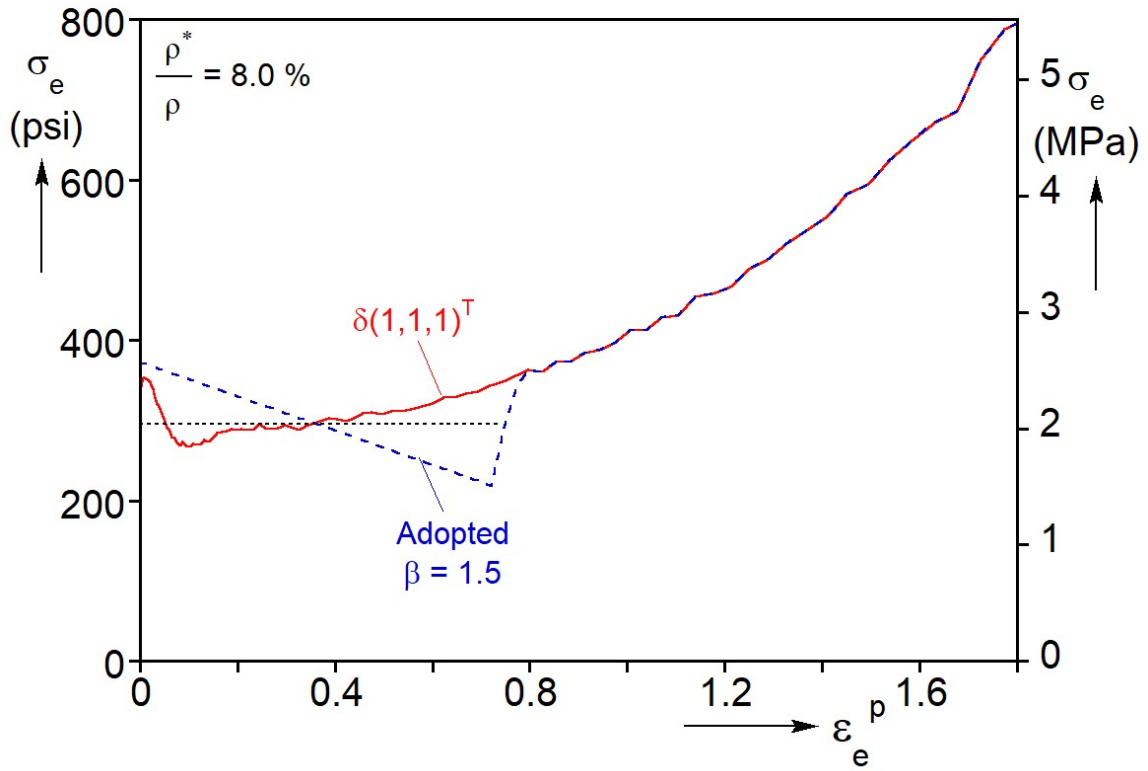
Fig. 4.2:   Random foam equivalent stress-strain response from the $(1,1,1)^T$ loading path and the partially unstable stress-strain response adopted for the homogenized material in Section 4.2.2.
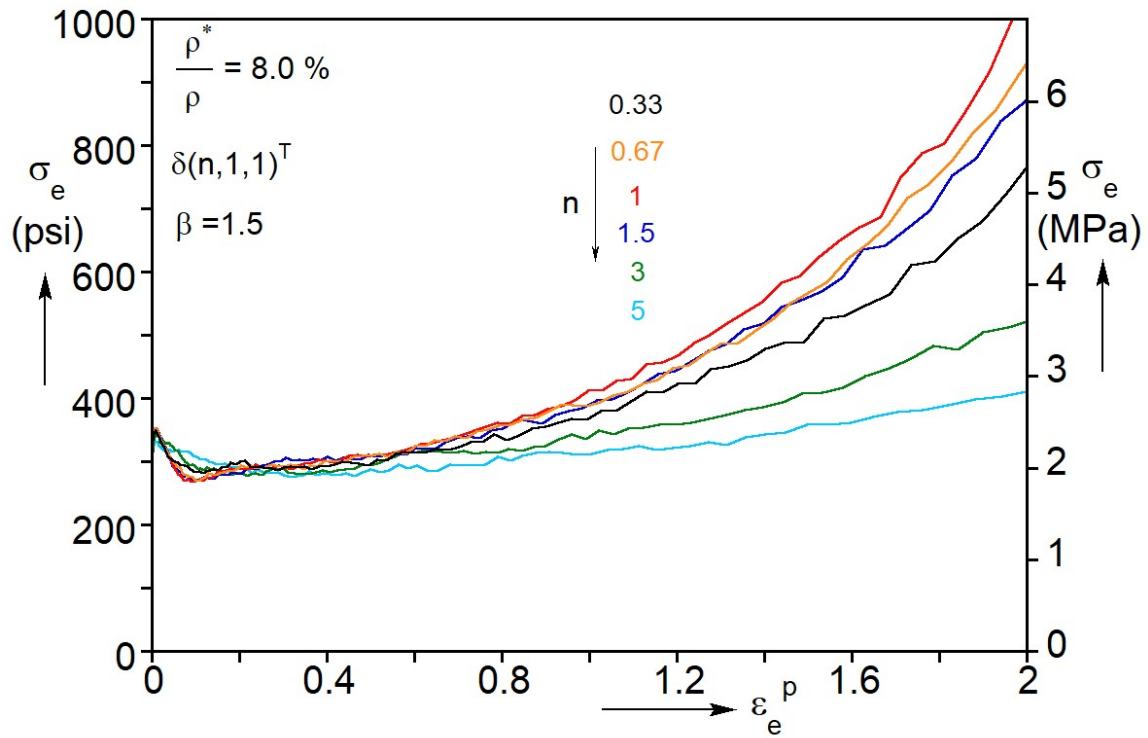
Fig. 4.3: Measured equivalent stress-strain responses for the $(n,1,1)^T$ family of loading paths for the random foam model.
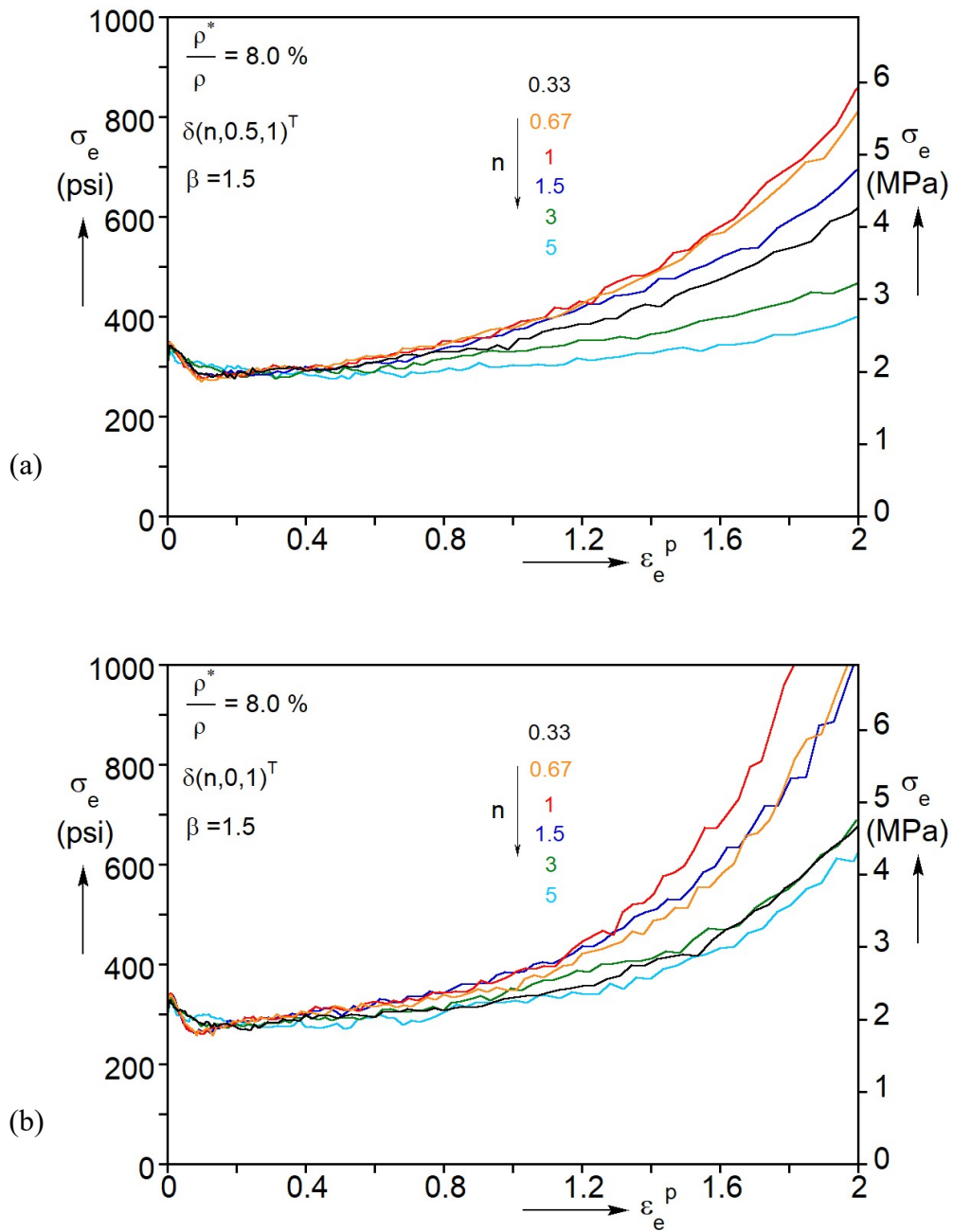
Fig. 4.4: Measured equivalent stress-strain responses for (a) the $(n,0.5,1)^T$, and (b) $(n,0,1)^T$ family of loading paths for the random foam model.
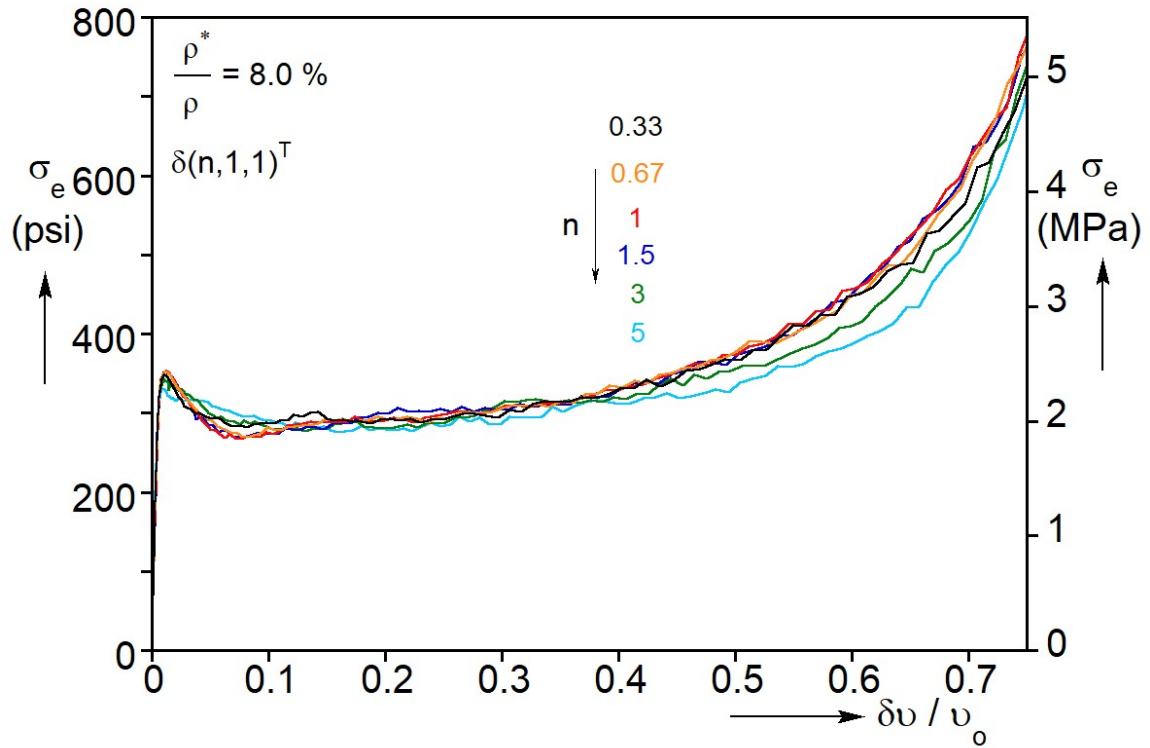
Fig. 4.5: Measured equivalent stress-change in volume responses for the $(n,1,1)^T$ family of loading paths for the random foam model.
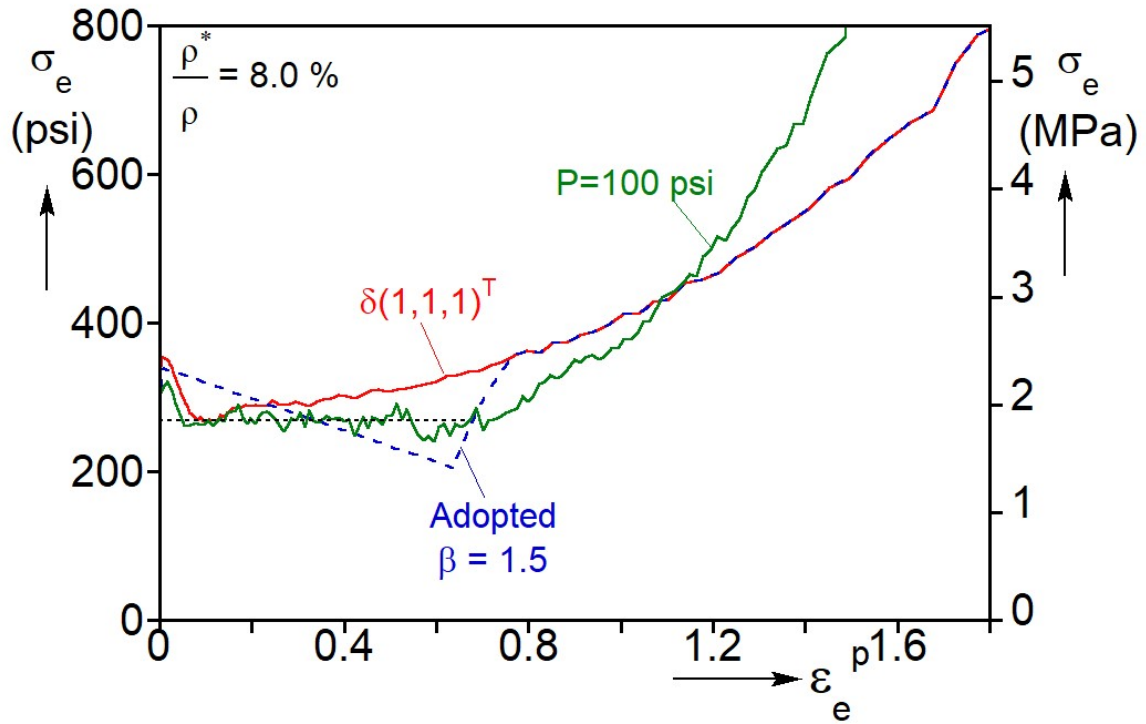
Fig. 4.6:   Random foam equivalent stress-strain response for the equi-triaxial test $(1,1,1)^T$, and partially unstable response adopted in Section 4.2.3. Included for comparison is the corresponding response from the $P = 100$ psi (0.69 MPa) triaxial test.

Chapter 5: True Triaxial Crushing of Homogenized Foam Models[6]

      In an effort to add to the understanding of crushing behavior of foams under multiaxial loads, Chapter 3 investigated the crushing behavior of an Al-alloy open-cell foam with relative density of 0.08 under true triaxial loadings. A micromechanically accurate foam model was crushed in three directions under displacement control for three sets of radial loading paths. For all loading paths, the crushing propagates in an inhomogeneous manner. A band of locally collapsed cells was developed at the boundaries in each direction and subsequently propagated to the rest of the domain until the whole domain is crushed. Clearly, a homogenized "alternative" of such foams must address this partially inhomogeneous crushing behavior under triaxial loads.

      Motivated by these results, Chapter 4 presented a compressible constitutive model that captures this inhomogeneous behavior. In this Chapter the constitutive model is incorporated in a solid finite element model that aims to reproduce the triaxial foam crushing at the continuum level. Section 5.1 describes the setup for the crushing simulations in the continuum setting. Sections 5.2-5.4 simulate the radial displacement triaxial crushing of Chapter 3 using the homogenized model. Section 5.5 describes results from parametric studies on the performance of the homogenized model. A significant part of the study in Chapter 4 and 5 appears in Yang and Kyriakides (2019b).

5.1 FINITE ELEMENT MODEL

5.1.1 Geometry and Mesh

      A cubical domain with size H as shown in Fig. 5.1 is used for all the crushing simulations of the homogenized foam model. It is discretized with 8-node incompatible linear brick elements (C3D8I) that allow the development of internal strain gradients. This type of element has been found to be effective in the modeling of solids exhibiting inhomogeneous deformations (e.g., Hallai and Kyriakides, 2013; Jiang et al. 2017a,

---

). To avoid biasing the anticipated localization and its evolution, the domain is discretized with the irregular mesh shown in Fig. 5.1. The mesh is generated by seeding each of the 12 edges with 25 elements and one diagonal of each face with 24. This results in a domain with a total number of 36,288 irregular brick elements.

To help initiate the instability, geometric imperfections in the form of three small depressions are introduced to the three moving faces of the cubical domain with normals in the positive (x,y,z) directions. Each depression is in the form of one half sine that covers the width of the moving plane. It starts at $0.05H$ and ends at $0.2H$ measured the adjacent stationary plane. Thus for example on the plane $x = H$ the sine imperfection of amplitude a, extends over $z = (0.05 - 0.2)H$ as shown in Fig. 5.1b.

5.1.2 Boundary and Loading Conditions

The cubical random foam microstructures in Chapter 3 were crushed by prescribing the displacements of orthogonal rigid planes surrounding the foam that formed a "true triaxial" test arrangement. To simulate the radial displacement crushing paths performed, $(\delta_x, \delta_y, \delta_z)^T$, the solid domain in Fig. 5.1a is compressed as follows:

- The normal displacements of the nodes on the faces $x = 0$, $y = 0$ and $z = 0$ are prescribed to be zero.

- The domain is compressed by prescribing incrementally the normal displacements, $\delta_x, \delta_y, \delta_z$ of all nodes on the faces $x = H$, $y = H$, and $z = H$. Figure 5.1b shows the boundary and loading conditions on the $y = H$ face.

- The same three families of radial path histories defined in Fig. 3.2: $\delta(n,1,1)^T$, $\delta(n,0.5,1)^T$ and $\delta(n,0,1)^T$ will be simulated using the homogenized model also.

The domain is compressed in ABAQUS/Explicit. To keep the simulation quasi-static, the loading history follows the scheme described in Section 3.1.2. The increment is slow enough to ensure that the kinetic energy is much smaller than the internal energy. The

average stress acting in each direction is evaluated by dividing the sum of the reaction forces acting on each stationary face by the current area of the face.

5.2 ANALYSIS OF THE SET $\delta(n,0.5,1)^T$

5.2.1 Triaxial Crushing: $\delta(3,0.5,1)^T$

For all loading paths studied in this Chapter, the tests were simulated numerically using the continuum constitutive model developed in Chapter 4. The crushing path $\delta(3,0.5,1)^T$ that exhibits different displacement histories in the x-, y- and z-directions, is analyzed first to describe the crushing behavior of the homogenized foam model in the three directions. The domain is loaded incrementally prescribing $\delta(t)$. Initially, the increments are relatively small in order to capture the anticipated onset of instability and localized deformation, and become larger once the stresses start tracing stress plateaus making for a total of 150 increments. Figure 5.2a plots the calculated true stress-displacement responses in the three directions together with the corresponding ones measured in the random foam. The stresses σ_i represent the sum of the reaction forces on the nodes on each of the three stationary faces divided by the current area of each face. Figure 5.3 shows a set of deformed configurations with strain contours superimposed, which illustrate the evolution of localized strain in the course of the loading history. The images correspond to the bullets marked on each stress-displacement response with different symbols and colors, and numbered in the case of the $\sigma_x - \bar{\delta}_x$ response. Figure 5.2b shows the corresponding mean stress-change in volume response, $\bar{\sigma} - \delta \upsilon / \upsilon_o$, where

$$\bar{\sigma} = (\sigma_x + \sigma_y + \sigma_z)/3,$$
$$\delta \upsilon / \upsilon_o = [1 - (1 - \bar{\delta}_x)(1 - \bar{\delta}_y)(1 - \bar{\delta}_z)], \ \bar{\delta}_i = \delta_i / H. \tag{5.1}$$

The three responses based on the homogenized model exhibit the same general characteristics as those of the random foam and, by-and-large, reproduce their trends. They start with stiff linearly elastic branches that terminate in local stress maxima and represent

98

the onset of localized deformation. The stresses then drop down to local minima, recover, and start tracing stress plateaus of different extents. In the process, deformation localizes in planar bands with strain levels of order 1.0, which gradually spread until the whole domain is so deformed. The domain then reverts back to homogeneous deformation that characterizes the behavior of densified material. The x-direction response traces a very similar path to that of the random foam. In the z- and y-directions the solid is compressed at rates that are respectively one-third and one-sixth that of the x-direction. These two responses follow those of the random foam in the first half of the crushing history, but the stresses tend to pick up at a lower rate in the latter parts of crushing.

The mean stress change in volume response in Fig. 5.2b follows quite closely the corresponding one from the random foam up to a volume reduction of about 50% and underestimates it somewhat at higher values of $\delta \upsilon / \upsilon_o$.

For better visualization of the early parts of the three responses, they are also shown expanded in Fig. 5.4a, and Fig. 5.4b shows the $\overline{\sigma} - \delta \upsilon / \upsilon_o$ response up to a volume change of 0.15. A set of corresponding deformed configurations is included in Fig. 5.5. The initial stiff branches follow the expected linear elastic, isotropic behavior. Each terminates into a local load maximum, which occur at very similar strain levels and consequently at different times in the loading history. Following each load maximum, a planar band of localized deformation initiates in the plane normal to the associated loading direction. Thus, σ_x reaches a maximum of 458 psi (3.16MPa) first and descends to a local minimum.

Image $\boxed{1}$ just after the stress minimum, shows a higher deformation band to have initiated from the depression on the plane $y = H$ that extends over the whole $y - z$ plane. It is worth noting that at this time σ_z is slightly below its local maximum value of 444 psi (3.06 MPa), and σ_y is even further below its own maximum value of 446 psi (3.07 MPa). In image $\boxed{2}$, the band has broadened and σ_x has completed the initial transient and started traversing a relatively flat plateau. σ_z is on its descending branch but σ_y remains still

99

below its local maximum. By stations $\boxed{3}$, σ_z is close to its local stress minimum and a second planar band of higher deformation has initiated in the $x-y$ plane from the imperfection on the $x = H$ plane. At this time σ_y has attained its local maximum level, σ_x is further along its plateau level, and the original band normal to the x-direction has broadened more. At stations $\boxed{4}$, σ_y is tracing its descending branch, σ_z is tracing its own stress plateau, σ_x is further along on its own plateau reaching a normalized displacement of 0.033, and both planar bands of higher deformation have broadened. By stations $\boxed{5}$, σ_y has gone past its local minimum and a third planar band of high strain has been initiated in the $x-z$ plane from the imperfection on the $z = H$ plane. Meanwhile the stresses along the other two directions have continued to traverse their individual stress plateaus. By stations $\boxed{6}$, the prescribed displacements are $\{\bar{\delta}_x, \bar{\delta}_y, \bar{\delta}_z\} = \{0.087, 0.0145, 0.029\}$ and all three stresses are traversing their respective plateaus.

Between displacements $\delta_i \in (0.01, 0.05)H$ the three stresses trace relatively flat plateaus with average values of $\{\sigma_x, \sigma_y, \sigma_z\} = \{369, 360, 370\}$ psi $\{2.55, 2.48, 2.55\}$ MPa. It is worth pointing out that if we consider parts of these plateaus where all three coexist the stresses change slightly to $\{\sigma_x, \sigma_y, \sigma_z\} = \{377, 366, 370\}$ psi $\{2.60, 2.52, 2.55\}$ MPa. These values correspond to an equivalent stress of 291 psi (2.01 MPa), which compares with the 295 psi (2.04 MPa) level of the equal area Maxwell stress of the adopted equivalent stress-strain response in Fig. 4.2.

The mean stress-change in volume response in Fig. 5.4b is in the main very similar to that of the random foam. A small difference around the first local maximum is observed caused by the somewhat different mechanism of initiation of instabilities in the homogenized material.

Observations:

-       The imperfections provide a local small riser over the stress state of the block causing the local stress to reach the level of the peak in the equivalent stress-strain response in Fig. 4.2. When this happens localized deformation nucleates. The nucleation results in an initial drop in the overall stress, which however recovers sometime later. The local increase in stress occurs when the displacement in each direction reaches a critical value, and this is responsible for the delay between the three nucleation events.

-       The levels of the three stress maxima in Fig. 5.4a are mainly governed by the stress peak in the up-down-up response constructed over the unstable branch in Fig. 4.2 and to a smaller degree by the amplitude of the imperfections.

-       The stress maximum in each direction occurs at very similar displacement levels of about $\delta_i \approx 0.0033H$. Thus each occurs at different time in the loading history.

-       The homogenized material lacks any of the microstructural characteristics of the random foam. Furthermore, it is crushed by prescribing nodal displacements on the three moving faces rather than by contact with rigid plates. Consequently, in the homogenized material localized deformation initiates from the geometric imperfections and develops into internal planes rather than at the contacting surfaces as in the random foams. The geometric imperfection provides enough of a local stress riser to progressively trigger each of the planar bands. This role of the imperfections will be the same for all loading paths considered.

-       Following the initial transients each response traces a stress plateau of similar level. More difference is observed between the three plateaus of the random foam primarily because of differences in the early evolution of localization in each direction. However, generally the two sets of plateaus have comparable levels.

For the subsequent evolution of the crushing behavior we return to Figs. 5.2 and 5.3. To help connect the two sets of results, stations and image ① correspond to stations and image ⑥ in Fig. 5.4 and Fig. 5.5. By station ② all three planar bands have broadened, with the one normal to the x-direction widening the most and the three stresses remaining relatively unchanged. The same goes for the station and image ③ except that the

broadening of the band normal to the *x*-direction starts to become the dominant mode of deformation. In image ④ the main band has consumed about one-third of the domain, while the broadening of the band normal to the *z*-direction is much more limited and that of the third band is relatively small. At this time σ_x remains relatively unchanged while σ_z and σ_y have started on an increasing trend presumably because of the much larger decrease in the cross sectional areas sustained in these two directions. In image ⑤ more than half of the domain has developed the higher strain mainly from the broadening of the $y-z$ planar band, and some increase in the broadening of the other two bands. Concurrently, σ_x remains essentially unchanged while the other two stresses continue their increasing trends. By image ⑥ most of the domain is in the higher strain with one main island of relatively undeformed material remaining on the side of the $x = H$ plane. Now all three stresses are on an increasing trend. While most of the deformed material is at a strain of about 1.0, part of the $x-y$ planar band is deformed to a higher level, and the same trend has started in the $x-z$ band. It appears that this higher strain may be required for compatibility of deformation in these two directions with the island of relatively undeformed material that remains. By image ⑦ the island of undeformed material is much smaller while the stresses in all the three directions have continued to increase. The higher deformation in the two bands that started in the previous station has broadened. In image ⑧ at an $\bar{\delta}_x \approx 0.6$ and a volume reduction of nearly 70%, but for the two narrow zones which underwent higher strain earlier, the block is essentially back to homogeneous deformation. The stress levels are $\{\sigma_x, \sigma_y, \sigma_z\} =$ {718, 429, 536} psi {4.95, 2.96, 3.70} MPa. Both sets of results are truncated at $\delta_x = 0.647H$ when $\sigma_x = 1000$ psi (6.90 MPa) for the random foam.

In summary, the three crushing responses of the homogenized material exhibit the same characteristics as those of the random foam and track them quite accurately. The mean stress-change in volume response reproduces reasonably well also that of the random material. The random foam was crushed between rigid planes, which caused crushing to initiate from the boundaries and move inwards. By contrast, the homogenized model is

crushed by prescribing the nodal displacements on the three moving faces. This resulted in a more uniform stress state requiring that localization be nucleated from geometric imperfections introduced in the domain. Since the homogenized foam lacks any other microstructural characteristics, the imperfections tend to govern the evolution of localized deformation. The thickness imperfections adopted progressively initiated a planar band of higher deformation normal to each loading direction. The one normal to the most compressed direction tended to propagate from one end to the other limiting the broadening of the other two bands.

5.2.2 Set of Triaxial Crushing Results for: $\delta(n, 0.5, 1)^T$

The responses in the x-, y-, and z-directions for the crushing simulations of the whole family of loading paths $\delta(n, 0.5, 1)^T$ are shown in Fig. 5.6, with n taking values, $n \in \{0.33, 0.67, 1.0, 1.5, 3.0, 5.0\}$. The corresponding random foam responses from Chapter 3 are included in each plot for comparison. The three pairs of responses are truncated at the same displacements. Figure 5.7 plots the mean stress against the change in volume for the six cases, which correspond to the random foam results in Fig. 3.25. Generally, the stress- displacement responses of the homogeneous models follow the trends of the random ones. They exhibit initial elastic branches that terminate in local stress maxima followed by extended stress plateaus, and stiffening branches in the densified material regime. The stable elastic branches are essentially identical to the measured ones. Load maxima develop progressively in each direction with the primary loading direction occurring first, the secondary second, and the least compressed direction third. Accordingly, for $\delta(5, 0.5, 1)^T$ the order of the maxima is $\{x, z, y\}$ while for $\delta(0.33, 0.5, 1)$ is $\{z, y, x\}$. As was observed for the base case, the maxima occur when the respective displacements reach $\delta_i \approx 0.0034H$ as a consequence of the stress in the respective imperfection reaching the level required to initiate localization. Deformation localizes first in the plane that is normal to the prevalent compression direction. This is followed by localization in the secondary

compression direction with the third direction coming last. Thus, for $n=0.33$ the first localization is in the $x-y$ plane, the second in the $x-z$ plane and the one in the $y-z$ plane initiating last. By contrast, for $n=5.0$ the $y-z$ plane localizes first and the $x-y$ plane last. For $n=1.0$ the maxima in σ_x and σ_z occurred simultaneously at respective strains of 0.00262 presumably because of the higher stress state induced to the two imperfections by the equi-biaxial compression.

Following each localization event, the corresponding stress drops down to a local minimum, recovers, and starts to trace a plateau. Figure 5.8 shows the early parts of the stress responses in each direction ($0<\delta_x<0.07$, $0<\delta_y<0.05$, $0<\delta_z<0.07$) from the homogenized foam model. Included are the corresponding results from the random foam model. The descending slopes are steeper than the corresponding ones from the random foam model. The plateaus corresponding to each n are at very similar levels and this holds for all three directions until the points when the stresses gradually pick up as crushing continues. More specifically, σ_x stays around 371 psi (2.56 MPa) until $\delta_x=0.07$ for all cases except for n =0.33 which has a value is 361 psi (2.49 MPa). The σ_z plateaus are at about 374 psi (2.58 MPa), with the value of $n=5.0$ somewhat higher at 393 psi (2.71 MPa). The σ_y plateaus vary somewhat more from each other with an average of around 359 psi (2.48 MPa). Collectively these stress levels correspond to an equivalent stress that is close to the equal area Maxwell stress of 295 psi (2.04 MPa) in Fig. 4.2. Generally plateaus levels are in good agreement with those of the random foam. As each plateau is traced the corresponding planar band broadens, however for different values of n the broadening differs in each direction and so does the extent of the stress plateaus.

Deformed configurations at a volume change of 50% for the six cases analyzed are shown in Fig. 5.9. For $n=0.33$ the broadening of the $x-y$ band is seen to have dominated, with that in the other two directions being rather limited. For $n=1.0$ the propagation along the x- and z-directions is balanced and dominant while along the y-direction is limited. For $n=5$ deformation propagates mainly along the x-direction with the other two bands

experiencing limited broadening. For the *n*-values in between, the trend is along similar lines. During the propagation the strain levels in the deformed material are of the order of 1.0 while the relatively undeformed material remains elastic at the strain corresponding to the current stress levels. Beyond the stress plateaus the stresses in Fig. 5.6 predicted using the homogeneous model exhibit the saturation type of behavior associated foam densification. The responses follow the trends of those of the random foams but underestimate them at higher strains.

The mean stress-change in volume responses in Fig. 5.7 are also in good agreement with those of the random foam in Fig. 3.25, but underestimate them at volume strains higher 50%. The energy absorbed per unit undeformed volume, $\mathcal{E}$, at different levels of $\delta\upsilon/\upsilon_o$ based on the homogenized model is compared to that measured for the random model in Fig. 5.10 for the six values of *n*. In concert with the random foam, the energy does not vary with *n*. Furthermore, the present predictions compare very well with results of the random foam results up to $\delta\upsilon/\upsilon_o$ of 0.5. For higher values the present model yields progressively lower values, which is a reflection of the lower stress levels predicted at higher displacements.

5.3 ANALYSIS OF THE SET $\delta(n,1,1)^T$

In this section, similar crushing calculations of homogenized foam models are presented for the second set of radial triaxial paths analyzed in Chapter 3 $\delta(n,1,1)^T$, where *n* takes the values $n \in \{0.33, 0.67, 1.0, 1.5, 3.0, 5.0\}$. The domain analyzed is the same and is meshed in the same manner. The symmetry imposed by having the crushing in the *y*- and *z*-directions equal made initiation of the instability somewhat more difficult so the domain is now perturbed with imperfections with amplitude of $0.015H$.

Initiation of localization was found to be particularly difficult for the simulation of the equi-triaxial crushing case of $\delta(1,1,1)^T$, and thus the performance of the homogenized model in this loading path is examined in some detail. Because of the symmetry imposed

by this loading, the domain tends to deform homogeneously tracing the negative branch of the equivalent stress-strain response adopted. The symmetry was broken by adopting a slightly larger rate of crushing in the x-direction by using $\delta(1.05,1,1)^T$. Furthermore, for this loading two linear orthogonal imperfections were used on each of the moving surfaces with amplitude of $0.02H$ as shown in Fig. 5.11.

Figure 5.12 plots the calculated three sets of true stress-displacement responses of the path $\delta(1.05,1,1)^T$ from the homogenized model, together with the true stress responses of the path $\delta(1,1,1)^T$ from the random foam model. Figure 5.13 shows a selected number of deformed configurations corresponding to the bullets marked on the $\sigma_x - \bar{\delta}_x$ response (marked at the same time step in the other two directions with different color symbols). The responses in the x-, y- and z-directions again exhibit a decently good agreement between the homogenized model and the random foam. They have identical linear elastic branches, which are terminated by local stress maxima. The three stress maxima in the homogenized setting, $\{\sigma_x,\sigma_y,\sigma_z\}$, are {467, 462, 462} psi {3.22, 3.19, 3.19} MPa, and occur the displacements $\{\bar{\delta}_x,\bar{\delta}_y,\bar{\delta}_z\} = $ {0.0025, 0.0023, 0.0023}. These values are slightly higher than the corresponding levels of 450 psi (3.10 MPa) of the random foam (Section 3.2.1). The stresses then drop to local minima, recover, and enter extended plateaus of very similar stress levels and extents. At larger displacements, the stresses pick up again but exhibit a lower trend than the random foam. In the plateau region the $\sigma_x - \bar{\delta}_x$ response is close to the other two responses, but become increasingly "faster" at larger displacement due to the larger rate of crushing $\dot{\delta}_x(t)$ (note the increasing difference between the displacements of the configurations).

In image ① the stresses just recover from the local minima and start to trace extended plateaus. Three planar bands of higher strain have been initiated from the imperfections on the moving surfaces. Displacement δ_x, is very close to δ_y and δ_z,

shown by the overlaps of the three bullets in Fig. 5.12 at this station. The three planar bands broaden at the same rate in the process. By station ③ at $\bar{\delta}_x = 0.125$, which is 5% larger than $\bar{\delta}_y$ and $\bar{\delta}_z$, the stresses are at the levels of the random foam. The three bands have broadened and the fronts propagate towards the corner at $\{x = H, y = H, z = H\}$. The bullet on the $\sigma_x - \bar{\delta}_x$ response is ahead of the other rest, with the three stress levels very close. In image ④, the bands of higher strain have consumed regions between the imperfections and the stationary planes, leaving behind a nearly pyramidal island of undeformed material. Now, the bands propagate nearly symmetrically towards the moving planes, progressively reducing the size of the island. At this station, the deformation has increased in narrow planes containing the imperfections (~1.5 compared to 1.0 in the rest of the deformed material). In image ⑤ at $\bar{\delta}_x = 0.247$, the stresses gradually increase, but at a milder rate than in the random responses. By stations ⑥ and ⑦, the stresses continue to climb but at a steeper rate and the higher deformation regions broaden in the three directions. In image ⑧, $\bar{\delta}_x = 0.395$, the higher deformation has spread over most of the domain, but a small size pyramidal island remains. The block is essentially back to homogeneous deformation as it is crushed further.

We next consider the loading path $\delta(3,1,1)^T$ as a representative case of the rest five radial paths of this loading family. Here the displacement history $\delta_x(t)$ is three times faster than the displacements along the y- and z-directions. The behavior of the homogenized foam model under this crushing path has similar trends as those reported for the loading path $\delta(3,0.5,1)^T$; thus it is presented here in less detail. Figure 5.14 shows the calculated true stress-displacement responses traced in the x-, y- and z-directions. Included for comparison are the corresponding results from the random foam. Figure 5.15 shows a set of deformed configurations at the numbered time step in the loading history shown in Fig. 5.14. The three responses from the homogenized model start with the expected linear stiff

branches that terminate into local stress maxima. The three maxima occur at $\bar{\delta}_i \approx 0.0032$, and thus they show up at different times, with σ_x achieving its maximum first and the other two later. Following the load maxima, localized deformation starts to nucleate from the three imperfections in each plane, in sequence. That is the $y-z$ plane localizes first and the localization in the $x-y$ and $x-z$ plane occur together at a later time.

In image ①, at $\bar{\delta}_x \approx 0.044$, the stresses have gone past their local minima. The planar bands of higher strain have initiated from the imperfections in all three directions, with the $y-z$ planar band wider. From station ② to ④, up to $\bar{\delta}_x \approx 0.322$, σ_x remains relatively unchanged and somewhat lower than that of the random foam, while σ_y and σ_z are in a mild increasing trend, comparable to the level of the dashed responses. All three planar bands of higher strains have broadened with main band in the $y-z$ plane consuming more than half of the domain. At station ⑤, σ_x starts on a gradual increasing trend, while the other two stresses follow a stiffer trajectory. At this station and beyond, the stress levels of the homogenized model are lower to those of the random foam. Now most of the domain has been consumed by a strain of the order of 1.0, and an island of essentially undeformed material remains close to the $x = H$ plane. Once again, planar zones containing the imperfections have developed a higher strain. As crushing continues, the stresses continue to increase and the size of the island is reduced. By station ⑦ only a narrow section close to $x = H$ remains relatively undeformed. In image ⑧ at $\bar{\delta}_x \approx 0.6$ the domain is essentially homogeneous while the volume has been reduced to $0.25H^3$.

The homogenized model results of the $\delta(n,1,1)^T$ family are presented in summary form in Figs. 5.16-5.18. The stress-displacement responses in the x- and y-directions are compared to the corresponding ones from the random foam in Fig. 5.16. The main features of the responses are similar to those described for the previous set except that now the evolutions of crushing in the y- and z-directions are very similar and so are the stress-displacement responses; for this reason the z-responses are not shown. The slopes of the

elastic branches are very close to those of the random foam. The limit loads are also at generally comparable values. Localization again initiates as a planar band that is normal to the prevailing crushing direction. Thus for $n = 5.0$, 3.0 and 1.5 a $y - z$ planar band initiates first when σ_x achieves its local maximum. The localization causes a drop in this stress down to a local minimum and as the band starts to broaden it recovers and starts tracing a plateau. The y- and z-directions achieve their stress maxima some time later simultaneously resulting in the nucleation of planar bands that are normal to these directions.

For $n = 0.67$ and 0.33 σ_y and σ_z achieve their maxima first, simultaneously initiating planar bands in the $x - z$ and $x - y$ planes. These stresses follow similar drops down to local minima and then recover to stress plateaus during which the bands broaden. σ_x achieves its maximum at a later time and results in the nucleation of a third localization band. For the nearly equi-triaxial case of $n = 1.05$, the three stresses reach nearly identical maxima at the same time and initiate three planar bands simultaneously.

As the crushing progresses all responses trace plateaus that are very comparable to those of the random foam. Good agreement is also observed for the mean stress-change in volume responses up to $\delta v / v_o$ of about 50% shown in Fig. 5.18. An impression of the evolution of higher strain in each domain is provided by the deformed configurations corresponding to volume change of 50% shown in Fig. 5.17. As mentioned above, for $n = 1.05$ the three planar bands propagate nearly symmetrically towards the moving planes leaving behind a nearly pyramidal island of undeformed material. At higher crushing displacements, the size of this island is reduced but at increasingly higher stresses. It is worth mentioning that for the corresponding random foam the undeformed island was in the center of the domain because in that case crushing initiated more symmetrically at the three pairs of rigid planes in contact with the domain.

As n increases to 1.5 and then to 3.0 and 5.0, the band normal to the x-direction becomes increasingly more dominant. Thus the propagation of higher strain becomes increasingly more oriented along the x-direction leaving behind unsymmetric islands of

undeformed material that are evident in the corresponding images in Fig. 5.17. Crushing of these islands requires an increasingly higher stress leading to the upswing in the stress-displacement responses in Fig. 5.18. We consider this increase in resistance to deformation to be partially due to constraints imposed by the finite domain being analyzed.

For n of 0.67 and 0.33 the opposite trend is observed, where the evolution of higher strain is dominated by the concurrent propagation of $x-y$ and $x-z$ planar bands. For $n = 0.67$, the $y-z$ planar band is seen in the corresponding image in Fig. 5.17 to be narrower than the other two and much narrower for $n = 0.33$. This spreading of higher strain results again in the formation of unsymmetrical islands of undeformed material, which requires higher stress to deform.

Overall the 6 responses track those of the random foam quite well for most of the deformation history, but again underpredict them at higher crushing displacements. This reflects also on the $\bar{\sigma} - \delta \upsilon / \upsilon_o$ responses in Fig. 5.18, which reproduce very well the corresponding results from the random foam in Fig. 3.15 up to a volume change of about 50%, but underpredict them at higher values. The energy absorbed per unit undeformed volume, $\mathcal{E}$, at different values of the change in volume for the six cases based on the homogenized model is plotted in Fig. 5.19. In concert with those of the random foam shown in empty symbols in the figure, the energy does not vary with n. Furthermore, the present predictions compare very well with results of the random foam results up to $\delta \upsilon / \upsilon_o$ of 0.5. An underestimation is observed at higher values of volume reduction, resulting from the stresses being lower at higher displacements.

In all cases during the propagation phase of the crushing history, material deformed to strain of about 1.0 coexists with material that remains at small elastic strains that correspond to the current state of stress. The evolution of higher strain in the models differs from that of the corresponding random foam for the same reasons given earlier.

5.4 ANALYSIS OF THE SET $\delta(n,0,1)^T$

The performance of the homogenized foam model is further examined by six crushing simulations for the third set of loading paths $\delta(t)(n,0,1)^T$. In this set of loading paths the random foam was crushed along the x- and z-directions with the y-displacement kept at zero. In these radial paths n takes the values $n \in \{0.33, 0.67, 1.05, 1.5, 3.0, 5.0\}$. For better performance, the symmetry imposed by the equi-biaxial loading is broken by adding a small perturbation to δ_x as follows $\delta(1.05,0,1)^T$.

We again choose $\delta(3,0,1)^T$ as a representative case and use the results to describe the behavior of the homogenized foam model along this loading family. Figure 5.20 shows the stress responses in the x- and z-directions from the homogenized model in solid lines, and the corresponding ones of the random foam in dashed lines. Figure 5.21 plots a selected number of deformed configurations corresponding to the numbered bullets marked on the response. The homogenized model reproduces the general trends of the random foam responses very well. The stress maxima in the x- and z-directions occur at $\overline{\delta}_x$ and $\overline{\delta}_z$ of about 0.0034, which indicates that they develop at different times. Following the load maxima, the stresses drop to local minima, and simultaneously planar localization bands nucleate from the imperfections in the $y-z$ and $x-y$ planes, again at different times. The two stresses then recover, and start to trace extended plateaus. Image ① in Fig. 5.21 shows the $y-z$ band along the prevailing crushing direction has broadened to a width of 3~4 elements, while the band normal to the z-direction has a width of about 2 elements. By this station at $\overline{\delta}_x \approx 0.061$, both stresses are tracing their own plateaus: σ_x is comparable to that of the random foam; σ_z takes a higher value than the response of the random foam. From station ② to ④, both planar bands are broadening, with the $y-z$ band widening significantly more than the $x-y$ band. From $\overline{\delta}_x \approx 0.138$ to 0.338, σ_x remains relatively unchanged, slightly below the value of the random foam. The levels of σ_z are comparable

111

for both models. At station ⑤, the dominant band has consumed most of the domain, leaving mainly two islands of relatively undeformed material near the $x = H$ and $x = 0$ planes. A zone of material of higher deformation appears in the $x - y$ plane, again probably due to the compatibility issue discussed in Section 5.2.1. The stresses in the x- and z-directions are lower than those of the random foam and start to increase beyond this point. At stations ⑥ and ⑦, the front of the dominant band continues to spread to both end planes along the x-direction. The stress continues to increase in the x-direction, but σ_z experiences a small dip following station ⑦, probably due to the disturbance caused by transformation of an island of relatively undeformed material at both end planes normal to the x-direction. By station ⑧ the deformation is essentially back to homogeneous.

The calculated stress-displacement responses in the x- and z-directions for all the six cases of this loading family appear in Fig. 5.22. Figure 5.23 depicts deformed configurations corresponding to volume change of 50%. The responses follow the same trends as the results of the other two loading families discussed in this chapter. They develop initial stress maxima followed by localization into planar bands of higher strain. The bands are now limited to the $y - z$ and the $x - y$ planes and they nucleate when the stress in the relevant imperfection reaches a critical value. Planar bands of higher strain appear first normal to the primary loading direction, in the less compressed direction second. Thus for n smaller than 1.0, the first localization is in the $x - y$ plane. By contrast, for $n = 1.5$, 3.0 and 5.0, the nucleation of the band of higher strain appears in the $y - z$ first. At $n = 1.05$, the localization initiates in two planes essentially in the same time step, with $\bar{\delta}_x$ recorded 1.05 times of $\bar{\delta}_z$. As the bands broaden the two stresses trace plateaus. The extents of the two sets of plateaus follow the order of n in the x-direction, and are reversed in the z-direction. The deformed configurations at $\delta\upsilon = 0.5\upsilon_o$ clearly illustrate the coexistence of material deformed to strain of about 1.0 and essentially undeformed zones. For n of 0.33 and 0.67, the $x - y$ plane bands broaden much more than those in the $y - z$ plane. For $n = 1.5$ and above, the $y - z$ plane bands become increasingly wider. It's

112

noted that the deformations for values of n and n^{-1} mirror each other. When n is closer to 1.0, the band broadening is essentially symmetric.

The mean stress-change in volume responses in Fig. 5.24 are nicely banded together. They reproduce the corresponding results of the random foam in Fig. 3.33 up to volume change of 50% but underestimate them somewhat for higher $\delta \upsilon$ values. Overall, the mean stress levels in Fig. 5.24 are somewhat lower than the values of the other two families which repeats the behavior of the random foam.

The energy absorbed per unit undeformed volume at different levels of $\delta \upsilon / \upsilon_o$ for the six loading cases from both the homogenized and random foam models are plotted in Fig. 5.25. The same trend is observed as those of the other two families. For each loading family, the energy absorbed at a given volume change was the same for each value of n. Figure 5.26 plots $\mathcal{E}$ against $\delta \upsilon / \upsilon_o$ for three loadings from each of the three families of radial paths. Similar to the random foam results, $\mathcal{E}$ is linearly related to $\delta \upsilon / \upsilon_o$ and no significant difference is observed between the values corresponding to the nine data points at each value of $\delta \upsilon / \upsilon_o$.

5.5 PARAMETRIC STUDY

5.5.1 Mesh Sensitivity of the Solution

The softening branch introduced to the stress-strain response in Fig. 4.2, implies that the solution may exhibit some sensitivity to the mesh adopted. The irregular mesh used to produce the results presented has 25 elements per edge making for a total of 36,288 elements. The sensitivity of the solution to the mesh is examined by recalculating the response of the base case of $\delta(3, 0.5, 1)^T$ for three additional meshes listed in Table 5.1.

Table 5.1: Four meshes used for the calculation of the loading path $\delta(3,0.5,1)^T$

No. of Elements	
Edge	Total
15	9,472
20	20,000
25	36,288
30	67,500

Figure 5.27 plots the stress-displacement responses produced by the four meshes. They are nearly identical confirming mesh refinement has limited effect on the global response. Each response achieved the same stress maximum; a $y-z$ planar band of higher strain nucleated first from the imperfection at $y=H$ and started propagating towards the $x=H$ moving plane. An $x-y$ planar band nucleates next followed by an $x-z$ band as described in Section 5.2.1. Figure 5.28 shows deformed configurations at $\delta_x/H=0.217$ from the four meshes. The higher strain is seen to have evolved in each model in a similar manner. In concert with other problems in which propagating instabilities are simulated by introducing a softening branch in the material response, the main effect of mesh refinement is in the width of the transition zone that separates the two deformation regimes (e.g., Hallai and Kyriakides, 2013; Jiang et al., 2017a, 2017b). Thus, the front is seen to be approximately one element wide in all four domains.

The widths of the initial planar bands initiated in each plane are also approximately one element wide and consequently become narrower as the mesh is refined. The narrowing of the band in turn implies that it nucleates at smaller applied displacement as the mesh is refined. Figure 5.27b shows the expanded early parts of the $\sigma_x - \delta_x/H$ response of each of the four meshes considered. The local stress maximum is the same for the four cases. (The value of the maximum depends to some degree on the size of the step increment, $\Delta\delta$, used but is independent of the mesh.) The descending branch that follows the maximum is, however, influenced by the mesh, as it becomes sharper as the mesh

114

density increases, and the local minimum that corresponds to the time when the band is fully developed occurs at increasingly smaller displacement. Nevertheless, this difference in the initial part of the response does not affect the subsequent propagation of high strain in the domain.

The sensitivity of the front separating the low and high strain domains to the mesh can, of course, be alleviated by regularizing the solution by making the constitutive model rate-dependent (Needleman, 1998). To this end, a powerlaw rate-dependence is introduced to the constitutive model as follows:

$$\left(\frac{\dot{\varepsilon}^p}{\dot{\varepsilon}_o}\right)^m = \frac{\sigma}{\Sigma(\varepsilon^p)}, \tag{5.2}$$

where ($\dot{\bullet}$) represents a time derivative, $\dot{\varepsilon}_o$ is a reference strain rate, $\Sigma(\varepsilon^p)$ is the measured stress-plastic strain relationship at the reference strain rate, and m is the rate exponent. In the following study, the reference rate is chosen as 10^{-4} s^{-1}, the material stress-strain response in Fig. 4.2 is adopted as the response at this rate, and m is assigned the value of 0.01.

Crushing simulations from the $(n,0.5,1)^T$ family were repeated using the rate-dependent constitutive model. Figure 5.29 shows an expanded view of the evolution of the $y-z$ planar band from the coarsest and finest meshes for both the rate independent and rate dependent constitutive models. The domain is crushed following the loading path $\delta(3,0.5,1)^T$ and the station is at $\overline{\delta}_x \approx 0.024$. Overall the localization patterns developed in Figs. 5.29a and b are very similar. However, in the case of the rate independent model refining the mesh makes the band narrower. By contrast, the rate dependence appears in Fig. 5.29b to have locked the width of the band and that of the transition zone. In other words, the regularization has worked and added more numerical stability to the solution (see also Hallai and Kyriakides, 2011; Jiang et al., 2017a).

The parameters m and $\dot{\varepsilon}_o$ of the rate dependent model reported above were selected for optimal performance of the regularization scheme. These parameters have undesirable effect of increasing the overall responses as illustrated in Fig. 5.30. Consequently, the rate dependence constitutive model was not adopted in the homogenized model simulations.

In summary, as in other problems in the propagating instability family for which partially unstable material responses are adopted, the main effect of mesh refinement is in the width of the transition. At the same time, this does not affect the evolution of higher strain in the domain.

It is worth pointing out that the irregular mesh used in this study reduces any biasing in the anticipated localization and its evolution. Figure 5.31 compares the responses produced using regular and irregular meshes for the $\delta(3,0.5,1)^T$ loading path. Whereas the overall trend of the two sets of responses are the same, the regular mesh responses are significantly more ragged over the early parts of the stress plateaus where the unstable branch of the material response is active (see Fig. 5.31b). This is because for the regular mesh localization tends to develop in a more discrete fashion, where a complete $y-z$ plane one element wide in the x-direction localizes at a given time. The plane of higher strain generated does not interact sufficiently with its two neighboring planes to help spread the high strain further. Consequently, initiation of localization in each plane requires a higher stress causing the recorded stresses to oscillate about mean values that correspond to those of the irregular mesh. By contrast, a zone of localized deformation in an irregular mesh provides enough disturbance to neighboring elements to facilitate the propagation of high deformation at a nearly constant stress level. Moreover, it was not possible to simulate the nearly symmetric responses like $\delta(1.05,1,1)^T$ with the regular mesh. In summary, the current irregular mesh is carefully chosen to capture the inhomogeneous behavior of foams under true triaxial crushing tests.

5.5.2 Imperfection Sensitivity

In the homogenized model the instability is initiated from small depressions introduced to the three moving surfaces of the cubical domain (see Fig. 5.1). The amplitude adopted for most cases is $a = 0.01H$. In Figure 5.32, the effect of this amplitude on the response of the loading path $\delta(3,0.5,1)^T$ is investigated by considering two additional amplitudes of $0.005H$ and $0.02H$. Figure 5.32 shows that imperfection amplitude has a negligible effect on the crushing response. Furthermore, no difference in the evolution of localized bands is observed from the three domains throughout the crushing history. In some of the loading histories considered the imperfection amplitude was found to change by a small amount ($\pm$ 1-2%) the limit stress, but had no other effect on the rest of the response.

Regarding the locations of the imperfections, they determine the position of the initial planar band in each plane and influence the direction of the subsequent propagation of the bands. However, this has minimal influence on the stress-displacement responses.

5.5.3 Effect of Constitutive Model

In all calculations presented in this chapter $E_t^p = -200$ psi (-1.38 MPa) was found to result in initiation stresses and stress plateaus that are very close to those of the random foam crushing calculations. In order to assess the effect of the "strength" of softening on the solution, two additional values of E_t^p are considered, -150 and -250 psi (-1.03 and -1.72 MPa), while keeping the rest of the up-down-up response the same as shown in Fig. 5.33a. The new material responses were used to perform crushing calculations for the base loading case of $\delta(3,0.5,1)^T$ using the mesh with 25 elements per edge used in most of this chapter. Figure 5.33b plots the early parts for the calculated $\sigma_x - \delta_x / H$ responses for the three solutions. As mentioned in Section 5.2.1, the level of the stress maximum is mainly influenced by the stress peak introduced to the stress-strain response by the negative slope

117

branch adopted. Consequently, the stress maximum for $E_t^p = -250$ psi (-1.72 MPa) is slightly higher and that of -150 psi (1.03 MPa) slightly lower than that of -200 psi (1.38 MPa). Beyond the maxima the three responses trace very similar trajectories starting with the stress decaying branches. At higher displacements, the stress plateaus and the densification branches at high volume changes are very similar too. The similarity in the responses corresponding to the three values of E_t^p was repeated for the y- and z-directions. Furthermore, no significant differences were observed in the corresponding evolution of higher deformation in the domains. It must however be pointed out that when E_t^p becomes steeper than about -300 psi (-2.07 MPa) the plateau stresses start to increase. Similarly, if the negative slope is not large enough, deformation does not localize and the coexistence of highly deformed and relatively undeformed materials does not take place. This for example was observed for $E_t^p = -100$ psi (-0.69 MPa).

In the development of the constitutive model in Section 4.1, it was reported that the constant β in the flow potential in Eq. (4.3), was assigned the value of 1.5 as it produces the best overall predictions of the stress plateaus for the whole set of radial paths performed. The effect of β on the responses for loading path $\delta(3,0.5,1)^T$ is demonstrated in Fig. 5.34 where the calculations were performed for values of $\beta = \{1.2,1.5,1.8,2.1\}$. Clearly, increasing β results in a decrease in the levels of the stress responses in the three directions, including the load maxima, minima, and plateau stresses. Furthermore the pickup in stress associated with densification is delayed. Included in the three sets of responses are the corresponding results from the random foam model. The responses for $\beta = 1.5$ are seen to be the ones closer to those of the random foam.

5.6 SUMMARY

Chapter 3 uses a true triaxial apparatus to numerically crush micromechanically accurate Al-alloy foam models under three sets of radial displacement paths. For all

loadings considered, deformation localized and then spread with limited additional effort, while crushed and essentially undeformed zones of cells co-existed.

This chapter presented a first attempt at representing this partially unstable behavior through a homogenized model. Multiaxial crushing of foam was simulated numerically by incorporating the constitutive model described in Chapter 4 into a cubical finite element model. An irregular mesh of incompatible elements was used in order to minimize biasing the anticipated localization. The domain is large enough to allow the localization and propagation of higher deformation bands to develop freely. The random foam crushing tests were simulated by fixing the normal displacements on three of the cube faces, and prescribing incrementally the normal displacements on the three opposite faces. Small geometric imperfections were introduced to the three moving faces to help initiate localization.

This modeling framework was used to simulate all three sets of multiaxial crushing tests on random foams in Chapter 3. On the whole, the localization and propagation of high strain deformation is reproduced, and by-and-large so are the recorded stress-displacement responses. The homogenized model lacks any microstructural characteristics so instability must be triggered by an external disturbance. Because of the symmetry of the geometry and loading, localization is in the form of narrow planar bands normal to each loading direction. A band nucleates from a local depression imperfection when the dominant normal displacement reaches a critical value. Bands nucleate progressively in the other two directions when the stress at the corresponding imperfection reaches a critical value of the same level. The average stress in each direction reaches a local maximum at the nucleation of localization. The stress then drops down to a local minimum, recovers, and starts tracing a stress plateau as the band broadens, and this is repeated in each direction, but at different times dictated by the prescribed displacements. A front of the order of one element wide separates a domain that is deformed to a strain of about 1.0 with domains that are still elastic. The extent of propagation in each direction depends on the displacement ratios. Thus, when the prescribed displacement in one direction is much larger than the other two

–e.g., $\delta(3,0.5,1)^T$ – the "crushing" is predominant in this direction and less in the other two. By contrast, when the displacements are more balanced –e.g., $\delta(1.05,1,1)$– the three high strain bands propagate in a more symmetric manner, gradually forming a nearly pyramidal zone of essentially undeformed material.

The model foams are crushed to volume reductions of about 70%. Beyond volume changes of about 50% the true stresses begin to trace increasing trajectories that mimic those of the random foam due to densification and the reduction in cross sectional areas. The homogenized model trajectories generally under-predict those of the random foam. This is at least partly related to the inability of the constitutive model to correctly reproduce hardening at larger strains for several of the loading histories (see Section 4.2.2). Furthermore, in the present model, high deformation nucleates at geometric imperfections that are close to the stationary planes and propagate towards the moving faces. By contrast, the random foam was crushed in the true triaxial apparatus between rigid planes, so crushing initiated at the contacting surfaces and moved towards the center of the domain.

The mean stress-change in volume responses reproduce the level and banded nature of the random foam results up to a volume reduction of about 50%, and under-predict them somewhat at higher volume changes. Interestingly, in concert with the random foam the energy absorption varies nearly linearly with volume reduction and is essentially the same for all three sets of radial paths.

(a)

(b)
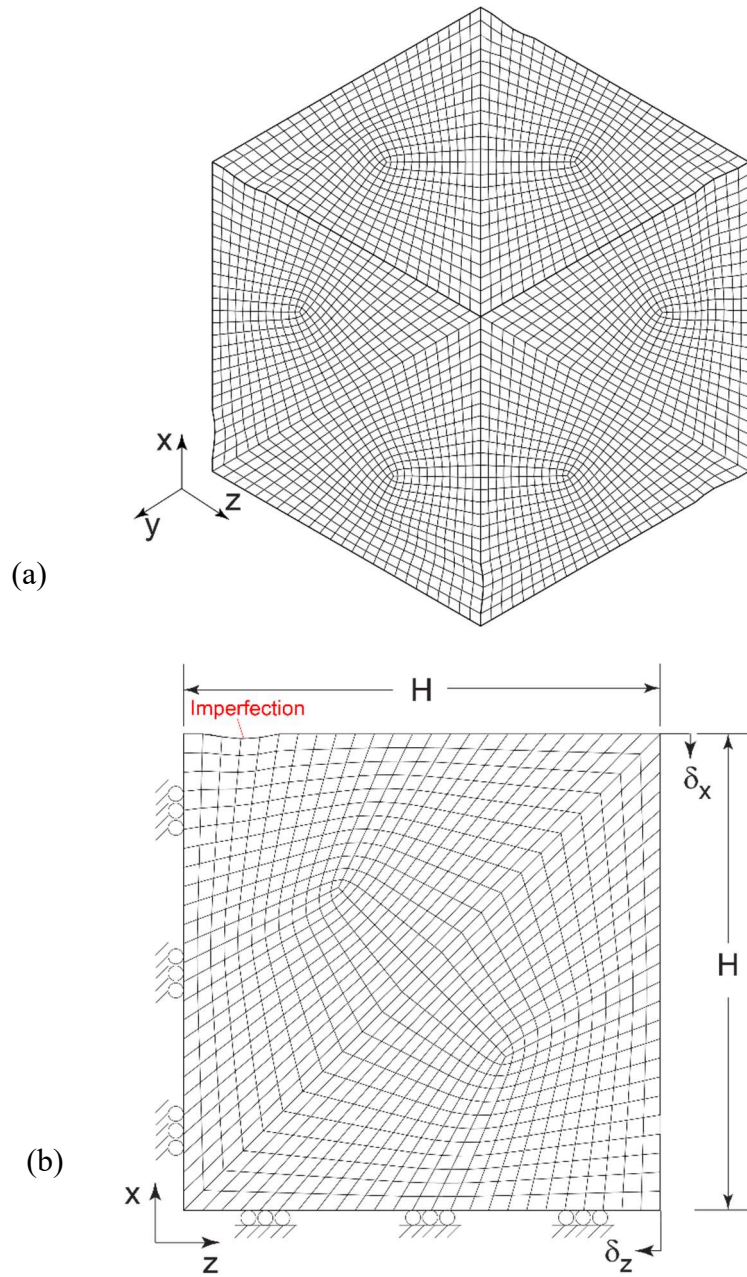
Fig. 5.1:   (a) Finite element mesh used for the homogenized model, and (b) $z-x$ planar view of the model showing the prescribed displacements.
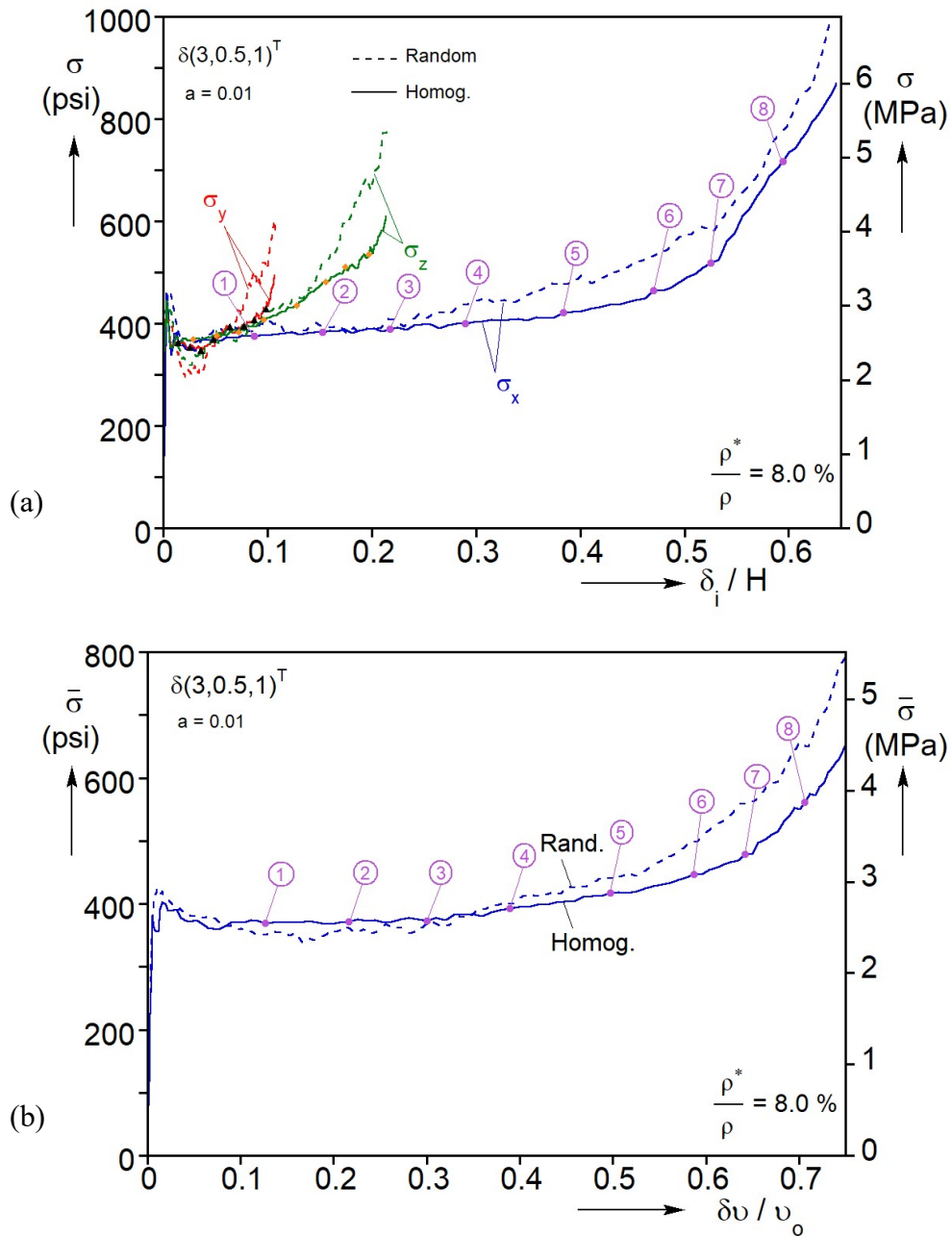
Fig. 5.2: (a) Calculated true stress-displacement responses in the *x*-, *y*-, and *z*-directions for the $(3, 0.5, 1)^T$ loading path from both the homogenized and random foam model, and (b) corresponding mean stress-change in volume responses.
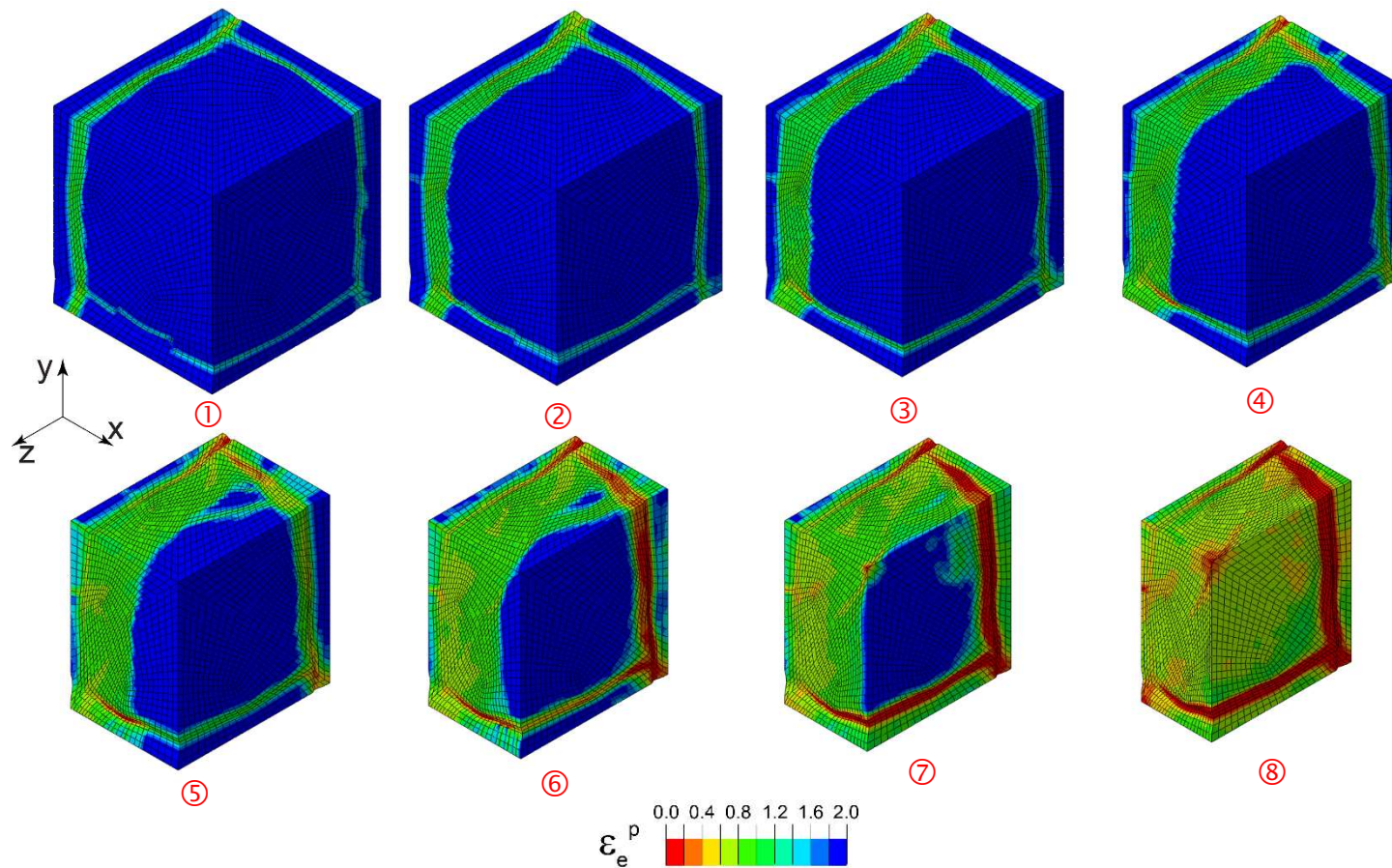
Fig. 5.3: Sequence of homogenized foam deformed configurations showing the three moving surfaces with strain contours superimposed corresponding to the numbered bullets on the $(3, 0.5, 1)^T$ responses in Fig. 5.2.
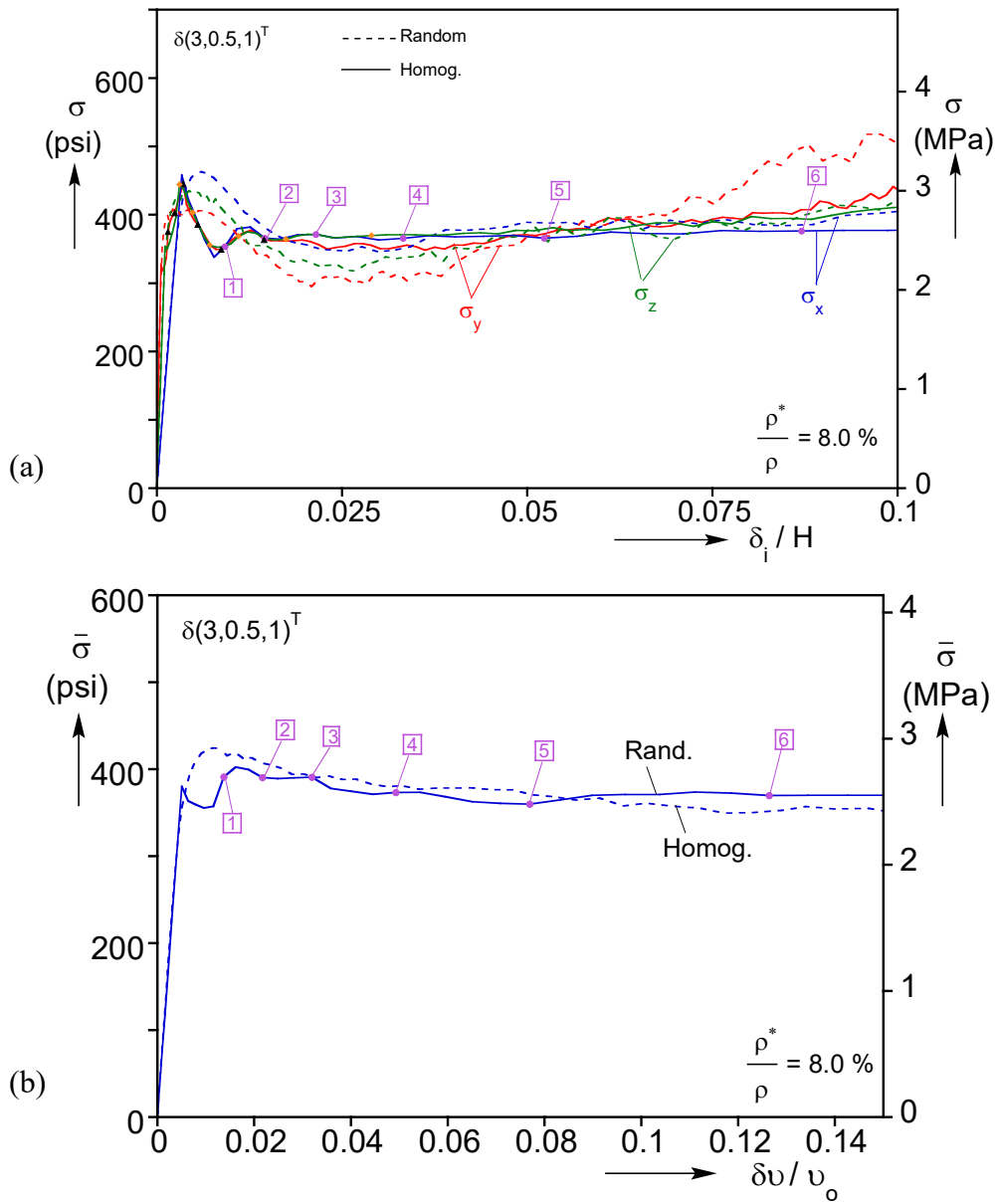
Fig. 5.4: Expanded plots showing the initial parts of (a) the calculated true stress-displacement responses in the x-, y-, and z-directions for the $(3,0.5,1)^T$ loading path, and (b) corresponding mean stress-change in volume response from both the homogenized and random foam model.
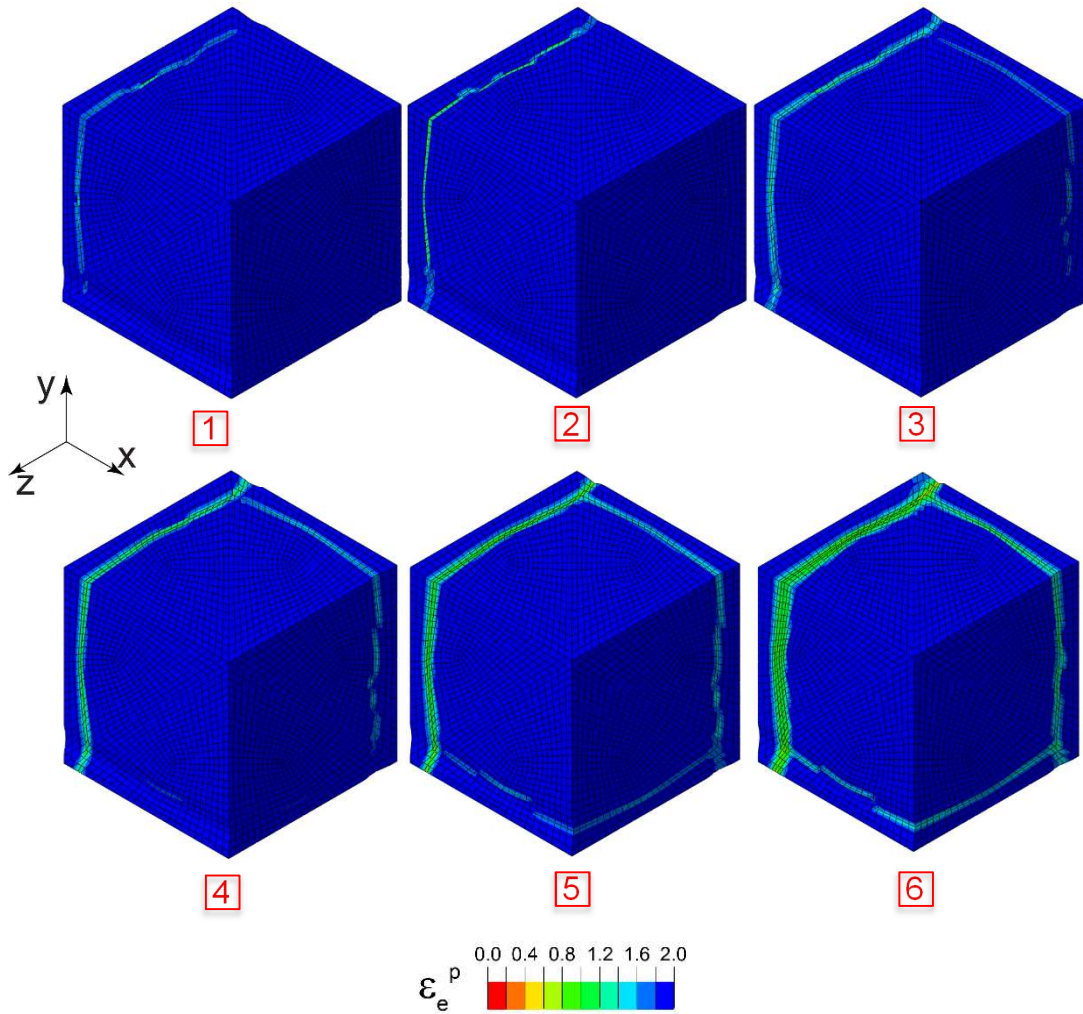
Fig. 5.5: Sequence of deformed foam images with strain contours superimposed showing the progressive initiations of the three planar bands corresponding to the numbered bullets on the responses for the $(3, 0.5, 1)^T$ loading path in Fig. 5.4.
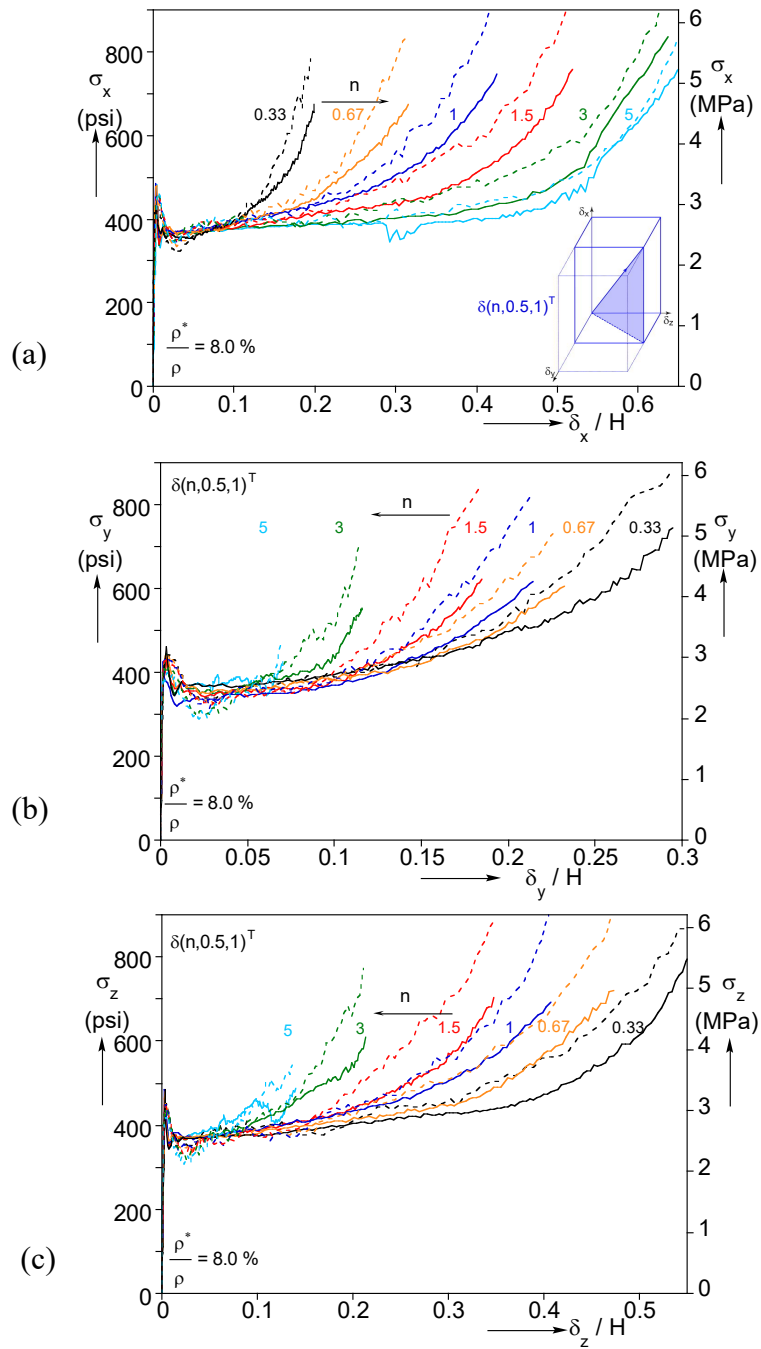
Fig. 5.6:   Comparison of homogenized and random foam model true stress-displacement responses for the $(n, 0.5, 1)^T$ loading paths: (a) in the *x*-direction, (b) *y*-direction, and (c) *z*-direction.
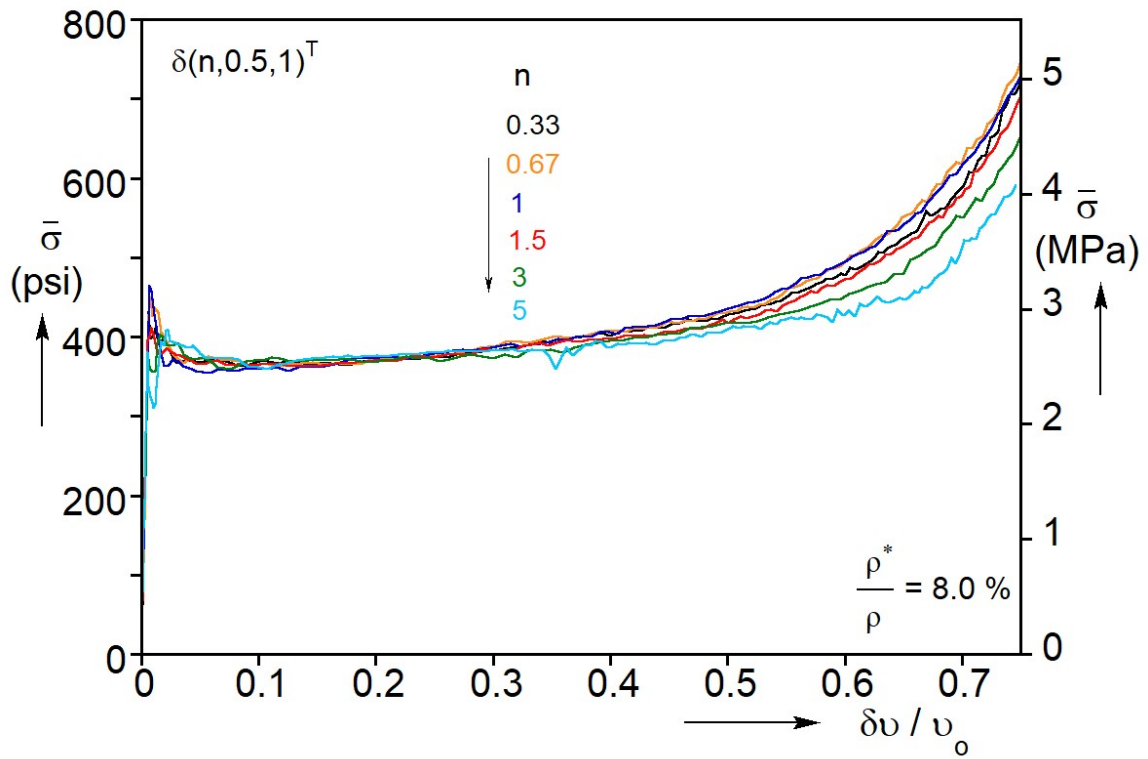
Fig. 5.7: Calculated mean stress-change in volume responses for the $(n, 0.5, 1)^T$ loading paths from the homogenized model.
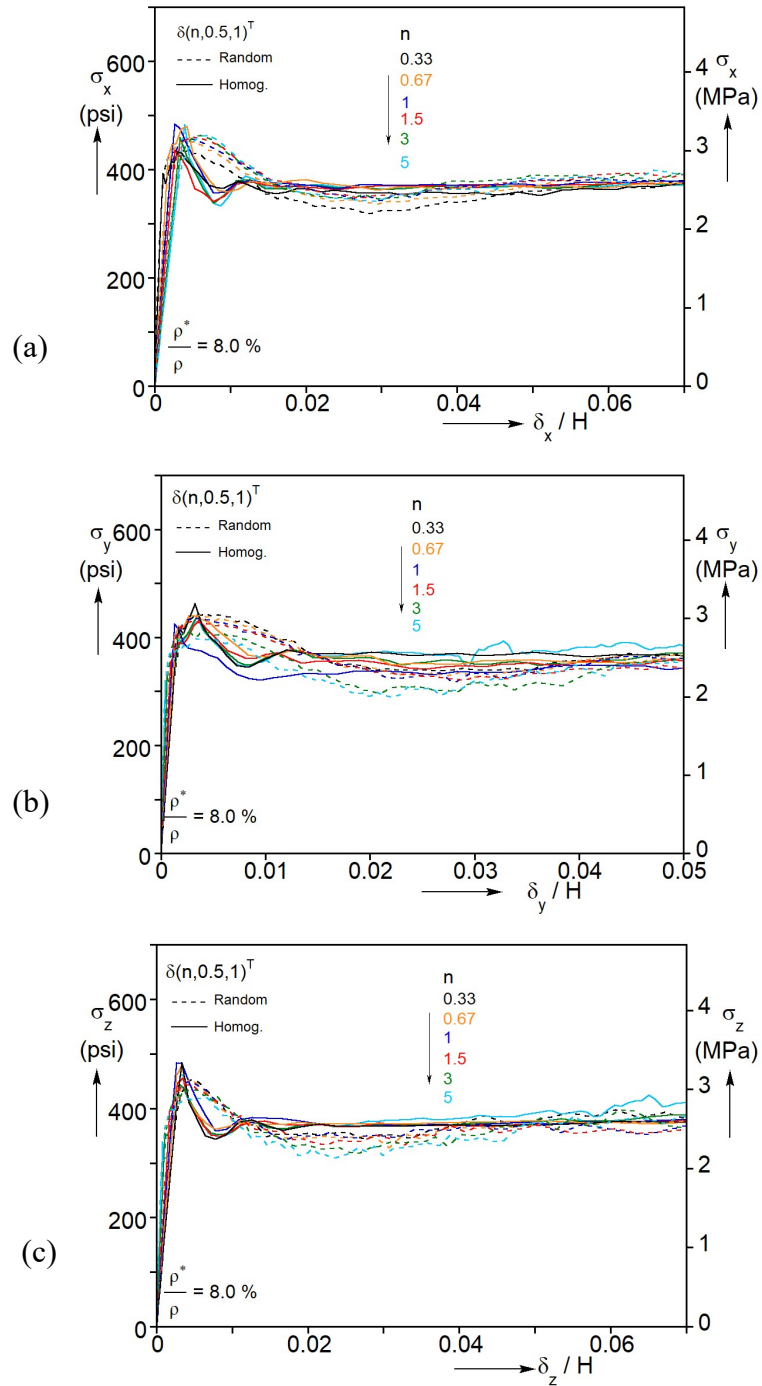
Fig. 5.8:   Expanded plots showing the initial parts of homogenized and random foam model true stress-displacement responses for the $(n, 0.5, 1)^T$ loading paths: (a) in the *x*-direction, (b) *y*-direction, and (c) *z*-direction.

128
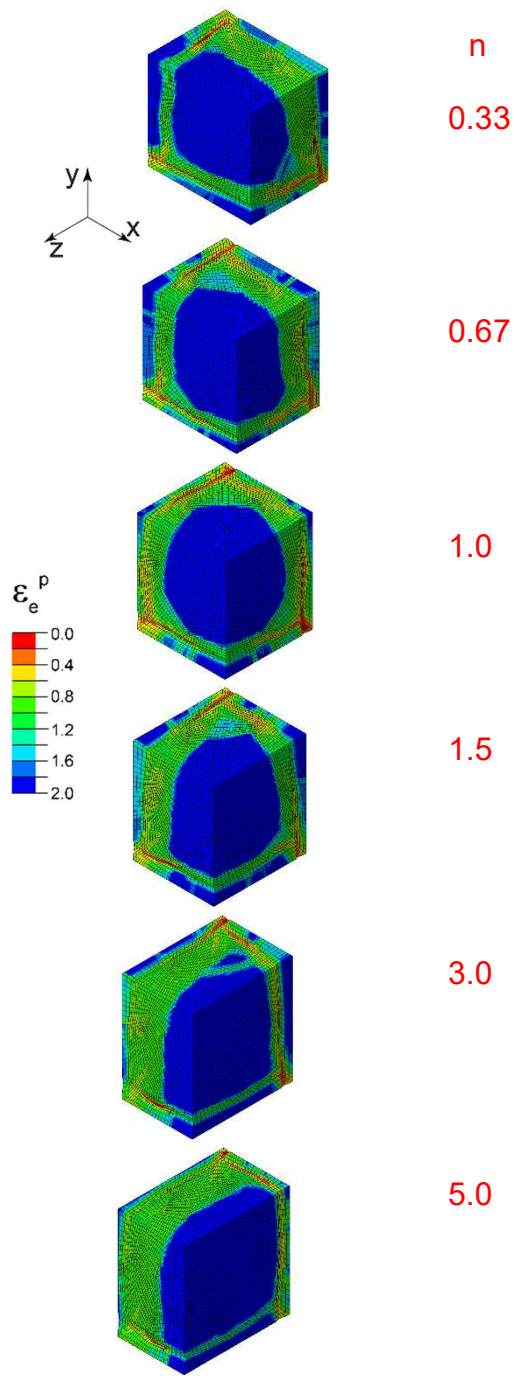
Fig. 5.9: Homogenized model deformed configurations corresponding to $\delta\upsilon / \upsilon_o \approx 0.5$ for different values of n for the $(n, 0.5, 1)^T$ loading paths.
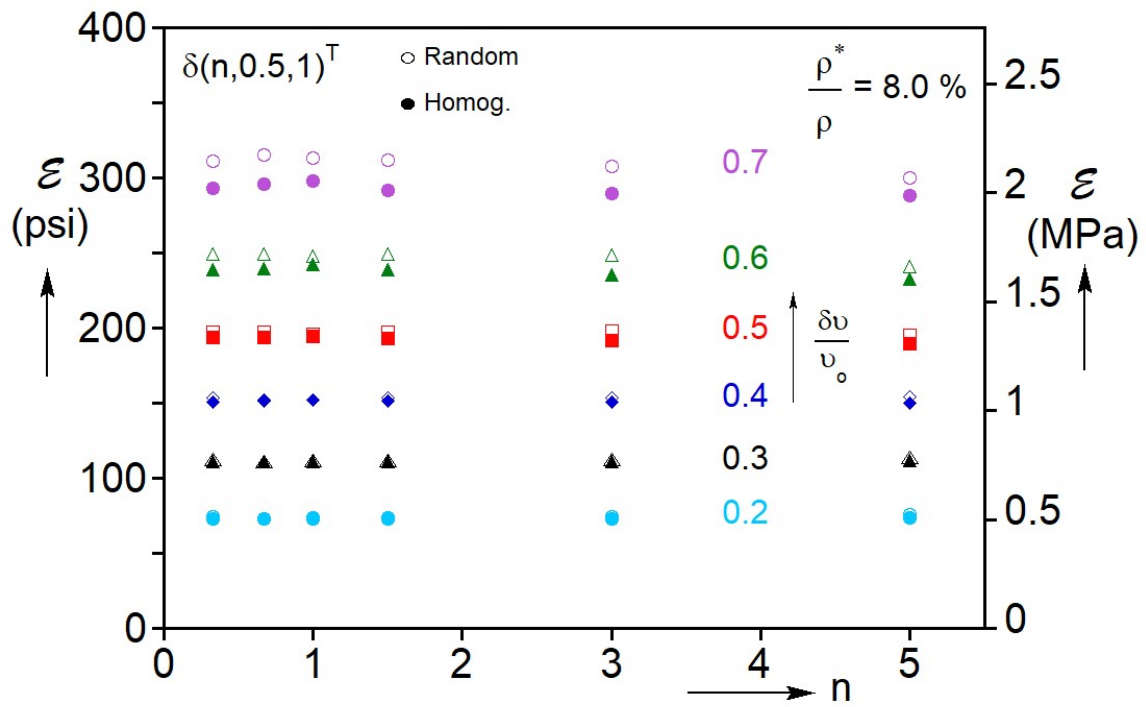
Fig. 5.10: Comparison of the homogenized and random foam model deformation energies for the $(n,0.5,1)^T$ loading paths. Plotted are energies for six values of n at different levels of $\delta\upsilon/\upsilon_o$.
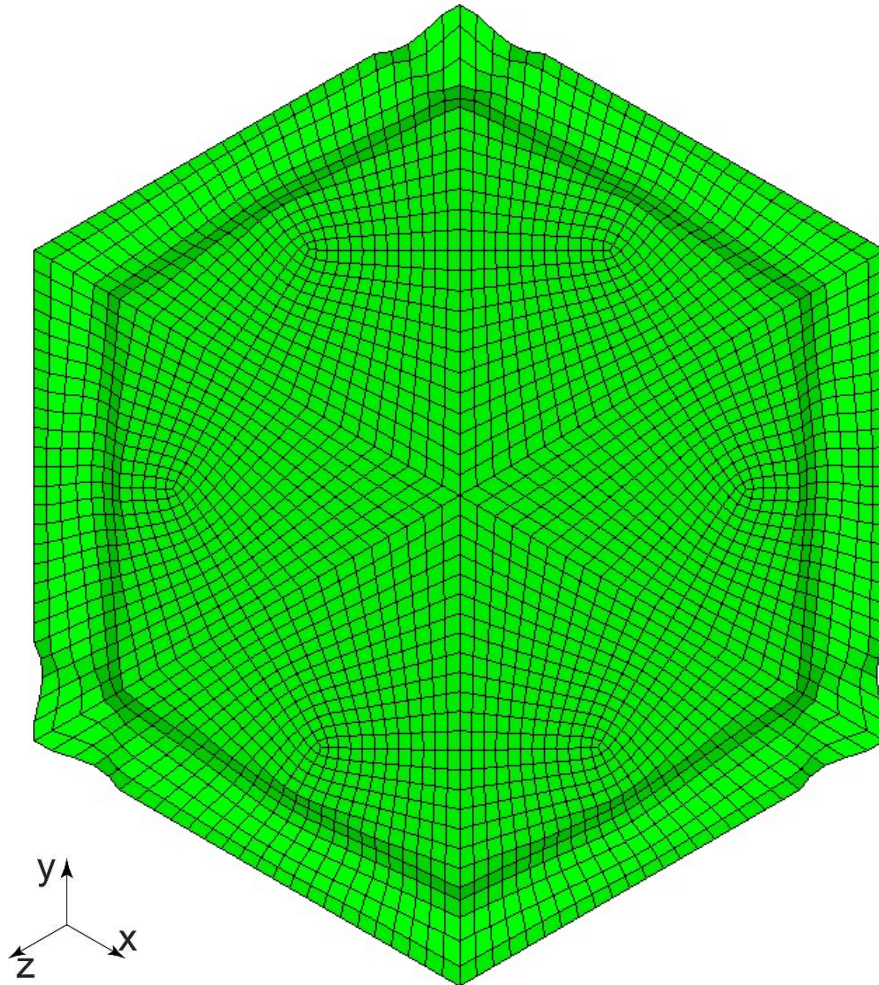
Fig. 5.11: The finite element model adopted for the $(1.05,1,1)^T$ loading path showing two orthogonal imperfections introduced to each moving face.
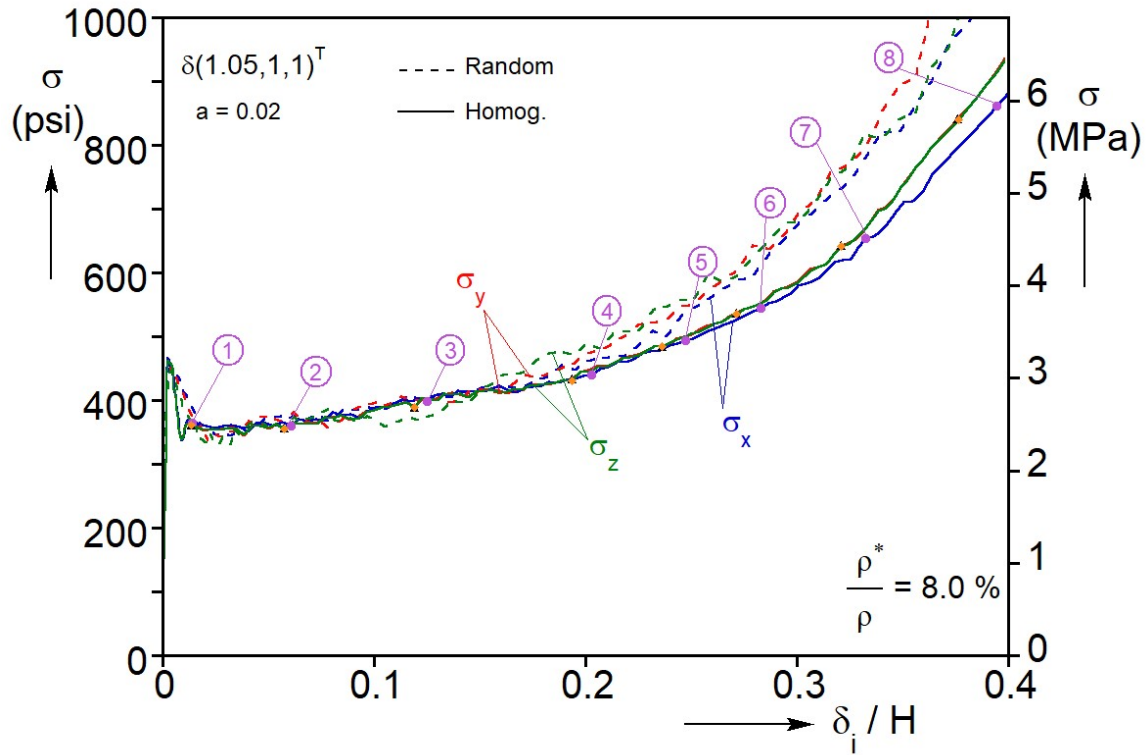
Fig. 5.12: Calculated true stress-displacement responses in the *x*-, *y*-, and *z*-directions for the $(1.05, 1, 1)^T$ loading path from the homogenized foam model, compared to the corresponding responses for the $(1, 1, 1)^T$ loading path from the random foam model.
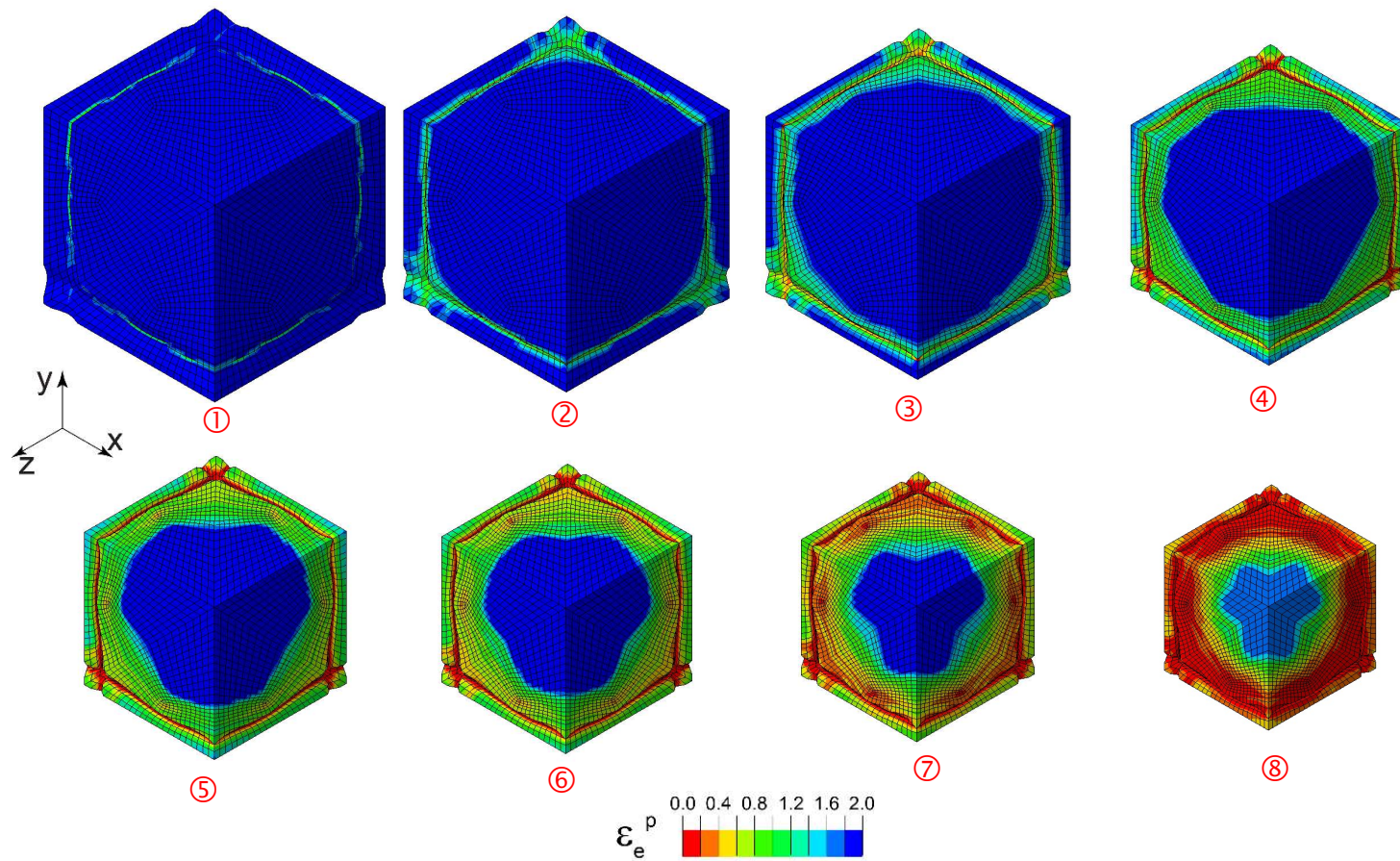
Fig. 5.13: Sequence of homogenized foam deformed configurations showing the three moving surfaces with strain contours superimposed corresponding to the numbered bullets on the $(1.05,1,1)^T$ responses in Fig. 5.12.

133
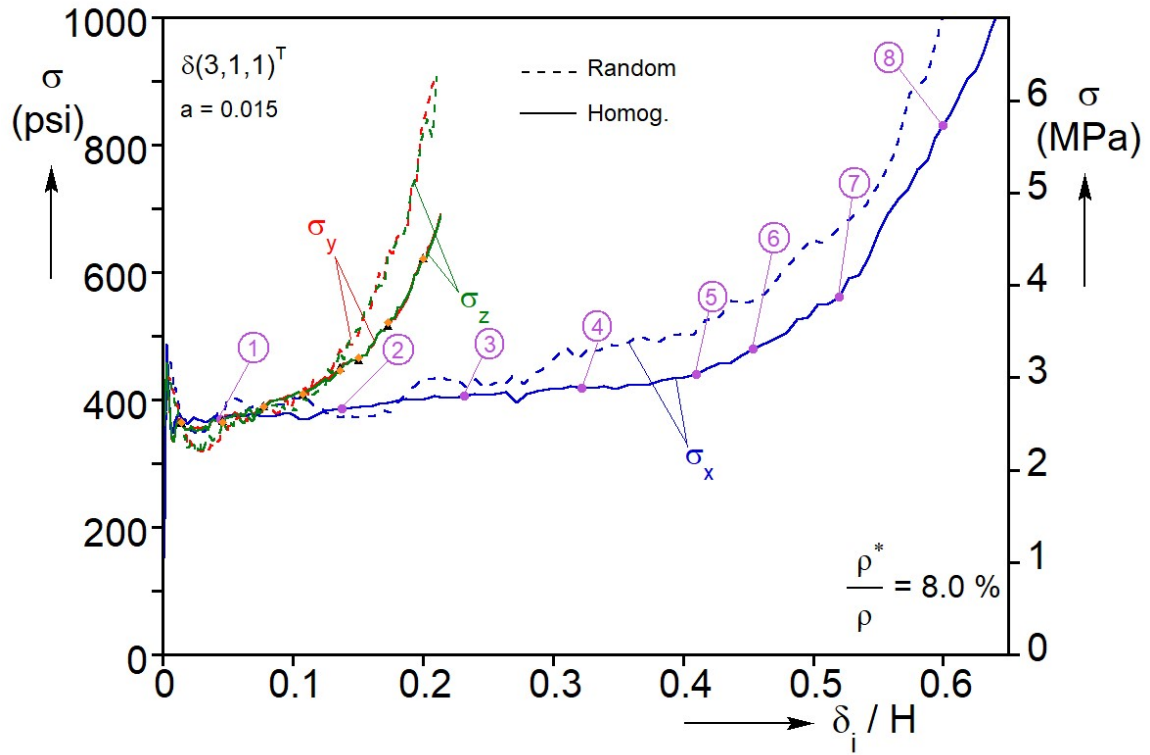
Fig. 5.14: Calculated true stress-displacement responses in the *x*-, *y*-, and *z*-directions for the $(3,1,1)^T$ loading path from both the homogenized and random foam model.
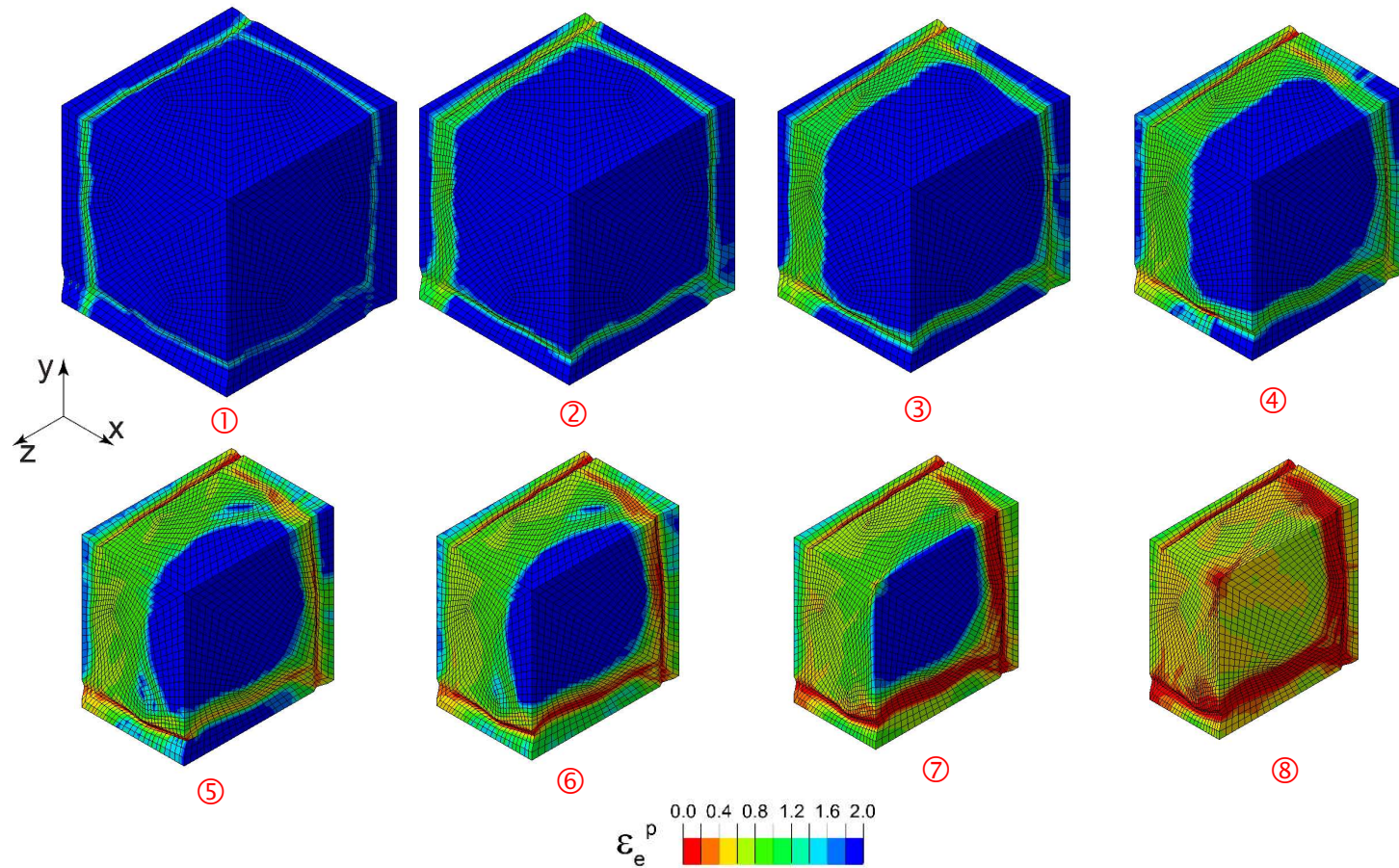
Fig. 5.15:   Sequence of homogenized foam deformed configurations showing the three moving surfaces with strain contours superimposed corresponding to the numbered bullets on the $(3,1,1)^T$ responses in Fig. 5.14.
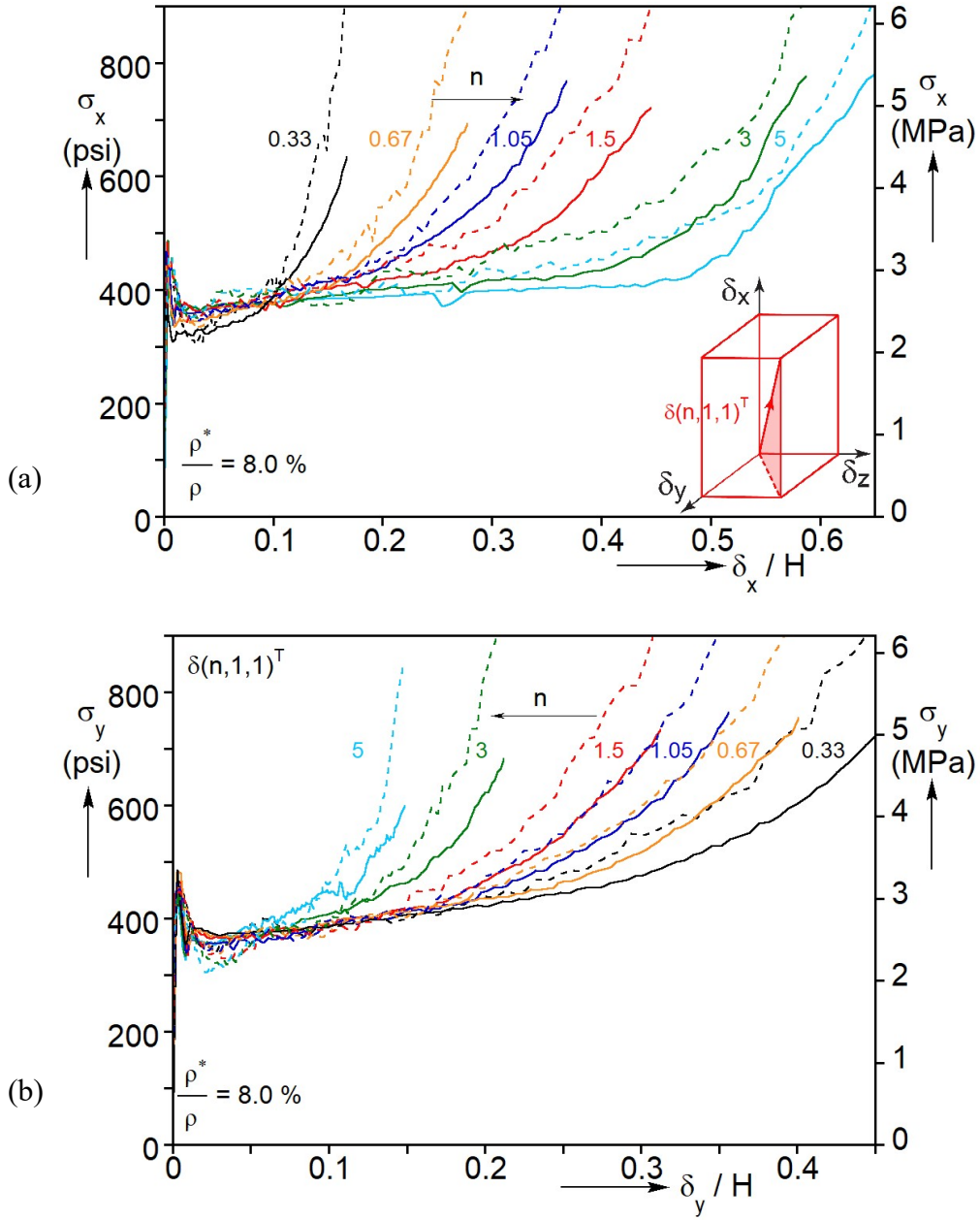
Fig. 5.16: Comparison of homogenized and random foam model true stress-displacement responses for the $(n,1,1)^T$ loading paths: (a) in the x-direction and (b) y-direction.
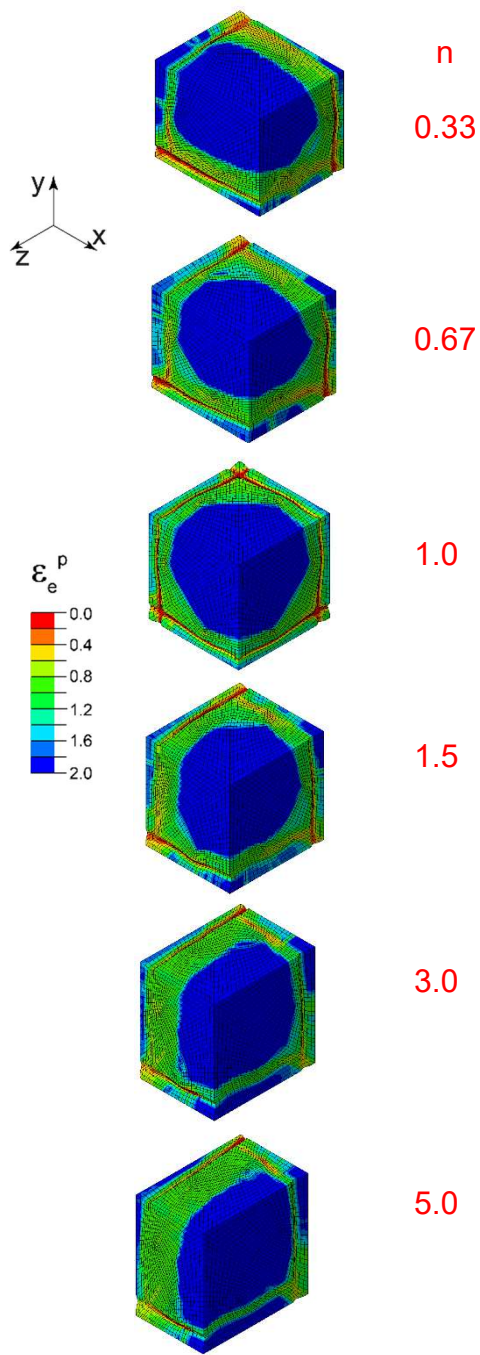
Fig. 5.17: Homogenized model deformed configurations corresponding to $\delta\upsilon/\upsilon_o \approx 0.5$ for different values of n for the $(n,1,1)^T$ loading paths.
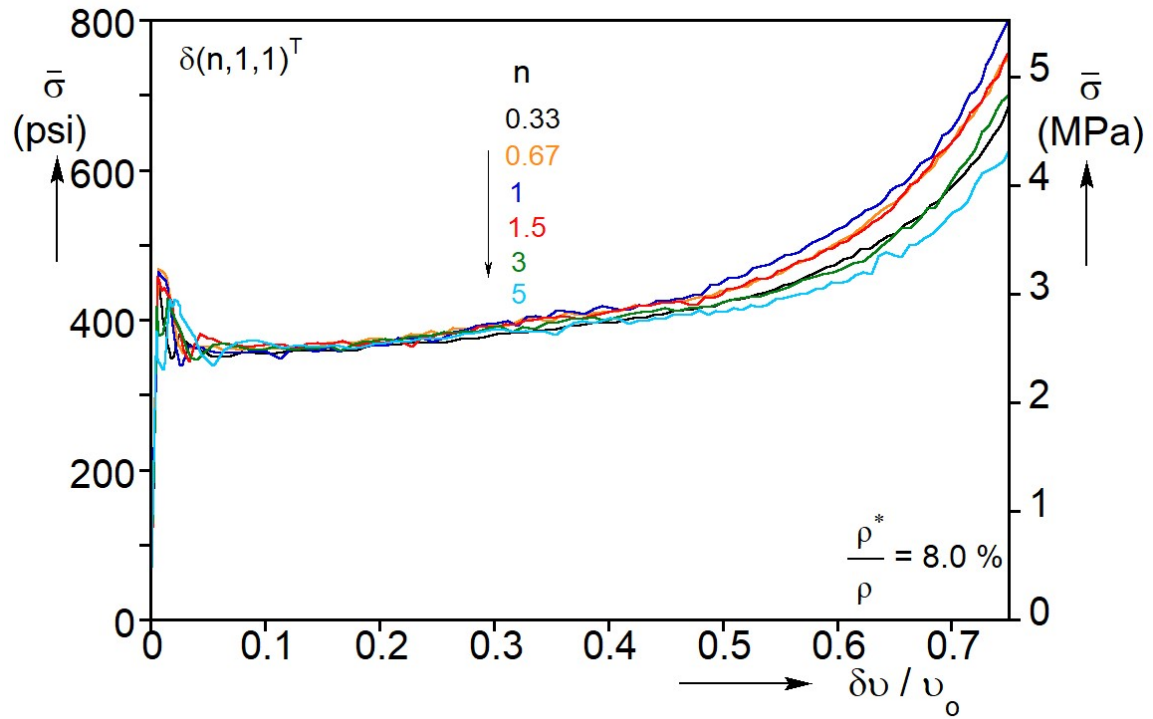
Fig. 5.18:   Calculated mean stress-change in volume responses for the $(n,1,1)^T$ loading paths from the homogenized model.
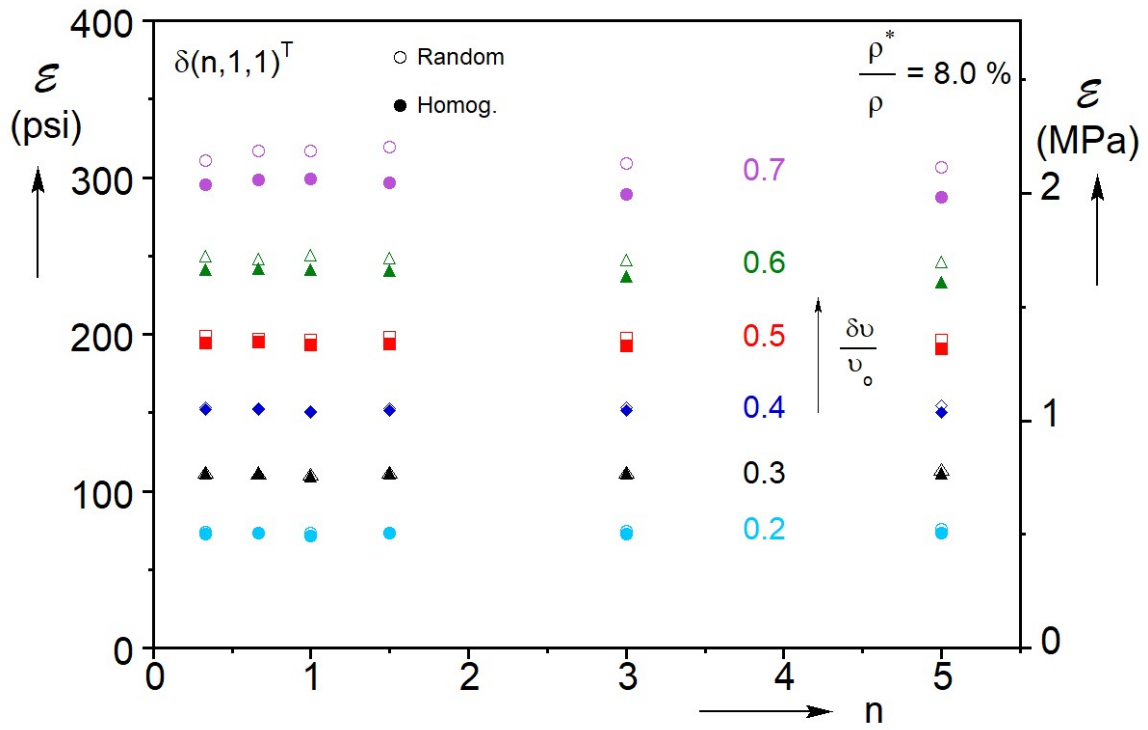
Fig. 5.19: Comparison of the homogenized and random foam model deformation energies for the $(n,1,1)^T$ loading paths. Plotted are energies for six values of n at different levels of $\delta\upsilon/\upsilon_o$.
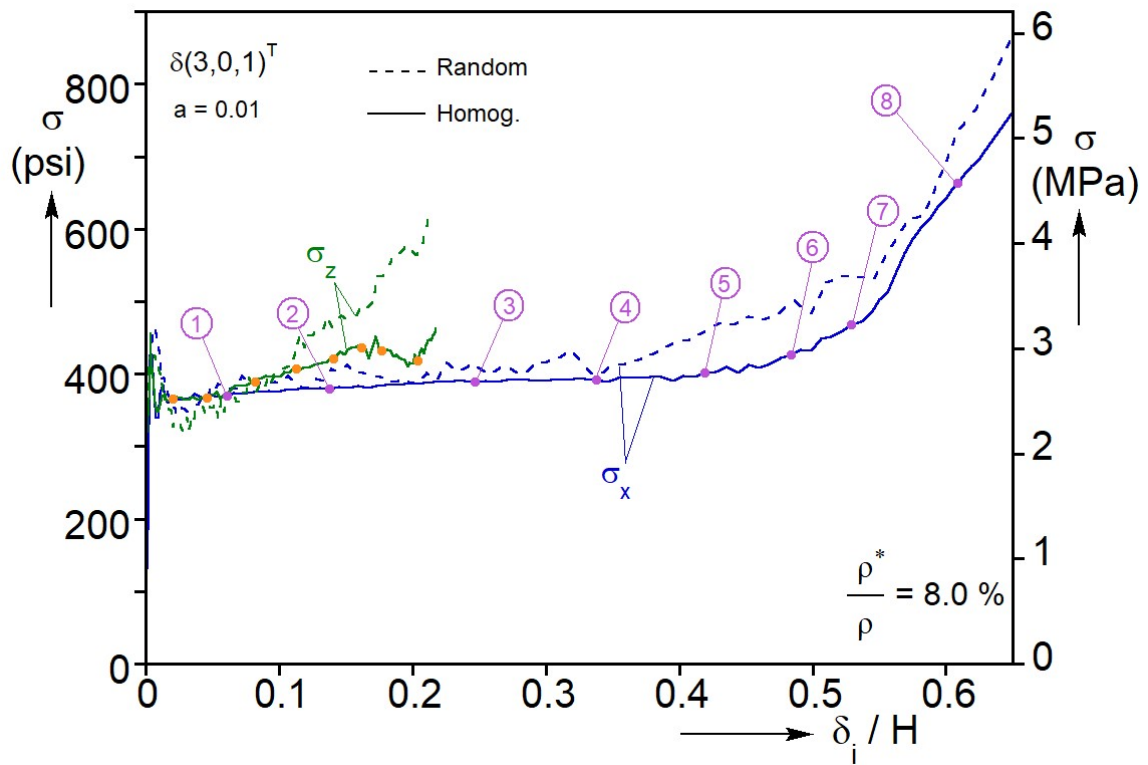
Fig. 5.20: Calculated true stress-displacement responses in the *x*-and *z*-directions for the $(3,0,1)^T$ loading path from both the homogenized and random foam model.
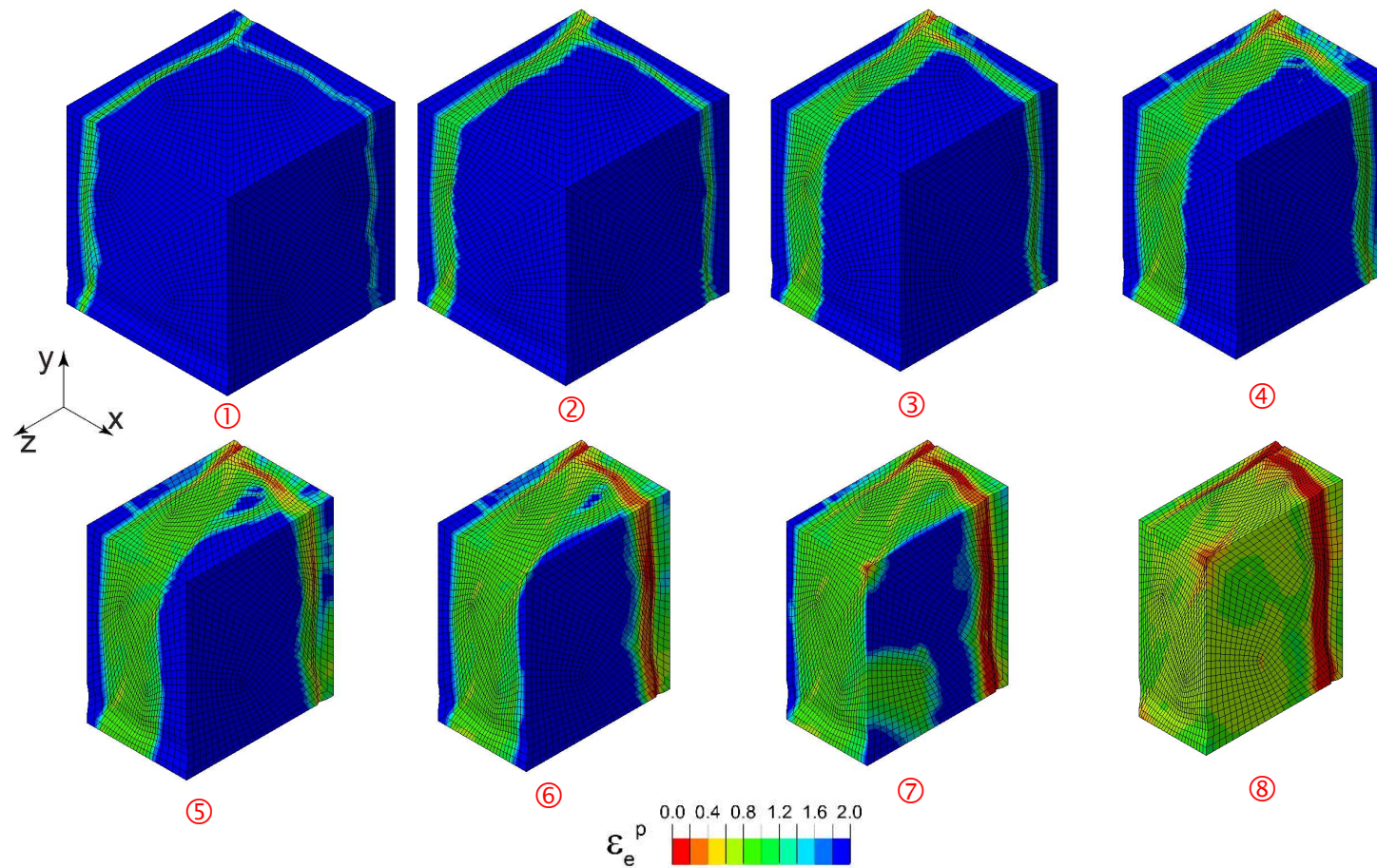
Fig. 5.21: Sequence of homogenized foam deformed configurations showing the three moving surfaces with strain contours superimposed corresponding to the numbered bullets on the $(3,0,1)^T$ responses in Fig. 5.20.
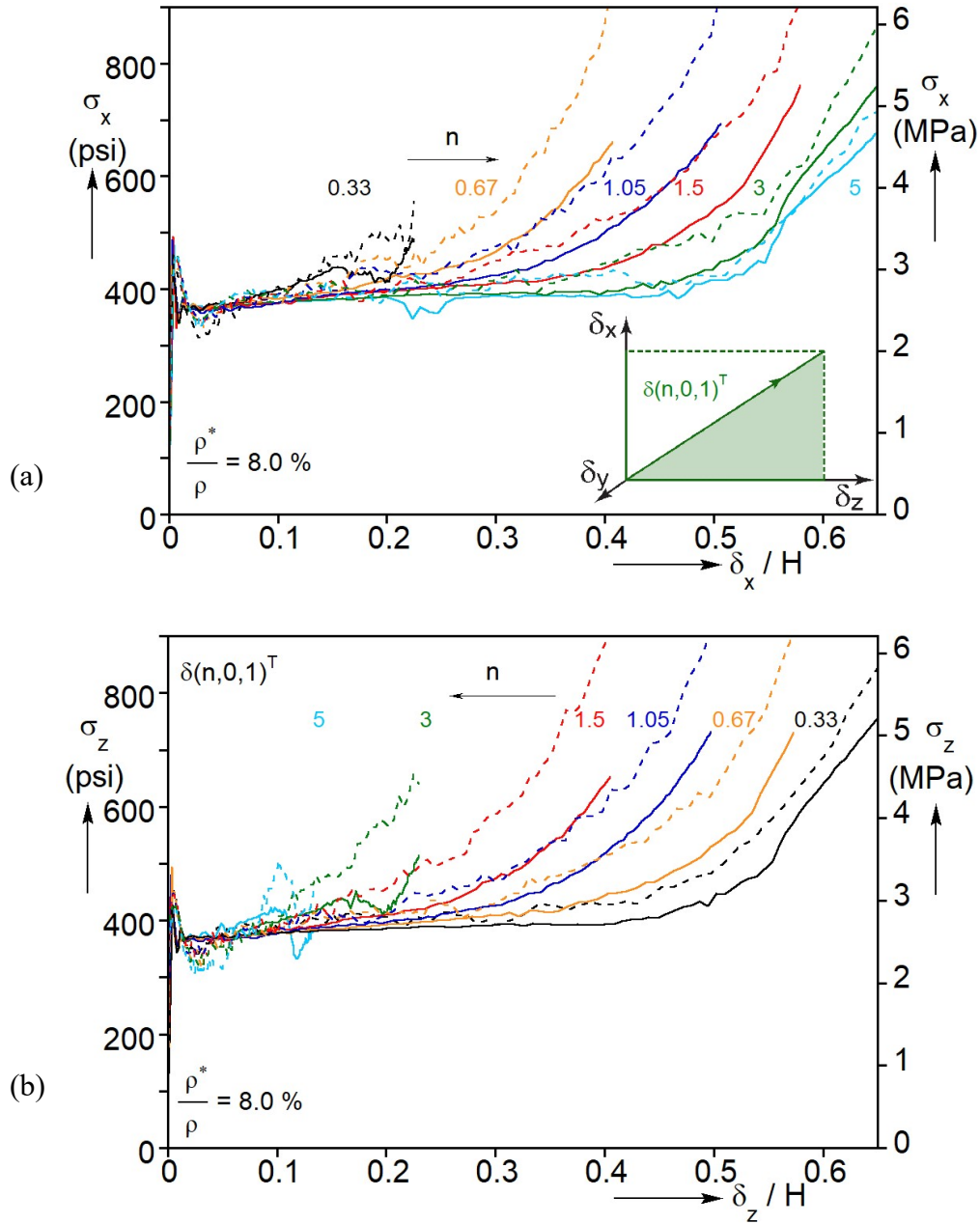
Fig. 5.22: Comparison of homogenized and random foam model true stress-displacement responses for the $(n,0,1)^T$ loading paths: (a) in the x-direction and (b) z-direction.
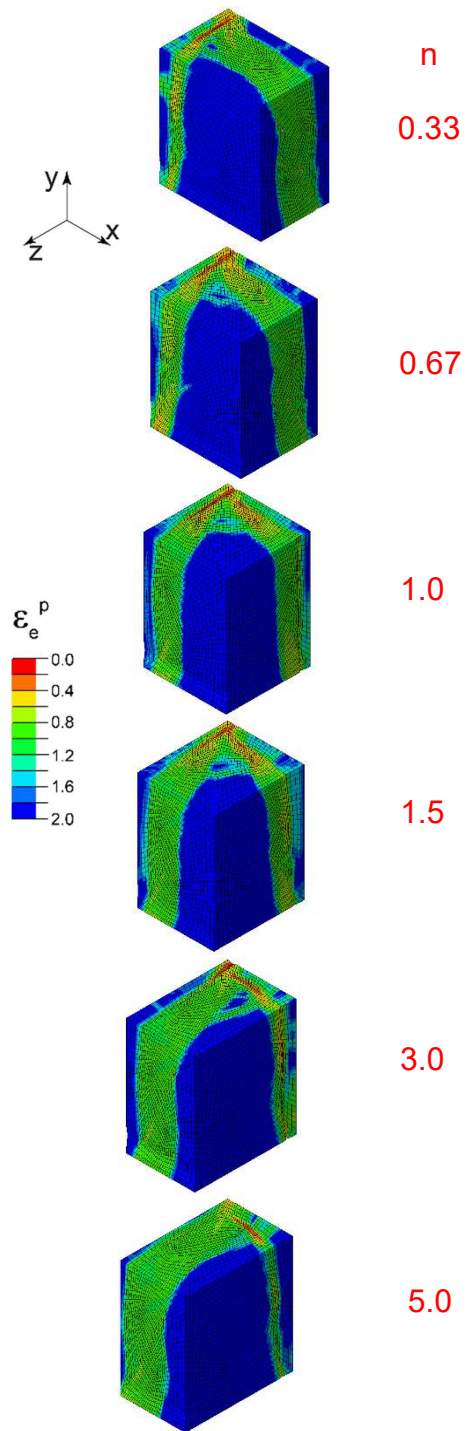
Fig. 5.23: Homogenized model deformed configurations corresponding to $\delta\upsilon / \upsilon_o \approx 0.5$ for different values of n for the $(n, 0, 1)^T$ loading paths.
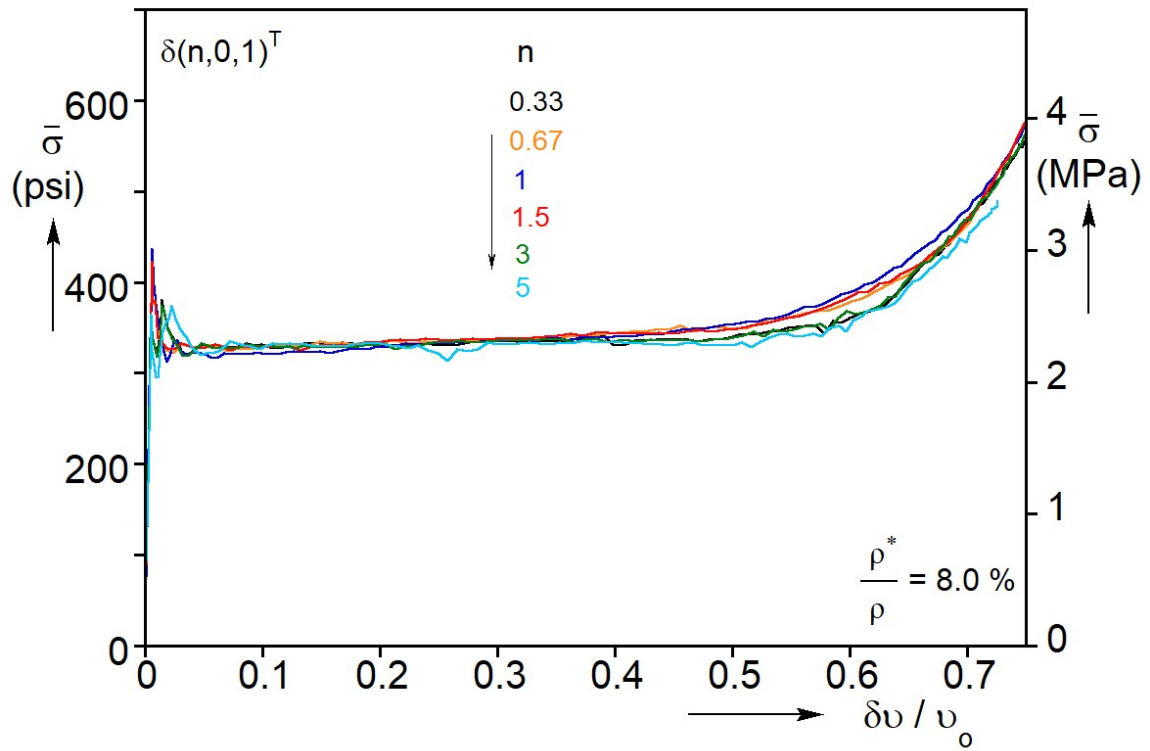
Fig. 5.24: Calculated mean stress-change in volume responses for the $(n,0,1)^T$ loading paths from the homogenized model.
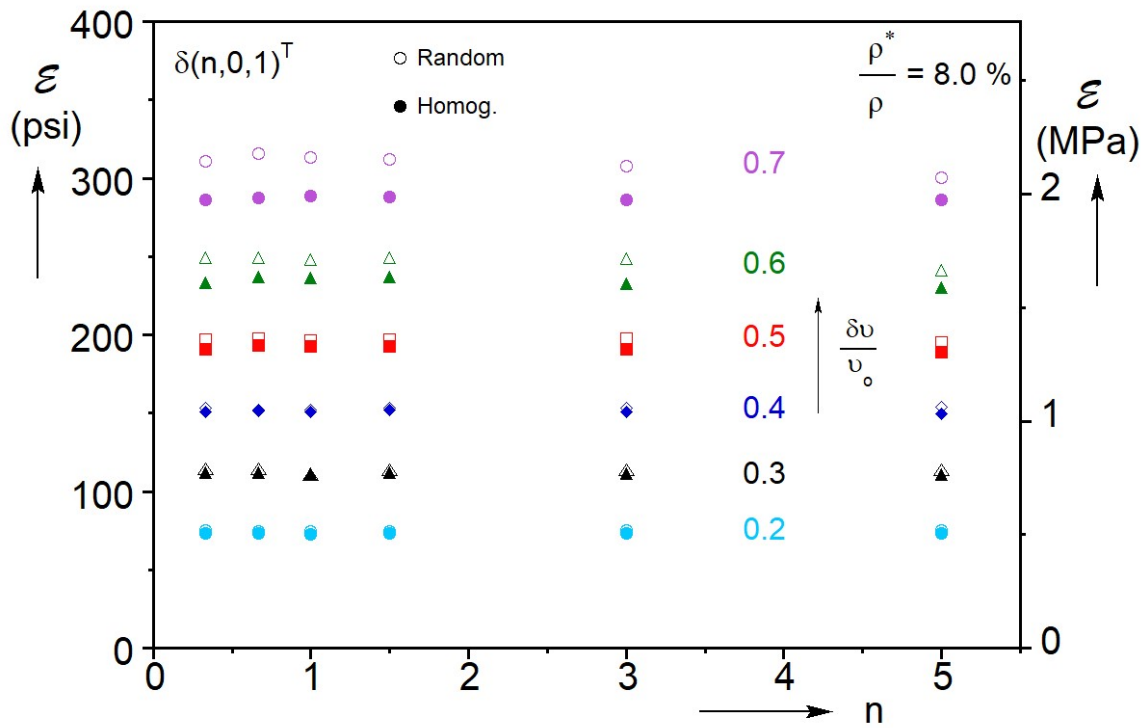
Fig. 5.25: Comparison of the homogenized and random foam model deformation energies for the $(n, 0, 1)^T$ loading paths. Plotted are energies for six values of n at different levels of $\delta \upsilon / \upsilon_o$.
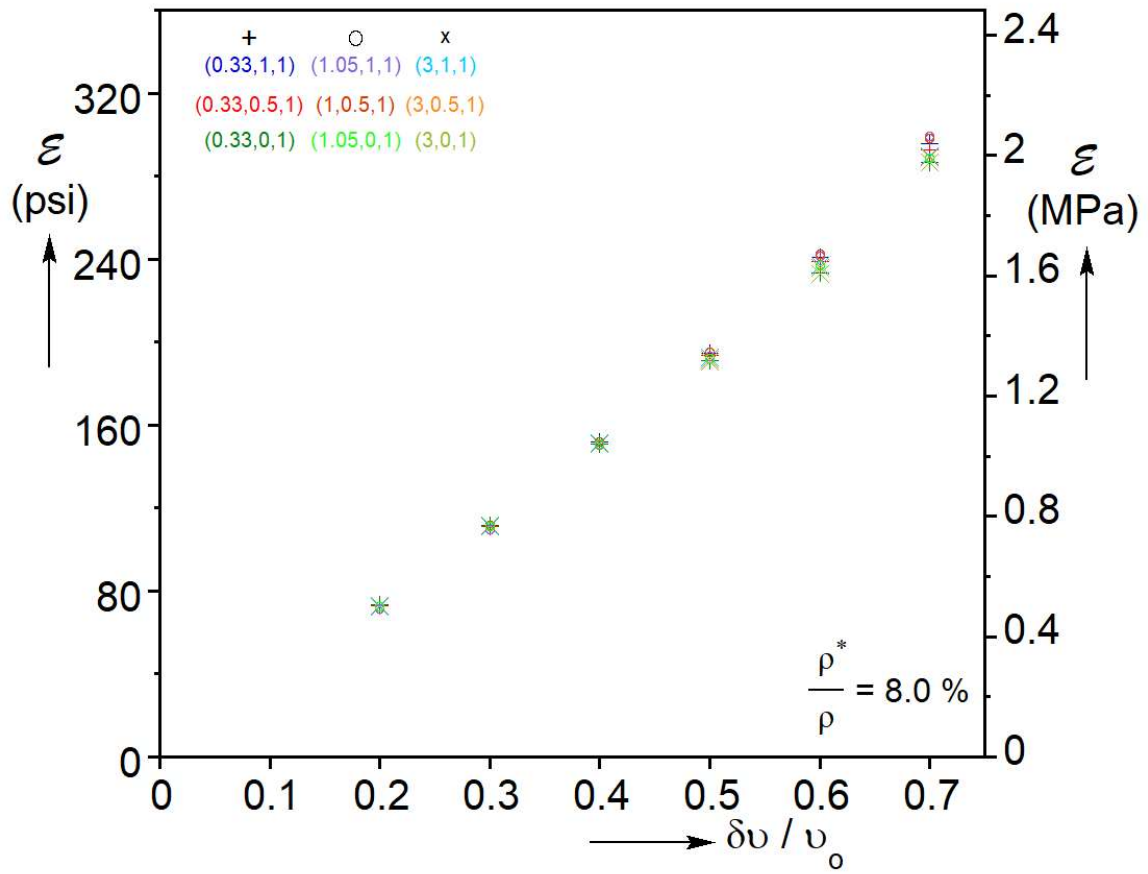
Fig. 5.26: Homogenized model crushing energies at discrete values of change in volume from nine loading paths.
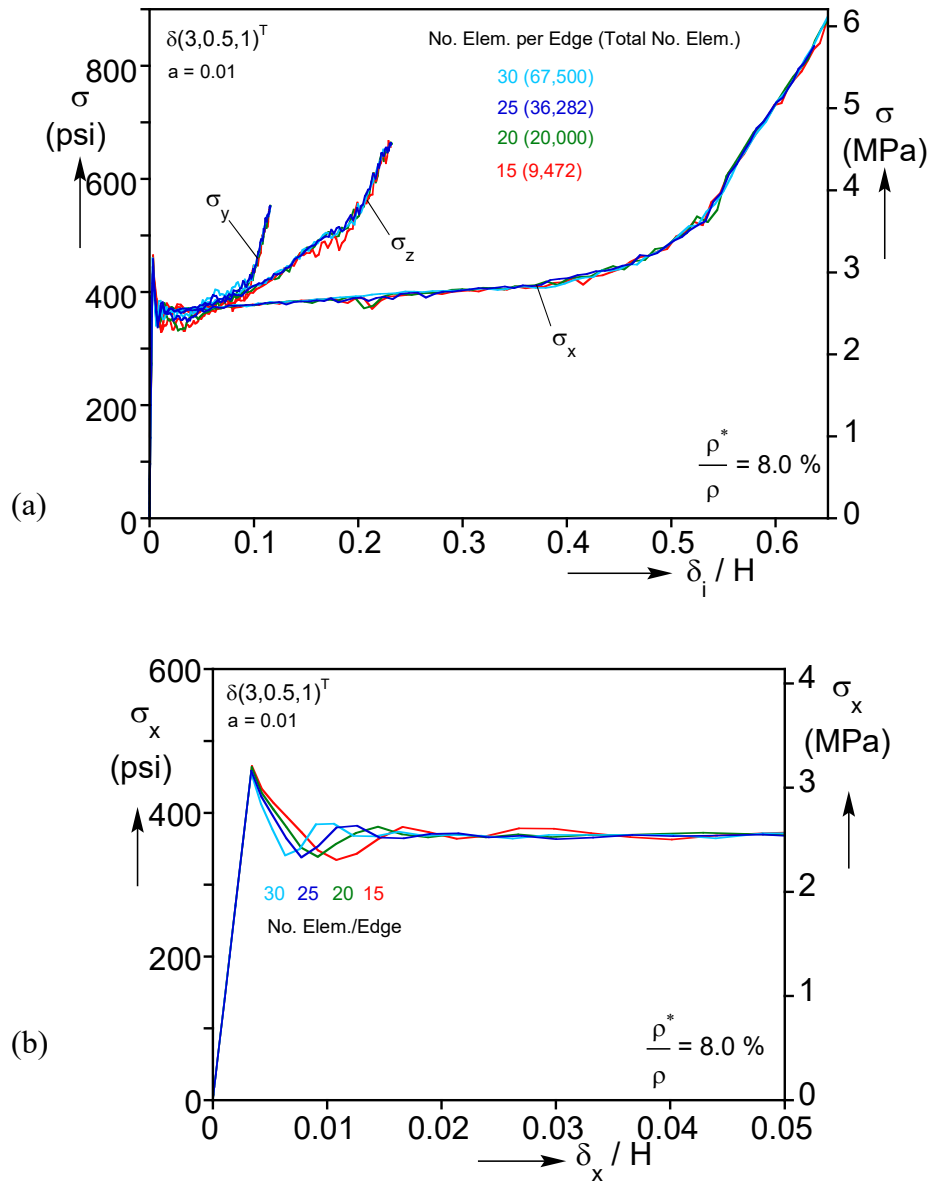
Fig. 5.27: (a) Comparison of stress-displacement responses in three directions for the $(3, 0.5, 1)^T$ path using four different mesh densities. (b) $\sigma_x - \delta_x / H$ responses showing the effect of the mesh on the initial descending branch associated with the nucleation of the first planar band.
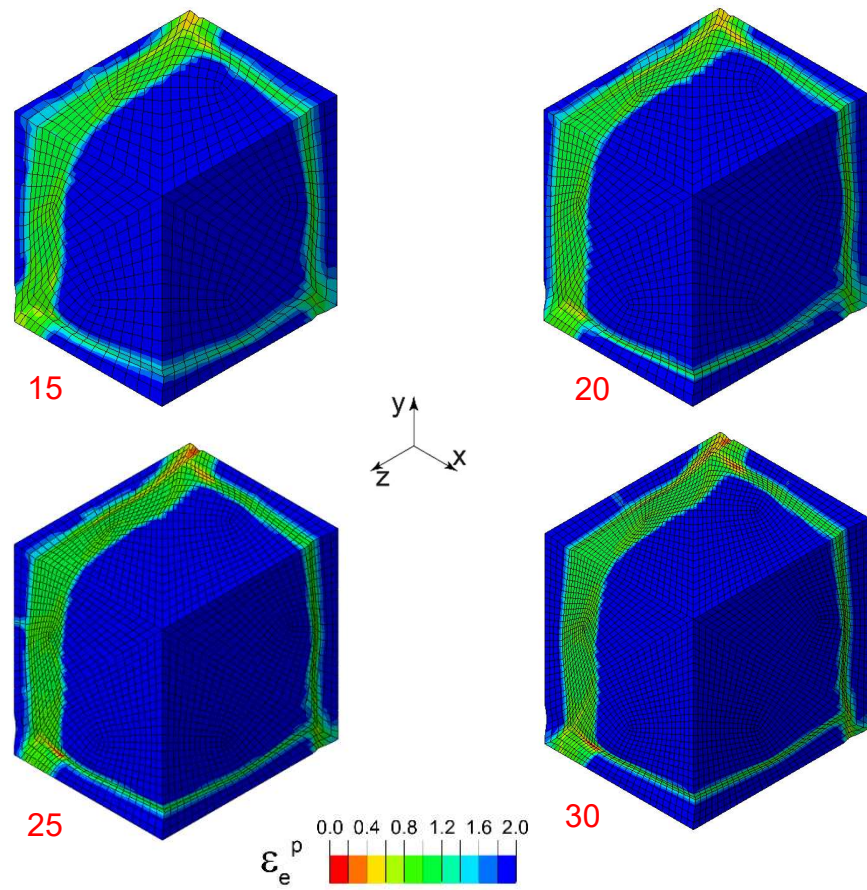
Fig. 5.28: Deformed configurations from the four meshes at $\delta_x / H = 0.217$ for the $(3, 0.5, 1)^T$ path. The main difference of mesh refinement is in the width of the transition zone that separates the two deformation regimes.
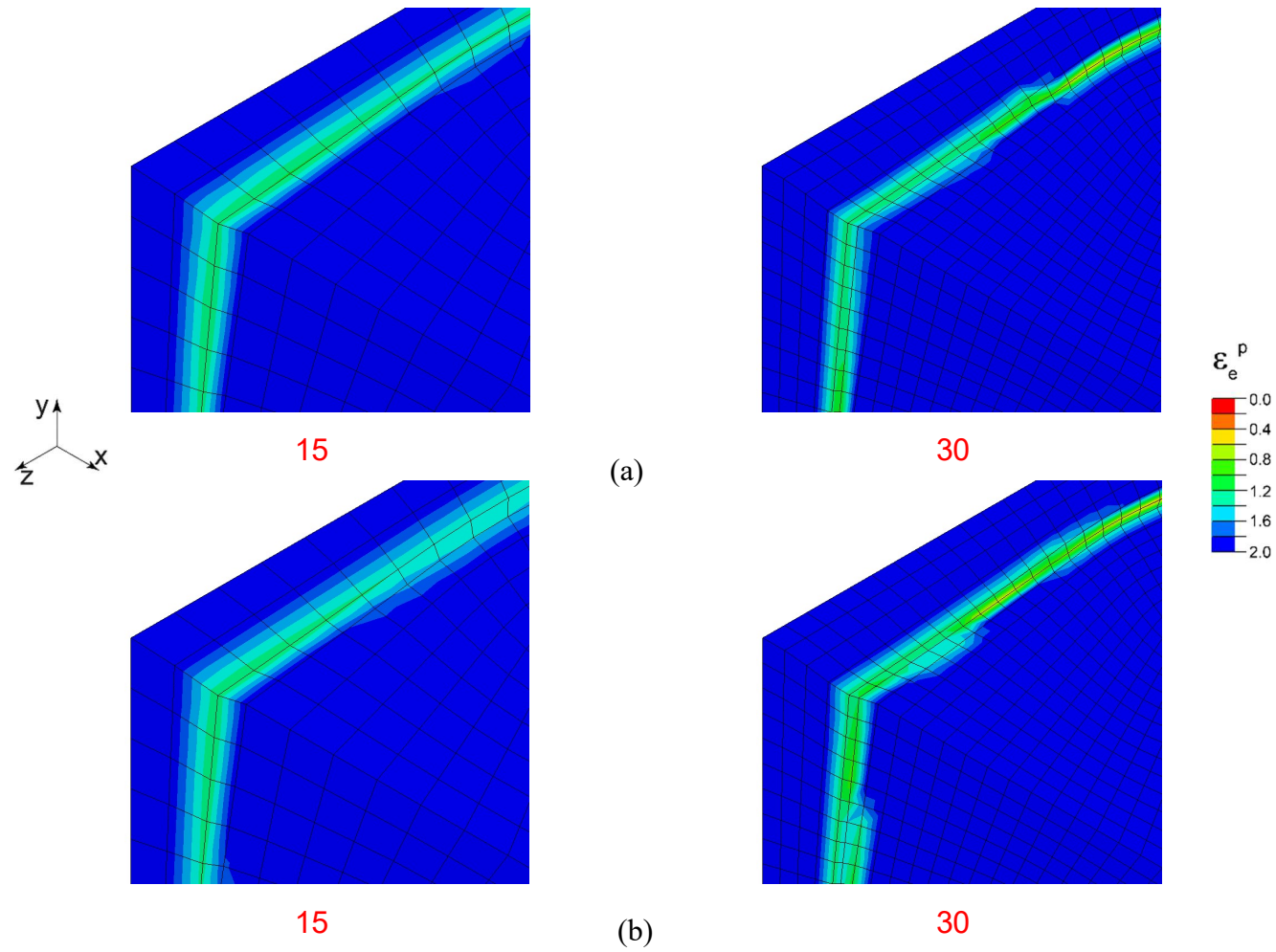
Fig. 5.29: Expanded view of the deformed configurations from the two meshes at $\delta_x / H = 0.024$ for the $(3, 0.5, 1)^T$ path. The constitutive model is (a) rate-independent and (b) rate dependent.
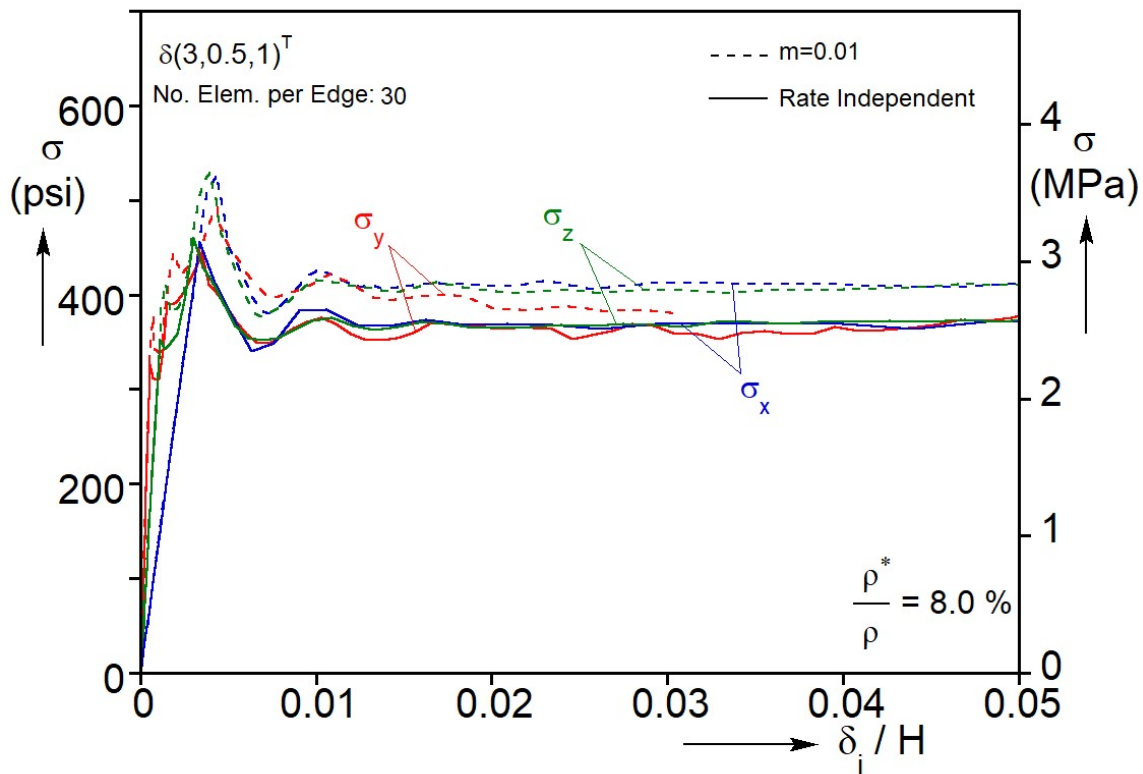
Fig. 5.30:   Early part of the overall stress-displacement responses in three directions for the $(3, 0.5, 1)^T$ path using the constitutive model that is (a) rate independent and (b) rate dependent.
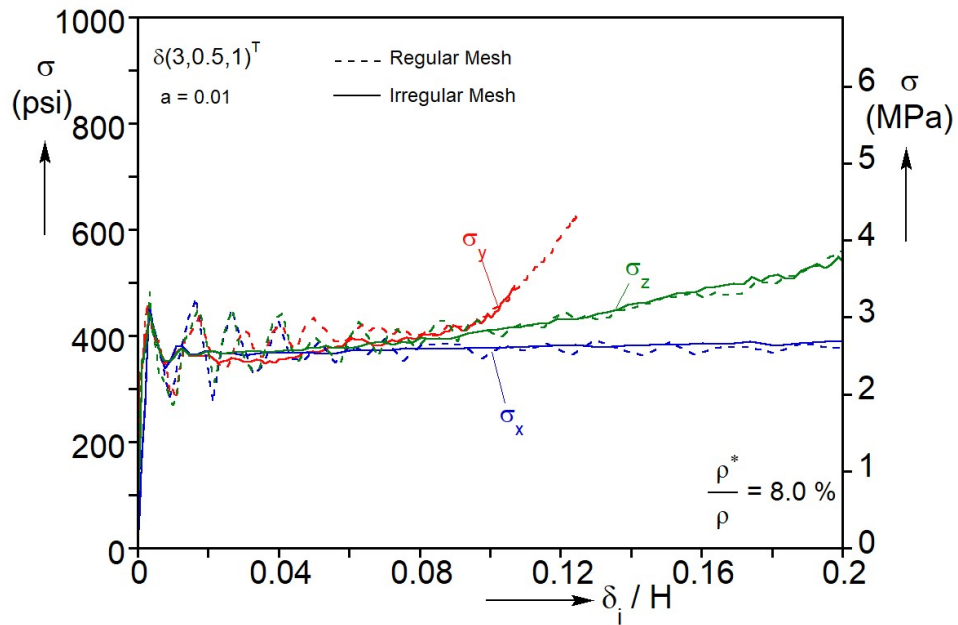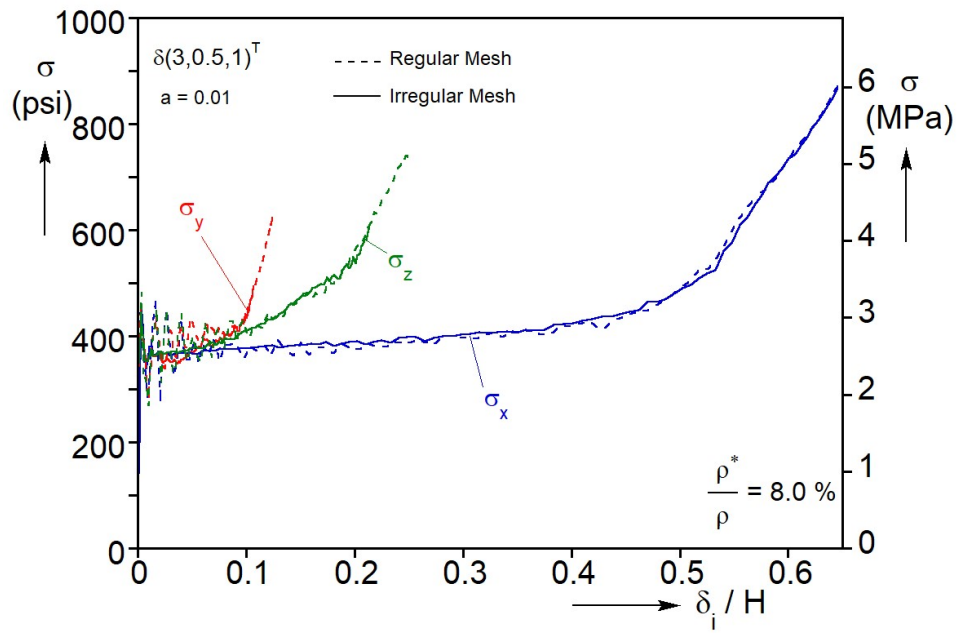
Fig. 5.31:   (a) Comparison of stress-displacement responses and (b) the expanded early
parts in three directions for the $(3, 0.5, 1)^T$ path using the regular mesh and
the irregular mesh adopted in this chapter.

151
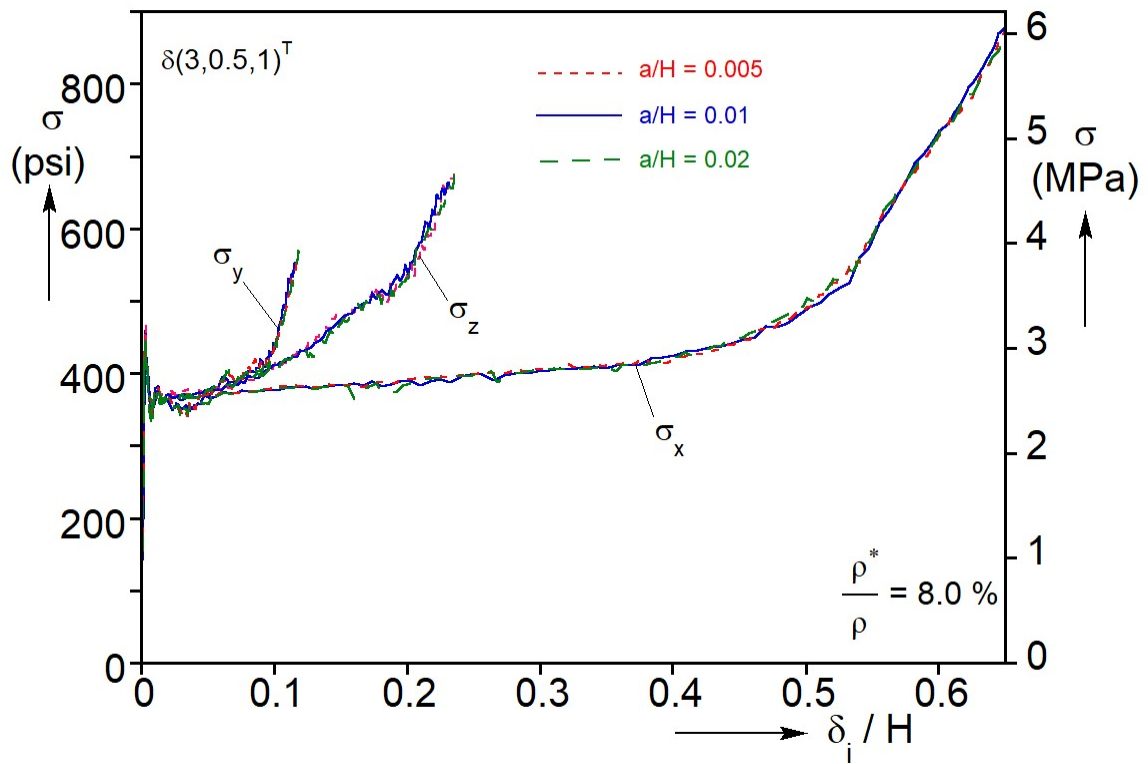
Fig. 5.32: (a) Stress-displacement responses in three directions for the $(3, 0.5, 1)^T$ path with three imperfection amplitudes.
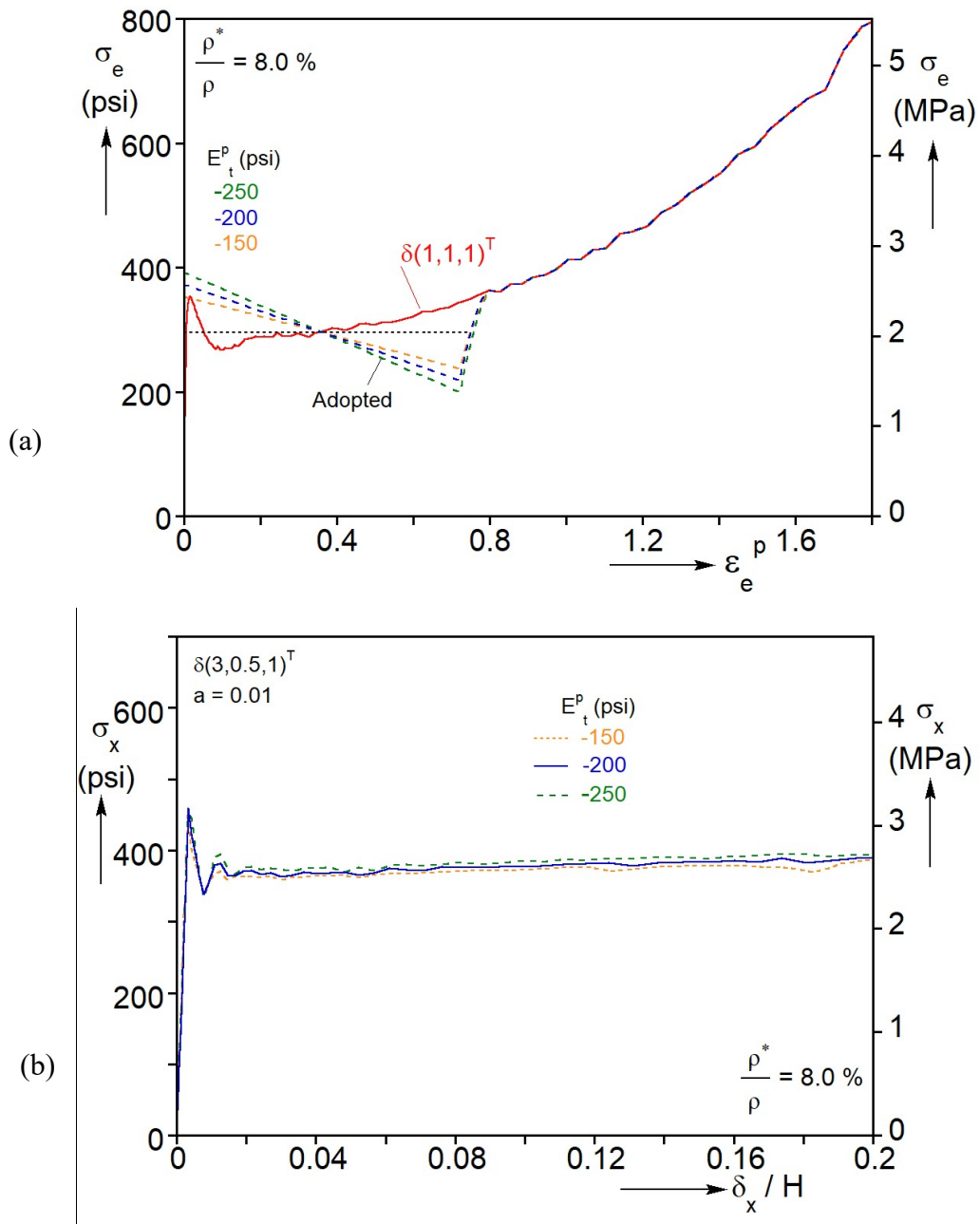
Fig. 5.33: (a) Equivalent stress-strain responses with three different slope softening branches. (b) Expanded early parts of $\sigma_x - \delta_x / H$ responses produced using the three stress-strain responses.
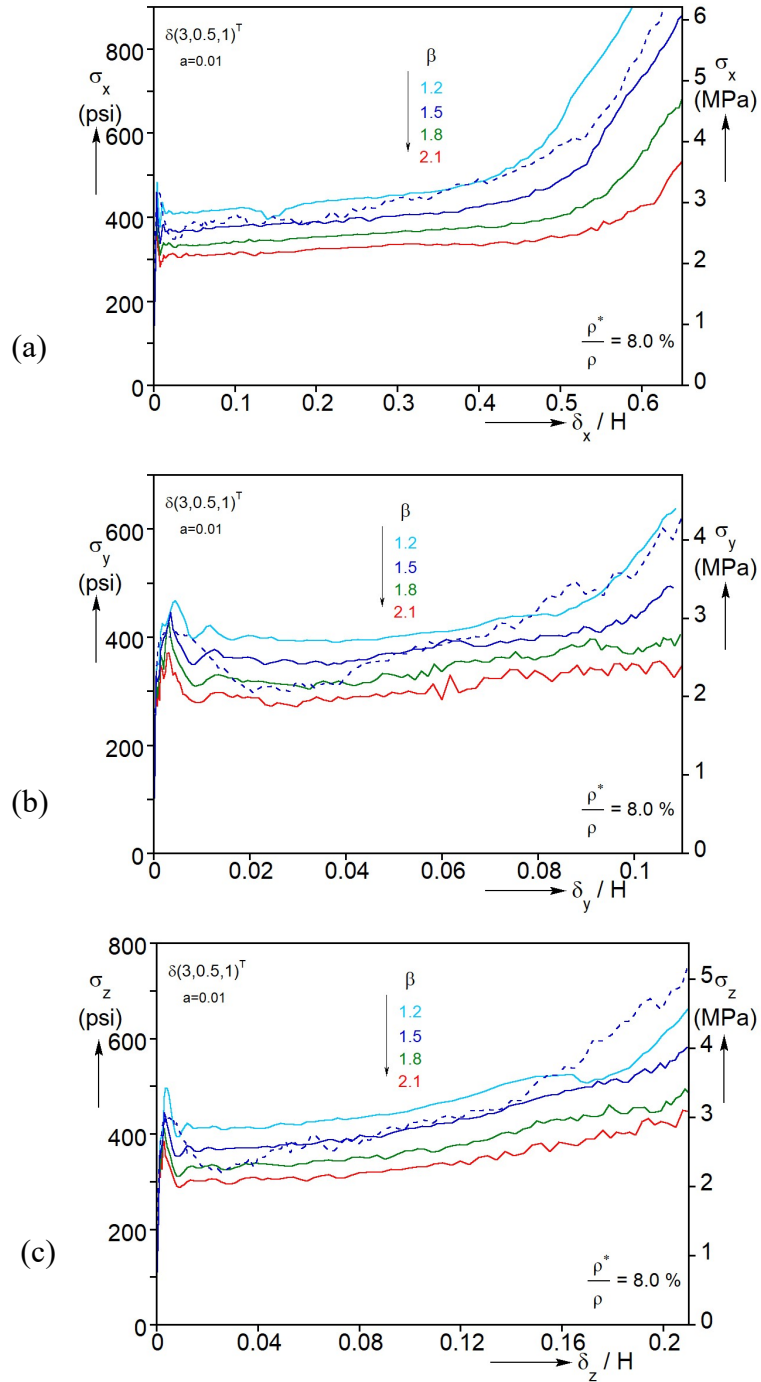
Fig. 5.34: True stress-displacement responses for the $(3, 0.5, 1)^T$ loading paths using four different β : (a) in the *x*-direction, (b) *y*-direction, and (c) *z*-direction.

154

Chapter 6: Conventional Triaxial Crushing of Low-Density Foams[7]

In Chapter 3 a true triaxial numerical apparatus was used to crush micromechanically accurate open-cell Al-alloy foams under three sets of radial displacement paths. It was shown that under this loading the foam deformed inhomogeneously exhibiting the same three deformation regimes observed under uniaxial compression. Chapter 5 showed that this inhomogeneous behavior can be reproduced at the continuum level using the compressible constitutive model developed in Chapter 4. This Chapter examines the crushing behavior of the same foams under different triaxial loading histories induced by the more conventional triaxial loading setup. Here the foam loaded under uniform external pressure is compressed in one direction under displacement control (e.g., see Triantafillou et al., 1989; Triantafillou and Gibson, 1990; Gioux et al., 2000; Deshpande and Fleck, 2000).

A set of triaxial tests at different pressure levels is first performed numerically on micromechanically accurate random foam models generated as described in Chapter 2. The compressible constitutive model developed in Chapter 4 is then used in a solid finite element model of the triaxial test to simulate the foam behavior. Section 6.1 describes conventional triaxial test results on the micromechanically accurate foam models. Section 6.2 describes corresponding triaxial crushing calculations based on the homogenized model. A significant part of the study in Chapter 6 appears in Yang and Kyriakides (2019c).

6.1 CRUSHING OF RANDOM FOAMS UNDER CONVENTIONAL TRIAXIAL LOADING

6.1.1 Triaxial Crushing Setup

The random foam test setup is shown in Fig. 6.1a. A cubical foam model with dimensions H^3 is placed between two rigid surfaces. Hydrostatic pressure, P, is applied first by applying point forces F to each node on the surfaces $x = H, y = H,$ and $z = H$ (e.g., see Fig. 6.1b). The level of the force $F = PA / N$, where A is the current area of the

---

face, and N is the number of nodes on the face (for this size random foam, about 200). The pressure is reacted at the three other faces of the cube, $x = 0, y = 0, z = 0$, by constraining the normal degrees of freedom of the ligament end nodes on each face.

The foam is compressed in the x-direction through two contacting rigid planes. The plane at $x = 0$ is fixed in space, while the plane initially at $x = H$ is prescribed incrementally a compressive displacement δ_x. Contact between the foam ligaments and the two planes is frictionless. The model is loaded by first gradually increasing the pressure to the desired level. With the pressure held constant, the specimen is compressed by prescribing δ_x. The calculation is performed in LS-DYNA, so to ensure that the loading is quasi-static, the displacement history is chosen slow enough to ensure that the kinetic energy is kept at a much lower level than the internal energy throughout the calculation.

6.1.2 Triaxial Crushing at $P = 100$ psi

Compression tests on the random foam models are performed at six pressure levels: $P = \{0, 50, 100, 150, 200, 250\}$ psi $\{0, 0.345, 0.69, 1.03, 1.38, 1.72\}$ MPa. The case of 100 psi (0.69 MPa) is described in detail in order to present the main characteristics of the crushing behavior at lower pressure levels. Figure 6.2 shows the calculated axial stress minus the pressure plotted against the applied displacement—$(\sigma_x - P) - \delta_x / H$— where σ_x is the reaction force on the bottom plate divided by the original area of the foam. The response is hitherto referred to as "deviatoric" stress-displacement response. Figure 6.3 shows the undeformed and a set of deformed configurations in the $x - y$ plane that correspond to the stations marked on the response in Fig. 6.2 with numbered bullets. The images are taken from the center of the foam block, and for better visualization they are limited to a thickness of $0.12H$—or a little thicker than one cell. Figure 6.4 shows expanded the early part of the response and Fig. 6.5 a set of corresponding deformed configurations. Image ⓪ in both sets of results corresponds to the initial undeformed configuration. Image ① in Figs. 6.5 shows the cross section at a low axial stress after the application of pressure. The pressure loading is seen to have distorted some of the ligaments at the edges, but the rest of the foam

156

is uniformly deformed. The foam initially reacts linearly to compression, but some gradual reduction in stiffness is observed for deviatoric stress larger than about 150 psi (1.03 MPa). Plasticization of ligaments leads to a limit load at station ③ with the stress at about 287 psi (1.98 MPa) and the axial strain at 1.76%. The edges appear more deformed, but the rest of the domain remains uniformly deformed. Increase in the axial compression leads to a drop in stress and localization of deformation. At station ⑤ in Fig. 6.4 at an average strain of about 5%, the stress is down to 230 psi (1.58 MPa), a band of collapsed cells has appeared at the lower right corner of the domain, and the edge at $x = H$ has developed some bowing.

For the foam response at higher displacements, we return to Fig. 6.3 in which station ① corresponds to station ⑤ in Fig. 6.4 and 6.5. Beyond the stress minimum at ①, the stress recovers somewhat and traces a ragged plateau at about 240 psi (1.66 MPa). In image ② at an average axial strain of 0.169, the crushed band of cells at the bottom has broadened. In image ③ at $\bar{\delta}_x = 0.255$, the crushing has spread upwards covering nearly one third of the domain. Although as is usual for random foam crushing, some "stiff" cells in the crushed zone remain relatively undeformed. This image clearly demonstrates the coexistence of mostly crushed and essentially undeformed cell domains, characteristic of materials that exhibit propagating instabilities. The upward propagation of the crushed zone continues in image ④ at $\bar{\delta}_x = 0.369$, while in image ⑤ at $\bar{\delta}_x = 0.461$ the crushing affects the whole domain. Further deformation of the now densified material requires additional effort with the stress following the usual increasing trend. At stations ⑥ and ⑦ at average strains of 0.536 and 0.627, the stress has risen to 331 psi and 427 psi respectively (2.28 MPa and 2.94 MPa).

6.1.3 Triaxial Crushing at $P = 200$ psi

The triaxial crushing results at a higher pressure, $P = 200$ psi (1.38 MPa) are presented next but in a less detail. Figure 6.6 shows the deviatoric stress-displacement response in the x-direction. Figure 6.7 shows the corresponding deformed configurations of a slice in the $x - y$ central plane corresponding to the numbered bullets on the response

in Fig. 6.6. The deviatoric stress response has a similar trend as reported for $P = 100$ psi (0.69 MPa). It starts with an elastic branch that terminates into a stress maximum about 216 psi (1.49 MPa) at $\bar{\delta}_x = 0.014$. Following the limit load, the stress drops to a local minimum, recovers, and enters an extended ragged plateau up to an average strain of about 49%. The plateau stress is at about 153 psi (1.05 MPa), approximately 87 psi (0.60 MPa) lower to the corresponding level for $P = 100$ psi (0.69 MPa). For larger displacements, the response follows a stiffening branch.

The deformation is inhomogeneous with crushed and uncrushed cells coexisting as the stress plateau is traced. Image ① in Figs. 6.7 shows that at $\bar{\delta}_x = 0.079$ a band of collapsed cell has initiated at the same lower right location as for $P = 100$ psi (0.69 MPa). The rest of the domain is uniformly deformed. However because of the higher pressure, a larger number of edge ligaments have distorted significantly. Subsequently as crushing continues, the localized band propagates upwards, with the cells in the crushed zone more compacted than for $P = 100$ psi (0.69 MPa). By station ④ at $\bar{\delta}_x = 0.398$, the crushing has consumed more than half of the domain, while the upper part remains essentially undeformed. In image ⑤ at $\bar{\delta}_x = 0.477$, the localization has spread to the cells adjacent to the $x = H$ plane, leaving some "stiff" zones in the upper part of the domain uncrushed. Soon after the station, the crushing covers the whole domain, and the deformation is back to homogeneous once more. The material has densified and so the stress increases with further compression. Thus at $\bar{\delta}_x = 0.561$ and 0.639 at stations ⑥ and ⑦, the stress has risen to 239 psi and 367 psi respectively (1.65 MPa and 2.53 MPa), which are lower than the corresponding values of $P = 100$ psi (0.69 MPa).

6.1.4 Response at Different Pressure Levels

The behavior of the random foam for triaxial tests at the other pressure levels considered is broadly similar, and consequently the results of the six pressure levels are discussed as a group. It's noted that the boundary conditions in the pure compression case, $P = 0$ psi, are consistent with the five other triaxial crushing cases and thus different from

158

the uniaxial compression setting reported in Gaitanaros et al. (2012). The crushing responses from $P = 0$ psi and uniaxial compression, however, are very similar. Figure 6.8 shows the six deviatoric stress-displacement responses calculated. All responses exhibit the same three-regime behavior as those of the two pressure cases already discussed. Each has an initial stiff and stable regime that terminates in a stress maximum during which the foam deforms uniformly. Beyond the limit stress, localized cell crushing initiates at an internal location with "weaker" cells. Subsequently, cell crushing gradually spreads through the domain while the stress traces a ragged plateau. By an axial strain of about 50%, crushing has consumed the whole domain. Further compression of the densified material requires additional effort resulting in a saturation-type stiffening response.

Figure 6.9 shows an expanded view of the early parts of the six responses. Included with dashed lines are estimates of the initial elastic slopes using

$$\frac{\sigma_x - P}{\varepsilon_x} = E^* \left[1 - \frac{(1 - 2\nu^*)}{\dfrac{\sigma_x}{P} - 2\nu^*} \right] \tag{6.1}$$

which is based on the average isotropic properties of the foam of $\{E^*, \nu^*\} = \{63.3 \text{ ksi–436 MPa}, 0.36\}$ from Chapter 4. For the lower pressures the initial elastic responses follow Eq. (6.1) well. However, as the pressure increases, inelastic bending of the end ligaments where the forces are applied tends to reduce the overall stiffness below the value for an infinite elastic medium.

Returning to the full responses in Fig. 6.8, increase in the pressure precipitates earlier plastification of the domain. This results in lower limit stress and makes the descending part of the response more abrupt. Increase in pressure lowers also the stress plateau and appears to increase somewhat its extent. The decreasing trend of the limit and average plateau stresses with pressure is demonstrated in Fig. 6.10 where the plateau stress traces a trajectory with a somewhat larger negative slope.

The inhomogeneous crushing that takes place as the deviatoric stress traces its plateau is demonstrated in Fig. 6.11, which shows a deformed configuration in the $x - y$

159

plane from each pressure loading taken at $\bar{\delta}_x = 0.37$. It is worth pointing out that for pressure levels up to and including 200 psi (1.38 MPa), local collapse of cells initiated at an internal site on the lower right as illustrated in image ① in Fig. 6.3. The coexistence of crushed and uncrushed cell domains is quite evident for all pressures. However as the pressure increases, the crushed zone becomes more compacted affecting a smaller part of the domain, while the uncrushed zone is less deformed. This behavior makes the two deformation regimes more distinct and is responsible for the apparent increase in the extent of the stress plateaus with pressure.

In physical triaxial experiments on foams and other compressible materials, pressure is usually applied through a membrane that surrounds the test specimen. In the present model, pressure loading is applied via single forces acting at the free ends of ligaments at three of the foam bounding planes. This has the drawback of causing inelastic bending of edge ligaments at an earlier stage than in the interior of the foam model. For example for $P = 300$ psi (2.07 MPa), this local action resulted in the collapse of the foam during the pressurization phase of the loading. For $P = 250$ psi (1.72 MPa) the specimen stayed intact during pressurization but, unlike the rest of the cases, localization first initiated at the top where excessive bending of edge ligaments created a weaker part of the domain. Local crushing initiated also at the lower end at a later stage, which resulted in the two crushed zones observed in the image in Fig. 6.11.

6.2 CRUSHING OF HOMOGENIZED FOAM MODELS UNDER CONVENTIONAL TRIAXIAL LOADING

The random foam test results reported above are now simulated at the continuum level using the compressible constitutive model of Chapter 4 in a finite element model of a solid cylinder under triaxial loading. The constitutive model is calibrated to the equivalent stress-strain relationship described in Section 4.2.3. The calculations are performed in ABAQUS/Explicit.

6.2.1 Triaxial Crushing Setup

As in most conventional triaxial tests, the solid domain analyzed is a circular cylinder of height H and diameter H as shown in Fig. 6.12. The domain is discretized with 8-node incompatible linear elements, C3D8I. The domain is divided into an outer thick cylinder covering $0.125 \leq r / H \leq 0.5$ and an inner solid core with $r \leq 0.125H$. The outer cylinder is meshed with 84 sectors with 4.3° angular span. The inner core is meshed with irregular elements in the plane, which are chosen so as to connect to the radial elements of the outer cylinder at $r / H = 0.125$ (see cross-sectional view in Fig. 6.12). There are a total of 1131 elements in the plane and 40 elements along the axial direction.

To minimize biasing of the anticipated localization of deformation, and facilitate a "smoother" propagation of higher deformation, the elements of the outer tubular domain are perturbed as follows: let x_o be the initial position vector of a node; then the perturbed position is given by $x = x_o + p\xi$ where $\xi_i, i = 1,3$ are the amplitudes of the perturbation and p is a distributed random number between -0.5 and 0.5 (same as in Section 4.5 of Jang et al. (2008)). Unless otherwise stated $|\xi| = 0.01H$ is used. Perturbation is applied to all elements of the outer cylinder except that the top and bottom surfaces were perturbed only in their planes, and the nodes on the outer cylindrical boundary were only perturbed in the x-direction. In addition, to help initiate localization, a small radial depression is introduced to the surface of the model covering the whole circumference at $0.3 \leq x / H \leq 0.4$ (Fig. 6.12). The depression is in the form of a half sine wave and has typical amplitude of $0.01H$.

The top and bottom surfaces of the cylinder are in contact with rigid planes as shown in Fig. 6.12. The bottom plane is fixed in space while the top one is used to prescribe incrementally compressive displacement δ_x to the cylinder. Pressure P is applied on the cylindrical and top surfaces through the "Dsload" distributed load command of ABAQUS. A general contact algorithm is applied for the contact between the rigid planes and the

domain. Lateral rigid body motion of the domain is prevented by introducing a small amount of friction (Coulomb coefficient $\mu = 0.1$) between the cylinder and the rigid planes.

As in the random model, pressure is incremented first to the desired level. The model is then compressed by incrementally prescribing δ_x up to a value of about 0.65 while the pressure is held constant. The calculations are performed in an Explicit code, thus in order to keep the displacement incrementation slow enough for the solution to be quasi-static, the loading history described in from Section 3.1.2 is adopted.

6.2.2 Performance of the Homogenized Model at $P = 100$ psi

The performance of the homogenized model is examined first through a conventional triaxial test at the relatively low pressure level of $P = 100$ psi (0.69 MPa). Figure 6.13 shows the calculated $(\sigma_x - P) - \delta_x / H$ response for an imperfection amplitude of $0.01H$ — σ_x is again the reaction force on the stationary base plane divided by the original cross sectional area of the cylinder. Figure 6.14 shows a set of corresponding deformed configurations of a cross sectional plane that passes through the axis of the cylinder (note that the deformation patterns are not axisymmetric). The response exhibits the same three behavior regimes as those of the random foam tests in Section 6.1.

The initial stiff and stable elastic response follows that of the random foam in Fig. 6.2. The load maximum of 277 psi (1.91 MPa) is about 3.5% lower than that of the random foam. This value is primarily governed by the maximum stress of the up-down-up response adopted, and to a lesser degree by the amplitude of the imperfection used. The response drops down to a local minimum, triggering localization in the form of a planar band of higher deformation normal to the direction of axial compression. Subsequently, the deviatoric stress starts tracing a ragged plateau that extends to about $\bar{\delta}_x \approx 0.49$. In the course, the higher deformation band spreads initially downwards and subsequently upward, while mostly remaining perpendicular to the direction of compression, until eventually the whole domain is consumed. The stress plateau has an average stress of about 232 psi (1.60 MPa), which is 2.9% lower than that of the random foam. The choice of the Maxwell stress

162

of the up-down-up response in Fig. 4.6 governs this degree of agreement. For strains larger than about 0.50, the response jumps to the level of the stiffening branch of the random foam and tracks it well for higher strains.

A more detailed view of the initiation of localized deformation in Fig. 6.15 plots expanded the early part of the $(\sigma_x - P) - \delta_x / H$ response, and Fig. 6.16 shows a set of corresponding configurations of the early evolution of the band. Here the axial section of the cylinder is shown truncated for improved visualization. Deformation localizes soon after the initial stress maximum is achieved. In image ① soon after the first stress valley at $\overline{\delta}_x = 0.024$, a band of higher deformation has initiated from the imperfection on the outer surface of the cylinder and has covered the whole cross section. The band with a strain that ranges between 0.2 to 0.6, is about one element wide but appears to be affecting parts of at least two elements (note that the incompatible elements used allow internal strain gradients). In image ② at $\overline{\delta}_x = 0.033$, the band is more distinct with parts of it having a strain that approaches 0.8, a value that is on the stiffening branch of the material response. In image ③ at $\overline{\delta}_x = 0.044$, the band is at least two elements wide but has also spread to the neighboring elements below it. The strain in the central part of its width is now about 0.8. The broadening of the band appears to be occurring is spurts that cover part of the cross section. Further spreading of this band across the cross section is temporarily terminated, and localization initiates at other sites in the same cross sectional plane. These progressive initiation and arrest events cause the stress undulations observed in Fig. 6.15. It is worth mentioning that the mesh perturbation adopted tends to reduce their amplitude. In image ④ at $\overline{\delta}_x = 0.052$, the band has propagated downward covering three elements; in image ⑤ at $\overline{\delta}_x = 0.066$, it has spread to at least four elements, and in image ⑥ at $\overline{\delta}_x = 0.076$ to nearly six. Away from the edges of the band, the strain is approximately 0.8 while in the rest of the domain the strain is at the value on the initial ascending branch that corresponds to the current level of stress.

Discussion of subsequent events will continue using the overall response and corresponding images in Fig. 6.13 and 6.14, where station and image ① correspond to ④ in Fig. 6.16. The band continues its downward propagation tracing a similar ragged stress plateau. Thus in image ② at $\bar{\delta}_x = 0.167$, it has deformed most of the domain below the imperfection. In image ③ at $\bar{\delta}_x = 0.259$, the higher strain band has reached the lower boundary and propagation continues upwards. In the process an island in the center of the cylinder is left undeformed, presumably the result of some local incompatibility between the perturbed elements in the outer domain and the unperturbed ones of the central core. This island of undeformed material causes the bowing of the propagating front observed in this image. In image ④ at $\bar{\delta}_x = 0.371$, the bowed front has propagated upwards and in image ⑤ at $\bar{\delta}_x = 0.457$ it has approached the upper boundary. Soon thereafter, the whole domain is deformed to the higher strain, and at $\bar{\delta}_x \approx 0.49$ the response takes an upward trajectory. It joins the stiffening branch of the random model with the whole domain deforming homogeneously as evidenced by images ⑥ and ⑦ at $\bar{\delta}_x = 0.538$ and 0.626 respectively.

In summary, the compressible constitutive model coupled with the up-down-up material response adopted have enabled the initiation and propagation of deformation in the homogenized model, and reproduced quite accurately the three-regime response of the random foam. In the absence of the random microstructure of the foam, the deformation patterns of the homogenized model are different, and in many respects are influenced by the mesh adopted.

6.2.3 Performance of the Homogenized Model at $P = 200$ psi

Results representative of higher pressure, $P = 200$ psi (1.38 MPa), are discussed next but with less detail. Figure 6.17 plots the calculated deviatoric stress-displacement response together with that of the random foam. Figure 6.18 shows a set of deformed configurations corresponding to the numbered bullets on the response. Overall the

calculated response reproduces the trends of the random foam. It exhibits the same three regime behavior. Following the limit load, the stress enters a ragged plateau up to an average strain of about 48%. The amplitude of the fluctuation is larger than those of the random foam; they are also somewhat larger than the fluctuations of $P = 100$ psi (0.69 MPa). The fluctuations are again attributed to the progressive initiation and arrest of higher strain reported in Section 6.2.2. The mean level of the stress plateau is at about 132 psi (0.91 MPa), 13.6% lower than that of the random foam. At higher displacements, the stress reverts to a stiffening branch, due to the densification of the model.

Figure 6.18 clearly shows that, as the stress plateau is traced, a high deformation zone and essentially undeformed zones coexist. In station ① at $\bar{\delta}_x = 0.081$, the stress has gone past the highly oscillatory trajectory in the early part of the crushing, and traces a less ragged plateau. A band of deformation of about 0.8 has initiated from the imperfection and in this image consumes 6~8 elements. Furthermore, the outer edges of the higher deformation zone cover only parts of planar rows of elements. Subsequently, the band spreads downwards. By station ③ at $\bar{\delta}_x = 0.313$, the band has consumed the lower half of the domain, and continues its propagation towards the upper boundary. The rest of the domain is essentially undeformed. In image ④ $\bar{\delta}_x = 0.398$, the band continues to spread upwards and by station ⑤ at $\bar{\delta}_x = 0.476$, the higher deformation zone is about to consume the whole domain. Soon thereafter, the band reaches the upper boundary. By stations ⑥ and ⑦ at $\bar{\delta}_x = 0.564$ and 0.641 respectively, the deformation is again back to homogeneous and the response traces a stiffening branch. In short, under triaxial loading at $P = 200$ psi (1.38 MPa), the continuum model captures the inhomogeneous behavior of the foam.

6.2.4 Performance of the Homogenized Model: Pure Compression

The pure compression case is worth special examination also. Figure 6.19 plots the stress-displacement response from the homogenized model in a solid line, and the corresponding one of the random foam in a dashed line. Figure 6.20 shows a set of deformed configurations corresponding to the numbered time steps in the loading history

shown in Fig. 6.19. The calculated stress response again follows a trajectory very similar to that of the random foam. It starts with an initial elastic branch that terminates into a stress maximum of about 327 psi (2.26 MPa) at $\bar{\delta}_x \approx 0.038$. Following the local maximum, the stress drops to the minimum, recovers, and traces an extended plateau at about 319 psi (2.20 MPa), which is about 1.6% higher than that of the random foam. At higher displacements, the response follows a gradual stiffening branch, nicely coalescing with that of the random foam.

In image ① in Fig. 6.20 at $\bar{\delta}_x = 0.082$, an inclined band of higher deformation has initiated from the imperfection at the outer surface of the cylinder and has formed a conical shape. It has an inclination of about 30 degrees in the outer domain and connects to a relatively flat dome over the central core. In image ② at $\bar{\delta}_x = 0.165$, the initial localized band has broadened upwards covering a width of about 13 elements in the center core and about 7 elements close to the outer surface. A second inclined band of higher deformation has initiated somewhere in the upper domain, and connected to the dominant band. Subsequently, the higher deformation zone continues to propagate upwards, leaving behind a ring of undeformed material over the circumference of the domain. This results in local bowing out observed in images 3-7. In image ④ at $\bar{\delta}_x = 0.356$ the band of higher deformation approaches the upper boundary and subsequently starts to spread downward. By station ⑤ at $\bar{\delta}_x = 0.449$, the band approaches the bottom plane close to the outer surface. Now, most of the domain is affected by the higher deformation and the stress starts to trace an increasing trend. In station ⑦ at $\bar{\delta}_x = 0.603$, the stress increases to 481.0 psi (3.32 MPa). The higher deformation zone has covered the whole domain except for the persistent ring.

6.2.5 Response at Different Pressure Levels Based on the Homogenized Model

Similar calculations are carried out for all triaxial test pressure levels using the homogenized model. The same depression imperfection was used for the five lower pressures, while for $P = 250$ psi (1.72 MPa) the imperfection was increased to $0.015H$.

The recorded behavior is broadly similar and will be discussed as a group. Figure 6.21 plots together the six deviatoric stress-axial displacement responses recorded. They all exhibit the same three-regime response with an initial elastic and stable branch, a limit load, an extended stress plateau, and a stable stiffening branch. As the pressure increases, the response traces an increasingly lower trajectory, with the six responses comparing quite well to the corresponding random responses in Fig. 6.8.

The elastic branches are in concert with the elastic properties adopted in the constitutive model. The stresses at the limit loads are plotted in Fig. 6.10 against pressure where they are seen to follow the same downward trend with pressure as that of the random foam, with most values also being quantitatively close. The stress plateaus traced are more ragged than the random foam stress plateaus in Fig. 6.8, with the amplitude of the fluctuations increasing with pressure. In all cases localization initiated from the imperfection. For the four higher pressures, higher strain propagated progressively along planar rows of elements normal to the direction of compression similar to the propagation described for $P = 100$ psi (0.69 MPa). The stress fluctuations are caused by partial propagation along such planes of elements, local arrest, and initiation at a different site in the same plane, or on immediately neighboring planes of elements. The local spread and arrest of high deformation continues with the front propagating towards the upper and lower boundaries similar to what is reported for $P = 100$ psi (0.69 MPa) in Fig. 6.14. We found the amplitude of these stress fluctuations to be influenced by the perturbation of the mesh adopted. It is quite possible that a different randomization of the mesh that includes the central core of the cylinder may reduce the amplitude of the fluctuations further, but this is not expected to affect the level of the stress plateau. It is worth contrasting the stress fluctuations of the homogenized model with those of the random foam, where the stress undulations on the stress plateaus are caused by the crushing front encountering "stronger" or "weaker" cells in its path. The average values of the six stress plateaus are plotted against pressure in Fig. 6.10 where they are seen to exhibit the same downward trend as the plateau stresses of the random foam. Furthermore they are also quantitatively in good agreement with the values of the random foam.

Figure 6.22 shows a set of deformed images from the solutions of the six pressures analyzed at $\bar{\delta}_x \approx 0.37$. The coexistence of two deformation regimes characteristic of materials that exhibit propagating instabilities is quite evident. For the three higher pressures, the propagating front remained planar and normal to the direction of compression. As reported earlier, for $P = 100$ psi (0.69 MPa) an island of undeformed material caused the propagating front to develop some curvature. For pure compression the initial localization that emanated from the depression imperfection developed a conical shape band (see Fig. 6.20). The conical shape band, together with the second angled band with the opposite inclination, subsequently resulted in local bulging of the deformed domain observed in Fig. 6.22. Similar inclined conical bands but with smaller inclinations developed for $P = 50$ psi (0.345 MPa) causing the more modest bulging observed in this image in Fig. 6.22.

For the five pressure cases propagation of higher deformation terminates at about $\bar{\delta}_x \approx 0.48$. For higher compressions, deformation is uniform with the stress tracing increasing but nearly parallel trajectories. In the case of pure compression, the response is influenced by the presence of the undeformed ring of material and starts increasing somewhat earlier.

6.2.6 Parametric Study

The sensitivity of the homogenized solution to several of the problem parameters is now examined in some detail.

(a)   Softening Modulus E_t^p

The slope of the negative branch of the up-down-up stress strain response adopted was assigned the value of -200 psi (-1.38 MPa) used also in Chapter 5. The effect of the softening modulus E_t^p is examined by crushing calculations for the $P = 100$ psi base case for additional values of E_t^p, -150, -250 and -300 psi (-1.03, -1.72, -2.07 MPa). Figure 6.23a

shows the assumed equivalent stress-strain relations for the four E_t^p values. Figure 6.23b plots the resultant four deviatoric stress–displacement responses. The main effect on the calculated response is on the initial stress maximum, where increase in the negative slope results in an increase in its value. For the three smaller values of E_t^p the mean levels of the stress plateaus are the same, and the amplitudes of the stress plateau fluctuations are similar. In the case of E_t^p = -300 psi (-2.07 MPa), the mean level of the stress plateau increases slightly, while the amplitude of the fluctuations is somewhat smaller. The extents of the plateaus for the four solutions are similar.

(b)   *Mesh Sensitivity of the Solution*

The sensitivity of the solution to the mesh density is examined next. The case of $P = 100$ psi (0.690 MPa) was recalculated using four different mesh densities with total number of elements ranging from about 16,000 to about 45,000, as listed in Table 6.1. The number of elements along the axial direction (i.e., from 25 to 40 elements) and in the cross sectional plane (i.e., two models with the same 40 elements axially) were varied.

Table 6.1:   Four finite element meshes used to examine the sensitivity of the solution to the mesh density

No. of Elements	
Axial	Total
25	15,950
32	20,512
40	25,460
40	45,240

Figure 6.24 plots the stress-displacement response produced by the four meshes. As the mesh density increases the limit stress changes slightly. The stress plateaus produced by the four mesh densities are very ragged but at similar levels, and have very similar extents. Some minor differences in the deformation patterns that develop during the propagation phase of the solution were observed, but overall the solutions presented can

be considered converged. It can thus be concluded that the mesh density has limited influence on the calculated response. As in other problems in which partially softening behavior is introduced, mesh refinement tends to reduce the width of the transition front (see more extensive discussion in Section 5.5.1). This can be avoided by judicious regularization or by inclusion of higher order gradients.

(c)   Mesh Perturbation

The mesh adopted in this Chapter can influence the propagation of the higher deformation and the associated stress fluctuations. The mesh adopted for the main part of the cylinder is based on a regular polar distribution in the plane and a regular axial distribution. For a more optimal solution this regularity was perturbed. The effect of the "strength" of the perturbation is examined by considering two perturbation amplitudes, $\xi / H = 0.0075$ and 0.01, for the $P = 100$ psi (0.69 MPa) loading case. Figure 6.25 plots the calculated deviatoric stress response-displacement responses for the two perturbations. Larger perturbation amplitude reduces the stress fluctuations during the propagation of the front. However, the amount of perturbation that can be applied is limited by excessive distortion of some elements. As a consequence, the perturbation amplitude adopted in this study is limited to 0.01. It is quite possible that a different randomization of the mesh that includes the central core of the cylinder may reduce the amplitude of the fluctuations further, without affecting the level of the stress plateau.

(d)   Imperfection Sensitivity

In order to ensure a recurring evolution of higher strain in the domain analyzed, a local depression imperfection that covers the periphery of the cylinder in Fig. 6.12a was used to initiate localization. The effect of the amplitude and location of the imperfection on the performance of the homogenized model is now examined. The position of the imperfection influences the location of first localization and to some degree the subsequent evolution of events. However it does not affect the stress plateau traced during the propagation of higher deformation, or the stiffening densification branch.

170

The effect of the amplitude of the imperfection on the response is examined using the $P = 0$ loading case. Figure 6.26 plots the calculated stress response for two imperfection amplitudes: $a / H = 0.01$, the value adopted in this study, and 0.015. The results show that with larger imperfection amplitude, the initial stress peak occurs slightly earlier, the stress plateau remains essentially unchanged, and its extent of the plateau is larger by a small amount.

(e)   Coefficient of Friction

A Coulomb friction between two rigid surfaces and the cylindrical domain is added to the model in order to prevent any rigid body motion. Frictionless boundary conditions definitely lead to excessive sliding of the model, while a large friction is quite different from the frictionless condition used in the random foam described in Section 6.1.1. Figure 6.27 shows the calculated deviatoric stress-displacement response for $P = 50$ psi (0.345 MPa) using friction coefficients $\mu = 0.05$ and 0.1. The two responses trace essentially the same trajectory throughout the crushing history. In this study, coefficient of friction $\mu = 0.1$ is adopted.

6.3 SUMMARY

This Chapter presented a complementary study of crushing of low-density foams under a more conventional triaxial loading that examines the behavior under different stress histories. Whereas in Chapters 3 and 5 the foam was crushed in three orthogonal axes under displacement control, in this Chapter micromechanically accurate random foams were compressed under displacement control in one direction while simultaneously loaded under external pressure. Crushing calculations were performed at six pressure levels, $P = \{0, 50, 100, 150, 200, 250\}$ psi, $\{0, 0.345, 0.690, 1.03, 1.38, 1.72\}$ MPa. The foam is found to exhibit the same three-regime behavior as that reported for uniaxial compression. An initial stiff response terminates into a load maximum, triggering localized crushing in a band of cells. Further compression causes the crushed zone to gradually spread with the stress tracing a plateau during which coexistence of crushed and essentially undeformed

171

zones of cells co-exist. The crushed zone is more compacted as the pressure increases. When the whole specimen is crushed, the densified material deforms again homogeneously tracing a hardening response. The level of external pressure tends to lower the limit stress, the stress plateau, and the rest of the response.

The random foam test results were subsequently simulated at the continuum level using a finite element model of a solid cylinder under triaxial loading. The foam material behavior is represented by the compressible constitutive model described in Chapter 4. The homogenized model is shown to capture with good accuracy the three-regime response of the random foam reproducing the limit stress, the plateau stress, its extent, the subsequent hardening of the densified material, and the dependence of these on external pressure. Localization is initiated from a small geometric imperfection introduced to the cylindrical surface covering the whole circumference. In the homogenized model the random microstructure of the foam is replaced by the finite element mesh. For the four higher pressures considered, localization is in the form of planar zones of higher strain normal to the direction of compression. For pure compression and $P = 50$ psi (0.345 MPa), localization results in a band of conical shape. Additional compression causes the bands to broaden while the stress traces a ragged plateau. The band spreading occurs in spurts that cover part of the cross section. This local propagation and arrest of high strain results in stress fluctuations about the mean level of the stress plateau. By perturbing the initially regular mesh of the domain, the amplitude of the fluctuations was reduced. It is quite possible that a better randomization of the mesh can result in a smoother stress plateau.

In summary, Chapter 6 demonstrates that the inclusion of a softening branch in a compressible constitutive model enables the reproduction of the inhomogeneous deformation exhibited by low-density foams under triaxial testing using a solid element model.

172

(a)

(b)
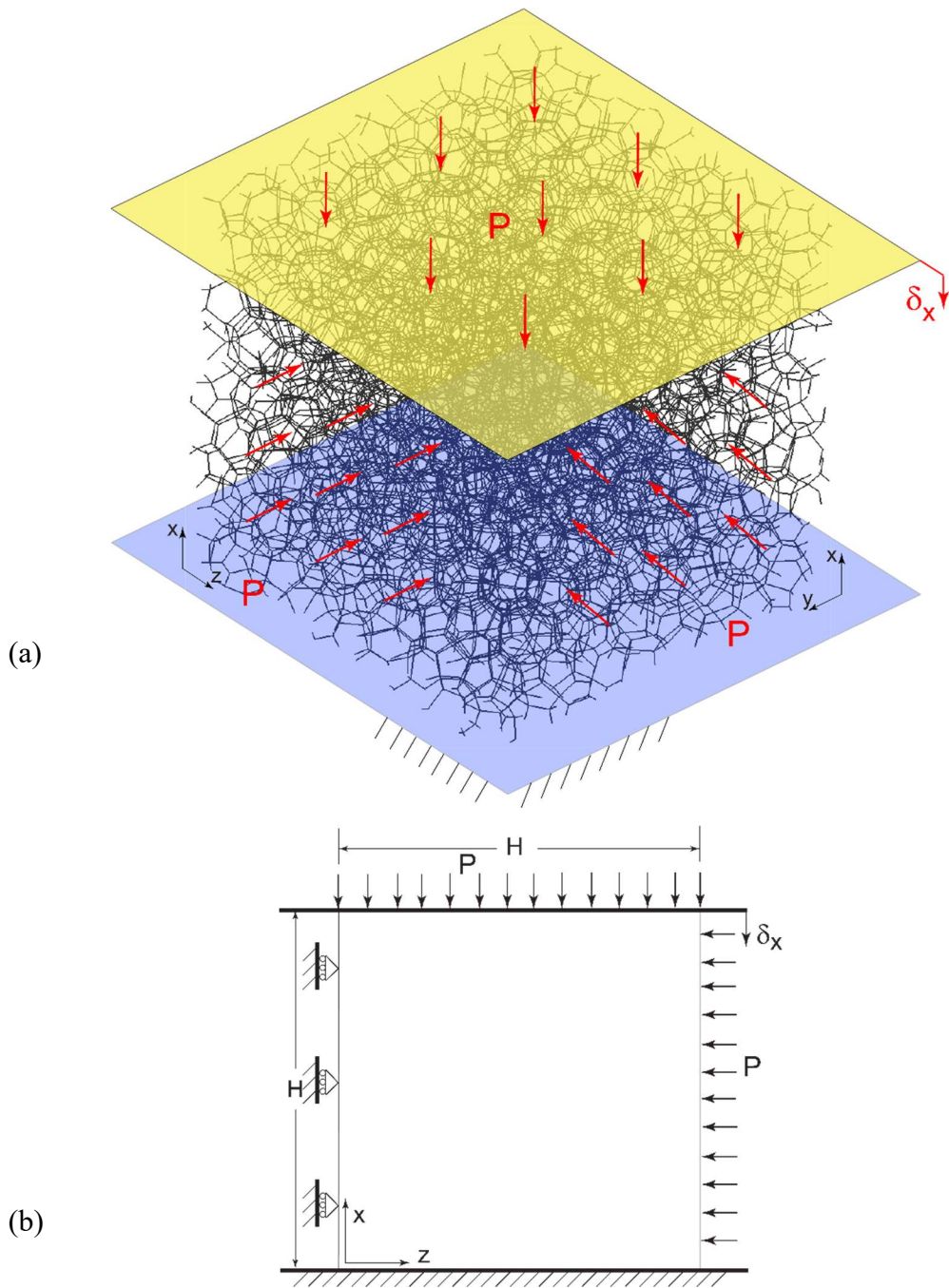
Fig. 6.1: (a) Triaxial test setup for random foam specimens loaded by constant pressure and compressed axially under displacement control. (b) Axial planar view showing the loading and boundary conditions.

173
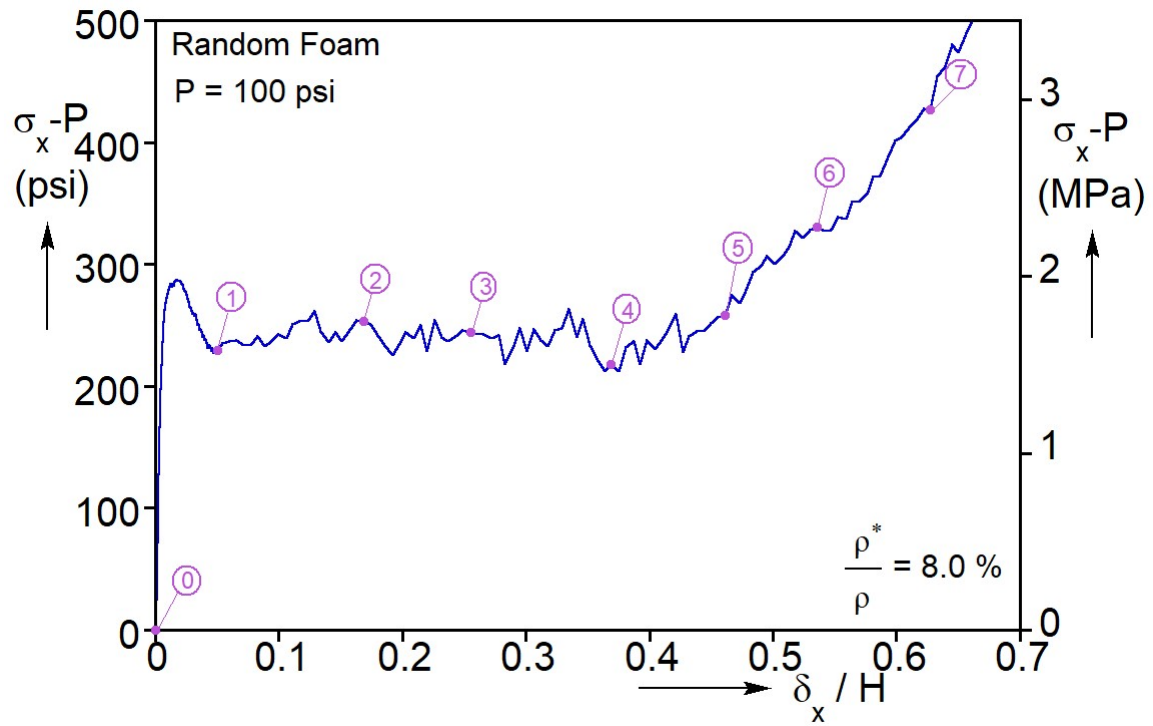
Fig. 6.2: Axial deviatoric stress-displacement response recorded for the triaxial test on the random foam specimen at $P = 100$ psi (0.69 MPa).
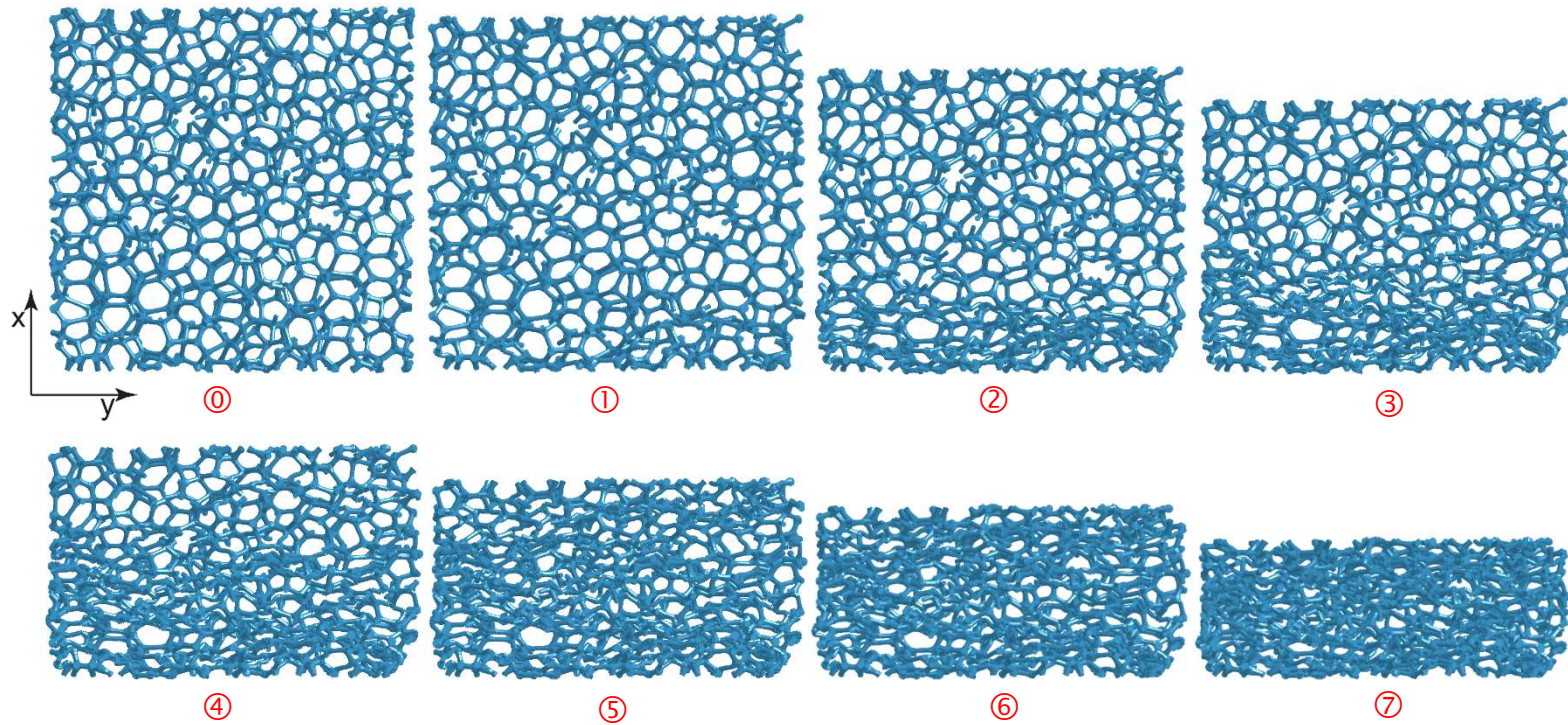
Fig. 6.3: Sequence of deformed foam images from the $x-y$ central plane corresponding to the numbered bullets on the response in Fig. 6.2.
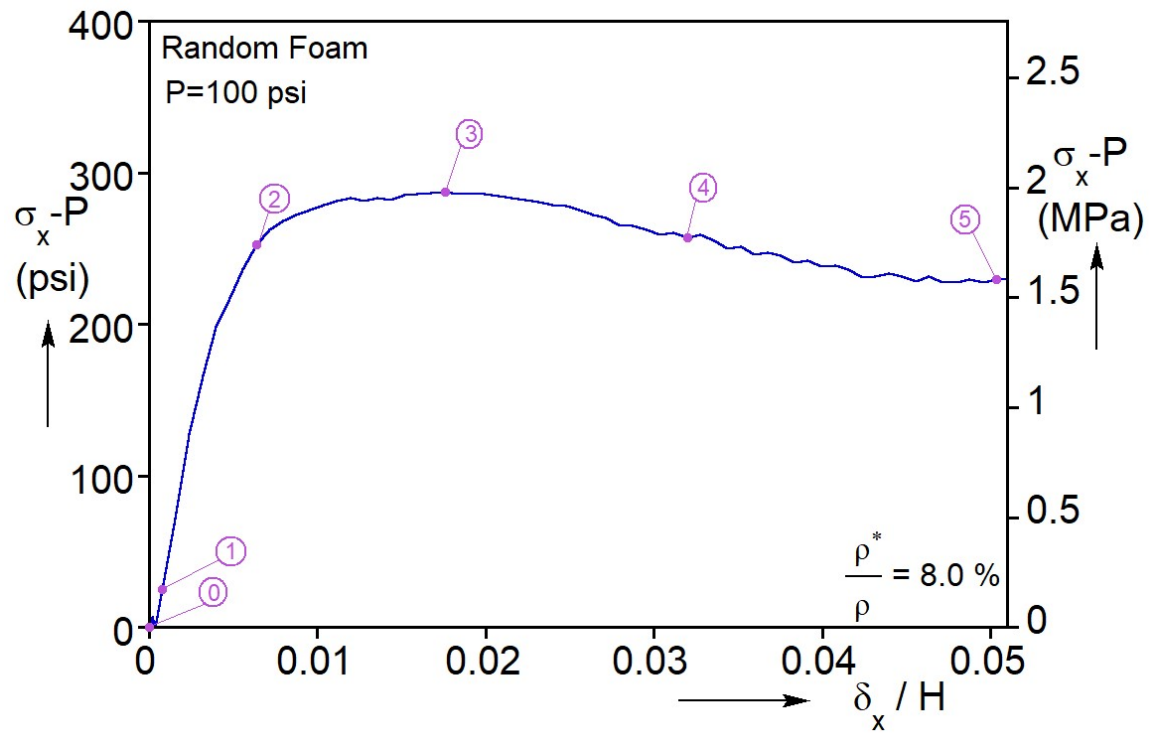
Fig. 6.4: Expanded plot showing the initial part of the axial deviatoric stress-displacement response of the random foam at $P = 100$ psi (0.69 MPa).
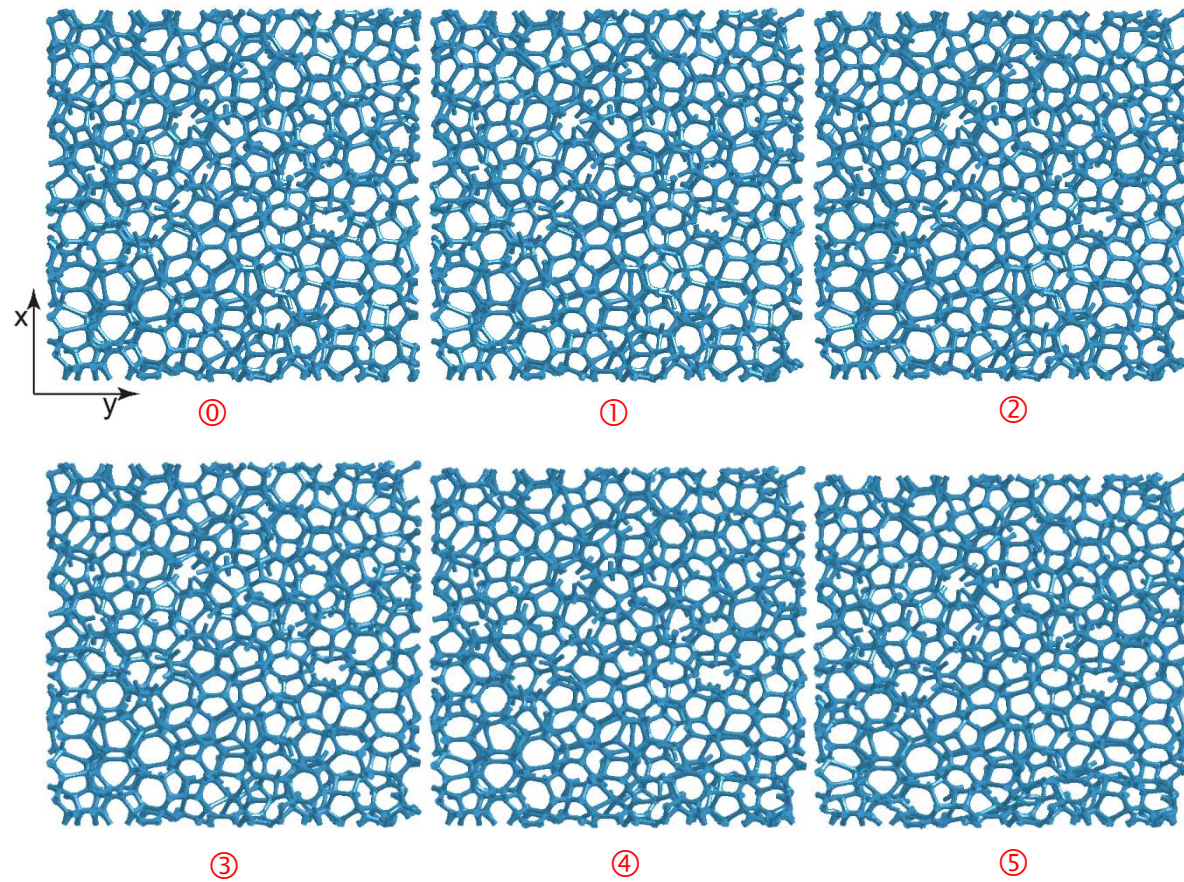
Fig 6.5:   Sequence of deformed foam images from the $x-y$ central plane corresponding to the numbered bullets on the response in Fig. 6.4.
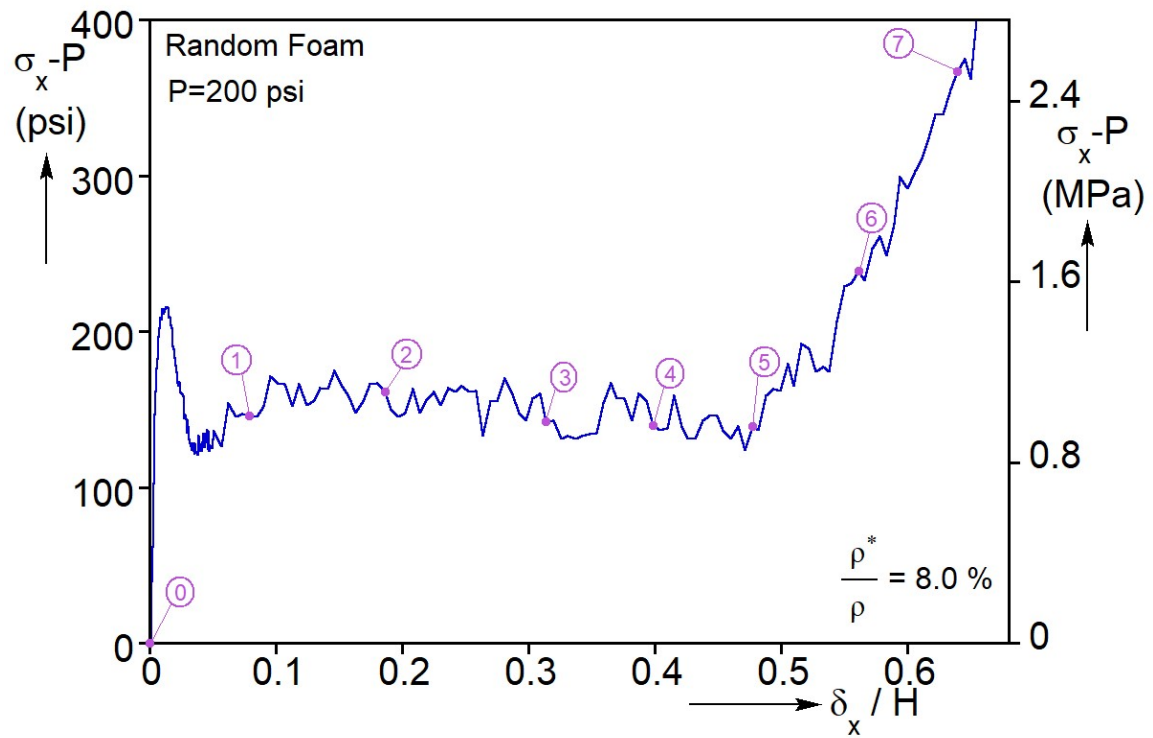
Fig. 6.6:   Axial deviatoric stress-displacement response recorded for the triaxial test on
the random foam specimen at $P = 200$ psi (1.03 MPa).
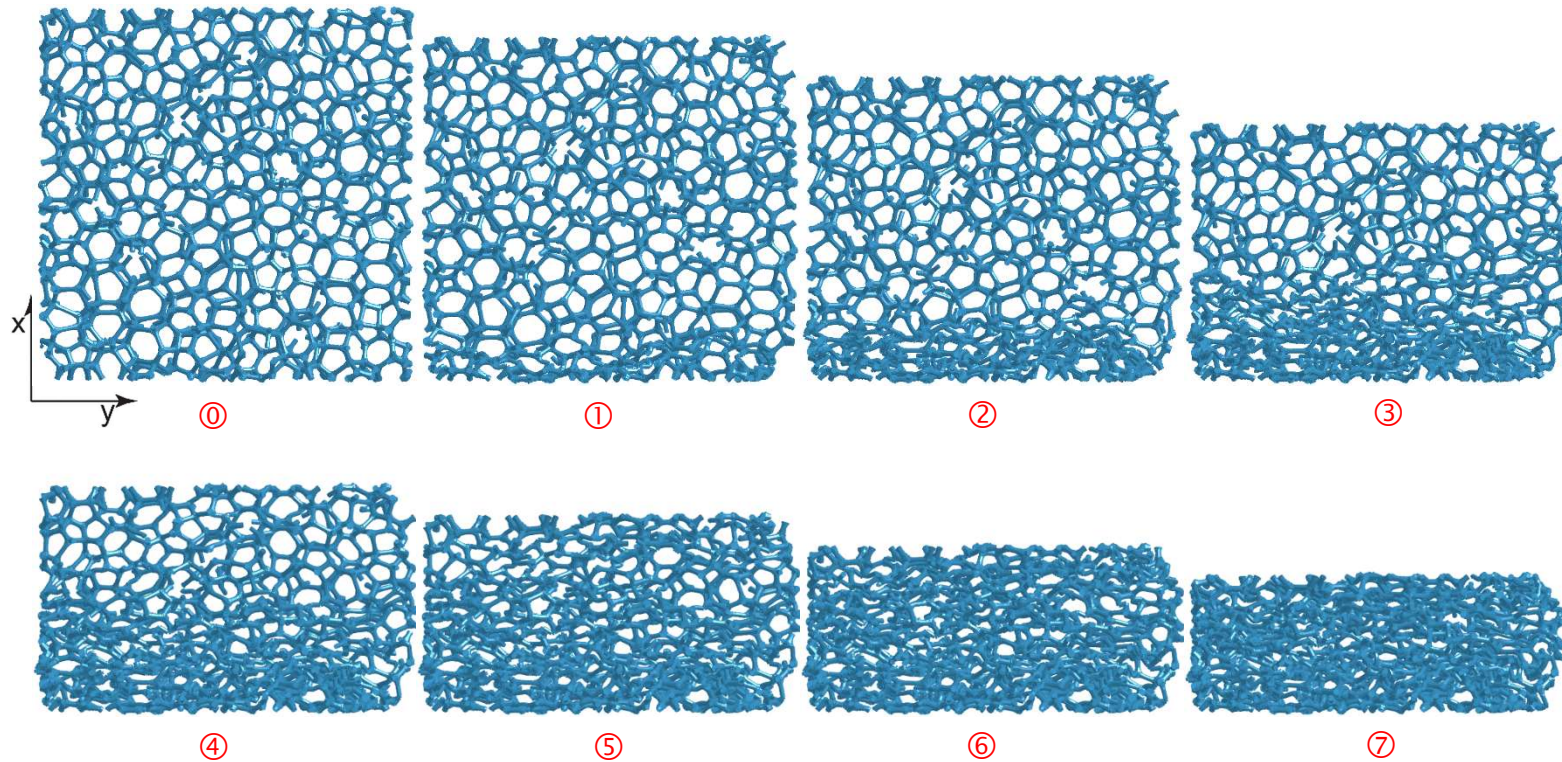
Fig 6.7: Sequence of deformed foam images from the $x-y$ central plane corresponding to the numbered bullets on the response in Fig. 6.6.
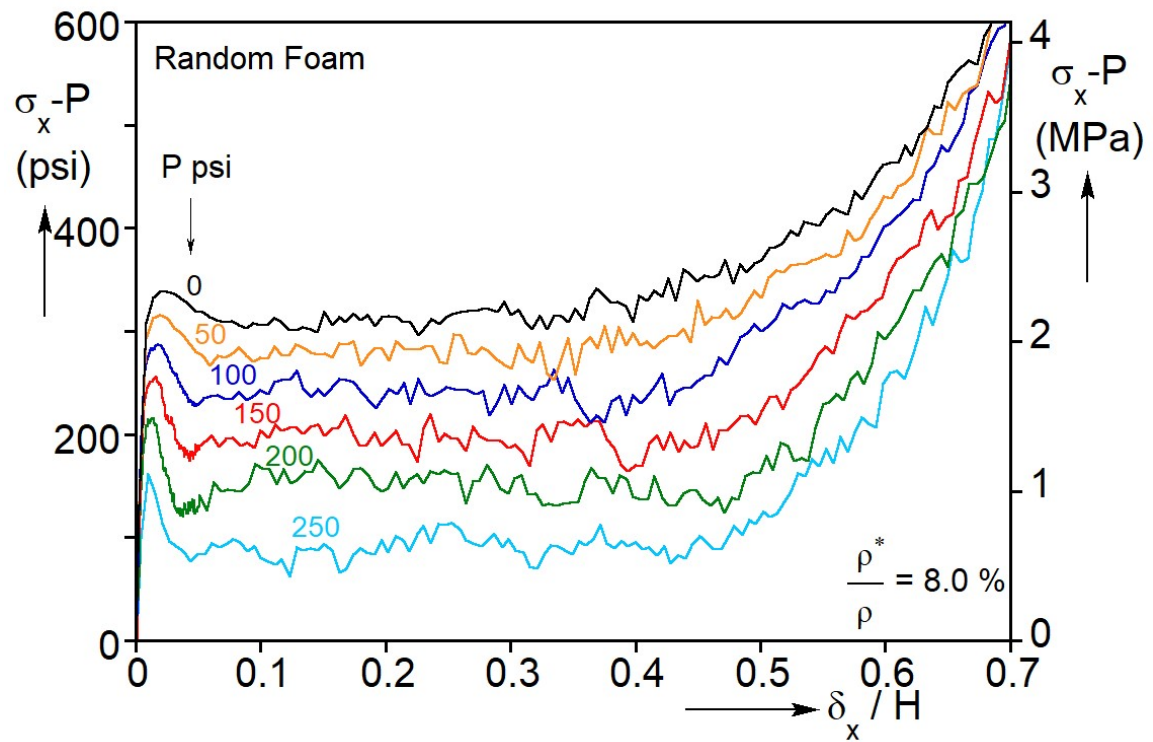
Fig 6.8: Axial deviatoric stress-displacement responses from triaxial tests on the random foam specimen at six pressure levels.
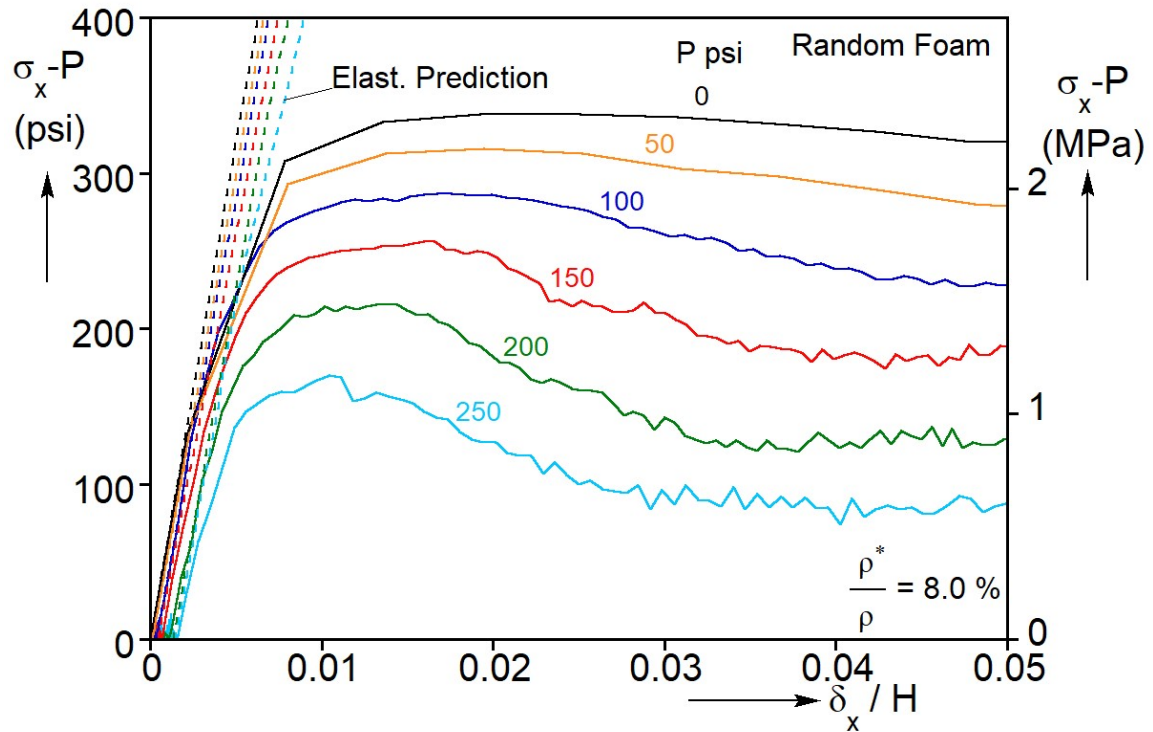
Fig. 6.9:   Expanded early parts of axial deviatoric stress responses at six pressure levels fit by corresponding isotropic elastic predictions based on $\{E^*, v^*\} = \{63.3$ ksi–436 MPa, 0.36$\}$.
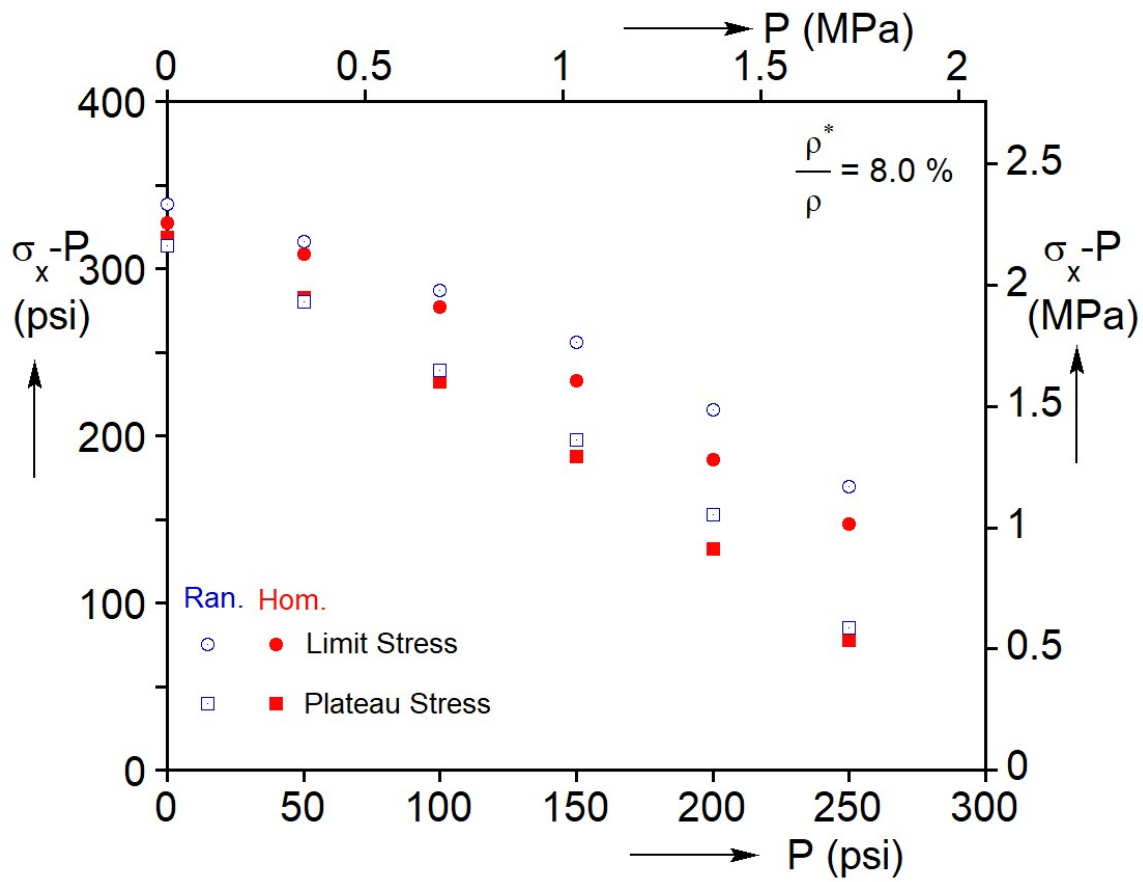
Fig. 6.10: Axial deviatoric stress at the limit load and average stress plateau vs. pressure; results from the random and homogenized model.
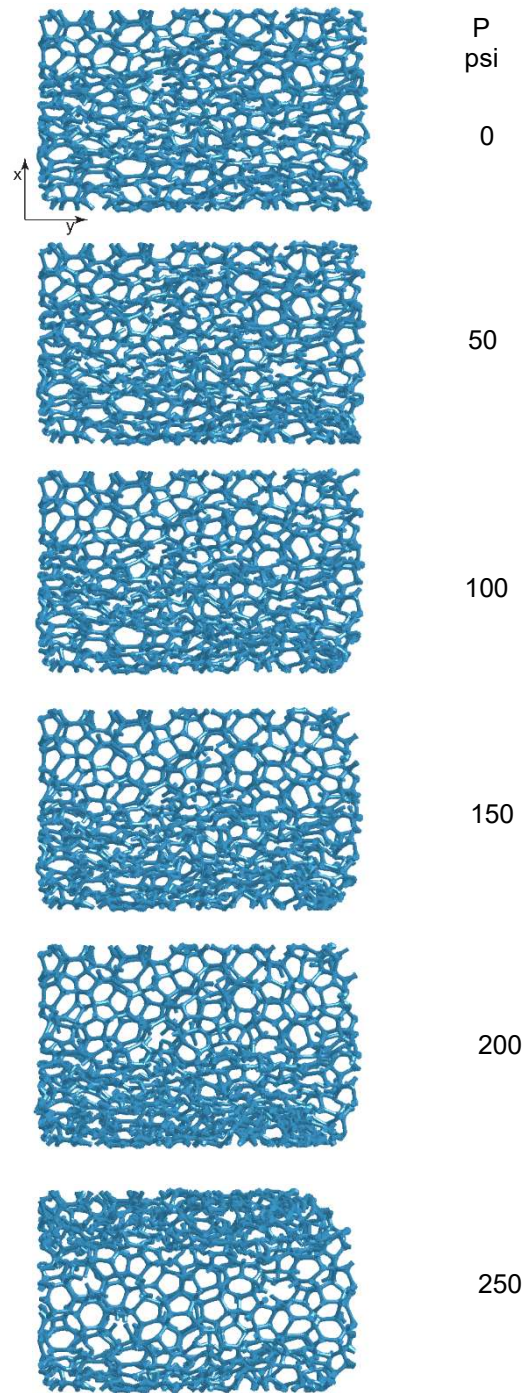
Fig. 6.11:   Deformed random foam images from the $x - y$ central plane at $\delta_x / L = 0.37$ for six pressure levels.

(a)

(b)
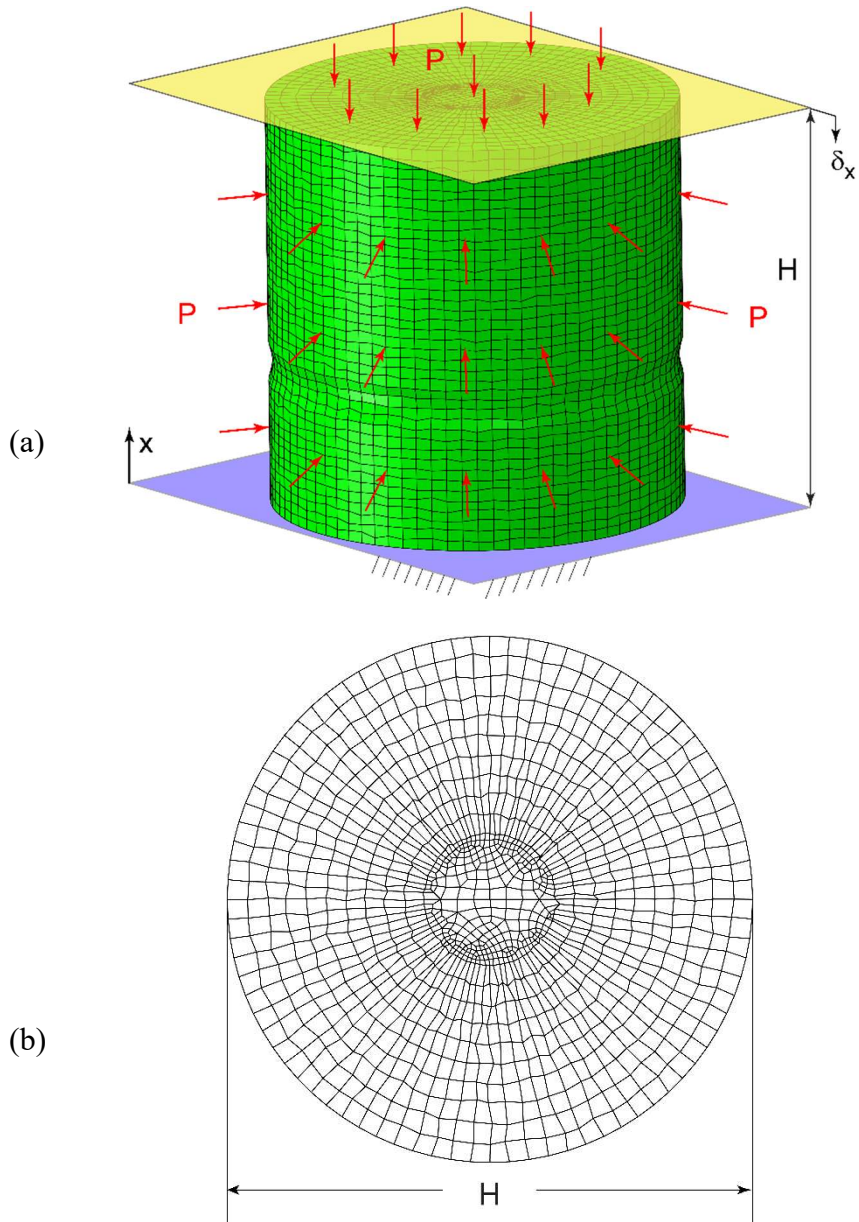
Fig. 6.12:   Specimen geometry and finite element mesh used for the homogenized model.
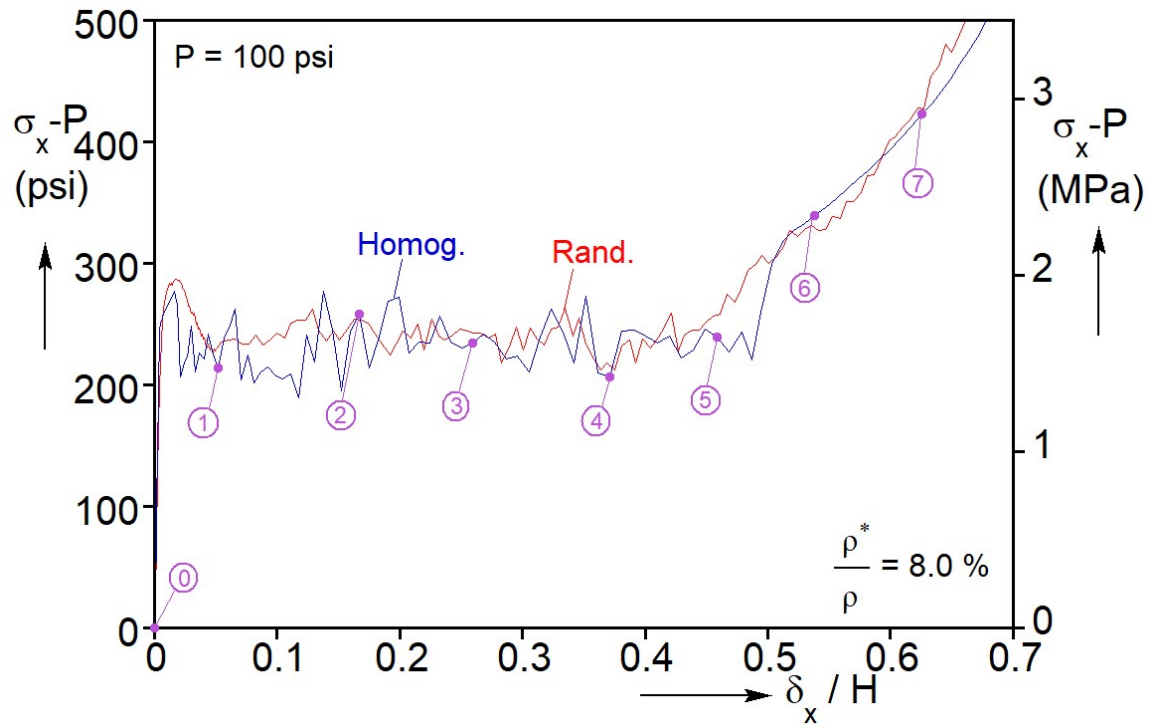
Fig. 6.13: Homogenized model axial deviatoric stress-displacement response for $P = 100$ psi (0.69 MPa) triaxial loading, and the corresponding response from the random foam model.

185
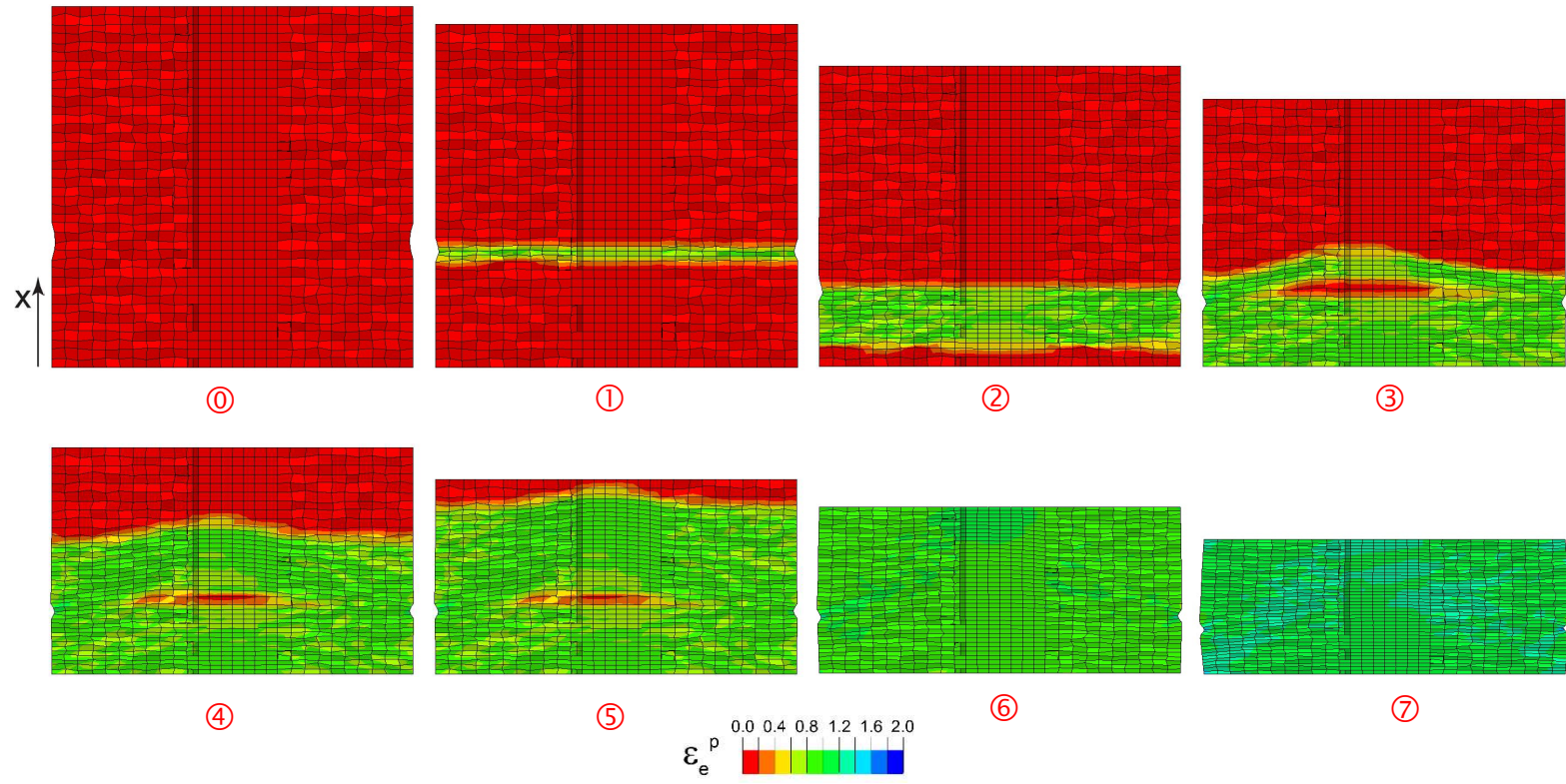
Fig. 6.14: Homogenized model deformed configurations from a central plane along the axis of the cylinder corresponding to the numbered bullets on the response in Fig. 6.13.

186
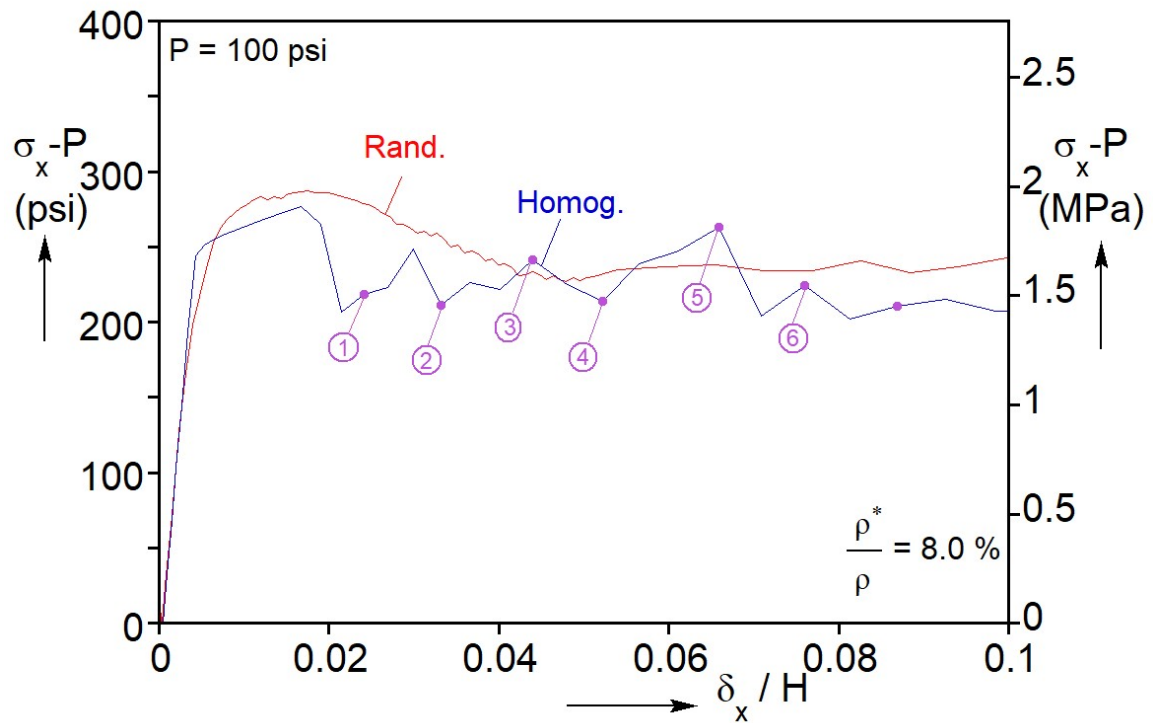
Fig. 6.15: Expanded plot showing the initial part of the axial deviatoric stress-displacement response of the homogenized model at $P = 100$ psi (0.69 MPa); included for comparison is the random foam response.
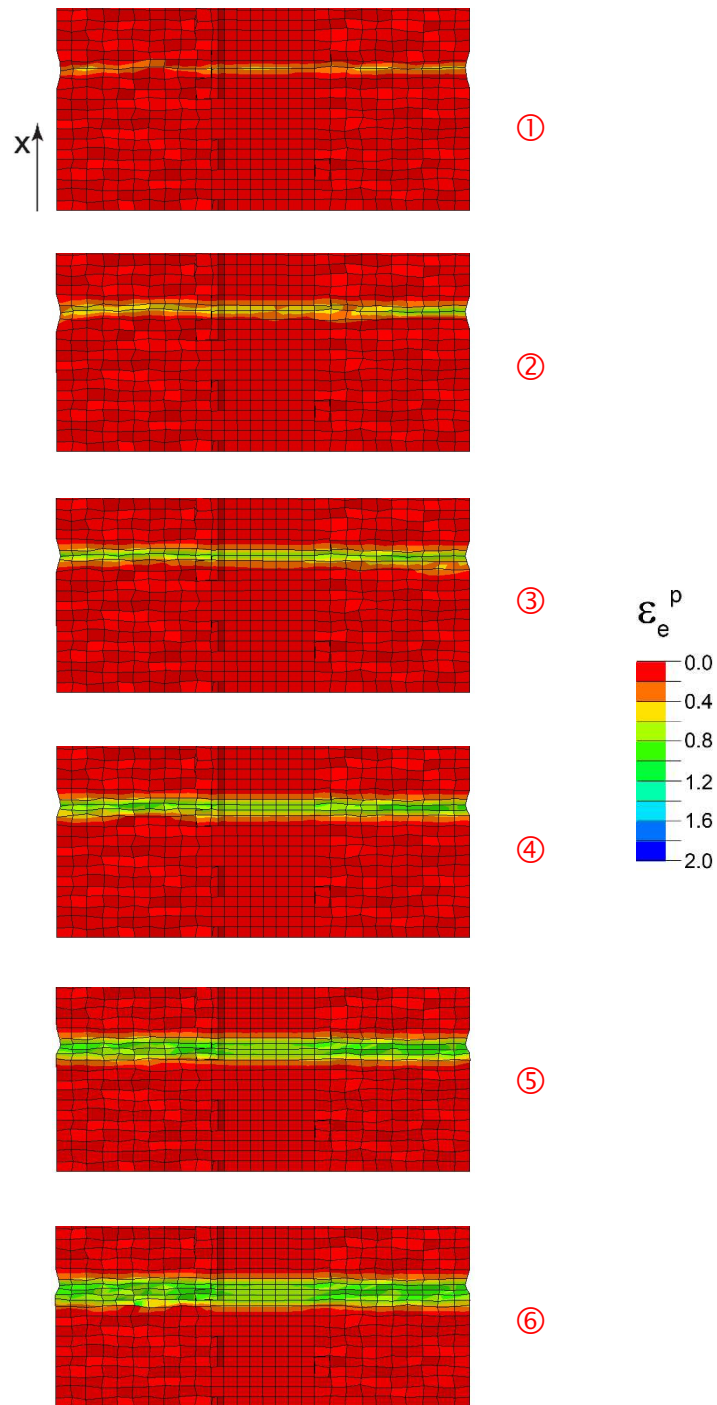
Fig. 6.16: Homogenized model deformed configurations for the early part of the response corresponding to the numbered bullets on the response in Fig. 6.15 (the upper half of the model is removed for better visualization).
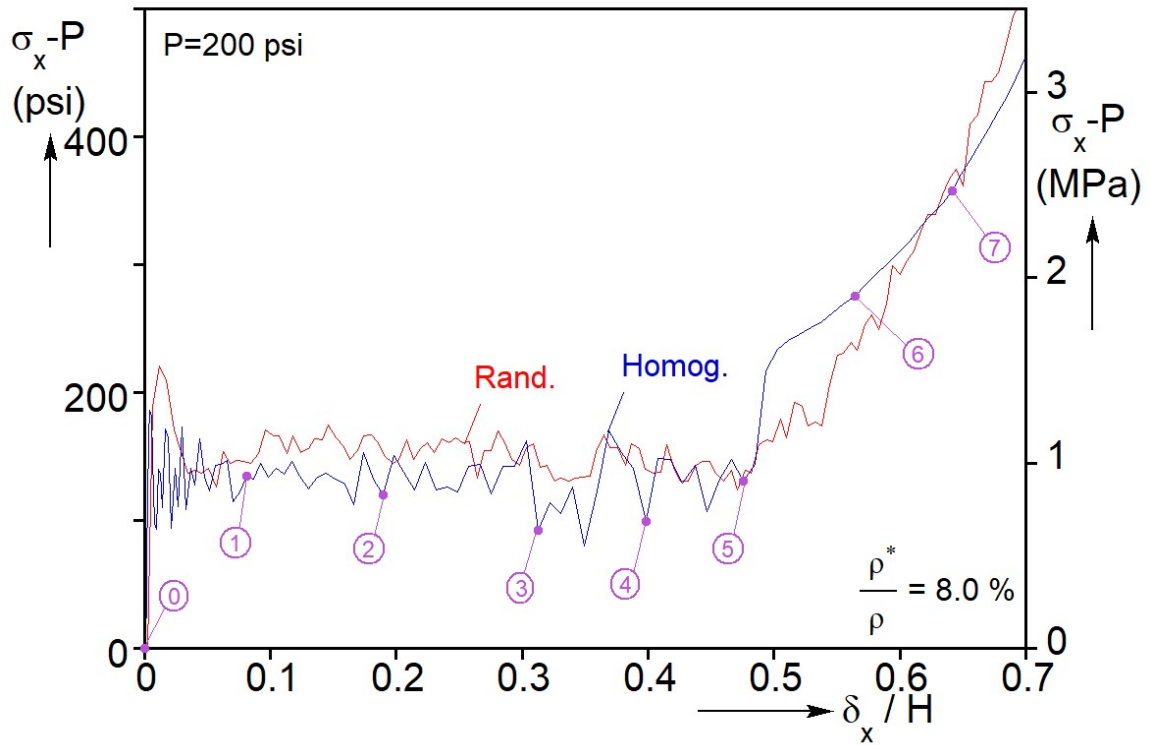
Fig. 6.17: Homogenized model axial deviatoric stress-displacement response for $P = 200$ psi (1.38 MPa) triaxial loading, and the corresponding response from the random foam model.
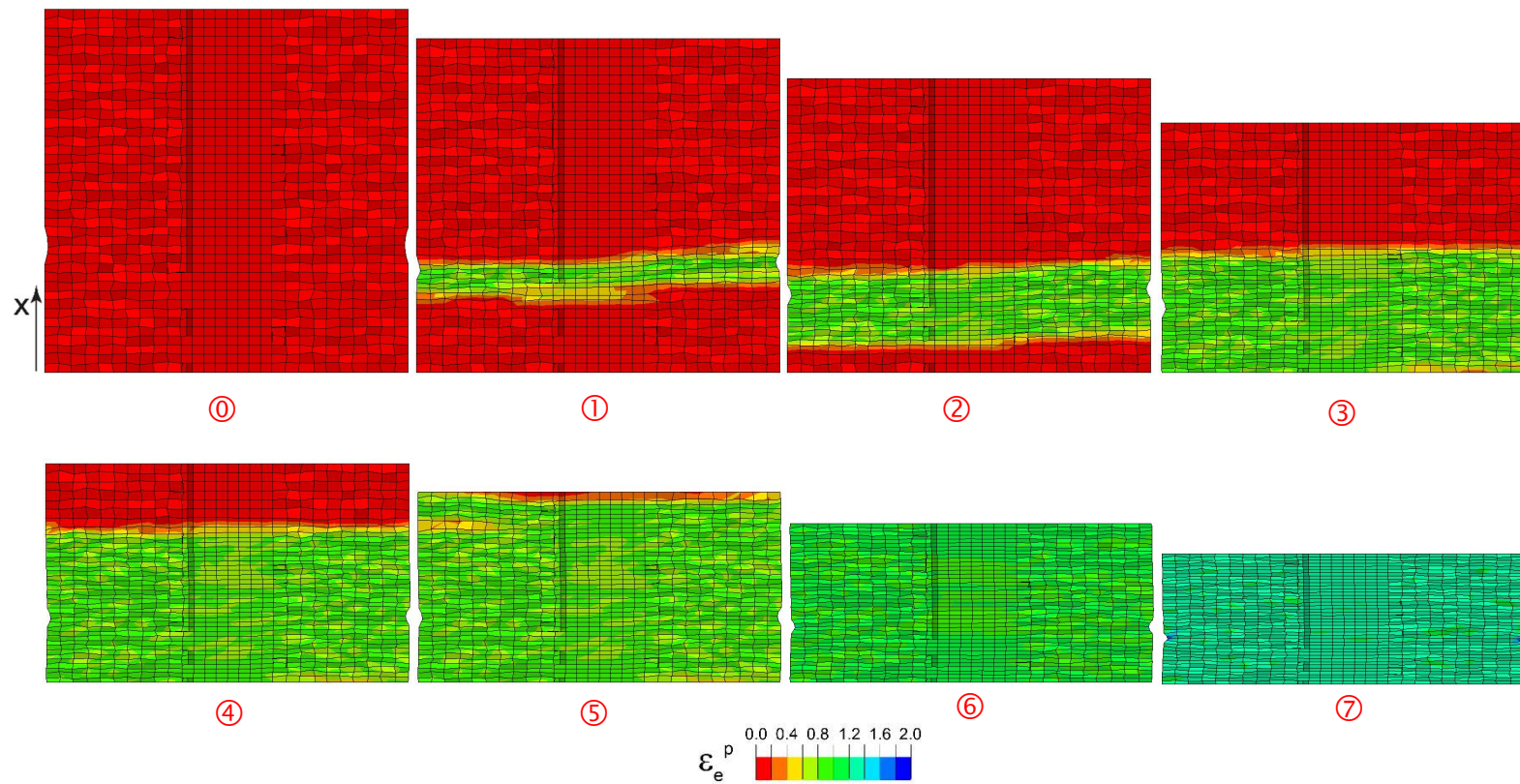
Fig. 6.18: Homogenized model deformed configurations from a central plane along the axis of the cylinder corresponding to the numbered bullets on the response in Fig. 6.17.
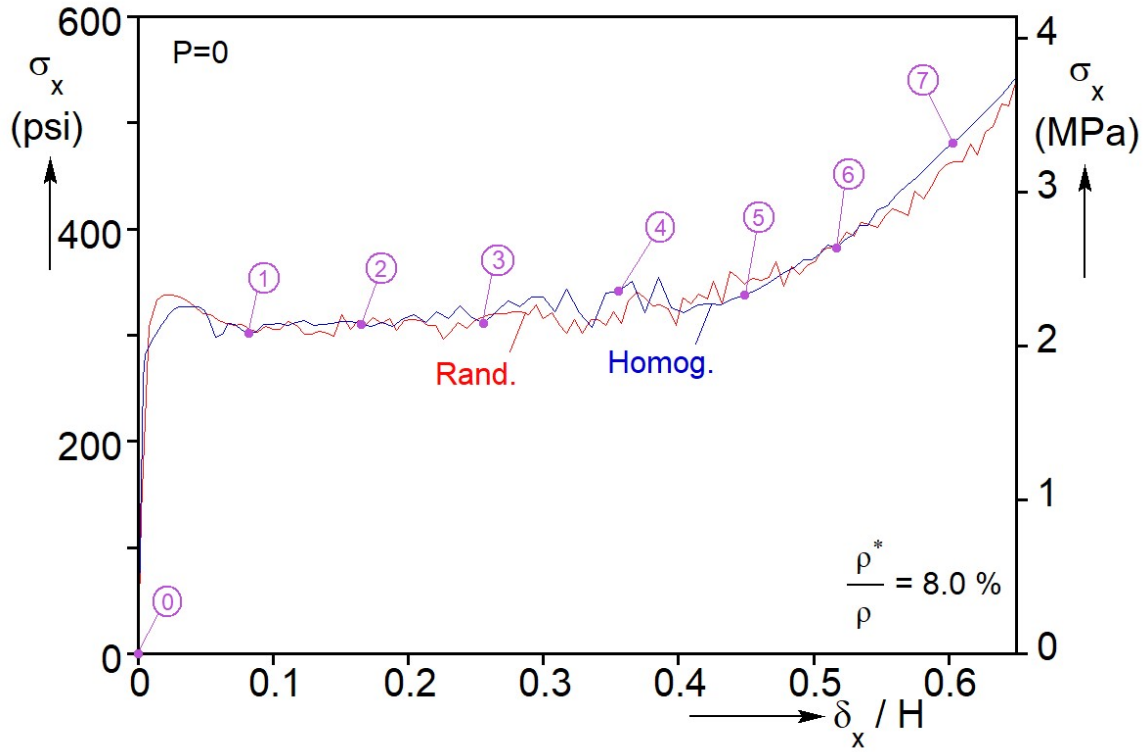
Fig. 6.19: Homogenized model axial deviatoric stress-displacement response for pure compression $P = 0$, and the corresponding response from the random foam model.
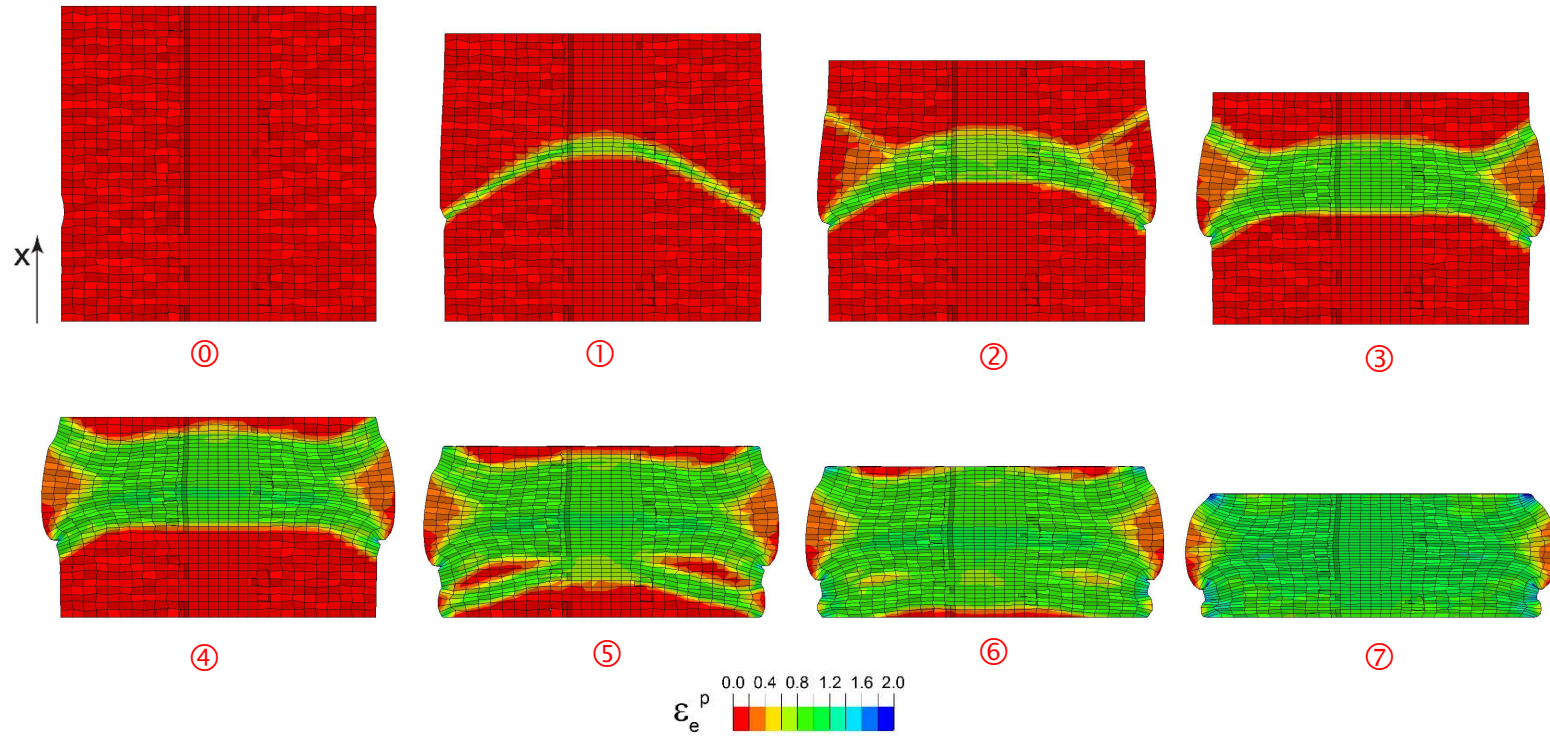
Fig. 6.20: Homogenized model deformed configurations from a central plane along the axis of the cylinder corresponding to the numbered bullets on the response in Fig. 6.19.

192
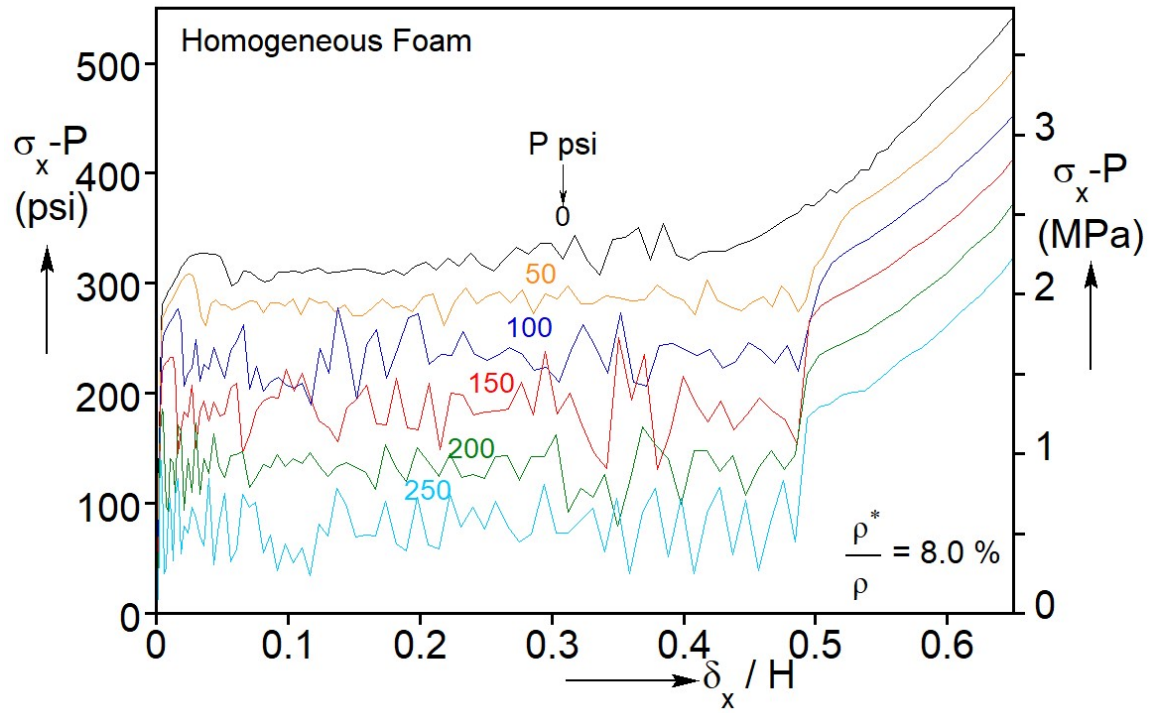
Fig. 6.21:   Homogenized model axial deviatoric stress-displacement responses for triaxial loading at six pressure levels.
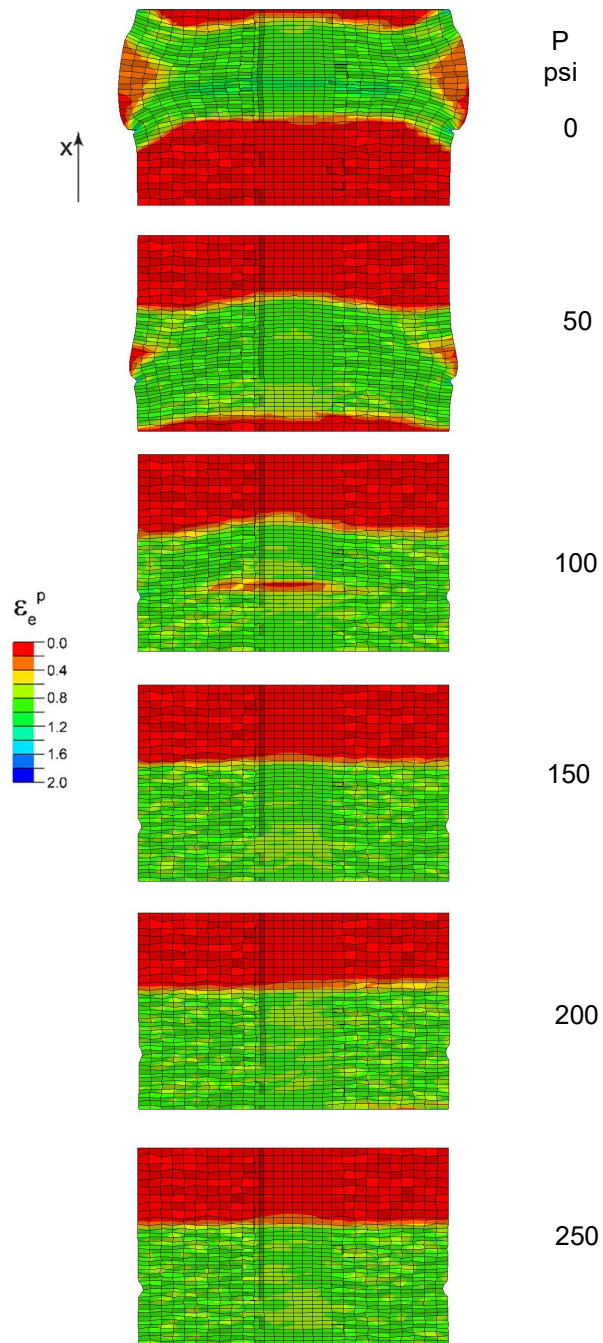
Fig. 6.22: Homogenized model deformed configurations at $\delta_x/L = 0.37$ for six pressure levels.

194
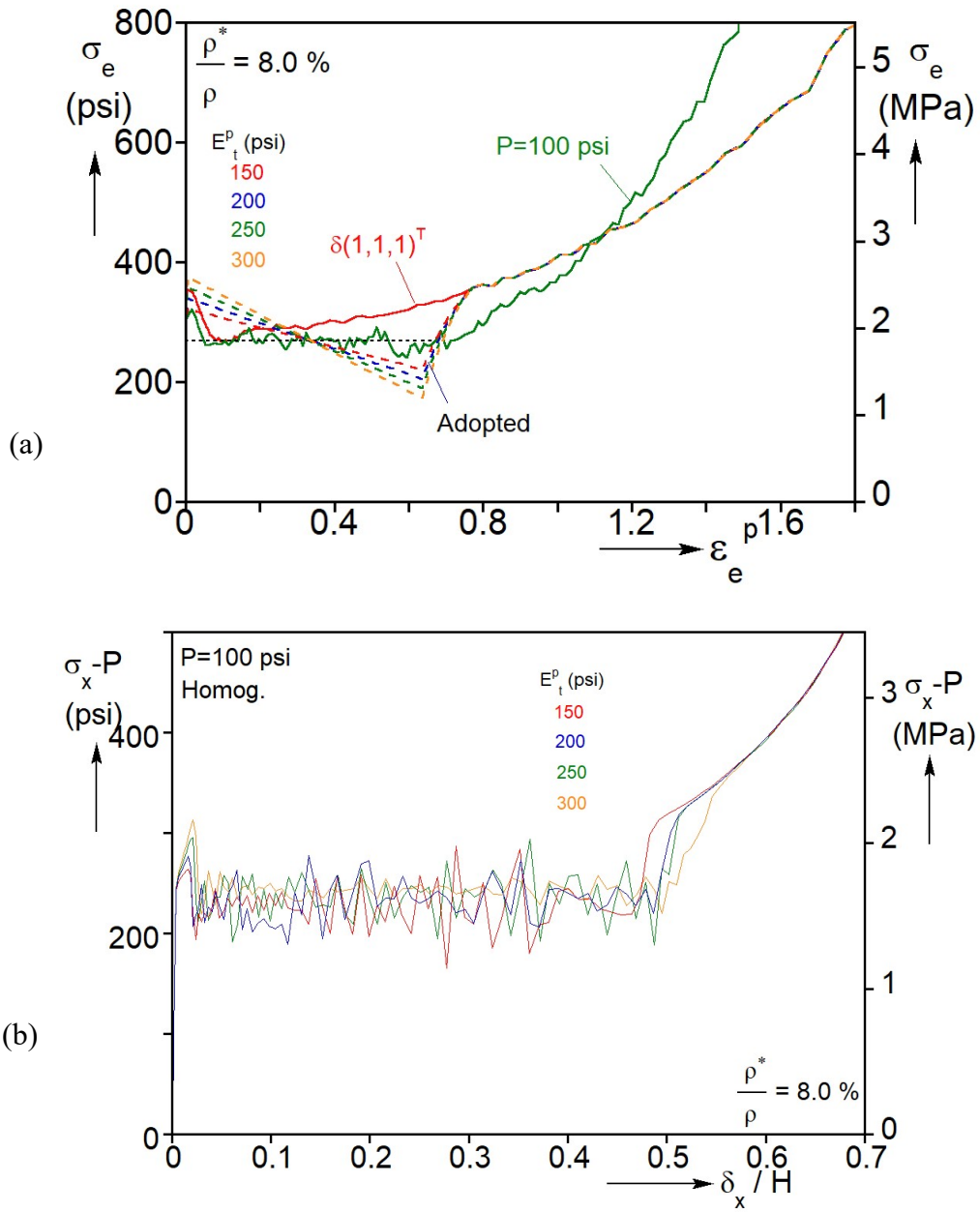
Fig. 6.23: (a) Equivalent stress-strain responses with four different slope softening branches. (b) Axial deviatoric stress-displacement responses at $P = 100$ psi (0.69 MPa) produced using the four stress-strain relations.
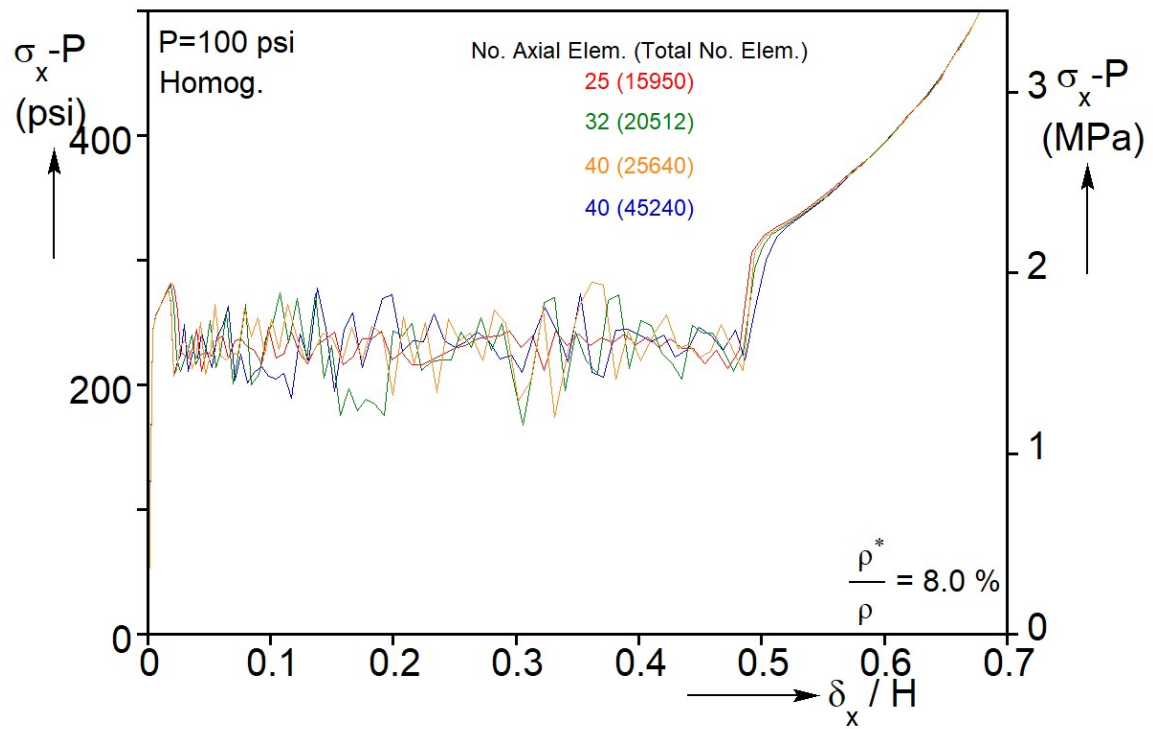
Fig. 6.24:   Comparison of axial deviatoric stress-displacement responses for P = 100 psi
             (0.69 MPa) using four different mesh densities.
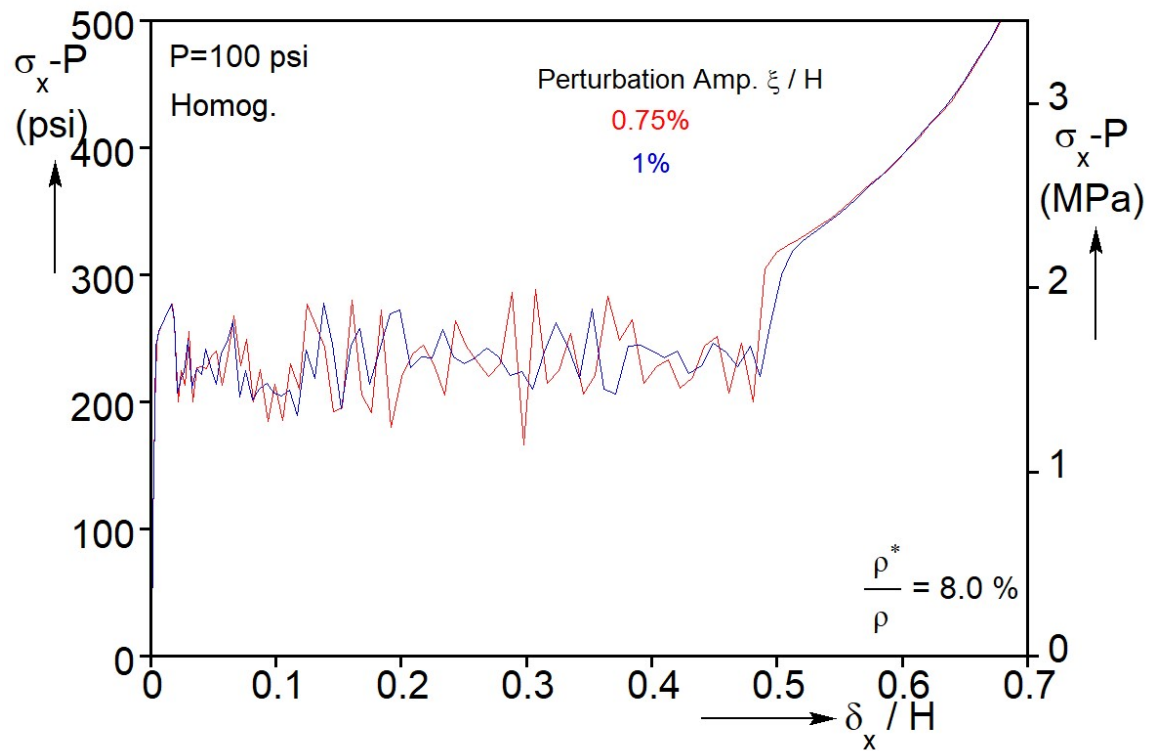
Fig. 6.25:   Axial deviatoric stress-displacement responses at P = 100 psi (0.69 MPa) produced using a mesh perturbed with two different amplitudes, ξ/H = 0.75% and 1%.

197
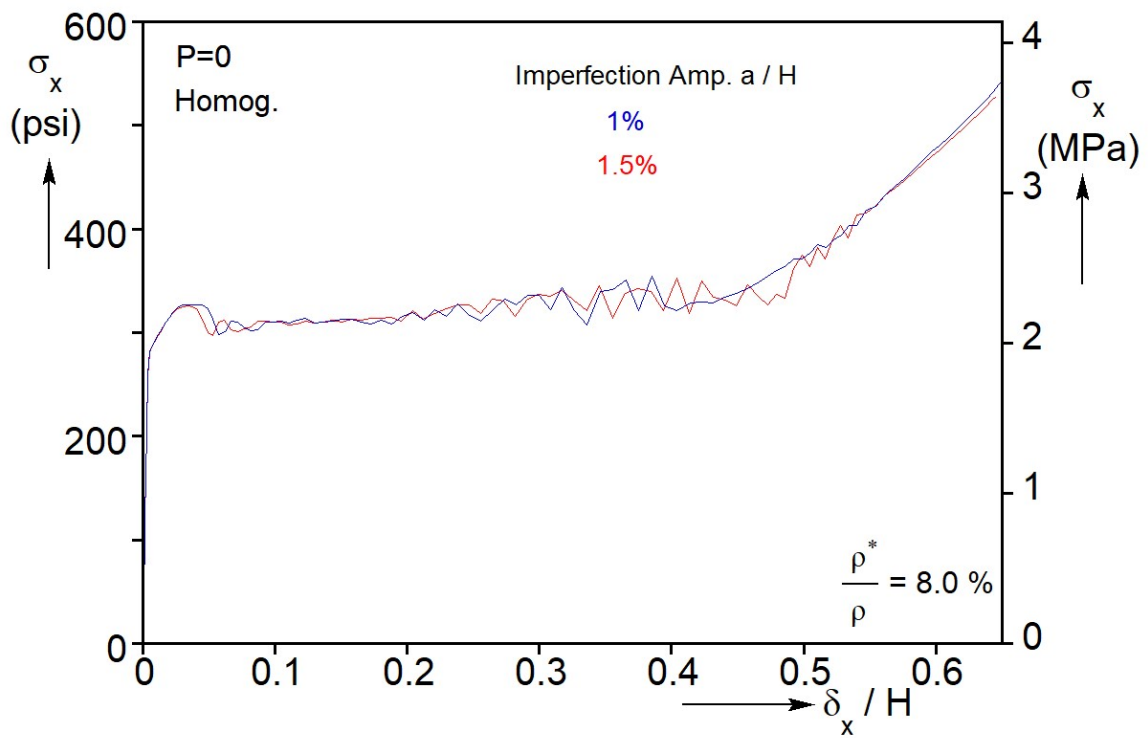
Fig. 6.26:   Axial stress-displacement responses for pure compression loading produced
using two imperfection amplitudes.
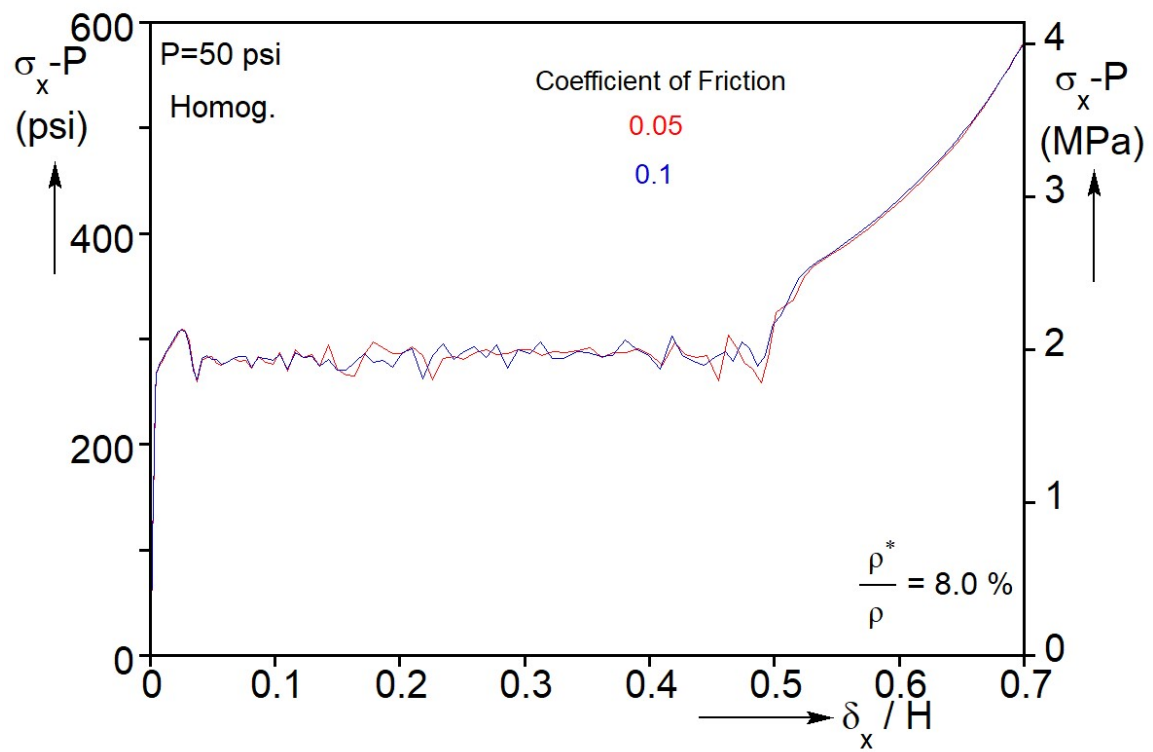
Fig. 6.27: Axial deviatoric stress-displacement responses for P = 50 psi (0.345 MPa) produced using two coefficients of friction.

Chapter 7: Summary and Conclusions

7.1 SUMMARY OF THE WORK

It is well established that low-density foams under compression initially exhibit an elastic and stable response, but at some stress level deformation localizes in narrow zones of crushing cells. The crushing propagates with the stress remaining relatively unchanged until the whole domain is crushed, and subsequently the densified material returns to stiff and stable response. Multiaxial crushing experiments on foams are difficult to perform because of the large volume changes involved and consequently the behavior of foams under triaxial loads to large deformation remains a challenging subject. The challenge has been addressed in the present study by numerical testing of micromechanically accurate models of an Al-alloy open-cell foam. Foams with random isotropic monodisperse cellular microstructure with relative density of 0.08 have been tested under true triaxial and conventional triaxial loadings. Homogenized "alternatives" have been developed to reproduce the inhomogeneous crushing behavior of the random foam.

The random foam model used in the study was developed in Chapter 2 based on the framework in Jang et al. (2008) and Gaitanaros et al. (2012). It is able to mimic the random microstructure of real foams and adopts a beam-to-beam contact algorithm essential for arresting local crushing of cells during the propagation phase of the response. The isotropic foam model used in this study has a cubical domain of 10^3 cells.

Cubical random foam models were first crushed in three orthogonal directions down to volume changes of about 70% using the numerical true triaxial apparatus described in Chapter 3. The apparatus is capable of prescribing displacements on foam blocks in the three directions simultaneously. Foams were crushed using three families of radial displacement loading paths. For all loading paths, the true stress-displacement responses traced in the x-, y- and z-directions show all the general characteristics observed in uniaxial crushing. They started with an initial linearly isotropic elastic branch that terminated into a stress maximum. Following the stress maxima, bands of locally collapsed cells initiated at boundaries and subsequently propagated to the rest of the domain, while the responses

started to trace plateaus. The plateaus in the three directions are extended in the primary loading direction, while limited in the other directions. As crushing continued, the propagation of the bands moved inwards, leaving the cells in the center of the domain essentially undeformed. At higher displacements, the responses traced stiff branches again. Other characteristics of the true triaxial crushing responses such as the mean stress-change in volume response and energy absorbed per unit undeformed volume were also reported. The study shows that low-density open-cell foams exhibit an inhomogeneous crushing behavior under true triaxial loadings.

Motivated by the triaxial crushing results of random foams, a compressible constitutive model has been developed in Chapter 4 aimed at capturing this partially inhomogeneous crushing behavior in the continuum setting. The model uses a Drucker-Prager type yield function, but with a non-associated plastic flow rule. The parameters for the constitutive model have been calibrated to the results of the triaxial crushing calculations reported in Chapter 3. An essential component of the modeling effort is the introduction of a softening branch to the material stress-strain response followed by a hardening branch.

The constitutive model was first incorporated in a cubical solid finite element model in Chapter 5 to analyze the crushing behavior under true triaxial loadings. The finite element model uses an irregular mesh of solid incompatible elements. The homogenized model was crushed along the same three sets of radial displacement paths used in the crushing of the random foams. Small geometric imperfections have been introduced to the three loading faces to help initiate localization. The results of these simulations show that the calculated crushing responses reproduce the trends of the random foam very well up to volume changes of about 50%. At higher displacements, the homogenized model results tend to under-predict those of the random foam. As pointed out by previous researchers, densification regime hardening appears to be deformation-dependent, a feature not captured by the simple compressible constitutive model adopted in this study.

The homogenized model lacks any of microstructural characteristics of the random foam. Consequently, the localization of deformation is driven by the geometric

imperfections introduced to the model. Thus for all cases analyzed localization nucleated from imperfections close to the stationary planes rather than at the contacting surfaces observed in the random foam. Despite these differences, as mentioned above, the calculated responses are reproduced quite accurately up to volume changes of about 50%.

The behavior of low-density foams under the more conventional triaxial loadings has been examined in Chapter 6. Random foam models were first crushed under six pressure levels by prescribing the displacement in one direction. For all loading paths the responses exhibit the same three-regime behavior as reported for true triaxial crushing results. During the propagation phase of crushing, local cell crushing initiated at an internal location with the "weakest" cells, and gradually spread with the stress tracing a plateau. The limit and plateau stresses follow decreasing trends with increase in pressure.

The conventional triaxial crushing tests have been simulated using the compressible constitutive model of Chapter 4 incorporated in a solid cylindrical finite element model. Localization, was initiated from small depression introduced to the outer surface and typically propagated in a planar manner until the whole domain was deformed. A ragged stress plateau was traced in the process. Perturbing the incompatible elements of the cylinder was found to result in smoother propagation. The homogenized model again captured all major aspects of the crushing responses of the random foam with good accuracy. The amplitude of the fluctuations mentioned above increased with the pressure level. It is quite possible that a better randomization of the mesh can result in a smoother stress plateau. In all stress histories, a band of higher deformation was developed from the imperfection and propagated to the rest of the domain.

7.2 CONCLUSIONS AND FUTURE WORK

The following main conclusions can be drawn for the work.

1.   The inhomogeneous crushing behavior previously observed in crushing experiments and modeling of open-cell Al-alloy foams has also been observed in the numerical triaxial tests reported in this work. This behavior was first observed in a set of radial displacement paths applied in the custom true triaxial apparatus

developed in Chapter 3. The inhomogeneous crushing was repeated in a set of conventional triaxial tests at different pressure levels. This behavior, reported for the first time, has implications when designing structures that include such foams.

2.   A compressible constitutive model calibrated to the true triaxial crushing results was incorporated in suitable finite element models and used to simulate the two sets of triaxial tests. The inclusion of a softening branch in the assumed material stress-strain relationship enabled the reproduction of the inhomogeneous crushing behavior for both sets of triaxial tests reported.

3.   Although the compressible constitutive model developed reproduces the inhomogeneous crushing behavior of random foams, the crushing responses at higher displacements tended to underestimate those of the random foams. Due to its simplicity the constitutive model exhibits a hardening dependence on equivalent strain. Alleviating this behavior will improve the constitutive model significantly. The fact that the equivalent stress–change in volume responses of the true triaxial tests coalesce may provide a useful insight in efforts to extend and improve the constitutive model.

4.   Crushing experiments under multiaxial loadings on foams that crush inhomogeneously under uniaxial compression are essential for expanded development of constitutive models that capture their behavior.

Appendix A: Isotropic Elastic Constitutive Relations of Foams under True Triaxial Crushing

The foam tested under triaxial loads in Chapter 3 exhibits in the initial stage of loading an isotropic elastic behavior and thus

$$\sigma_i = \frac{E^* v^*}{(1+v^*)(1-2v^*)} \varepsilon_{kk} + \frac{E^*}{1+v^*} \varepsilon_i, \quad i = x, y, z \tag{A.1}$$

where $\{\sigma_i, \varepsilon_i\}$ are true stresses and the logarithmic average strains the three directions. For each of the three families of radial loading paths described in Chapter 3, strains in the three directions are in a certain ratio (e.g., for $\delta(n,1,1)^T$ $\varepsilon_x = n\varepsilon_y = n\varepsilon_z$). Using Eq. (A.1), the constitutive relation in the x- and y-directions for the set $\delta(n,1,1)^T$ can be written as:

$$\frac{\sigma_x}{\varepsilon_x} = \frac{E^*}{(1+v^*)(1-2v^*)} \frac{n(1-v^*) + 2v^*}{n},$$

$$\frac{\sigma_y}{\varepsilon_y} = \frac{E^*}{(1+v^*)(1-2v^*)} (1+nv^*). \tag{A.2}$$

Similarly, constitutive relations in Eq. (3.7) for the $\delta(n,0.5,1)^T$ and Eq. (3.8) for $\delta(n,0,1)^T$ are derived.

The constants $\{E^*, v^*\}$ in Eq. (A.1) are determined from each family of loading paths as follows. First, σ_i / ε_i in the three directions are recorded from all six crushing calculations of each family. Each σ_i / ε_i is compared to one analytical solution $(\sigma_i / \varepsilon_i)_{analytical}$ from Eqs. (3.5), (3.7) and (3.8) with a guess for $\{E^*, v^*\}$ included. The error function for each σ_i / ε_i is thus designed as

$$err = \left[\sigma_i / \varepsilon_i - (\sigma_i / \varepsilon_i)_{analytical} \right]^2, \quad i = x, y, z. \tag{A.2}$$

A nonlinear optimization command *fminsearch* in Matlab is used to search for the values of $\{E^*, v^*\}$ for each loading family that minimize the sum of the error function from each σ_i / ε_i. The optimized elastic moduli for the three families appear in Figs. 3.16, 3.23 and 3.31 and are listed in Table 3.3.

Appendix B: Non-associated Plasticity

The yield surface adopted in Section 4.1, was calibrated to a set of triaxial stress states on random foams generated using the true triaxial apparatus in Chapter 3. In Fig. 4.1 and related text in Section 4.2.1 it was pointed out that the plastic flow direction $\left(\dfrac{3\partial g}{\partial I_1}, \dfrac{1}{\sqrt{3}}\dfrac{\partial g}{\partial J_2^{1/2}}\right)$ and the local normal $\left(\dfrac{3\partial f}{\partial I_1}, \dfrac{1}{\sqrt{3}}\dfrac{\partial f}{\partial J_2^{1/2}}\right)$ are different. The flow direction is determined form the random foam stress-strain increments as follows. Normality implies that for each loading path, the strain increment in the x- and z-directions can be expressed as

$$d\varepsilon_x^p = \Lambda\left(\frac{\partial g}{\partial I_1}\frac{\partial I_1}{\partial \sigma_x} + \frac{\partial g}{\partial J_2^{1/2}}\frac{\partial J_2^{1/2}}{\partial \sigma_x}\right),$$

$$d\varepsilon_z^p = \Lambda\frac{\partial g}{\partial \sigma_z} = \Lambda\left(\frac{\partial g}{\partial I_1}\frac{\partial I_1}{\partial \sigma_z} + \frac{\partial g}{\partial J_2^{1/2}}\frac{\partial J_2^{1/2}}{\partial \sigma_z}\right). \tag{B.1}$$

Using $\dfrac{\partial I_1}{\partial \sigma_i} = 1$ and $\dfrac{\partial J_2^{1/2}}{\partial \sigma_i} = \dfrac{s_i}{2\sqrt{J_2}}$, $i = x, z$, in (B.1) the flow direction components can then be expressed as

$$\frac{\partial g}{\partial I_1} = \frac{1}{3\Lambda}\left[3d\varepsilon_x^p - (d\varepsilon_x^p - d\varepsilon_z^p)\frac{s_x}{\sigma_x - \sigma_z}\right],$$

$$\frac{\partial g}{\partial J_2^{1/2}} = \frac{1}{\Lambda}\frac{2\sqrt{J_2}}{(\sigma_x - \sigma_z)}(d\varepsilon_x^p - d\varepsilon_z^p). \tag{B.2}$$

Normalizing by $1/\Lambda$, we obtain the flow direction

$$\left(\frac{3\partial g}{\partial I_1}, \frac{1}{\sqrt{3}}\frac{\partial g}{\partial J_2^{1/2}}\right) = \left(3d\varepsilon_x^p - (d\varepsilon_x^p - d\varepsilon_z^p)\frac{s_x}{\sigma_x - \sigma_z}, \frac{2\sqrt{3}J_2^{1/2}}{3(\sigma_x - \sigma_z)}(d\varepsilon_x^p - d\varepsilon_z^p)\right) \tag{B.3}$$

where σ_i is the true stress, s_x the deviatoric stress in the x-direction, and $d\varepsilon_i^p$ is the incremental plastic strain at the corresponding state.

Now, the flow direction can be calculated in the form of unit vectors using the measured stress and strain components at plastic work of $W^p = 0.09$ psi (0.62 kPa). The calculated flow direction is then compared to the local normal on the yield surface shown in Fig. 4.1. The results support that the model has a non-associated plastic flow.

References

Aakash, B.S., Bi, S., Shields, M.D., Gaitanaros, S., 2019. On the high-temperature crushing of metal foams. *Int'l J. Solids Structures* **174-175**, 18-27.

ABAQUS Analysis User's Manual. V. 6.13. Dassault Systems Simulia Corporation, 2014.

Ashby, M.F., Evans, A., Fleck, N.A., Gibson, L.J., Hutchinson, J.W. and Wadley, H.N.G., 2000. *Metal Foams: A Design Guide*. Butterworth-Heinemann.

Ayyagari, R.S., Vural, M., 2015. Multiaxial yield surface of transversely isotropic foams: Part I – Modeling. *J. Mechanics Phys. Solids* **74**, 49-67.

Ayyagari, R.S., Vural, M., 2016. On the nature of pressure dependence in foams. *Int'l J. Solids Structures* **78-79**, 160-173.

Banhart, J., 2003. Aluminum foams: on the road to real applications. *MRS Bull.* **28**, 290-295.

Bart-Smith, H., Bastawros, A.-F., Mumm, D.R., Evans, A.G., Sypeck, D.J., Wadley, H.N.G., 1998. Compressive deformation and yielding mechanisms in cellular Al alloys determined using X-ray tomography and surface strain mapping. *Acta Mater.* **46**, 3583-3592.

Bastawros, A.-F., Bart-Smith, H., Evans, A.G., 2000. Experimental analysis of deformation mechanisms in a closed-cell aluminum alloy foam. *J. Mechanics Phys. Solids* **48**, 301-322.

Blazy, J.-S., Marie-Louise, A., Forest, S., Chastel, Y., Pineau, A., Awade, A., Grolleron, C., Moussy, F., 2004. Deformation and fracture of aluminium foams under proportional and non-proportional multi-axial loading: statistical analysis and size effect. *Int'l J. Mech. Sciences* **46**, 217-244.

Brakke, K.A., 1992. The Surface Evolver. *Experimental Mathematics* **1**, 141-165. Available at http://www.susqu.edu/facstaff/b/brakke/evolver/

Chen, C., Lu, T.J., 2000. A phenomenological framework of constitutive modelling for incompressible and compressible elasto-plastic solids. *Int'l J. Solids Struct.* **37**, 7769-7786.

Combaz, E., Bacciarini, C., Charvet, R., Dufour, W., Mortensen, A., 2011. Multiaxial yield behaviour of Al replicated foam. *J. Mechanics Phys. Solids* **59**, 1777-1793.

Deshpande, V.S., Fleck, F.A., 2000. Isotropic constitutive models for metallic foams. *J. Mechanics Phys. Solids* **48**, 1253-1283.

Deshpande, V.S., Fleck, F.A., 2001. Multi-axial yield behaviour of polymer foams. *Acta Mater.* **49**, 1859-1866.

Drucker, D.C. and Prager, W., 1952. Soil mechanics and plastic analysis for limit design. *Quart. Appl. Math.* **10**, 157-165.

Enlighten presented by Altair website: https://altairenlighten.com/in-depth/sandwich-structures/

ERG website: http://ergaerospace.com/materials/duocel-aluminum-foam/

Fanelli, P., Evangelisti, A., Salvini, P., Vivio, F., 2017. Modelling and characterization of structural behavior of Al open-cell foams. *Mat'l. Design* **114**, 167-175.

Fischer, F., Lim, G.T., Handge, U.A., Altstadt, V., 2009. Numerical simulation of mechanical properties of cellular materials using computed tomography analysis. *J. Cellular Plastics* **45**, 441-460.

Fuganti, A., Lorenzi, L., Hanssen, A.G., Langseth, M., 2000. Aluminium foam for automotive applications. *Advanced Engineering Materials* **4**, 200-204.

Gaitanaros, S., Kyriakides, S., Kraynik, A.M. 2012. On the crushing response of random open-cell foams. *Int'l J. Solids Structures* **49**, 2733-2743.

Gaitanaros, S., Kyriakides, S., 2014. Dynamic crushing of aluminum foams: Part II – Analysis. *Int'l J. Solids Structures* **51**, 1646-1661.

Gaitanaros, S., Kyriakides, S., 2015. On the effect of relative density on the crushing and energy absorption of open-cell foams under impact. *Int'l J. Impact Eng.* **82**, 3-13.

Gaitanaros, S., Kyriakides, S., Kraynik, A.M., 2018. On the crushing of polydisperse foams. *Europ. J. Mech. A/Solids* **67**, 243-253.

Gdoutos, E.E., Daniel, I.M., Wang, K.-A., 2002. Failure of cellular foams under multiaxial loading. *Composites: Part A* **33**, 163-176.

Gibson, L.J., Ashby, M.F., 1997. *Cellular Solids: Structure and Properties, 2nd Ed.* Cambridge University Press.

Gioux, G., McCormack, T.M., Gibson, L.J., 2000. Failure of aluminum foams under multiaxial loads. *Int'l J. Mech. Sci.,* **42**, 1097-1117.

Gong, L., Kyriakides, S., Jang, W.-Y., 2005a. Compressive response of open-cell foams. Part I: Morphology and elastic properties. *Int'l J. Solids Structures* **42**, 1355-1379.

Gong, L., Kyriakides, S., 2005. Compressive response of open-cell foams Part II: Initiation and evolution of crushing. *Int'l J. Solids Structures* **42**, 1381-1399.

Gong, L., Kyriakides, S., Triantafyllidis, N., 2005b. On the stability of Kelvin cell foams under compressive loads. *J. Mech. Physics Solids* **53**, 771-794.

Hallai, J.F., Kyriakides, S., 2011. On the effect of Lüders bands on the bending of steel tubes. Part II: Analysis. *Int'l J. Solids & Struct.* **48**, 3285-3298.

Hallai, J.F., Kyriakides, S., 2013. Underlying material response for Lüders-like instabilities. *Int'l J. Plasticity* **47**, 1-12.

Hambly, E.C., 1969. A new true triaxial apparatus. *Geotechnique* **19**, 307-309.

Hassen, A.G., Langseth, M., Hopperstad, O.S., 2000. Static and dynamic crushing of square aluminium extrusions with aluminium foam filler. *Int'l J. Impact Eng.* **24**, 347-383.

Hughes, T.J.R., Liu, W.K., 1981. Nonlinear finite element analysis of shells-Part II. Two-dimensional shells. *Computer Meth. Applied Mech. Eng*. **27**, 167-181.

Jang, W.-Y., Kraynik, A.M., Kyriakides, S., 2008. On the microstructure of open-cell foams and its effect on elastic properties. *Int'l J. Solids & Structures* **45**, 1845-1875.

Jang, W.-Y., Kyriakides, S., 2009a. On the crushing of aluminum open-cell foams: Part I experiments. *Int'l J. Solids & Structures* **46**, 617-634.

Jang, W.-Y., Kyriakides, S., 2009b. On the crushing of aluminum open-cell foams: Part II analysis. *Int'l J. Solids & Structures* **46**, 635-650.

Jang, W.-Y., Kyriakides, S., Kraynik, A.M., 2010. On the compressive strength of open-cell foams with Kelvin and random cell structures. *Int'l J., Solids Structures* **47**, 2872-2883.

Jiang, D., Kyriakides, S., Bechle, N.J, Landis, C.M., 2017a. Bending of pseudoelastic NiTi tubes. *Int'l J. Solids & Structures* **124**, 192-214.

Jiang, D., Kyriakides, S., Landis, C.M., Kazinakis, K., 2017b. Modeling of propagation of phase transformation fronts in NiTi under uniaxial tension. *Euro. J. Mech. A/Solids* **64**, 131-142.

Jung, A., Diebels, S., 2017. Microstructural characterization and experimental determination of a multiaxial yield surface for open-cell aluminum foams. *Mat'l. Design* **131**, 252-264.

Jung, A., Grammes, T., Diebels, S., 2015. Micro-structural motivated phenomenological modelling of metal foams: experiments and modelling. *Arch. Appl. Mech.* **85**, 1147-1160.

Kraynik, A.M., 2003a. Foam Structure: Foam soap froth to solid foams. *MRS Bulletin* **28**/4, 275-278.

Kraynik, A.M., Reinelt, D.A., van Swol, F., 2003b. Structure of random monodisperse foam. *Physical Review E* **67**, 031403/1-11.

Kraynik, A.M., Reinelt, D.A., van Swol, F., 2004. Structure of random foam. *Phys. Rev. Lett.* **93**/20, 208301/1-4.

Kraynik, A.M., Reinelt, D.A., van Swol, F., 2005. Sturcture of random bidisperse foam. *Colloids and Surfaces A* **263**, 11-17.

Kraynik, A.M., 2006. The structure of random foam. *Advanced Engineering Materials* **8**/9, 900-906.

Laroussi, M., Sab, K., Alaoui, A., 2002. Foam mechanics: Nonlinear response of an elastic 3D-periodic microstructure. *Int'l J. Solids Structures* **39**, 3599-3623.

LS-DYNA Theory Manual, Livermore Software Technology Corporation, 2019.

Luxner, M.H., Stampfl, J., Pettermann, H.E., 2007. Numerical simulations of 3D open-cell structures – influence of structural irregularities on elasto-plasticity and deformation localization. *Int'l J. Solids Structures* **44**, 2990-3003.

Matzke, E.B., 1946. The three-dimensional shape of bubbles in foam-An analysis of the role of surface forces in three-dimensional shape determination. *American Journal of Botany* **33**, 58-80.

Miller, R.E., 2000. A continuum plasticity model for the constitutive and indentation behaviour of foamed metals. *Int'l J. Mech. Sciences* **42**, 729-754.

Mills, N.J., Fitzgerald, C., Gilchrist, A., Verdejo, R., 2003. Polymer foams for personal protection: cushions, shoes and helmets. *Composites Sci. Tech.* **63**, 2389-2400.

Mohr, D., Doyoyo, M., 2003. A new method of the biaxial testing of cellular solids. *Exp. Mech.* **43**, 173-182.

Needleman, A., 1988. Material rate dependence and mesh sensitivity in localization problems. *Comput. Methods Appl. Mech. Eng.* **67**, 69-85.

Papka, S.D. and Kyriakides, S., 1999a. Biaxial crushing of honeycombs: Part I Experiments. *Int'l J. Solids Structures* **36**, 4367-4396.

Papka, S.D. and Kyriakides, S., 1999b. In-plane biaxial crushing of honeycombs: Part II Analysis. *Int'l J. Solids Structures* **36**, 4397-4423.

Pearce, J.A., 1971. A new true triaxial apparatus. *Proceedings of the Roscoe Memorial Symposium*, Ed. R.H.G. Parry, G.T. Foulis & Co., pp. 330-339.

Plateau, J.A.F., 1873. Statique experimentale et theorique des liquids soumis aux seulex forces moleculaires. 2 Volumes, Gauthier-Villars, Paris.

Ruan, D., Lu, G., Ong, L.S., Wang, B., 2007. Triaxial compression of aluminium foams. *Composites Sci. Tech.* **67**, 1217-1234.

Schuler, P., Fischer, S.F., Buhrig-Polaczek, A., Fleck, C., 2013. Deformation and failure behaviour of open-cell Al foams under quasistatic and impact loading. *Materials Sci. & Eng. A* **587**, 250-261.

Shafiq, M., Ayyagari, R.S., Ehaab, M., Vural, M., 2015. Multiaxial yield surface of transversely isotropic foams: Part II Experimental. *J. Mech. Physics Solids* **76**, 224-236.

Tagarielli, V.L., Deshpande, V.S., Fleck, N.A., Chen, C., 2005. A constitutive model for transversely isotropic foams, and its application to the indentation of balsa wood. *Int'l J. Mech. Sciences* **47**, 666-686.

Takahashi, Y., Okumura, D., Ohno, N., 2010. Yield and buckling behavior of Kelvin open-cell foams subjected to uniaxial compression. *Int'l J. Mech. Sciences* **52**, 377-385.

Triantafillou, T.C., Zhang, J., Shercliff, T.L., Gibson, L.J., Ashby, M.F., 1989. Failure surfaces for cellular materials under multiaxial loads - II. Compression of models with experiment. *Int'l J. Mech. Sciences* **31**, 665-678.

Triantafillou, T.C., Gibson, L.J., 1990. Multiaxial failure criteria for brittle foams. *Int'l J. Mech. Sciences* **32**, 479-496.

Wang, Y., Gioia, G., Cuitino, A.M., 2000. The deformation habits of compressed open-cell solid foams. *ASME J. Eng. Mater. Tech.* **122**, 376-378.

Warren, W.E., Kraynik, A.M., 1997. Linear elastic behavior of a low-density Kelvin foam with open cells. *ASME J. Appl. Mech.* **64**, 787-793.

Weaire, D., Hutzler, S., 1999. *The Physics of Foams*. Oxford University Press, Oxford.

Wood, D.M., 1975. Explorations of principal stress space with kaolin in a true triaxial apparatus. *Geotechnique* **25**, 783-797.

Xue, Z., Hutchinson, J.W., 2004. Constitutive model for quasi-static deformation of metallic sandwich cores. *Int.l J. Numer. Meth. Eng.* **61**, 2205-2238.

Yang, C., Kyriakides, S., 2019a. Multiaxial crushing of open-cell foams. *Int'l J. Solids & Structures* **159**, 239-256.

Yang, C., Kyriakides, S., 2019b. Continuum modeling of crushing of low-density foams. *J. Mechanics Phys. Solids,* https://doi.org/10.1016/j.jmps.2019.103688.

Zhang, J., Lin, Z., Wong, A., Kikuchi, N., Li, V.C., Yee, A.F., Nusholtz, G.S., 1997. Constitutive modeling and material characterization of polymeric foams. *J. of Eng. Mater. Tech.* **119**. 284-291.

Zhu, C., Zheng, Z., Wang, S., Zhao, K., Yu, J., 2019. Modification and verification of the Deshpande-Fleck foam model: a variable ellipticity. *Int'l J. Mech. Sciences* **151**, 331-342.

Zhu, W., Blal, N., Cunsolo, S., Baillis, D., 2017. Micromechanical modeling of effective elastic properties of open-cell foam. *Int'l J. Solids & Structures* **115-116**, 61-72.

Vita

Chenglin Yang was born in Nanchang, China on October 25, 1992, the son of Jinghui Shi and Yujiang Yang. He entered University of Science and Technology of China in August 2008 and graduated with a B.S. degree on Theoretical and Applied Mechanics in May 2012. Since August 2012, he has been studying at the University of Texas at Austin in pursuit of a Ph.D. degree in Engineering Mechanics. He made a number of presentations at national and international conferences, and co-authored the following journal publications:

Yang, C., Kyriakides, S., 2019. Multiaxial crushing of open-cell foams. *Int'l J. Solids Structures* **159**, 239-256. https://doi.org/10.1016/j.ijsolstr.2018.10.005.

Yang, C., Kyriakides, S., 2019. Continuum modeling of crushing of low-density foams. *J. Mech. Phys. Solids,* https://doi.org/10.1016/j.jmps.2019.103688.

Yang, C., Kyriakides, S., 2019. Crushing of low density foams under triaxial loadings. *Extreme Mechanics Letters* (accepted)

Permanent email: yclin19@utexas.edu

This dissertation was typed by the author.